



Characterization and pre-treatment of
Jatropha curcas seed cake for co-firing with coal

Buddhike Neminda Madanayake, BEng (Hons)

Department of Chemical and Environmental Engineering

Student ID: 012265

Thesis submitted to the University of Nottingham for the
degree of Doctor of Philosophy

2016

Abstract

In the light of growing concern over greenhouse gas emissions and limited fossil fuels, the use of renewable energy sources such as biomass is becoming more vital. *Jatropha curcas* seed cake, which is a waste product of biodiesel production, has been identified as a potential candidate to be co-fired with coal in existing boilers. There is a dearth of information on the effective utilisation of *Jatropha curcas* seed cake in this manner, and this research work contributes to bridging this knowledge gap. The seed cake received was divided into two distinct classes based on appearance and texture, identified as type A (harder and lower oil content) and type B (the more abundant class). As an initial step, the fundamental fuel properties of the seed cake were determined; these include the proximate and ultimate analyses, higher heating value (HHV) and inorganic content. The HHV of type A and type B was 20.76 MJ/kg and 24.06 MJ/kg, respectively; their dry ash content was 5.9% and 4.4%, respectively. K was the most abundant inorganic element present.

The main hindrances to co-firing of a typical biomass with coal arise due to the difference in properties of biomass and coal. Torrefaction and leaching were carried out with the aim of bringing the thermochemical (primarily the HHV) and chemical (inorganic content) properties, respectively, of the seed cake closer to those of coal. An envelope of torrefaction conditions was recommended – ~250°C for 45-60 min for the type A, and <5 min at >280°C to >45 min at 220°C-250°C for the type B. These conditions ensured that the HHV of the type A and type B were enhanced to >24.5 MJ/kg and >27 MJ/kg, respectively, while not compromising excessively on the energy yield. Leaching at 20°C for <24 h was considered adequate in the case of the untorrefied seed cake, and this resulted in a reduction of the potassium content (the most abundant and critical inorganic element in the seed cake) by 85%. Leachability of the torrefied biomass was markedly reduced, and leaching at least at 50°C was deemed necessary.

Combustion modelling using Ansys Fluent 14.0 was carried out to assess the combustion and co-firing characteristics of untorrefied and torrefied *Jatropha curcas* seed cake. The effect of torrefaction on the devolatilisation characteristics, flame properties and consequently NO_x pollutant formation was established. Compared to the torrefied biomass, the untorrefied seed cake devolatilised earlier, had a more dispersed flame and higher NO formation. The higher reactivity of the biomass was shown to have a positive effect on the devolatilisation rate of the less reactive coal under co-firing simulations.

Publications

- Madanayake, B. N., Gan, S., Eastwick, C., Ng, H.K., 2016. Thermochemical and structural changes in *Jatropha curcas* seed cake during torrefaction for its use as coal co-firing feedstock. *Energy*, 100, 262-272.
- Madanayake, B. N., Gan, S., Eastwick, C., Ng, H.K., 2015. Leaching as a Pretreatment Process to Complement Torrefaction in Improving Co-firing Characteristics of *Jatropha curcas* Seed Cake. *Waste and Biomass Valorization*. (Accepted, available online).
- Madanayake, B. N., Eastwick, C., Gan, S., Ng, H.K., 2014. The Effects of Torrefaction Parameters on the Thermochemical Properties of *Jatropha curcas* Seed Cake. *World Sustainable Energy Days Next 2014* (Conference Proceedings), 155-162.

Under review:

- Madanayake, B. N., Gan, S., Eastwick, C., Ng, H.K., 2016. Biomass as an energy source in coal co-firing and its feasibility enhancement via pre-treatment techniques. *Waste and Biomass Valorization*.
- Madanayake, B. N., Gan, S., Eastwick, C., Ng, H.K., 2016. An investigation into the use of CFD to model the co-firing of *Jatropha curcas* seed cake with coal. *International Journal of Green Energy*.

Conferences/presentations

- Speaker at World Sustainable Energy Days 2014 (hosted by ÖO Energiesparverband) in Wels, Austria.
- Poster presentation at the annual Research Showcase 2015 at the University of Nottingham Malaysia Campus.

Acknowledgments

I would like to express my sincere gratitude to my supervisors, Prof Gan Suyin, Dr Carol Eastwick and Prof Ng Hoon Kiat, for their endless support, guidance and patience over the course of my PhD work.

This study would not have been possible without the support from the Faculty of Engineering of the University of Nottingham (UK and Malaysia) under the Engineering InterCampus PhD Scholarship. I would also like to thank ACGT Sdn. Bhd. (Malaysia) and Dr Cheah Suan Choo for providing the *Jatropha curcas* seeds.

I am also deeply grateful to Seyed Amirmostafa Jourabchi, Orla Williams, Tom Bennet, Archi Sarroza, Gary Newbolt, Timipere Farrow and Miguel Castro Diaz for their valuable assistance at various stages of my work. Thanks are also due to Dr Scott Young, Lolit Wilson and Saul Reina Vazquez at the School of Biosciences for arranging the ICP-MS and ion chromatography.

Finally, I wish to thank my parents, Ranjith and Tharanga, and my sister, Yeshmitha, for their unconditional support over the years.

Contents

1. INTRODUCTION	1
1.1 Background	1
1.2 Aim and objectives	7
1.3 Thesis structure	8
2 LITERATURE REVIEW	9
2.1 Introduction	9
2.2 Biomass	9
2.3 Biomass characterization	11
2.3.1 Chemical properties	12
2.3.2 Thermochemical properties	16
2.4 Biomass combustion	19
2.4.1 Drawbacks of biomass combustion/co-firing	20
2.4.2 Biomass co-firing technology	22
2.5 Biomass pre-treatment	26
2.5.1 Leaching	26
2.5.2 Torrefaction	38
2.5.3 Mechanical pre-treatment	50
2.5.4 Biological pre-treatment	522
2.5.5 Energy/cost considerations	53
2.6 Combustion modelling	56
2.6.1 Overview	56
2.6.2 CFD sub-models	58
2.7 <i>Jatropha curcas</i>	65
2.8 Concluding remarks	67
3 METHODOLOGY	69
3.1 Introduction	69
3.2 Biomass feedstock	71
3.3 Pre-treatment	73
3.3.1 Torrefaction	73
3.3.2 Leaching	75
3.4 Characterisation	79
3.4.1 Thermogravimetric analysis	79
3.4.2 Calorimetry	86
3.4.3 CHON elemental analysis	89
3.4.4 XRF spectrometry	92

3.4.5	¹³ C NMR spectroscopy.....	94
3.4.6	ICP-MS.....	97
3.4.7	Ion chromatography	99
3.5	Drop tube furnace testing.....	100
3.6	Concluding remarks.....	103
4	BIOMASS CHARACTERISATION.....	104
4.1	Introduction.....	104
4.2	Proximate analysis	104
4.3	Ultimate analysis.....	106
4.4	HHV.....	108
4.5	Inorganic content	109
4.6	Devolatilisation kinetics	111
4.7	Comparison with other biomass varieties	115
4.8	Concluding remarks.....	117
5	TORREFACTION	118
5.1	Introduction.....	118
5.2	Primary torrefaction study	120
5.2.1	Mass yield, HHV, energy yield	121
5.2.2	Fixed carbon (FC) content.....	129
5.2.3	Ultimate analysis	132
5.2.4	¹³ C NMR spectroscopy.....	136
5.2.5	Differential thermogravimetry.....	139
5.3	Secondary torrefaction study	147
5.3.1	Mass yield, HHV, energy yield	148
5.3.2	Fixed carbon (FC) content.....	154
5.4	Discussion.....	157
5.5	Concluding remarks.....	162
6	LEACHING	163
6.1	Introduction.....	163
6.2	Preliminary leaching study	165
6.2.1	Inorganic content – ICP-MS/IC.....	165
6.2.2	Inorganic content - XRF.....	171
6.2.3	Summary of preliminary results	176
6.3	Primary leaching study	177
6.3.1	Physical appearance	177
6.3.2	Electrical conductivity (EC).....	178
6.3.3	Ion analysis of leachate	182

6.3.4	Inorganic content - XRF	184
6.3.5	Dry ash free volatile matter (DAF VM) content and higher heating value (HHV)	191
6.4	Secondary leaching study	193
6.5	Discussion	196
6.6	Concluding remarks	199
7	COMBUSTION MODELLING	201
7.1	Introduction	201
7.2	Geometry and meshing	203
7.2.1	Mesh optimisation	206
7.3	Sub-models	208
7.3.1	Turbulence	208
7.3.2	Chemistry and turbulence-chemistry interaction	209
7.3.3	Discrete phase	210
7.3.4	Radiation	212
7.3.5	NO _x	213
7.4	Model validation	215
7.4.1	Drop tube furnace testing	215
7.4.2	Sensitivity analyses	217
7.4.3	Stochastic tracking	225
7.5	Finalised model and results	228
7.5.1	Material properties	228
7.5.2	Individual biomass/coal combustion	229
7.5.3	Coal co-firing	233
7.6	Concluding remarks	237
8	CONCLUSIONS AND FUTURE WORK	239
8.1	Conclusions	239
8.2	Future work	242
	References	244
	Appendices	262
	Appendix 1 – Matlab script to calculate devolatilisation kinetics	262
	Appendix 2 – Matlab script for DTG processing	263
	Appendix 3 – Full data sets: Characterisation	264
	Appendix 4 – Full data sets: Torrefaction	267
	Appendix 5 – Full data sets: Leaching	274
	Appendix 6 – Regression plots for HHV vs DAF FC content	277
	Appendix 7 – Lenth’s pseudo-standard-error	279

List of figures

Figure 2-1: Overview of co-firing configurations.....	23
Figure 2-2: Schematic diagrams of co-firing configurations: (a) direct, (b) indirect, (c) parallel. 23	
Figure 2-3: Effect of torrefaction temperature on grinding energy consumption (Yan & Acharjee, 2009)	49
Figure 3-1: Overview of methodology used in this thesis.....	70
Figure 3-2: Jatropha curcas seed cake (a) as received, (b) type A, (c) type B.	72
Figure 3-3: (a)(b) Ball mill, (c) sieve shaker used on type A biomass.....	72
Figure 3-4: Horizontal tube furnace used for torrefaction.....	73
Figure 3-5: Schematic diagram of HTF used for torrefaction.....	74
Figure 3-6: Shaking water bath used for the leaching runs.....	76
Figure 3-7: Glass jars with Milli-Q water used for the leaching runs.....	76
Figure 3-8: Jars with biomass loaded, secured in the water bath.....	76
Figure 3-9: Filtration to separate biomass from leachate.....	78
Figure 3-10: Drying of leached biomass samples in vacuum oven.....	78
Figure 3-11: TA Instruments Q500 used for thermogravimetric analysis (TGA).....	80
Figure 3-12: Typical TGA trace used for proximate analysis.....	80
Figure 3-13: Weight loss profiles for preliminary TGA runs carried out with full-length temperature profile.....	82
Figure 3-14: IKA C5000 bomb calorimeter.....	87
Figure 3-15: (a) Sample in combustible bag, (b) combustion vessel (c) suspended crucible.....	87
Figure 3-16: Control panel of calorimeter with display showing the progress of the run.....	87
Figure 3-17 (a) FlashEA CHON analyser (b) MAS 200 autosampler.....	90
Figure 3-18: Typical chromatogram obtained from the EA instrument.....	90
Figure 3-19: Tin container (a) before sample is loaded, (b) folded into capsule.....	90
Figure 3-20: Bruker S8 Tiger XRF spectrometer.....	93
Figure 3-21: (a)(b) Plastic sample container, (c) steel holder with sample container within.....	93
Figure 3-22: (a) Zirconia rotor for holding sample, (b) tool for compressing sample in rotor.....	95
Figure 3-23: Bruker NMR system.....	95
Figure 3-24: Unprocessed NMR spectrum.....	96
Figure 3-25: NMR spectrum after post-processing.....	96
Figure 3-26: Digestion of solid samples on hot plate.....	98
Figure 3-27: Digested samples of (a) untorrefied, (b) torrefied biomass.....	98
Figure 3-28: Thermo iCAP-Q ICP-MS unit.....	98
Figure 3-29: Eppendorf tube with biomass sample and deionised water.....	99
Figure 3-30: Schematic diagram of DTF.....	101
Figure 3-31: Heater controls for the DTF.....	102

Figure 3-32: (a) Top of DTF showing feeder probe with funnel attached, (b) bottom section of DTF showing end of collector probe.	102
Figure 4-1: Inorganic content of <i>Jatropha curcas</i> seed cake.....	111
Figure 4-2: Devolatilisation DTG curves of type A seed cake.	112
Figure 4-3: Devolatilisation DTG curves of type B seed cake.....	112
Figure 4-4: Coats-Redfern plots for type A seed cake.	113
Figure 4-5: Coats-Redfern plots for type B seed cake	113
Figure 4-6: Variation of HHV with O/C ratio for different types of biomass	116
Figure 5-1: Flowchart of overall methodology of torrefaction study.....	119
Figure 5-2: Interaction plot for the mass yield, grouped by holding time.....	122
Figure 5-3: Interaction plot for the mass yield, grouped by torrefaction temperature.	122
Figure 5-4: Interaction plot for the HHV, grouped by holding time.	123
Figure 5-5: Interaction plot for the HHV, grouped by torrefaction temperature.....	123
Figure 5-6: Interaction plot for the energy yield, grouped by holding time.	126
Figure 5-7: Interaction plot for the energy yield, grouped by torrefaction temperature.....	126
Figure 5-8: Main effects plots for (a) mass yield, (b) HHV, (c) energy yield.....	128
Figure 5-9: Interaction plot for the DAF FC content, grouped by holding time.	130
Figure 5-10: Interaction plot for the DAF FC content, grouped by torrefaction temperature.	130
Figure 5-11: Scatter plot of HHV against DAF FC content.....	132
Figure 5-12: Interaction plots for elemental (a) dry C, (b) dry H, (c) dry N, (d) dry O.	133
Figure 5-13: van Krevelen diagrams of (a) torrefied <i>Jatropha</i> seed cake grouped by holding time,	135
Figure 5-14: ¹³ C NMR spectra for (a) untreated <i>Jatropha</i> seed cake and <i>Jatropha</i> seed cake torrefied for 60 min at (b) 200°C, (c) 250°C, (d) 300°C.....	137
Figure 5-15: DTG plot of untreated type B.....	140
Figure 5-16: DTG plots for type B biomass torrefied for (a) 0 min, (b) 30 min, (c) 60 min.....	142
Figure 5-17: DTG plots for type B biomass torrefied at (a) 200°C, (b) 250°C, (c) 300°C.	143
Figure 5-18: Interaction plot for the P1 peak height.	145
Figure 5-19: Interaction plot for the P2 peak heights.....	145
Figure 5-20: DTG plots of untreated type A and type B biomass.....	146
Figure 5-21: Interaction plot for mass yield, grouped by holding time.....	148
Figure 5-22: Interaction plot for the mass yield, grouped by torrefaction temperature.	148
Figure 5-23: Interaction plot for the HHV, grouped by holding time.	150
Figure 5-24: Interaction plot for the HHV, grouped by torrefaction temperature.....	150
Figure 5-25: Interaction plot for the energy yield, grouped by holding time.	151
Figure 5-26: Interaction plot for the energy yield, grouped by torrefaction temperature.....	151
Figure 5-27: Main effects plots for (a) mass yield, (b) HHV, (c) energy yield.....	153
Figure 5-28: Interaction plot for the DAF FC content, grouped by holding time.	154

Figure 5-29: Interaction plot for the DAF FC content, grouped by torrefaction temperature.	154
Figure 5-30: Scatter plot of HHV vs DAF FC content.....	155
Figure 5-31: Contour plots of (a) HHV, (b) energy yield (EY), (c) overlay of HHV and EY for type B.....	158
Figure 5-32: Contour plots of (a) HHV, (b) energy yield (EY), (c) overlay of HHV and EY for type A.....	160
Figure 6-1: Flowchart of overall methodology of leaching study.....	164
Figure 6-2: Inorganic content of untorrefied type B biomass, measured by ICP-MS/IC.....	167
Figure 6-3: Inorganic content of untorrefied, leached type B biomass, measured by ICP-MS/IC.....	168
Figure 6-4: Inorganic content of torrefied, leached type B biomass, measured by ICP-MS/IC..	169
Figure 6-5: Inorganic content of untorrefied, leached type B biomass, measured by XRF spectrometry.....	172
Figure 6-6: Inorganic content of torrefied, leached type B biomass, measured by XRF spectrometry.....	173
Figure 6-7: Pareto charts of XRF-measured (a) K, (b) Mg, (c) Ca.....	174
Figure 6-8: Progression of mean EC with time.....	179
Figure 6-9: Final EC after 24 h (type B).....	181
Figure 6-10: Average leaching rate of type B biomass.....	181
Figure 6-11: Net ion concentration and EC after 24 h (type B).....	183
Figure 6-12: Total inorganic content from XRF for leached and unleached type B.....	185
Figure 6-13: Factorial plots for XRF content of type B (a) K interaction, (b) Mg interaction, (c) P interaction, (d) Cl interaction, (e) Ca main effects and (f) S main effects.....	187
Figure 6-14: Interaction plot of type B DAF VM content.....	192
Figure 6-15: Interaction plot of type B HHV.....	193
Figure 6-16: Inorganic content from XRF (untorrefied type A and type B).....	194
Figure 6-17: Factorial plots for XRF content of type A (a) K interaction, (b) Ca interaction, (c) Mg interaction, (d) P interaction, (e) Cl main effects, (f) Cl interaction and (g) S interaction.....	195
Figure 7-1: Overall workflow for combustion modelling study.....	202
Figure 7-2: Schematic of DTF, showing the volume that is modelled (Sarroza et al., 2004).	203
Figure 7-3: Geometry created in Ansys DesignModeler.....	205
Figure 7-4: Generated mesh (mesh no. 3) showing boundary names and flow direction.....	205
Figure 7-5: Variation of monitors with maximum face size.....	207
Figure 7-6: Variation of no. of cells and average time per iteration with maximum face size. ..	208
Figure 7-7: Interval plot of the empirical VMCs, error bars show the standard error.....	217
Figure 7-8: Type A particles as observed by (a) Camsizer, (b) SEM.....	219
Figure 7-9: Particle distribution for untorrefied type A, measured by Camsizer.....	219
Figure 7-10: Variation of VMC with particle diameter (untorrefied case).....	220

Figure 7-11: Variation of VMC with particle diameter (torrefied case)	220
Figure 7-12: Variation of VMC with particle density	223
Figure 7-13: Variation of VMC with shape factor	224
Figure 7-14: Variation of VMC with emissivity	225
Figure 7-15: Particle tracks with stochastic tracking enabled for (a) untorrefied, (b) torrefied biomass.....	227
Figure 7-16: Temperature distributions for (a) inert particle, (b) coal, (c) untorrefied biomass, (d) torrefied biomass.....	231
Figure 7-17: Devolatilisation rate for (a) untorrefied, (b) torrefied biomass.	232
Figure 7-18: Effect of co-firing ratio on coal VMC	233
Figure 7-19: Temperature distribution for co-firing with (a)25%, (b)50%, (c)75% untorrefied biomass	234
Figure 7-20: Temperature distribution for co-firing with (a)25%, (b)50%, (c)75% torrefied biomass	235
Figure 7-21: Effect of co-firing ratio on normalised NO emissions (untorrefied biomass)	236
Figure 7-22: Effect of co-firing ratio on normalised NO emissions (torrefied biomass)	237

List of tables

Table 2-1: Summary of biomass characterisation methods.....	18
Table 2-2: Bibliographic compilation of the advantages and disadvantages of the three types of combustion systems	25
Table 2-3: Bibliographic compilation of selected leaching studies.....	32
Table 2-4: Differences in properties between coal and biomass (Demirbaas, 2003)	38
Table 2-5: Bibliographic compilation of selected dry torrefaction studies	40
Table 2-6: Mass and energy yields of dry and wet torrefaction	47
Table 2-7:Energy and mass yields of pine biomass following torrefaction (Yan & Acharjee, 2009)	48
Table 2-8: H/C and O/C ratios of pine biomass following torrefaction (Yan & Acharjee, 2009)	48
Table 2-9: Summary of major pre-treatment techniques.....	55
Table 2-10: Comparison of experimental and CFD investigations	56
Table 2-11: Recent biomass combustion/co-firing modelling studies	64
Table 2-12: Characterisation of Jatropha seeds (Doshi et. al, 2014; Singh et. al, 2008).....	67
Table 3-1: Summary of changes made to TGA profile.	83
Table 4-1: Proximate analysis of Jatropha curcas seed cake.....	105
Table 4-2: Ultimate analysis of Jatropha curcas seed cake.	107
Table 4-3: As-measured CHN content of Jatropha curcas seed cake and BBOT reference material.	108

Table 4-4: HHV of <i>Jatropha curcas</i> seed cake and benzoic acid reference material.....	109
Table 4-5: Inorganic content of <i>Jatropha curcas</i> seed cake.....	110
Table 4-6: Devolatilisation kinetic parameters of <i>Jatropha curcas</i> seed cake.	114
Table 4-7: Comparison of thermochemical properties of common biomass varieties.	116
Table 5-1: Comparison of HHV enhancement obtained in recent torrefaction studies.....	125
Table 5-2: p- and F-values from ANOVA test of mass yield, HHV, energy yield data.....	127
Table 5-3: Main effects changes in mean mass yield, HHV, energy yield over full range of factors.	129
Table 5-4: Regression coefficients and statistics for HHV vs DAF FC.....	132
Table 5-5: p-values from ANOVA of dry CHON.....	134
Table 5-6: Temperatures at which lignocellulosic components undergo decomposition.....	140
Table 5-7: p-values from ANOVA test of P1 and P2 peak heights.....	144
Table 5-8: p- and F-values obtained from ANOVA test on mass yield, HHV, energy yield data.	152
Table 5-9: Main effects changes in mean mass yield, HHV, energy yield over full range of factors.	152
Table 5-10: Regression coefficients and statistics for HHV vs DAF FC.....	156
Table 6-1: p-values from ANOVA of type B ICP-MS/IC data.....	170
Table 6-2: Significance of factors and interactions obtained from Pareto charts.....	176
Table 6-3: p-values from ANOVA of type B XRF data	188
Table 6-4: p-values from ANOVA of type A XRF data	194
Table 7-1: Summary of fundamental DTF settings and dimensions.....	204
Table 7-2: Summary of boundary conditions used.	204
Table 7-3: Mesh properties	206
Table 7-4: Summary of models and model parameters used	214
Table 7-5: Calculation of volatile matter conversion % (VMC).....	217
Table 7-6: Key material/particle properties used in the finalised model.....	228

Nomenclature

CFD – computational fluid dynamics

HTF – horizontal tube furnace

DTF – drop tube furnace

TGA – thermogravimetric analysis

DTG – differential thermogravimetry

ICP-MS – inductively coupled plasma mass spectroscopy

IC – ion chromatography

XRF – X-ray fluorescence (spectrometry)

NMR – nuclear magnetic resonance (spectroscopy)

HPLC – high performance liquid chromatography

DAF – dry, ash-free

FC – fixed carbon

VM – volatile matter

HHV – higher heating value

EC – electrical conductivity

CV – coefficient of variation

AFI – ash fusibility index

FBC – fluidized bed combustor

PFC – pulverised fuel combustor

CFB – circulating fluidised bed

UT – untorrefied

LT – torrefied at 200°C for 30 min

MT – torrefied at 250°C for 30 min

HT – torrefied at 300°C for 30 min

VMC – volatile matter conversion

DPM – discrete phase model

EDM – eddy dissipation model

ST – stochastic tracking

E – activation energy
 A – pre-exponential factor
 R – universal gas constant
 T – absolute temperature
 V – dry volatile matter content
 A – dry ash content
 i – chemical species
 Y_i – local mass fraction of chemical species
 J_i – diffusion flux of chemical species
 R_i – net rate of production of chemical species by reaction
 u_p – particle component velocity
 u – velocity
 ρ_p – particle density
 ρ – fluid density
 F_D – drag force
 g_x – gravitational force component
 m_p – particle mass
 C_D – drag coefficient
 Re – Reynold's number
PSE – pseudo-standard error
K – potassium
Mg – magnesium
Ca – calcium
P – phosphorous
S – sulphur
Cl – chlorine
C – carbon
H – hydrogen
O – oxygen

1. INTRODUCTION

1.1 Background

At present, annual global energy consumption stands at approximately 507 EJ, with approximately 80% of this energy being derived from fossil fuels, i.e. coal, oil and natural gas (IEA, 2015). Such a high dependency on fossil fuels for our energy requirements represents a significant problem on a global scale.

The nature of this problem is two-fold. The combustion of fossil fuels poses environmental risks in terms of emissions. The primary concern with emissions is with regard to carbon dioxide (CO₂), a known greenhouse gas and a contributor to global warming. CO₂ levels have increased post-industrialization from 280 ppm to approximately 400 ppm, with the rise being primarily attributed to fossil fuel use (IPCC, 2014; NASA, 2016). Global mean temperatures have increased by 0.85°C over the period from 1880 to 2012 (IPCC, 2014). According to various models – for instance by Meehl et al. (2005) and the IPCC (2007) – the average global temperature at the end of the 21st century could increase by as much as 6°C. It is well-established that global warming at this rate would have devastating environmental, biological, and socio-economic effects. Rising sea-levels would cause widespread destruction in low-lying countries in terms of both human property and animal habitats. The changing rainfall patterns resulting from the climatic changes would adversely affect agriculture. Increasing temperatures have already been proven to reduce crop yields (Lobell & Field, 2007; Peng et al., 2004).

The other facet of this issue is the non-renewable nature of fossil fuels. Fossil fuels which include coal, petroleum and natural gas are formed by pre-historic biological matter (dead organisms) being trapped under layers of rock and undergoing compaction, hardening and chemical transformation under the effects of extreme

temperature and pressure (Novaczek, 2000; Speight, 2005). The problem lies in the fact that this process occurs over a geological timescale, often hundreds of millions of years (Hubbert, 1949; Mann et al., 2003). Hence, the rate at which new deposits are formed is negligible compared to the rate at which they are consumed, and hence fossil fuels are considered a finite source of energy. There are varying estimates as to how long these reserves would last. The US Energy Information Administration (EIA, 2013a; EIA, 2013b) estimates that the total global coal reserves as standing at 948,000 million short tons, while current global consumption is about 8100-8200 million short tons per annum; at current consumption rates, coal reserves would thus be depleted in just over 115 years. The World Energy Council (WEC, 2010) claims a coal reserves to production ratio of 128 years. However, it should be noted that the consumption rate of fossil fuels is continuously increasing, and this would potentially have a significant effect on these estimates. Coal is expected to see the greatest surge in consumption, with the WEC (2010) estimating an increase of more than 60% and the IEA (2007) predicting one of 73%, by 2030. A model by Shafiee & Topal (2009), which attempts to account for increasing consumption, forecasted a depletion time of 107 years.

Coal is the most abundant of the fossil fuels. Reserves of petroleum and natural gas are predicted to be exhausted even before those of coal. According to the EIA, the global oil reserves and consumption stand at 1360 billion barrels and 31 billion barrels per year, respectively (EIA, 2013e; EIA, 2013f); those of natural gas are 6670 trillion cubic feet and 119 trillion cubic feet per year, respectively (EIA, 2013c; EIA, 2013d). At these consumption rates, petroleum reserves would last 44 years, while natural gas would run out in 56 years. Shafiee & Topal's (2009) aforementioned model predicted oil and natural gas to run out in 35 and 37 years, respectively. The IEA (2007) meanwhile expects oil reserves to be sufficient only until 2030.

Thus, it is clear that there should be a decrease in our dependence on fossil fuels as an energy source. The switch to clean and renewable sources of energy is imperative due to the criticality of the aforementioned issues associated with traditional fossil fuels. This is reflected in the attention given to renewable energy in policies implemented at both national and international levels. One key piece of legislation is the Renewable Energy Directive formulated by the European Union (EU, 2009). This directive makes it mandatory for EU member nations to reach certain targets with regard to the use of renewable energy, so that a minimum 20% of the entire EU's energy production is from renewable sources by 2020. Another more recent development is the launching of the United Nations' Sustainable Energy for All initiative (UN, 2012). Among the key objectives of this initiative is doubling the share of global energy obtained from renewable sources by 2030 (UN, 2013; United Nations Foundation, 2013). The importance of this project lies in the fact that it has a global outreach and aims to promote renewable energy on a global scale. Hence, its focus lies on decreasing the dependency on fossil fuels of both developing and developed nations, which require different strategies. In addition to these international initiatives, policies and legislation have been introduced on a national level by various countries as well. These include the US Clean Energy Standard Act (US Senate, 2012), the Japanese Basic Energy Plan (Ministry of Economy Trade and Industry of Japan, 2010), and China's Renewable Energy Law (National People's Congress, 2005).

By definition, renewable energy is obtained from sources which are considered to be non-finite. Some of them – wind power, solar power, hydropower and tidal power – do not “consume” a resource and depend on naturally-occurring phenomena. Geothermal power taps into and technically “consumes” energy stored in the Earth's crust, but this energy is abundant enough to be considered non-finite. Energy derived

from biomass can be considered renewable as long as the consumed biomass is grown sustainably and is replenished (Frey & Linke, 2002).

The electricity generation sector is rapidly adopting renewable energy sources. As of end-2014, about 23% of electricity being produced and more than half of new generation facilities installed that year employed renewable sources (REN21, 2015).

Biomass is one of the most important of the renewable resources, and has the potential to become one of the key contributors towards the switch to renewable energy in the future. Currently, biomass represents about 10% of the global energy mix. This is a significant portion, and means that biomass trails only coal, oil and natural gas in terms of energy share. However, a large portion (approximately 60%) of the total global bioenergy demand is in the form of so-called traditional biomass, where the biomass is directly combusted (usually inefficiently) for heating, cooking or industrial purposes. However, the trend in the use of biomass for power generation has been very positive, with capacity growing by 9% in 2014 (REN21, 2015).

One of the key drivers behind the use of biomass is that the energy conversion technology employed is very similar to that used for fossil fuels (if the combustion route is employed). This means that biomass combustion is a promising method of increasing the share of renewables in the global energy mix in the short to medium term. Other conversion techniques include thermochemical methods such as pyrolysis and gasification, as well as the biochemical approach. However, combustion remains the most important conversion route for the present and the near future, accounting for a significant percentage of biomass power generation (Demirbas, 2004; Demirbas, 2006).

Biomass can be combusted by itself in power generation facilities, which are very similar in operating principle to power plants which utilise conventional solid fossil fuels, i.e. coal. It can also supplement coal in existing power generation facilities, and thus avoid the high initial installation costs which can prove to be a deterrent to the implementation of new renewable energy technology. Of these two options (pure biomass combustion and co-firing with coal), co-firing is currently the preferable method. Compared to combusting biomass as a single fuel, co-firing biomass with coal reduces the impact on the power plant's operation by seasonal changes in availability of biomass. Also, dedicated biomass plants are typically in the range of 20 MW to 100 MW and have high capital costs, whereas conversion of existing conventional coal power plants to co-firing plants incurs a lower capital cost and also provides capacity of several hundred MW (Bakis, 2007; Chum et al., 2011; Hein & Bemtgen, 1998). More than 200 co-firing plants are known to be in operation globally, with the majority of them in Northern Europe and the United States, followed by Asia and Australia (IEA-ETSAP & IRENA, 2013).

The feedstock of interest in this project is *Jatropha curcas*. *Jatropha curcas* is garnering increasing attention as a source of bioenergy. Also known as Physic or Barbados nut, *Jatropha curcas* is a species of shrub which belongs to the genus *Euphorbiacea*. There are several attributes of the plant that makes it attractive as a source of bioenergy. It is resistant to droughts, and thrives in Central and South America, South East Asia, India and Africa. It is well adapted to the arid conditions in some of these areas (Gübitz et al., 1999). Another important characteristic of *Jatropha* is its toxicity (which makes it non-edible) – this ensures that the energy industry does not have to compete with the food industry over the plant's bioresources, as is the case

with other bioenergy sources such as palm oil and sugar cane (Wever et al., 2012). This in turn improves the economic viability of using the products from *Jatropha*.

Currently, most research in this particular area focuses on the extraction of oil from the *Jatropha* seed. The oil can be used directly in certain diesel engines, or it can be processed into conventional biodiesel (Sricharoenchaikul & Atong, 2009). Unprocessed *Jatropha* oil has seen successful use in diesel engine trials, and has shown low exhaust emissions compared to fuel-oil obtained from other vegetation sources, and has also shown favourable power outputs and fuel consumption figures when compared to conventional diesel. For use in higher-speed diesel engines (for instance, those used in road vehicles), the oil has to be transesterified by using methanol or ethanol (Gübitz et al., 1999). However, the yield of fuel oil is only about 18% by mass of the dry *Jatropha* fruit. Hence, during the production of oil/diesel from *Jatropha*, a considerable amount of biomass is discarded as waste, and there is the potential to extract energy from this waste seed cake as well via other means. This would maximise the usage of the *Jatropha* fruit, and could possibly double or triple the total energy yield from the fruit (Singh et al., 2008). Investigating the feasibility of co-firing the *Jatropha curcas* seed cake is thus a worthy avenue of research.

1.2 Aim and objectives

There is currently a dearth of information on the potential use of the *Jatropha curcas* seed cake as a fuel. The aim of this project is to investigate the effective utilization of *Jatropha* seed cake as a solid fuel to be co-fired with coal, for instance in pulverised fuel boilers. This would involve characterization of the fuel, exploring the use of torrefaction and leaching pre-treatments to make it suitable for co-firing, and assessing the combustion behaviour of the seed cake.

The specific objectives of this work are as follows:

1. Determine the fundamental fuel properties of *Jatropha curcas* seed cake.
2. Investigate the relative effects of varying torrefaction temperature and holding time on the fundamental fuel properties of *Jatropha curcas* seed cake and develop a set of recommended guidelines for the torrefaction of *Jatropha curcas* seed cake.
3. Investigate the underlying chemical/structural changes occurring in *Jatropha curcas* seed cake during the torrefaction process.
4. Identify the most significant factors affecting the leaching efficacy of *Jatropha curcas* seed cake and develop a set of recommended guidelines for the leaching of *Jatropha curcas* seed cake.
5. Conduct combustion modelling to assess the combustion and co-firing characteristics of untorrefied and torrefied *Jatropha curcas* seed cake.

1.3 Thesis structure

This thesis is composed of eight chapters, as follows:

Chapter 1 provides a background to the problem and the key drivers behind this research work. The main aim as well as the specific objectives of the work are defined.

Chapter 2 is a literature review, which begins with a comprehensive introduction to biomass and its characterisation, and the state of co-firing technology. Following this is a detailed review of contemporary biomass pre-treatment techniques. The existing literature with regard to modelling of biomass combustion and co-firing is then reviewed. Finally, the state of research concerning *Jatropha curcas* is presented.

Chapter 3 outlines the experimental methodology followed. The *Jatropha curcas* seed cake used as well as the experimental methods and equipment are detailed here. These include the torrefaction and leaching procedures as well as the characterisation and combustion testing techniques.

Chapter 4 presents the fundamental characterisation results of the *Jatropha curcas* seed cake used.

Chapters 5 and 6 present the experimental design and the results from the torrefaction and leaching studies, respectively. In each case, the practical implications of the results are discussed and guidelines are recommended.

Chapter 7 encompasses the combustion modelling study. This includes the methodology followed and the sub-models used, followed by a validation of the model using experimental data from the combustion testing. The results from the model are then discussed, and their reliability and implications assessed.

Chapter 8 discusses the overall conclusions from the work and makes recommendations for future work.

2 LITERATURE REVIEW

2.1 Introduction

This chapter begins with a comprehensive introduction to biomass and its physicochemical characterisation as a fuel. Following this is a review on current biomass co-firing technology and the difficulties encountered – biomass co-firing is not without its own set of drawbacks. These issues are primarily caused by the difference in properties between coal and biomass. To minimise the implications thereof, various biomass pre-treatment techniques have been investigated and implemented with success. The major part of this chapter is devoted to a detailed review on pre-treatment techniques which are applicable to a wide range of biomass feedstock. A particular emphasis is placed on torrefaction and leaching which are potentially two of the most important strategies to improve the fuel properties of biomass, and explores these two techniques in greater detail. The final section of this chapter reviews the use of computational fluid dynamics (CFD) as a tool to model the combustion and co-firing of biomass.

2.2 Biomass

The term “biomass” refers to a solid product which is a combination of organic and inorganic matter. Its distinguishing characteristics are that it is formed by life processes (biogenic) and is contemporaneous (as opposed to fossil fuels such as coal) (Vassilev et al., 2010; Vassilev et al., 2012). The most crucial biological process involved in the natural production of biomass is photosynthesis. Photosynthesis is the process by which the chlorophyll pigment in plant matter uses sunlight to convert atmospheric CO₂ and water to produce carbohydrates. What is essentially being carried out is that the energy in sunlight is being stored in chemical bonds in the carbohydrates formed. This energy can be recovered for human consumption by

carrying out an appropriate process on the biomass, for example combustion. The cycle completes, and CO₂ and water are once again produced, while the energy stored in the bonds is extracted.

As Pérez et al. (2002) describes, these carbohydrates are the basis of the biomass matter, and can be classified into three main groups – cellulose, hemicellulose and lignin (collectively termed lignocellulose). Hemicellulose consists of several sugars linked to form polymer chains. Cellulose is also a polymer, but consists primarily of glucose, and has a higher average molecular weight than hemicellulose. Lignin has the highest average molecular weight and consist of interlinked carbon chains and rings; it is also the most difficult to decompose into its constituents. These three classes of carbohydrates have different physical and thermochemical behaviours. Hence, depending on the relative proportions of each class present, different biomass varieties can have a wide range of characteristics.

Biomass can be classified in several ways, but a typical breakdown would be woody biomass, herbaceous biomass, aquatic biomass and wastes (which include manure, sewage, refuse containing biological matter, etc.). The method of utilising a particular type of biomass typically depends on which of the above categories it falls into. An overview of biomass energy conversion options by McKendry (2002a; 2002b) explains the correlation between the type of biomass and the conversion method. The moisture content is a primary deciding factor in choosing which energy conversion process to use, and the moisture present varies greatly from category to category. The latter two generally have the highest moisture content, and is more suited to biochemical methods (which do not require a dry substrate). Such methods include fermentation and anaerobic digestion. Anaerobic digestion is typically used for biomass with moisture content ranging from 80% to 90% (McKendry, 2002b). Woody

biomass has the lowest moisture levels, while herbaceous biomass has an intermediate range. Most industrial applications have been centred about thermochemical processes which utilise woody biomass and low-moisture varieties of herbaceous biomass. These processes include combustion, gasification and pyrolysis.

Combustion entails burning the biomass in the presence of oxygen (O_2), whereby the energy stored in the chemical bonds within the carbohydrate molecules, is converted into heat and mechanical energy. Temperatures exceeding 800°C can be reached. Gasification involves applying high temperatures ($800\text{-}900^\circ\text{C}$) in order to cause partial oxidation of the biomass. This results in the evolving of a gas which can be combusted as a fuel, or used to manufacture other chemicals such as methanol. Pyrolysis is a non-oxidative process, where the biomass is heated in an inert atmosphere to about 500°C . The subsequent thermochemical decomposition results in the production of solid, liquid, and gaseous components. The solid charcoal, liquid bio-oil, and the evolved gases can all be used as fuels for energy (Demirbas, 2005; McKendry, 2002a).

2.3 Biomass characterization

The characterization of any solid fuel (any type of coal, biomass, etc.) is one of the initial and most crucial steps that should be undertaken, when investigating the application of the fuel. This characterization could be in terms of physical, chemical, thermal properties as well as mineralogical and geochemical features (Vassilev et al., 2010). A summary of the methods of biomass characterisation is given in Table 2-1.

2.3.1 Chemical properties

Studies by Vassilev et al. (2010) and Jenkins et al. (1998) place emphasis on the chemical composition of different biomass varieties. The techniques evaluated in this work are invaluable for any future studies on any type of biomass. The chemical analysis can generally be considered in three stages – the proximate analysis, ultimate analysis and ash analysis. Proximate analysis is the most superficial of the three, and thus represents an important initial step. It involves determining the fixed carbon, volatile matter, ash yield, and moisture content of the solid fuel. Ultimate analysis and ash analysis is used to evaluate the composition of the fuel at the elemental level. Ultimate analysis focuses on quantitative determination of carbon (C), oxygen (O), hydrogen (H), sulphur (S), nitrogen (N) – the organic components. Ash analysis is associated with inorganic elements such as potassium (K), sodium (Na), silicon (Si), aluminium (Al), iron (Fe), etc.

2.3.1.1 Proximate analysis

Carrying out the proximate analysis typically involves the application of heat to the sample (under controlled conditions), and monitoring the mass loss of the sample as a function of time and temperature. This technique is known as thermogravimetric analysis (TGA). The first stage uses a nitrogen (N₂) atmosphere, so that combustion cannot occur. The first distinct mass drop corresponds to the moisture content of the fuel, and is essentially a drying step where the water that is bound physically to the structure of the fuel is lost. The second mass drop represents the volatile matter – a slow pyrolysis process has set in here due to the high temperature and the O₂-free atmosphere. The final phase involves switching the atmosphere from N₂ to O₂. This initiates combustion, and the mass remaining upon achieving complete combustion is considered the ash yield. Since the total initial mass of the sample is considered the

sum of moisture, volatile matter, fixed carbon and ash yield, the fixed carbon content can be then be calculated by difference.

$$\text{fixed carbon (\%)} = 100 - (\text{moisture (\%)} + \text{ash (\%)} + \text{volatile matter (\%)}) - \text{Eqn 2-1}$$

Care should be taken when choosing the heating profile to be used in the TGA – the profile should ensure that plateaus are reached at every distinct mass loss phase (a differential thermogravimetry curve – DTG – would be useful in determining this) i.e. the different phases in the TGA (drying, devolatilisation, etc.) are distinct without any overlap. An optimization procedure following parametric tests, would be required to arrive at the heating rate, final temperature, holding time, etc. which would be most suitable for a particular type of biomass. Mayoral et al. (2001) explored the use of such a procedure (the simplex method) to optimize TGA profiles for coal and biomass. However, whichever profile is utilised, it is important that it is standardised throughout the study.

2.3.1.2 Ultimate analysis

The ultimate analysis can be carried out using elemental analysers. Although a BSI (British Standards Institution) standards publication exists for the determination of C, H, N, via instrumental methods, it merely lays down guidelines and do not offer specific details – the elemental analysers vary among their methods of operation (BSI, 2011b). Often, the content of C, H, N, and sometimes S, can be determined simultaneously by the instrument. The fundamental concept utilised is the catalytic combustion of the fuel in the presence of oxygen (O₂). The combustion should take place such that there is complete conversion of the C and H to carbon dioxide and water, and S to sulphur dioxide, while all of the N content should be reduced to gaseous N₂. A quantitative analysis of these products can then be carried out using a suitable

detection system such as thermal conductivity detectors or flame ionisation chromatography (Stahl & Henrich, 2004).

Determination of S and Cl content however, is detailed out in a BSI standards publication. A combustion bomb is utilised to combust the sample, whereby the sulphur and chlorine content is released as acidic gases, i.e. SO₂ and HCl. Ion chromatography is the recommended detection technique, although acceptable alternatives exist such as inductively coupled plasma (ICP) mass spectroscopy (BSI, 2011c).

One direct method of determining O content is by carrying out a catalytic conversion to CO. The CO formed is subsequently converted to CO₂, which is then measured using a thermal conductivity detector (Stahl & Henrich, 2004; Wever et al., 2012). O content can also be calculated from difference, by subtracting from 100 the sum of C, H, N, S and ash by percentage (Telmo et al., 2010) as shown in Equation 2-2.

$$O (\%) = 100 - (C (\%) + H(\%) + N(\%) + S(\%) + ash(\%)) - \text{Eqn 2-2}$$

2.3.1.3 Ash analysis

A proximate analysis yields information about the total ash content of a fuel i.e. the amount of solid residue that is remaining following combustion. However, the composition of the ash is just as crucial as the total content. An ash analysis is a vital requirement to predicting the behaviour of a solid fuel in a combustion system as it provides information on the inorganic elements present in the fuel which are responsible for many of the drawbacks of biomass combustion. A BSI standards publication (BSI, 2011a) outlines the procedure for the determination several influential inorganic elements in the ash, which includes Na, K, Mg, Al and Si. The

method involves the treatment of the sample with several reagents – hydrogen peroxide (H₂O₂), nitric acid (HNO₃), hydrogen fluoride (HF) – accompanied by heating steps. This can be applied either directly to the fuel, or to a sample of ash which has been prepared at 550°C (the procedure varies accordingly). The objective of this treatment is to “digest” the sample. Following this, several analytical techniques can be used to determine the concentrations of the inorganic elements in the “digested” sample – inductively coupled plasma mass spectroscopy (ICP-MS), inductively coupled optical emission spectrometry (ICP-OES), atomic absorption spectroscopy (AAS), or flame emission spectroscopy (FES).

While the chemical composition evaluation by Vassilev et al (2010) was ultimately an exercise in systematic classification and trend analysis, that of Jenkins et al (2008) was far more specific and related to the combustion of biomass in energy conversion systems. The effect of chemical composition on emissions, fouling and slagging was investigated – in short, the real-world implications. Fouling, slagging and corrosion of boiler surfaces was found to be influenced mostly by alkali and alkaline earth metals (such as K) and Cl. Leaching these elements from the fuel using water dramatically improved these ash-related problems. This technique could be investigated further in future work, and represents a potential biomass pre-treatment stage.

While both these studies had several specific conclusions drawn, perhaps one of the most important issues addressed was the need for a more systematic approach. While research methodologies for coal have been laid out, these have not been implemented consistently for biomass. Also, standard engineering practices and protocols have to be laid out in a more comprehensive manner with regard to biomass energy conversion. This is also a potential area for further study.

2.3.2 Thermochemical properties

2.3.2.1 Heating/calorific value

The principal thermochemical property of a solid fuel is usually considered to be the heating value, or calorific value. It is a measure of the amount of energy released during the combustion of a unit mass of the fuel, at constant volume. There are two variations – the lower heating value (LHV) and the higher heating value (HHV). The LHV assumes that the water produced by the reaction remains in the vapour phase, while the HHV considers it to be in the liquid phase – the HHV is the higher value since it also includes the energy released when the product water condenses from vapour to liquid phase (the latent heat of vaporisation of water). It is common practise to use the HHV when comparing the energy content of different solid fuels. A bomb calorimeter is employed to measure the HHV of a sample of fuel (Jenkins et al. 1998).

The HHV can also be calculated using data from proximate and ultimate analyses. Demirbas (1997) presented the formula shown in Equation 2-3 to calculate the HHV by using the fixed carbon (FC) content.

$$HHV (MJ/kg) = 0.196 \times FC (\% \text{ by weight}) + 14.119 - \text{Eqn 2-3}$$

This correlation was able to predict the HHV with an error ranging from 0.1% to 4.0%, when compared against measured HHV values (using a bomb calorimeter). 16 lignocellulosic biomass varieties were used to test the correlation.

Another equation was obtained by Demirbas et al. (2007) to calculate HHV, which uses the C, H, N, O content (by % weight):

$$HHV (MJ/kg) = 33.5 \times C + 142.3 \times H - 15.4 \times O - 14.5 \times N - \text{Eqn 2-4}$$

In this case, the error did not exceed 0.54%. However, this correlation was only tested on 3 varieties of raw lignocellulosic biomass (olive husk, wheat straw, corncob).

2.3.2.2 Flame temperature

Although the HHV is the property which is most commonly utilised to compare solid fuels, it has the limitation that it cannot be used on its own to predict the efficiency of the combustion system. The maximum efficiency that can be attained is a function of the flame temperature. The flame temperature in turn depends on both the calorific value and the chemical composition of the fuel, since the chemical composition dictates the amount of air required for combustion (stoichiometry) – if less air is required, less non-reacting components of the air (mostly nitrogen) needs to be heated to the flame temperature. The higher oxygen content of biomass means that less air is required for combustion, compared to typical hydrocarbon fuels (Jenkins et al. 1998). Hence biomass fuels have the potential to have higher combustion efficiencies compared to other hydrocarbon fuels. This is a promising avenue for further investigations.

The flame temperature can be calculated using the ultimate analysis (Demirbas, 2003). It can also be directly measured using a flame imaging system which can generate a two-dimensional temperature distribution of the flame (Molcan et al., 2009).

Table 2-1: Summary of biomass characterisation methods

Type of analysis		Method of analysis	Reference/BSI standard
Chemical analysis	Proximate analysis	Thermogravimetric analysis (TGA)	
	Moisture		BS EN 14774-1:2009
	Fixed carbon		[calculated by difference]
	Volatile matter		BS EN 15148:2009
	Ash content		BS EN 14775:2009
	Ultimate analysis	Elemental analyser – catalytic conversion + detection by chromatography/spectroscopy	
	C, H, N		BS EN 15104:2011
	S, Cl		BS EN 15289:2011
	O		Stahl & Henrich 2004; Wever et al. 2012
	Ash analysis	Treatment with H ₂ O ₂ , HNO ₃ , HF and heating + detection by spectroscopy	
Na, K, Mg, Al, Si, etc.	BS EN 15290:2011		
Thermochemical analysis	Higher heating value (HHV)	Bomb calorimeter	
		Calculation from proximate analysis data (FC content)	Demirbas 1997
		Calculation from ultimate analysis data	Taylor et al. 2007
	Flame temperature	Flame imaging system	(Molcan et al., 2009)
		Calculation from ultimate analysis	(Demirbas, 2003)

2.4 Biomass combustion

Although there are several energy conversion techniques available for biomass, combustion remains the most important option on a short- to medium-term time scale; currently more than 95% of the energy extraction from biomass is carried out via combustion (Demirbas 2005). As explained in more detail in the Introduction, perhaps the most important reasons to look into biomass as a source of energy are with regard to the environment, namely its renewability and alleged CO₂-neutral conversion. Fossil fuels take millions of years to form, and hence have a continuously diminishing stock (non-renewable). Biomass on the other hand can be cultivated sustainably to replace stocks that are being used, within a practical time scale. The CO₂-neutrality results from the absorption of CO₂ during the lifetime of the plant, which compensates for the CO₂ which is released during combustion of the resulting biomass. However, both the renewability and CO₂-neutrality are dependent on sustainable consumption, so that all of the biomass which is used for energy is replaced, and the overall stock of biomass is hence not depleted (Demirbas, 2005; McKendry, 2002a).

There is rising global concern regarding the use of non-renewable fossil fuels such as coal in thermal power stations, and the greenhouse effect caused by excessive CO₂ emissions. Hence, substituting coal with biomass is a very important aspect of future energy generation. Directly firing the biomass itself, or co-firing of biomass with coal (hence reducing the total usage of coal) are both possible alternatives that show promise (Jenkins & Williams, 1999; Rüdiger et al., 1996).

Another advantage of co-firing biomass with coal involves the higher volatility of biomass. This has the effect of improving the reactivity and ignition characteristics of the fuel, compared to pure coal (Gani et al., 2005).

2.4.1 Drawbacks of biomass combustion/co-firing

The major drawbacks of biomass firing, namely deposit formation, corrosion and erosion within the boiler system, are related to the ash formed. Two modes of deposit formation can be identified – slagging and fouling. Slagging is dominant in the high-temperature radiative sections of the boiler and occurs due to molten ashes, while fouling is primarily found in the low-temperature convective sections and is related to ash deposits during cooling (Teixeira et al., 2012). Slag and fouling deposits are primarily composed of the chlorides, sulphates, hydroxides and silicates of alkali and alkaline earth metals. The slag forms when ash gets fused or partially-fused. This requires high temperatures, typically exceeding 1000°C (Savolainen, 2003), which is why the phenomenon occurs predominantly in the regions of the boiler which are subjected to heating by radiation. Fouling occurs when alkali compounds condense on the metal surfaces, and also when fly ash gets quenched below its melting temperature and gets deposited. Both these phenomena occur due to the falling temperatures in the heat-recovery sections, where heat transfer is by convection (Bryers, 1996).

A further related problem which is unique to fluidised bed combustors (FBC) is the agglomeration of bed media due to the presence of the biomass ash. This would result in a reduction of heat transfer, as well as in plant downtime. This issue is considered noteworthy, as FBC can otherwise be regarded as one of the more desirable biomass combustor technologies due to the low, stable operating temperatures it uses, as well as the fuel flexibility it affords (Öhman et al., 2000).

With regard to these deposition phenomena, it would be useful to have the ability to quantify the phenomenon, so that a more objective comparison can be made between different biomass varieties/blends. One basic technique is to use the ash fusibility behaviour; the ash fusion temperature would offer an approximate prediction of the

slagging tendency of the fuel, since fusion of ash is the basis of slag formation. The ash fusion temperature can be defined at different percentages of molten ash (for example, the temperature at which 70% of the ash mass is molten), and care should be taken to maintain uniformity throughout the comparison (Stam et al., 2009). Various other indices have also been defined for this purpose. Two commonly used such indices are $R_{B/A}$ and R_S . $R_{B/A}$ uses the proportion of basic oxides to acidic oxides in the ash, while R_S is a similar ratio that also incorporates the sulphur content (Teixeira et al., 2012). Degereji et al. (2012) also proposed a numerical slagging index that takes into account ash viscosity, ash fusibility and ash loading. However, these 3 indices have all been defined for coal. Since the ash resulting from biomass and coal combustion vary significantly in composition, these indices may not be reliable in predicting slagging/fouling in biomass; biomass ash deposition depends primarily on sodium and potassium chlorides, sulphates, hydroxides, etc., while coal ash consists of an alumino-silicate system. However, they would still find use in predicting the ash behaviour of biomass/coals blends which contain a low percentage of biomass (Stam et al., 2009).

Teixeira et al. (2012) proposed an ash fusibility index (AFI) that is based on 2 ash fusion temperatures (initial deformation temperature and hemispherical temperature). The AFI was defined in such a way that it could be applied to biomass, coals, as well as blends, in order to predict slagging and agglomeration. Turn et al. (1997) used the total mass of alkali oxide (K_2O and Na_2O) per unit energy as a measure of the fuel's fouling potential, while the normalized percentages of SiO_2 , CaO , K_2O on a phase diagram were used to predict the ash fusion temperatures which in turn was used as an index for slagging potential; in this study too, the indices were applied to biomass fuels (rice straw and wheat straw).

Further theoretical work in slagging prediction was carried out by Degereji et al. (2012). Here, CFD and modelling techniques have been shown to be reasonably effective in the in-furnace temperature profiles and heat fluxes as well as slag deposition. Future developments in the field of computer simulation would prove extremely useful in predicting ash deposition problems, without the need for expensive and time-consuming field tests.

2.4.2 Biomass co-firing technology

Dai et al. (2008) identified three ways in which biomass co-firing plants can be configured, as summarised in Figure 2-1 and Figure 2-2. Direct co-firing systems utilise where a single common boiler. This boiler may be powered by burners using either a blend of coal and biomass, or using coal and biomass separately. The common boiler means that existing conventional coal power plants can start co-firing biomass with minimal modifications, making it an attractive proposition economically. Hence, direct co-firing is the predominant configuration in the power generation industry. Parallel co-firing systems have separate boilers for coal and biomass. The final option, indirect co-firing, relies on gasification of the biomass component. This method has the potential to utilise a high biomass:coal ratio during the co-firing, and also affords great fuel flexibility. Problems arising from biomass combustion, such as slagging, are also avoided. However, it is expensive and sees little implementation at present (EUBIA, 2013; Maciejewska et al., 2006).

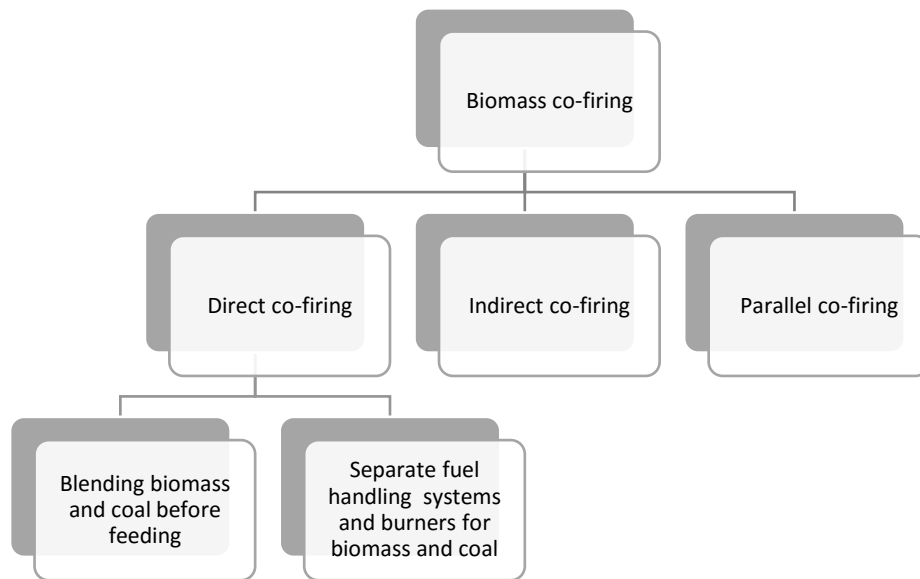


Figure 2-1: Overview of co-firing configurations

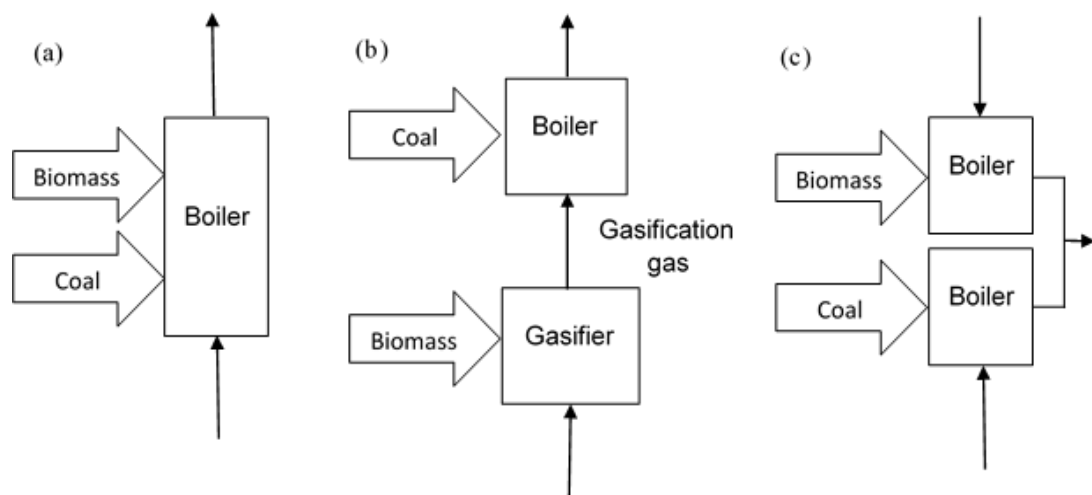


Figure 2-2: Schematic diagrams of co-firing configurations: (a) direct, (b) indirect, (c) parallel.

There are also three major classes of furnaces that are currently in use: fixed bed/packed bed/grate furnaces, fluidised bed combustors (FBC) and pulverized fuel combustors (PFC). Comprehensive overviews of these have been published by Dai et al. (2008), van Loo & Koppejaan (2008), and EUBIA (2013), and the summary of these is as follows:

Grate furnaces have the most elementary design of these, and consists simply of fuel being combusted over a grate. There are no special provisions for circulation of

air. This design is simple and hence the capital cost of the furnace is the lowest. Operating costs are also low. However, the downside is a low conversion efficiency and low fuel flexibility when mixtures are used. They are acceptable when single (non-blended) fuels are used, and hence see use in indirect and parallel combustion setups.

FBCs contain a bed of a medium (such as sand), with which the fuel is mixed. The bed acts as a buffer to maintain high combustion temperatures, even if the fuel contains impurities, high moisture or low calorific value. Hence, relatively high efficiencies can be maintained despite variations in the fuel used, and this affords the design very good flexibility with regard to the fuel used. Also, existing coal-fired FBCs can be easily adapted to a co-firing arrangement (Veijonen et al., 2003). This means that this design is a very suitable candidate for direct biomass co-firing, and already has been proven on a commercial scale. One problem that is exclusive to this design is the probability of bed agglomeration occurring when biomass with a high alkali/alkaline earth metal content is used.

In PFCs, the solid fuel has to be mechanically reduced in particle size (typically to less than 10-20 mm). The fine particles are then introduced pneumatically into the burner. This is the most widespread technology employed for electricity generation using coal, due to the high efficiency and low NO_x emissions. They can be adapted to direct co-firing with biomass. However, fuel properties (particularly a small particle size and a low moisture content) have to be carefully controlled, along with fuel blending and feeding.

Table 2-2 is a bibliographic compilation of the advantages and disadvantages of the three major types of furnaces currently employed.

Table 2-2: Bibliographic compilation of the advantages and disadvantages of the three types of combustion systems

Reactor type	Advantages	Disadvantages
Grate furnaces	<ul style="list-style-type: none"> • Low investment costs for plants <20 MWth and low operating costs (van Loo & Koppejaan, 2008) • Can use almost any type of wood (Veijonen et al., 2003) • Appropriate for biomass fuels with high moisture content (10–60 wt% wb) (Tuurna et al., 2003; van Loo & Koppejaan, 2008). • Suitable for fuels with high ash content and varying particle sizes (with a limitation regarding the amount of fine particles) (van Loo & Koppejaan, 2008). 	<ul style="list-style-type: none"> • Mixtures of wood fuels can be used, but mixtures of fuels with different combustion behaviour and ash melting points (e.g. blends of wood with straw or grass) are not possible (van Loo & Koppejaan, 2008); • Increase of temperature may cause ash melting and corrosion (Tuurna et al., 2003)
FBCs	<ul style="list-style-type: none"> • Large fuel flexibility in calorific value, moisture content, and ash content, enabling fuel diversification and increasing the scope of fuels in existing power plants (Maciejewska et al., 2006) • Combustion temperature in bed is low, resulting in low NO_x emissions (EC, 2000; van Loo & Koppejaan, 2008) • Provides an option to directly inject limestone to remove sulphur cost-effectively (instead of flue-gas desulphurisation equipment) (Maciejewska et al., 2006) • Maximized combustion efficiency even with low-grade fuels (Maciejewska et al., 2006) • Environmental performance of FBC installations is good, with low emissions of CO NO_x and high boiler efficiencies (about 90%) (EC, 2000) • Fluidized bed technology can be converted from coal to biomass/coal co-combustion with relatively little investment (Veijonen et al., 2003) 	<ul style="list-style-type: none"> • Despite the flexibility with regard to fuel specifications, it is not always possible to use the existing feeding system for biomass by premixing the fuels (the cheapest option). In cases where the feeding characteristics of the co-fired fuels vary too much from the primary fuel, a separate feeder needs to be installed (Maciejewska et al., 2006) • Slagging and fouling on boiler walls and tubes when burning fuels with high alkali content (Maciejewska et al., 2006) • Bed agglomeration when burning fuels of high alkaline and/or aluminium content (Maciejewska et al., 2006) • Cl-corrosion on heat transfer surfaces (e.g. superheater tubes) (EC, 2000) • High investment costs • Low flexibility in particle size, high dust load in the flue gas, loss of bed material with the ash (van Loo and Koppejan, 2008) • Incomplete combustion of fuels and high unburned carbon content in the ash, especially in CFB (Maciejewska et al., 2006).
PFCs	<ul style="list-style-type: none"> • Increased efficiency due to low excess oxygen, high NO_x reduction possible when appropriate burners used (van Loo and Koppejan, 2008). 	<ul style="list-style-type: none"> • Particle size of biomass is limited to <10–20 mm (van Loo and Koppejan, 2008). • Low moisture content required (typically <15 wt%, wb) for pneumatic feeding and decreased efficiency for high-moisture fuels (Maciejewska et al., 2006)

2.5 Biomass pre-treatment

The use of biomass in power-generation systems, either on its own or when co-fired with coal, is an attractive proposition due to the reasons discussed in the previous sections. However, in practice, biomass combustion still faces several challenges. One potential route to mitigating the negative effects of biomass combustion is the pre-treatment of the fuel prior to being fired in the boiler. This pre-treatment could be mechanical, thermal, chemical, biological, or a combination of these.

2.5.1 Leaching

2.5.1.1 Overview

As mentioned earlier, one of the main concerns with using biomass is its high alkali content which causes a host of ash-related problems. The alkali and alkaline earth metals react with other inorganic non-metallic components to produce deposit-forming compounds. Among the common such compounds are the silicates, chlorides and sulphates of potassium (an alkali metal) and calcium (an alkaline earth metal). These deposits result in slagging in grate-fired combustors, fouling of heat transfer surfaces, and bed agglomeration in fluidised bed combustors (Baxter et al., 1998; Turn et al., 1997; Vamvuka et al., 2008; Werther et al., 2000). The fouling impedes the heat transfer rate, while the slagging obstructs fuel feeding, combustion and ash removal (Baxter, 1993; Jenkins et al., 1998). As Kargbo et al. (2009) points out, all of these occurrences have the combined effect of lowering the performance of the energy transfer system in terms of combustion efficiency, and also have a negative impact on plant reliability, maintenance costs, and overall operating costs.

The presence of chlorine and sulphur also results in the formation of acidic products upon combustion. This would invariably cause accelerated corrosion of metal

surfaces within the combustion system, and would also act as atmospheric pollutants (Dayton et al., 1999)

Thus, reducing the content of alkali and alkaline earth metals as well as chlorine would be one of the primary objectives of the pre-treatment procedure. Washing of the biomass with water or an acid has been demonstrated as an effective method to accomplish this. This washing or leaching can occur naturally due to the biomass being exposed to rain prior to harvesting, or it can be carried out as an artificial process. Table 2-3 presents a bibliographic compilation of selected leaching studies.

2.5.1.2 Natural leaching

Jenkins et al. (1999) investigated the feasibility of using naturally leached rice straw in conventional commercial power plants. The straw had been exposed to 717 mm of cumulative precipitation over a period of 7 months, and then blended at 20-25% with the standard fuel. The standard fuel consisted of forest wood and urban/agricultural wood for the grate-fired boiler and circulating fluidized bed (CFB) boiler, respectively. Compared to using only the standard fuel, co-firing with the leached straw resulted in an increase in the total fuel ash, which could be attributed to the higher ash content of the straw. Despite this, there was no marked increase in slagging that could be attributed to the presence of the straw. Unexpectedly, the rate of deposit-formation on surfaces decreased following the co-firing, which reflected a reduced fouling rate; no justification for this behaviour was offered by the authors. Also, the co-firing with straw did not result in any bed agglomeration. Thus, in these full-scale trials, the natural leaching of the straw appears to have mitigated the ash-related problems to a great extent, although the corrosion issue still persists due to the higher chlorine content of the blended fuels.

Although the passive leaching process by natural precipitation is a low-cost and potentially effective method of mitigating the ash-related problems caused by alkali/alkaline earth metals, it is very much dependent on local weather conditions. Hence, there would be restrictions on the geographical location of the harvest as well as the time of the year. The relatively long exposure time required would cause complications in keeping to the harvesting and plant operation schedules. Also, the unpredictable nature of rainfall patterns would make it difficult to standardise the quality of the fuel with respect to the metal content. Hence, leaching should not only be restricted to the natural process, and artificial washing techniques are also required.

2.5.1.3 Laboratory-based leaching

Another study by Jenkins et al. (1995) investigated – in addition to rainfall-exposed biomass – the effectiveness of three laboratory-based washing techniques which could be applied to rice and wheat straw:

1. Hand-spraying water over a bed of straw which was 30 mm thick and held on a steel mesh, for a duration of 1 min.
2. Pouring a specified quantity of water (200 ml per gram of straw) over milled straw which had been spread over a fine steel mesh – flushing.
3. Leaving the straw submerged in water for 24 h – soaking.

All three techniques reduced the total ash content, although flushing and soaking proved to be more effective. Following an elemental analysis, it was found that there was a marked reduction in the content of chlorine (Cl), potassium (K), sodium (Na), sulphur (S) and phosphorous (P) following the washing. The most significant reduction appeared to be that of K and Cl, followed by Na. Again, flushing and soaking had a more substantial leaching effect compared to hand-spraying (for example, Cl

content was reduced by approximately 50% by hand-spraying, but experienced a 90-92% decrease following flushing/soaking). This study also examined straw samples that had been exposed to natural rainfall. In this case, the positive effects observed were on par with those following flushing/soaking. However, the afore-mentioned issues associated with natural leaching (time required and unpredictability of results) discourage dependence on this method.

Carrillo et al. (2014) also conducted a study investigating different laboratory-based techniques on sorghum biomass:

1. Pouring water evenly over 1 kg of biomass at a slow rate (7.6 l in 45 s) with the biomass placed in a muslin bag – single wash.
2. The above treatment repeated once – double wash.
3. The above treatment repeated twice – triple wash.
4. Submerging 1 kg of the biomass in 7.6 l of water for 1 h – soaking.

As in the observations by Jenkins et al. (1995) discussed above, the washing and soaking treatments had comparable results. For instance, the ash content decreased by 14% and 20% for the single and triple washes, respectively; that of the soaked biomass decreased by 18%. Again, K and Cl showed the most marked reductions following the leaching.

Although these two studies investigated different techniques, most investigations into laboratory-scale leaching are based on soaking the biomass for a controlled period of time. This method has been employed on a wide variety of biomass, both herbaceous and woody. The soaking method is especially relevant in laboratory-scale experiments since it allows parameters such as water temperature and leaching time to be controlled and their effects investigated. It also allows the progress of the leaching process to be

studied in greater detail by analysing leachate samples taken at intervals (Ho et al., 2005; Jenkins et al., 1995; Jensen et al., 2001).

The effect of the leaching water temperature was explored by Deng et al. (2013) and Lam et al. (2014). The temperature was varied between 25°C and 90°C. Both studies pointed to a marked increase in the leaching efficacy of K as the water temperature was increased, while there were mixed results for the other elements. Deng et al. (2013) proposed that at higher temperatures, more K-containing organic complex molecules are able to escape the biomass matrix.

A wide range of soaking times have been used across the available literature, extending up to 24 h (see Table 2-3). Chin et al. (2015) looked at the effect of varying the leaching time from 30 min to 120 min – with an intermediate 60 min – for six types of biomass. The wood species that were investigated typically showed an increase in leaching efficiency as the leaching time was increased to 120 min. The empty fruit bunch (EFB, a type of fibrous biomass) however did not gain a significant benefit from being leached for more than 30 min. Another leaching study on EFB found that there was no statistically significant decrease in the ash content beyond 1 min of leaching (Lam et al., 2014). The authors however recognised that the very small amount of material used in the experiments (5 g) would result in a leaching equilibrium being attained in a short period of time. Furthermore, the mean particle size of the biomass was 0.31 mm, while those used by Chin et al. (2015) were an order of magnitude higher in size. Thus, it is evident that the effect of the leaching time is dependent on several other factors including the type of biomass, the particle size and the amount of material used.

2.5.1.4 Industrial-scale leaching

Turn et al. (1997) subjected banagrass (a potential energy crop which is rich in K and Cl) to a pre-treatment regimen consisting of a combination of mechanical dewatering and rinsing processes. However, before this was carried out, size reduction was carried out on the material by the use of a forage chopper which gave a mean particle size of approximately 4 mm, or a Jeffco cutter which results in a mean particle size of about 1 mm. An analysis showed that Mg, Na, K and Cl were leached out to a greater extent when the particle size is smaller. Phosphorous leaching showed an extremely strong response to the greater particle reduction, while S leaching seemed to be unaffected by the particle size.

This study is significant in that unlike the small-scale laboratory-based methods which were used by Jenkins et al. (1995), it used industrial-scale methods and involved large quantities of test material. In addition to the effect of particle size, the authors also studied the effectiveness of mechanical dewatering as a method of reducing the content of such elements as Na, K and Cl. A single dewatering step halved the Cl content, and also decreased the Na and K levels by approximately 20% and 40%, respectively. A subsequent rinsing and second dewatering step caused further reductions; approximately 12%, 57%, and 30% of the original levels of Cl, Na, K – respectively – were left. Thus, mechanical dewatering by the use of hydraulic cylinders (coupled with rinsing) was shown to be reasonably effective as a means of reducing the content of elements which cause ash-related problems, on an industrial scale. As previously stated, the removal can be made more effective by using finer particle-reduction systems (on average, an improvement of 15-20% was observed when the mean particle size was reduced from 4 mm to 1 mm).

A compilation of selected leaching studies is presented in Table 2-3.

Table 2-3: Bibliographic compilation of selected leaching studies

Feedstock	Particle size	Process	Analysis technique	Elements analysed	Comments	Reference
- Rice straw - Wheat straw	- Whole straw - Hammer-milled (19 mm) - Pulverised (20 mesh)	Water at 20-25°C, 100 g samples: - Hand-spraying tap water for 1 min over straw bed supported on steel mesh. - Pouring 20 l of tap/distilled water in 1 l increments through sample supported on fine steel mesh screen; leachate sampled at each increment. - Pouring 7 l of distilled water in 0.5 l increments through 50 g pulverised sample placed on paper element paper; vacuum leaching. - Soaking sample in 7 l of distilled water for 24 h; leachate sampled at intervals. [70 ml/g]	Solid samples: - Moisture and ash content - Heating value - Elemental composition (both in dry fuel and ash) - Ash fusibility (qualitative) - Furnace tests of pellets (qualitative) - Phase (SEM – qualitative) Leachate: - Electrical conductivity - Ion concentration (HPLC)	Solid samples: - C, H, N, S, Cl - SiO ₂ , Al ₂ O ₃ , TiO ₂ , Fe ₂ O ₃ - CaO, MgO - Na ₂ O, K ₂ O - P ₂ O ₅ , SO ₃ Leachate: - Na ⁺ , K ⁺ - Mg ²⁺ , Ca ²⁺ - HCO ₃ ⁻ - Cl ⁻ - SO ₄ ²⁻		(Jenkins et al., 1995)
Banagrass	- Forage-chopped: 3.9 mm mean, 1.9 mm s.d. - Jeffco-cut: 1 mm mean, 2.2 mm s.d.	Initial weight 18.2 kg for each treatment: - Dewatered using 91 tonne press in cylindrical cage; dried for several days using ambient temperature forced-air dryer. - Dewatered; rinsed using 52 l of tap water in barrel and agitated by hand for 3 min; drained; dewatered; dried for several days using ambient temperature forced-air dryer. [2.86 ml/g]	Solid samples: - Proximate analysis - Ultimate analysis - Chlorine content - Heating value - Ash analysis Leachate: - Electrical conductivity - Sugar monomers (HPLC)	Solid samples: - C,H,O,N,S Ash: - Cl - Oxides of Si,Al,Ti,Fe,Ca, Mg,Na,K,P,S Leachate and tap water used for rinsing: - K,Na,Cl,Ca,Si, Al,Fe,Mg,P,S	- Slagging/fouling indicators used: (K ₂ O+Na ₂ O) kg/GJ; (Cl) kg/GJ; (SO ₃) kg/GJ. - HHV increases with increasing leaching severity as ash content decreases	(Turn et al., 1997)

Table 2-3 (contd.)

<ul style="list-style-type: none"> - Rice straw - Wheat straw - Switchgrass - Mixed wood fuel - Banagrass - Sugarcane bagasse 	<p>Milled through 20 mesh</p>	<p>- Soak for 24 h in distilled water; drain; repeat cycle once. [40 ml/g]</p>	<p>Molecular beam mass spectroscopy (MBMS) following combustion</p>	<ul style="list-style-type: none"> - CO₂⁺, CO⁺, ³⁴O₂⁺, NO⁺, SO₂⁺ - HCl⁺, KCl⁺, NaCl⁺ - K⁺, Na⁺ 	<p>Treated samples collected from other studies and analysed using MBMS</p>	<p>(Dayton et al., 1999)</p>
<p>Wheat straw char (after pyrolysis)</p>	<ul style="list-style-type: none"> - Full-size char particles - 0.153 mm - 0.049 mm 	<p>400 ml of distilled water heated to required temperature; 0.5 g of char particles added; mixed with magnetic stirrer at 360 rpm; 20 ml samples drawn with syringe at regular time intervals with equal volume of clean water re-injected. [800 ml/g]</p>	<ul style="list-style-type: none"> - Flame photometry - Ion chromatography 	<p>K, Cl</p>	<p>- Water temperatures: 25°C and 80°C</p>	<p>(Jensen et al., 2001)</p>
<ul style="list-style-type: none"> - Wheat straw - Wood waste - Microgranular cellulose 	<ul style="list-style-type: none"> - 0.5 to 2 mm - 0.05 to 0.5 mm 	<p>0.100 g sample used for each technique:</p> <ul style="list-style-type: none"> - Sample placed on filter paper and rinsed with 5 or 20 ml of Milli-Q water at 20-25°C; allowed to dry in dessicator for 24 h. [50, 200 ml/g] - Sample immersed in 5 ml of 1M acetic acid at room temperature for 4 h; filtered; rinsed with 10 ml of Milli-Q water; allowed to dry. - Sample immersed in Milli-Q water at 80°C for 2 h. 	<p>- Treated sample heated at 20°C/min under N₂; surface ionisation detector measures concentrations of compounds in vapour.</p>	<p>Na, K</p>	<ul style="list-style-type: none"> - Water washing technique aims to simulate large-scale leaching applications. - Cellulose analysed to determine effectiveness of treatment in removing Na and K bound to organic structure. 	<p>(Davidsson et al., 2002)</p>

Table 2-3 (contd.)

<ul style="list-style-type: none"> - Olive kernel - Olive tree wood 	<p>850 to 1150 μm</p>	<p>Samples pre-dried in oven to 1% moisture; treated with 120 ml/g pure double distilled water at 80°C for 2 h; dried in oven to 1% final moisture. [120 ml/g]</p>	<p>Solid samples:</p> <ul style="list-style-type: none"> - Proximate analysis - Ultimate analysis (elemental analyser) - Calorific value - Combustion tests in atmospheric lab-scale fluidised bed reactor <p>Bed material:</p> <ul style="list-style-type: none"> - SEM/EDX - Mineralogical analysis (XRD) <p>Fly ash:</p> <ul style="list-style-type: none"> - Atomic absorption spectrometry - XRD 	<p>Ultimate analysis:</p> <ul style="list-style-type: none"> - C,H,N,O,S <p>Fly ash:</p> <ul style="list-style-type: none"> - Cl - Oxides of Si,Al,Fe,Mg,Ca, Na,K,Ti,Mn,P,S 	<ul style="list-style-type: none"> - Slagging/fouling indicators used: Alkali index = $(\text{K}_2\text{O}+\text{Na}_2\text{O}) \text{ kg/GJ}$; Base-to-acid ratio = $\%(\text{oxides of Fe,Ca,Mg,K,Na}) \div \%(\text{oxides of Si,Ti,Al})$; Bed agglomeration index = $\%(\text{Fe}_2\text{O}_3) \div \%(\text{K}_2\text{O}+\text{Na}_2\text{O})$. - Usage of mineral additives (kaolinite, clinochlore, ankerite) to mitigate slagging, fouling, agglomeration investigated. 	<p>(Vamvuka et al., 2008)</p>
<ul style="list-style-type: none"> - Wheat straw - Rice straw - Corn stalk 	<p>280-450 μm</p>	<p>- 12.5 g of biomass submerged in 1 l of deionised water for 3 h. [80 ml/g]</p>	<ul style="list-style-type: none"> - Proximate analysis - Ultimate analysis - Ash analysis 	<p>Ultimate analysis:</p> <ul style="list-style-type: none"> - C, H, N, S, O, Cl 	<ul style="list-style-type: none"> - Fouling tendency determined by base-to-acid ratio = 	<p>(Deng et al., 2013)</p>

Table 2-3 (contd.)

<ul style="list-style-type: none"> - Cotton stalk - Candlenut wood - Rice husk 		<ul style="list-style-type: none"> - Leaching temperatures of 30°C, 60°C, 90°C. - Leached samples air-dried at 105°C for several hours. - All runs duplicated. 	<ul style="list-style-type: none"> - Higher heating value (HHV) - TGA kinetics – pyrolysis and combustion tests at constant heating rate (20°C/min) to 1200°C in N₂ and 1000°C in air, respectively. - Ash fusibility – imaging sintering point testing 	<p>Ash:</p> <ul style="list-style-type: none"> - Oxides of Si, Al, Ti, Fe, Ca, Mg, Na, K, S, P 	<ul style="list-style-type: none"> %(oxides of Fe,Ca,Mg,K,Na)÷ %(oxides of Si,Ti,Al) - K, S, Cl effectively removed, with K leaching efficiency increasing with temperature. - HHV increases slightly following leaching. - Ash fusion temperatures increase following leaching - Under pyrolysis, aximum devolatilisation rate increases and hemicellulose, cellulose peaks move further apart following leaching; under combustion, devolatilisation and char combustion delayed following leaching. 	
---	--	---	---	---	---	--

Table 2-3 (contd.)

Sorghum	Stalks processed with wood chipper	Tap water at approx. 20°C used; 1 kg of biomass put into a muslin cloth bag for each treatment (triplicated): - Evenly pouring 7.6 l of water over sample in 45 s (single rinse). - As above, double rinse. - As above, triple rinse. - Sample immersed in 7.6 l of water for 1 h. All leached samples dried at approx.. 50°C for 3 days.	- Proximate analysis - Ultimate analysis - Calorific value - Halogen content - Ash analysis - Lignin content analysis	Ultimate analysis: - C,H,N,O,S - Total halogen (Cl, Br, I) - Cl Ash: - Oxides of Si, Al, Ti, Fe, Ca, Mg, Na, K, S, P	- Alkali index = (K ₂ O+Na ₂ O) kg/GJ used - Lignin concentration and calorific value increased following leaching.	(Carrillo et al., 2014)
- Empty fruit bunches - Palm kernel shells	Milled to <4 mm	- 5 g of biomass with 100 ml of distilled water for each run. [20 ml/g] - Stirrer at 360 rpm. - Leaching times of 1, 3, 5, 10, 30, 60, 120 min. - Leaching temperatures of 25°C, 40°C, 55°C. - Vacuum filtration and drying at 105°C	- Ash content (proximate) - Inductively coupled plasma optical emission spectrometry (ICP-OES)	Al, Ca, Fe, K, Mg, Na	- Kinetic model fitting was done to the leaching process by using a second-order mechanism. - Higher leaching temperatures had no significant impact on the ash reduction, but was more effective in removing certain specific metals such as K.	(Lam et al., 2014)
- Oil palm trunk - 4 species of fast-growing timber	Woody biomass chipped to <1 mm	- Leaching carried out in distilled water or 1M dilute acetic acid at room temperature (27±2°C).	- Ash content (proximate) - ICP-OES - Higher heating value (HHV) - Ash melting characterisation	Al, Si, Ca, K, Mg, P	- Water-leaching only effectively removed K and P.	(Chin et al., 2015)

Table 2-3 (contd.)

<p>- Empty fruit bunch</p>	<p>thickness, 1—15 mm diameter</p>	<p>- Leaching times of 30 min, 60 min, 120 min. - 10 g of biomass leached in 100 ml of liquid in 200 ml conical flask placed in water bath. [10 ml/g] - Leached samples oven-dried at 105°C for 24 h.</p>			<p>- Acetic acid-leaching removed most ash-forming elements. - Slight increase in HHV following leaching. - The authors recognised the need for further technical and economic feasibility evaluation to implement leaching on an industrial scale.</p>	
----------------------------	------------------------------------	--	--	--	---	--

2.5.2 Torrefaction

2.5.2.1 Overview

The properties of biomass differ from those of coal in several key aspects. In addition to the differences in chemical composition that have been discussed earlier, there are also dissimilarities with respect to physical properties. Biomass generally has a higher moisture content and a lower energy density than coal (Baxter, 2005; Demirbaas, 2003; Rapagna et al., 2000). It is desirable to bring the physical properties of biomass as close to those of coal as possible. This would make it possible to use existing conventional power plants to fire biomass, with minimal modifications to the handling and combustion equipment. The matching of properties is especially important if the biomass is being co-fired with coal. The low energy density of biomass results in a low burning rate, and coupled with poor blending characteristics, makes co-firing of biomass and coal problematic (Hughes & Tillman, 1998; Tillman, 2000). Table 2-4 adapted from Demirbaas' report (2003) shows typical values of certain properties of biomass and coal to illustrate the differences between them.

Table 2-4: Differences in properties between coal and biomass (Demirbaas, 2003)

	Biomass	Coal
Fuel density (kg/m³)	~500	~1300
Particle size	~3 mm	~100 μm
Dry heating value (MJ/kg)	16	25
Moisture (% of fuel)	6.5±0.8 (oak wood) / 7.3±1 (wheat straw)	4.8±2.6

A pre-treatment technique that has shown encouraging results in resolving these issues is torrefaction. Torrefaction is a thermal pre-treatment. There are two types of torrefaction available – dry torrefaction and wet torrefaction – they differ in the method of application as well as the mechanism in which the products are evolved.

2.5.2.2 Consequences of torrefaction

In dry torrefaction, the biomass is heated in an O₂-free environment (typically in an inert or N₂-filled surroundings) at temperatures upto 300°C, resulting in a mild pyrolysis reaction where the biomass undergoes a non-combustive thermochemical decomposition (Chen & Kuo, 2010). Extensive studies have to be carried out to ascertain the effects of dry torrefaction on various types of biomass. A bibliographic compilation of some of these studies is presented in Table 2-5. The process is effectively a low-temperature pyrolysis reaction.

Table 2-5: Bibliographic compilation of selected dry torrefaction studies

Type of biomass	Torrefaction temperature(s)	Holding time(s)	Key findings	Reference
Hardwood sawdust	200-295	5-30	Torrefaction temperature had a more significant effect on mass loss than residence time; Significant increase in calorific value as torrefaction temperature increases.	(Nimlos et al., 2003)
Pine, lucern, sugar cane bagasse, wood pellets, straw pellets	230-280	60-180	Woody biomass gave a higher fraction of solid product, compared to agricultural residue; Mass yield decreases with increasing torrefaction temperature and residence time.	(Ferro et al., 2004)
Miscanthus, birch, salix, wood and straw pellets	230-280	60-180	At higher temperatures and longer holding times, carbon content increased and hydrogen, oxygen content decreased; calorific value increased.	(Zanzi et al., 2004)
Larch, willow, beech, straw	230-270	15-60	Reaction time had smaller influence than temperature on torrefaction outcome; Particle size had negligible effect on outcome; Energy required for milling (size reduction) decreased by up to 85% following torrefaction; Energy yield remains high (more than 95%) at temperatures up to 250°C but; beyond 270°C, energy yield is below about 80%, and has to be controlled by limiting the reaction time.	(Boersma et al., 2005)
Wood briquettes	220-270	30-90	Composition did not undergo much change at 220°C; Torrefaction temperature had a much greater influence on composition than residence time; Temperatures between 250°C and 270°C recommended.	(Felfli et al., 2005)

Table 2-5 (contd.)

Rice straw, rape stalk	200-300	30	Heating value increased by up to 17% following torrefaction; Torrefied product more easily pulverised.	(Deng et al., 2009)
Eucalyptus wood	220-280	60	Mass loss was found to be a good indicator of treatment intensity, and expressions were derived to predict energy properties as a function of mass loss.	(Almeida et al., 2010)
Rice husks, sawdust, peanut husks, bagasse, and water hyacinth	250-300	60-120	Moisture content and volatile matter content reduced; Ash, fixed carbon content, energy density increased; In combustor, torrefied husks ignite faster and result in higher bed temperatures.	(Pimchuai et al., 2010)
Cotton stalk, wheat straw	200-300	30	With increasing torrefaction temperature, energy density increased and energy yield decreased; Grindability improved with increasing torrefaction temperature; Optimum conditions were 230-250°C, for 30 min.	(Guijun et al., 2011)
Pine chips, logging residue	225-300	30	Proximate, elemental compositions of biomass was made similar to those of coal, following torrefaction; Specific energy consumption for grinding was decreased by a factor as high as 10.	(Phanphanich & Mani, 2011)
Bamboo, banyan, willow (pulverised)	230-290	60	O/C ratio decreased with increasing torrefaction temperature; Calorific value was increased by a factor as high as 1.46 following torrefaction.	(Chen et al., 2011a)
Lauan wood	220-280	30-120	Torrefaction increased calorific value and carbon content; At 280°C, the mass loss was considered too steep (more than 50%); Grindability was improved following torrefaction at 250°C for more than 1 h.	(Chen et al., 2011b)

Table 2-5 (contd.)

Woody biomass (L. Leucocephala)	200-275	30-900	Significant increase in carbon content and calorific value with increasing torrefaction temperature and holding time; Longer the holding time, more cross-linking reactions occur in the solid product.	(Wannapeera et al., 2011)
Beech wood	200-300	50	Analysis by C-13 nuclear magnetic resonance (NMR) spectroscopy revealed that hemicellulose and lignin decomposition start at just above 200°C, while cellulose degradation occurs at >270°C. Lignin undergoes decomposition over a wide range of temperatures.	(Melkior et al., 2012)
Pine, black poplar, chestnut woodchips	240-300	11-43	Grindability (determined in terms of particle distribution) improved with torrefaction at higher temperatures; Temperature was more significant factor than residence time.	(Gil et al., 2015)
Loblolly pine	225-275	15-45	C-13 NMR spectroscopy results showed that hemicellulose showed significant decomposition after torrefaction at 225°C and complete degradation at 275°C (30 min residence time). Cellulose degradation was observed only at higher torrefaction intensities (>250°C at 30 min residence time).	(Neupane et al., 2015)
Waste wood, logging residue, palm kernel shell, bagasse	250-350	30	Moisture, volatile matter content reduced; Ash content, calorific value increased; Fuel ratio and combustibility index were used to determine the viability of using the torrefied biomass in blends with coal.	(Ohm et al., 2015)
Olive mill waste	150-300	120	The C content and calorific value increased by 21% and 14%, respectively, as the torrefaction temperature was increased; 200°C was found to be the optimum torrefaction temperature in terms of maximising calorific value and minimising energy loss; Accelerate solvent extraction (ASE) results showed that residual olive oil was depleted from the biomass following torrefaction, and completely removed at 300°C-torrefaction.	(Benavente & Fullana, 2015)

An inevitable effect of the heating is a reduction in moisture, which in turn has several consequences. The removal of water results in a reduction of the H and O content of the biomass. The reduction of C content during the torrefaction process is less substantial (Chen et al., 2012). Hence, the moisture reduction causes a reduction in the H/C and O/C ratios (Narvaez & Orio, 1996). These two ratios are significant because they reflect on the heating value of the fuel. The energy released when a C-O or a C-H bond is broken is less than that released when a C-C bond is broken. Hence, the decrease in the H/C and O/C ratios due to the torrefaction ultimately results in an increase in the heating value (McKendry, 2002a). This increase in heating value was confirmed by experimental studies, where a rise of up to 17% was reported after torrefaction of herbaceous biomass (Sadaka & Negi, 2009), while a maximum increase of 37% was reported after torrefaction of woody biomass (Arias et al., 2008).

A further result of the torrefaction is that its propensity to reabsorb water is reduced. This can be attributed to the loss of -OH (hydroxyl) groups during the process; it is these -OH groups that cause untreated biomass to take up water, since the water molecules form hydrogen bonds with these groups (Pastorova et al. 1993). Furthermore, the reduction in the hydroxyl groups also corresponds with the H/C and O/C ratios (Phanphanich & Mani, 2011). The low tendency of the treated biomass to reabsorb moisture is a very desirable characteristic since it allows the fuel to be stored stably for extensive periods of time without its moisture levels increasing significantly. Also, the treatment makes the biomass resistant to microbial colonization (Trifonova et al., 2009), which means that there would be less tendency for bio-degradation to occur during storage.

The poor grindability of biomass is another issue that can be alleviated by torrefaction. When co-firing biomass with coal, it is vital to maintain a uniform particle

size to aid in blending; to achieve this, the fuels would have to undergo mechanical size reduction (for instance milling), and good grindability hence becomes a necessary attribute. Raw biomass tends to be highly fibrous in nature, and the fibres form linkages which results in the resistance to milling/pulverising. Torrefied biomass has been observed to lack these fibres. The treatment process also reduces the size of the particles at a microscopic level, and also makes them more spherical. The combined outcome of these effects is to improve the grindability and flowability of biomass, as well as improve handling characteristics (Arias et al., 2008). A practical gauge of the improvement in grindability is the reduction in energy required for grinding a unit mass of the fuel. The specific grinding energy can be reduced by as much as 6 to 10 times, and this is a significant incentive in terms of energy cost. Torrefaction of wood at 275°C to 300°C resulted in a grinding energy similar to that of coal (Phanphanich & Mani, 2011). Further, Bridgeman et al. (2010) were able to use torrefaction to bring the grindability and particle size distribution of two biomass varieties (the herbaceous miscanthus and the woody willow), close to those of coal. Gil et al. (2015) measured the grindability of wood chips in terms of particle distribution following pulverisation; there was a significant enhancement in the grindability after torrefaction, and this was improved with increasing torrefaction temperature.

The tendency of the torrefaction process to make the particles smaller and more spherical has the effect of increasing the surface area of the particles. This invariably leads to a higher combustion efficiency, and more effective co-firing with coal since the coal and biomass particles are more evenly matched (Tumuluru et al., 2011).

Biomass is composed of hemicellulose, cellulose and lignin (Section 2.2). During the torrefaction process, these components would undergo changes as the structure of the biomass disintegrates. C-13 nuclear magnetic resonance (NMR) spectroscopy has

been used as a tool to look at the effect of torrefaction on the lignocellulosic content. Hemicellulose is the most volatile component; it starts degrading at $<225^{\circ}\text{C}$ and decomposes completely at moderate torrefaction intensities, i.e. less than 275°C . Cellulose is more stable, and typically shows marked degradation only at temperatures in excess of 250°C . Lignin undergoes decomposition over a wide range of temperatures – it can start degrading at temperatures as low as 200°C , and would continue to do so at temperatures $>300^{\circ}\text{C}$ (Melkior et al., 2012; Neupane et al., 2015).

Wet torrefaction also results in many of the aforementioned beneficial effects of dry torrefaction, although the two mechanisms differ. Wet torrefaction is also known as hydrothermal pre-treatment, in that it uses hot compressed water as a treatment medium (as opposed to a N_2 environment in dry torrefaction). The treatment temperature range is generally slightly lower than that of dry torrefaction – typically the process is carried out at 260°C or lower. The pressure is maintained at about 700 psi. Both dry and wet torrefaction result in the formation of a solid product as well as evolved gases. The difference is that wet torrefaction also results in an aqueous solution being formed, consisting primarily of dissolved sugars. However, for the purposes of combustion/co-firing, the focus lies on the characteristics of the solid product. A comparison of the mass and energy fractions of the solid products is given below in Table 2-6 (Yan & Acharjee, 2009):

Table 2-6: Mass and energy yields of dry and wet torrefaction

	Dry torrefaction	Wet torrefaction
Mass yield	60-80%	55-90%
Energy yield	70-90%	80-95%

Yan & Acharjee (2009) carried out a comparative study on the effects of both dry and wet torrefaction on loblolly pine, a form of woody biomass. Both processes share the positive effects of torrefaction which have been discussed in depth earlier, but the magnitudes of the changes differ between the wet and dry techniques.

With regard to hydrophobicity, wet torrefaction was observed to cause a greater increase. The equilibrium moisture content (EMC) was used as a measure of hydrophobicity – a lower EMC translates to a greater resistance to moisture uptake, which is more desirable. At a relative humidity of 84%, the EMC of the raw biomass decreased from 16% to 9% and 5%, following dry and wet torrefaction, respectively.

Table 2-7 and Table 2-8 show the energy and mass yields, and the ultimate analyses of the solid products obtained, respectively, from the wet and dry torrefaction (Yan & Acharjee, 2009). The dry technique increased the C content by 1-9% (depending on the treatment temperature utilised), while the wet technique increased it by a much more significant 9-43%. The O and H content were altered by much smaller percentages in both scenarios. It can be inferred directly from these observations that the decrease in H/C and O/C ratios would be much greater in the case of the wet method – this is ascertained by calculating the actual H/C and O/C ratios using the data from the analyses in Table 2-8. As explained before, these ratios have a direct impact on the heating value. The expected trend in the heating value is established by the actual measured values – higher energy densification ratios (which is a measure of the

increase in heating value due to the torrefaction process) are achieved when the wet torrefaction is carried out. With respect to the mass yield, no significant differences are observed between the two methods.

Table 2-7: Energy and mass yields of pine biomass following torrefaction (Yan & Acharjee, 2009)

Pre-treatment	Temperature (°C)	Mass yield (%)	HHV (cal/g)	Energy densification ratio	Energy yield (%)
Wet torrefaction	200	88.7	5043.3	1.08	95.8
	230	70.6	5276.8	1.13	79.8
	260	57.0	6342.5	1.36	77.5
Dry torrefaction	250	83.8	5005.4	1.07	89.7
	275	74.2	5207.2	1.12	83.1
	300	60.5	5627.4	1.21	73.2

Table 2-8: H/C and O/C ratios of pine biomass following torrefaction (Yan & Acharjee, 2009)

Pretreatment	Temperature (°C)	C (%)	H (%)	O (%)	H/C	O/C
Raw biomass		50.25	5.97	43.34	0.119	0.862
Wet torrefaction	200	54.72	6.03	39.11	0.110	0.715
	230	56.05	5.94	37.92	0.106	0.677
	260	72.07	4.9	22.89	0.068	0.318
Dry torrefaction	250	50.73	6.21	42.94	0.122	0.846
	275	52.27	6.13	41.45	0.117	0.793
	300	54.81	5.94	39.11	0.108	0.714

Hence, this study concludes that although both torrefaction strategies result in an improvement in the solid biomass fuel for combustion/co-firing purposes, wet torrefaction is the more favourable option based on hydrophobicity and energy density. More extensive research has to be carried out with respect to the advantages and drawbacks of each technique.

2.5.2.3 Effect of torrefaction parameters on fuel properties

Another important feature of torrefaction that was highlighted in this study was the effect of torrefaction temperature on the properties of the solid product obtained. With reference Table 2-8, it can be seen that an increase in the process temperature leads to a reduction in the H/C and O/C ratios, and hence an increase in the heating value of the torrefied fuel. However, the increasing temperatures also lead to a reduction in the mass yield (there is a greater mass loss due to loss of moisture and volatile components), which in turn causes a reduction in the energy yield. This trend was true in both the dry and wet treatments. Sadaka & Negi (2009) investigated the effects of torrefying temperature as well as residence time of the biomass at this temperature. Increasing temperature and residence time were found to cause greater moisture loss and an increase in the amount of fixed carbon, which relates to the observed increase in the heating value, which corroborates with the findings of Yan & Acharjee (2009). Grindability characteristics also appear to improve with increasing temperature and residence time (Bridgeman et al., 2010; Gil et al., 2015). This is also illustrated in Figure 2-3 (adapted from Yan & Acharjee, 2009).

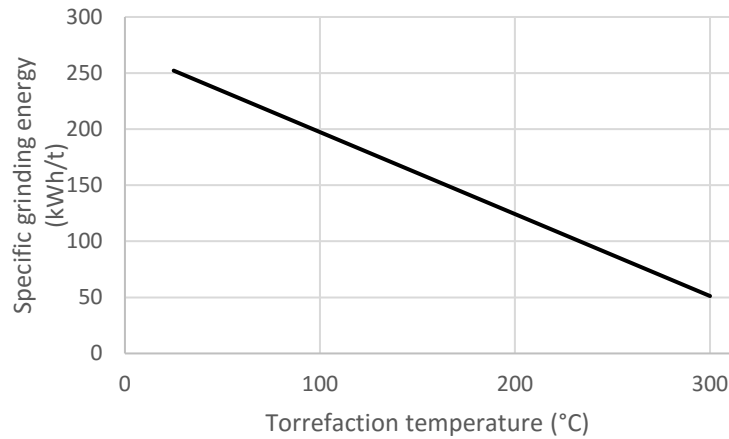


Figure 2-3: Effect of torrefaction temperature on grinding energy consumption (adapted from Yan & Acharjee, 2009)

Hence, it can be seen that an optimal treatment temperature and residence time should be found, to strike a balance between heating value, mass and energy yields, and grindability. This issue is further compounded by the fact that the extent to which the torrefaction occurs varies with different types of biomass under similar process conditions. Woody biomass tends to have higher mass and energy yields than herbaceous biomass; this can be attributed to the varying proportions of cellulose, hemicellulose and lignin, each of which has its own pyrolysis characteristics (Bridgeman et al., 2008). However, torrefied herbaceous biomass would have better grindability than torrefied woody biomass when subjected to the same treatment. This emphasises the need to optimize the torrefaction temperature and residence time in order to bring the properties of the biomass as close to coal as possible.

2.5.3 Mechanical pre-treatment

2.5.3.1 Grinding/milling

Following torrefaction, the inevitable next stage of pre-treatment would be mechanical grinding. Also, improvement in grindability characteristics is one of the incentives for carrying out torrefaction. As explained in the previous section, mechanical size reduction by grinding/milling is an important requisite, especially for co-firing biomass with coal. This is in order to allow a closer match in particle size distributions between coal and biomass, which in turn would improve blending characteristics and would result in more even combustion of the blend. This, together with the increase in total surface area of the biomass particles, would increase the efficiency of the combustion process (Kargbo et al., 2009; Tumuluru et al., 2011).

2.5.3.2 Pelletizing

One of the main problems involving the use of biomass as a fuel is its low density, which leads to high handling and transport costs. This is a major factor which would limit the large-scale use of biomass for energy production. Pelletizing is a mechanical compacting process which has been shown to address this issue.

The pelletizing process consists of three main stages – drying, grinding/milling and compaction. The moisture content of the biomass is first reduced to about 10% by weight. A variety of drying equipment are available to carry this out including rotary drum dryers, superheated steam dryers and belt dryers. Following this, the mechanical size reduction can be carried out by using, for example, a hammer mill. A press mill is then used to compact the dried and milled biomass particles into pellets of the required size. The particles are bound together by moisture and natural binders which are released from the biomass itself due to heat; artificial binders and stabilizers may

also be added. The pellets are then cooled to about 5°C, which causes further hardening.

As mentioned earlier, pelletizing has the effect of increasing the density of the biomass. Typical densities of raw biomass is approximately 40-150 kg/m³ and 300-700 kg/m³ for herbaceous and woody biomass species, respectively. Biomass pellets can have densities in the range of 1000-1400 kg/m³. Since there is virtually no loss in the energy content of the biomass during the pelletizing process, this translates to an increase in the energy density. Since less volume is occupied by the biomass providing the same quantity of energy, there is subsequently a reduction in transportation, storage and handling costs. Another consequence of the pelletizing process is that the varying moisture content of the raw biomass is reduced and made more uniform. Also, the homogeneity of the pellets with regard to size and structure means that they can be used in existing automated feeding systems (which have been designed with standardized particle size limits) in industrial combustors (Stelte et al., 2011a; Stelte et al., 2011b).

2.5.4 Biological pre-treatment

Biological treatment is currently being investigated mainly for the production of biofuels such as ethanol, and any application on biomass intended for combustion/co-firing is speculative. Pérez et al. (2002) and Sindhu et al. (2015) have presented reviews of the biodegradation of lignocellulose (a major component of biomass). A variety of fungi and bacteria produce enzymes which break down lignocellulose into more elementary components. The focus is on the use of this process for the production of biofuels such as ethanol, and also in the pulp and paper industries. Kirk & Cullen (1998) also discussed the biological break-down of wood by enzymes secreted by certain fungi. Future research can be carried out on the possible use of these biological processes in the pre-treatment of biomass that is to be fired/co-fired in conventional boilers. Potential benefits of biodegradation into simpler components include easier leaching out of undesirable elements in biomass (such as K, Cl, toxic elements, etc.), improved fuel conversion efficiency, and reduced energy requirements for mechanical processing.

2.5.5 Energy/cost considerations

One important aspect that has to be considered with respect to pre-treatment is the overall energy/efficiency benefit. Although the higher energy density of the pre-treated fuel translates into lower storage and transportation costs, energy is also consumed in the treatment processes (particularly in grinding, torrefaction, and compaction). Also, about 10% of the calorific content of the straw was found to be lost during leaching. However, pre-treatment is necessary to overcome the issues inherent to energy extraction from biomass. Kargbo et al. (2009) emphasized on the need for a detailed economic analysis to be carried out. Such an analysis would enable to optimize the pre-treatment procedures to be carried out (for instance, which methods should be applied and how much of energy should be spent on it), in order to obtain the best cost/benefit balance. This is especially important since ultimately, economic considerations are a primary driving factor in industrial applications.

Torrefaction and pelletisation are both taking their first steps towards commercialisation, with several commercial-scale demonstrations appearing over the past five years. For instance, Topell Energy in the Netherlands operates a multi-reactor torrefaction system that can produce up to 10 tons/hour of torrefied biomass, and is claimed to be flexible with respect to the type of biomass (Topell Energy BV, 2015). A test run was carried out where 2300 tons of pelletised, torrefied biomass supplied by Topell was successfully co-milled and co-fired – up to 25% biomass – in a power plant in the Netherlands (ECN, 2014). A detailed economic case study was carried out based on Topell's torrefaction system to examine the feasibility of torrefied wood pellets vis-à-vis untorrefied wood pellets (Koppejan et al., 2012). The model included the cost of pelletisation and torrefaction at plants in North America, land and sea transport to Europe, and co-firing at a pulverised coal power plant. Various financial and

operational factors were also taken into account. The untorrefied and torrefied pellets had a final cost of approximately 13 USD/GJ and 10 USD/GJ, respectively. It was found that the additional cost of torrefaction is more than compensated for by the lower milling and transport costs, owing to the improvement of the grindability and energy density. A typical coal cost at the same power plant is approximately 5 USD/GJ. The extra cost associated with co-firing is essentially the price paid for reduced CO₂ emissions.

Table 2-9 presents a summary of the major biomass pre-treatment techniques which have been discussed in this section.

Table 2-9: Summary of major pre-treatment techniques

Pre-treatment technique	Benefits of application
Leaching	<p>Reduces content of elements such as Na, K, Cl</p> <p>Reduces total ash content</p> <p>Increases ash fusibility temperature</p> <p>Hence reduces slagging/fouling problems during combustion</p> <p>Increases heating value</p>
Torrefaction	<p>Reduction in moisture</p> <p>Increase in heating value</p> <p>Increases hydrophobicity</p> <p>Improves grindability characteristics</p> <p>Improves flowability and handling characteristics</p> <p>Increases total surface area of particles – higher combustion efficiency</p>
Grinding/milling	<p>Improves blending characteristics</p> <p>Increases total surface area of particles</p> <p>Hence increases combustion efficiency</p>
Pelletizing	<p>Increases energy density</p> <p>Hence reduces transport, storage and handling costs</p> <p>Reduces moisture content</p> <p>Increases homogeneity with respect to size and structure</p>

2.6 Combustion modelling

2.6.1 Overview

Historically, progress in the field of combustion technology – particularly with traditional fossil fuels such as coal – has been dependent on empirical data. This data can be sourced from either large-scale plants or laboratory/pilot-scale experiments. A limited number of measurements (such as those of effluent samples) can be obtained from large-scale plants, and they are also restrictive in terms of the range of process parameters. Smaller-scale experimental rigs solve these two issues, but have the disadvantage of questionable applicability when the results are extrapolated. Combustion modelling provides an intermediate stage in the process of designing and improving of combustion systems, whereby the two modes of empirical data can be linked (Eaton et al., 1999). For a model’s predictions to be useful, they should be validated against experimental data. However, the usage of modelling allows confident predictions to be made using a small pool of experimental data, thus representing a cost saving (Barnes, 2014). Table 2-10, reproduced from Barnes (2014), illustrates the advantages and disadvantages of CFD modelling compared to experimental investigations.

Table 2-10: Comparison of experimental and CFD investigations

Experiments	Simulations
Quantitative description of flow phenomena using measurements <ul style="list-style-type: none"> • For one quantity at a time; • At a limited number of points and time instants; • For a laboratory-scale model; • For a limited range of problems and operating conditions 	Quantitative prediction of flow phenomena using CFD software <ul style="list-style-type: none"> • For all desired quantities with high resolution in space and time; • For the actual flow domain; • For virtually any problem and realistic operating conditions
Error sources: measurement errors, flow disturbances by the probes	Error sources: modelling, discretisation, iteration, implementation

As stated by Williams et al. (2002), there has been a shift of the desired outcome of combustion modelling from mere qualitative trends to quantitative results. This is due to the advent of more detailed models describing the combustion process, which in turn was made feasible by the ever-increasing power and capability of computer systems. The state of the art of coal combustion modelling described by Douglas Smoot (1984) three decades ago explicitly recognised its minimal applicability in practical industry at the time. Fifteen years later, computational fluid dynamics (CFD) models have been applied with increasing accuracy in sub-scale as well as industrial-scale coal furnaces (Brewster, 1996; Eastwick et al., 1999; Gera et al., 2001; Jones et al., 1999). CFD research then progressed to encompass modelling of blends of different coals (Backreedy et al., 2005b; Sheng et al., 2004). Current research in coal combustion modelling is at an advanced state, investigating detailed issues such as toxic and trace elements (James et al., 2014; Jassim, 2015) and boiler erosion (Pillai, 2014).

However, CFD expertise in biomass and coal/biomass blends has been lagging relative to that of coal. Biomass combustion/co-firing in itself has its share of issues (as seen in Section 2.4), and so has its computational modelling. The thermochemical structure of biomass adds to the complexity of the model (Stroh et al., 2015). Also, the size and shape of the particles potentially has a more significant effect in the modelling of biomass, as opposed to coal; this is a consequence of internal heat transfer within the particles (Gubba et al., 2011; Gubba et al., 2012). Finally, the difference in moisture content between biomass and coal has to be taken into account. In contrast to coal, where the drying and devolatilisation are merged into a single step, biomass (especially types with high moisture contents) could potentially require a separate drying step in the model (Williams et al., 2001).

2.6.2 CFD sub-models

The fundamental principle behind the CFD modelling of coal/biomass (co)combustion is the conservation of mass, momentum, energy and species. These conservation equations are solved for the fluid (continuous) and particle phases using discretisation methods, of which volumetric discretisation is the preferred method (Wang & Yan, 2008). A CFD model encompasses sub-models which deal with different aspects of the fluid and particle phases. Some of the fundamental sub-models are outlined in the following sub-sections.

2.6.2.1 Particle phase

Particle motion and heating

A significant contributor to different behaviour of biomass particles with respect to coal particles is that they are typically larger in size and lower in density compared to pulverised coal particles. This affects the motion and the heating of the biomass particles.

The simplest particle sub-models involve treating both coal and biomass particles as spheres, as done by Yin et al. (2010) in modelling coal/straw co-firing. This can be justified if the particle size is less than a few hundred μm ; the mean diameter of pulverised coal particles is less than 100 μm (Yin et al., 2004). The spherical assumption affects the drag force on the simulated particle and hence its movement in the fluid phase (Morsi & Alexander, 1972). In the context of particle heating, the spherical/isothermal sub-model implies the assumption that there is a uniform temperature inside the particle; a simple heat transfer occurs at the surface of the particle by convection and radiation, until the particle temperature reaches the vaporisation temperature (Tabet & Gökalp, 2015).

One method of taking into account the effect of irregular shape of biomass particles on their movement is the use of a shape factor. The shape factor is defined as the ratio of the surface area of a sphere having the same volume as the particle to the actual surface area of the particle (Haider & Levenspiel, 1989). This approach has been utilised by several co-firing studies involving woody and herbaceous biomass (Backreedy et al., 2005a; Bhuiyan & Naser, 2015; Ma et al., 2007; Nikolopoulos et al., 2013).

More complex alternatives for the isothermal heating model have been suggested for biomass particles (Gubba et al., 2011; Lu et al., 2010; Yang et al., 2008; Yuen et al., 2007). These models involve discretisation of the particle and establishing the temperature gradient within the particle. The spherical/isothermal model was suggested to be inadequate by Lu et al. (2010) when the particle size exceeds 300 μm , while Yang et al. (2008) identified the threshold to be 200-250 μm .

Devolatilisation

The particle devolatilisation sub-models available can be classified into lumped models and distributed models (Sharma et al., 2015).

Lumped models

In lumped models, the reaction products are grouped into gas, tar and char. These are the most commonly used devolatilisation models (see Table 2.11).

The constant rate model is the simplest, where the volatiles are released at a steady rate. Hence, only this single parameter has to be defined in the model. Pillai (1981) determined this rate to be 12 s^{-1} for coal. However, this rudimentary model is not in widespread use today as it can be considered oversimplified given the current state of computational power.

The single first-order reaction model (SFOR) determines the devolatilisation rate to be dependent on the amount of volatiles remaining. It employs a single Arrhenius correlation, and hence requires two parameters to be defined – the exponential energy (E) and the pre-exponential factor (A) (Badzioch & Hawksley, 1970). This model is widely used for predicting the devolatilisation of a range of biomass including olive waste (Álvarez et al., 2014), sawdust (Bonefacic et al., 2015), straw (Yin et al., 2010; Gubba et al., 2012), palm kernel (Gubba et al., 2011) and cardoon (Nikolopoulos et al., 2013) in co-firing modelling studies.

The two competing rates model (also known as the Kobayashi model (Kobayashi et al., 1977)) sees widespread use in the modelling of coal devolatilisation (Gu et al., 2014; Son & Sohn, 2015; Park et al., 2015b; Zhou et al., 2014). A few recent studies have attempted to apply the Kobayashi model to biomass as well (Ghenai & Janajreh, 2010; Li, 2014). This model consists of two parallel devolatilisation reactions, of which one becomes more dominant at higher temperatures. Each reaction is of the first order Arrhenius form, and hence four fundamental kinetics parameters need to be defined – the exponential energy (E) and the pre-exponential factor (A) for each parallel reaction (Kobayashi et al., 1977).

Distributed models

Distributed models, also known as network models, utilise the chemical structure of the fuel. They are more detailed than lumped models and have the advantage of being able to predict the composition of the volatiles (Tabet & Gökalp, 2015; Williams et al., 2000).

The FG-DVC model was originally developed for coal, and features both a functional group (FG) component for predicting gas yields and a depolymerisation,

vaporisation, crosslinking (DVC) component for char/tar formation (Solomon & Serio, 1994). This model was adapted by Chen et al. (1998) for use with biomass. Ma et al. (2007) utilised this model – subsequently named FG-biomass – in a biomass-only combustion study, while Backreedy et al. (2005a) did so in a co-firing study; in both cases, woody biomass was used in a 1 MW combustion facility.

Niksa (2000) presented another devolatilisation model known as bio-FLASHCHAIN, which is based on the depolymerisation of chain macromolecules.

The chemical percolation model (CPD) was originally developed for coal (Fletcher et al., 1990). It uses information regarding the structure of the coal, obtained from nuclear magnetic resonance (NMR). This method was later adapted to cover hemicellulose, cellulose and lignin – the major components of biomass (Sheng & Azevedo, 2002). This modified method – called bio-CPD – has been used by Wan et al. (2015) and Wang et al. (2015) to model devolatilisation in coal/biomass co-pyrolysis studies. Wang et al. (2015) recognised the potential applicability of the pyrolysis study results to future co-firing studies.

Char combustion

There are three sub-models which are commonly used to describe the heterogeneous solid-gas combustion (see Table 2). The simplest is the diffusion-limited rate model, where the rate of the reaction at the surface of the particle is governed by the rate at which gaseous oxidant diffuses to this surface. The kinetic/diffusion-limited rate model incorporates the reaction kinetics (in the form of an Arrhenius equation of which the activation energy E and pre-exponential factor A have to be defined) as well, in addition to the diffusion rate. The intrinsic model, also known as Smith's model, is similar to the kinetic/diffusion-limited model in that it

includes both diffusion and kinetics effects. However, a more elaborate equation is used to calculate the kinetics effect; this utilises the intrinsic chemical and pore diffusion rates (ANSYS Inc., 2011a). Álvarez et al. (2014) used another possible sub-model known as the multiple-surface-reactions model. Here, a custom char combustion mechanism involving several surface reactions can be defined, with the reaction kinetics being input for individual reactions. The overall combustion rate depends on diffusion as well as these individual reactions. In contrast, the first three sub-models (diffusion-limited, kinetic/diffusion limited and intrinsic) use a single-step char burnout reaction.

2.6.2.2 Continuous phase

There are three fundamental facets to the modelling of the continuous/fluid/gas phase – turbulence, chemistry and the turbulence-chemistry interaction (ANSYS Inc., 2011a; Tabet & Gökalp, 2015).

A range of turbulence sub-models are available in commercial CFD code, which are based on Reynolds-Averaged Navier Stokes (RANS) methods; RANS essentially involves expressing the fundamental equations of fluid flow (Navier-Stokes equations) with a time-averaged component and a fluctuating component. RANS-based turbulence sub-models include Spalart-Allmaras (one governing equation), $k-\varepsilon$ (two equations), $k-\omega$ (two equations) and Reynolds Stress Model (most complex with five equations) (ANSYS Inc., 2011a). The most commonly-used ones for co-firing applications are the three variations of $k-\varepsilon$ (standard, RNG and realisable) (Tabet & Gökalp, 2015; Wang & Yan, 2008). Recent studies have favoured the realisable $k-\varepsilon$ variation, touting its pragmatic compromise between accuracy and computational demand, and better convergence of the solution (Black et al., 2013; Li et al., 2009; Park et al., 2015a; Rezeau et al., 2012).

The chemistry model (reaction mechanism) that can be used is dependent on the turbulence-chemistry interaction that is selected. The eddy dissipation model (EDM) and its derivative finite rate/EDM is suitable for one-step and two-step chemistry models; the eddy dissipation concept (EDC) model should be used if more than two steps are involved in the chemistry model (ANSYS Inc., 2011a). EDM and finite rate/EDM are the most commonly employed sub-models for co-firing, followed by EDC (see Table 2.11). Another, albeit less-used, approach is the use of mixture-fractions, where a chemical equilibrium system is assumed; this has been demonstrated by Ghenai & Janajreh (2010) for modeling wheat straw combustion.

Table 2-11 presents a bibliographic compilation of recent biomass combustion/co-firing CFD studies.

Table 2-11: Recent biomass combustion/co-firing modelling studies

Biomass type	Devolatilisation sub-model	Char combustion sub-model	Turbulence sub-model	Turbulence-chemistry interaction sub-model	Radiative sub-model	Reference
Straw	SFOR (biomass)	Diffusion-limited	Std. $k-\varepsilon$	EDM	DO (Discrete ordinates)	(Yin et al., 2004)
Wood	FG-biomass (biomass) FG-DVC (coal)	Intrinsic	RNG $k-\varepsilon$	EDM	P-1	(Backreedy et al., 2005b)
Wheat straw	Kobayashi (both)	Intrinsic	RNG $k-\varepsilon$	mixture-fraction	P-1	(Ghenai & Janajreh, 2010)
Straw	SFOR (biomass)	Diffusion-limited	Std. $k-\varepsilon$ Realisable $k-\varepsilon$	EDM EDC	DO	(Yin et al., 2010)
Wood Palm kernel expeller	SFOR (both)	Intrinsic	Std. $k-\varepsilon$ RNG $k-\varepsilon$	EDC	DO	(Gubba et al., 2011)
Straw	SFOR (biomass)	Kinetic/diffusion-limited	Realisable $k-\varepsilon$	EDM	DO	(Gubba et al., 2012)
Cardoon	SFOR (biomass)	Kinetic/diffusion-limited	Std. $k-\varepsilon$	Finite rate/EDM	P-1	(Nikolopoulos et al., 2013)
Olive waste	SFOR (biomass) FG-DVC (coal)	Multiple surface reactions	RNG $k-\varepsilon$	EDC	DO	(Álvarez et al., 2014)
Spruce sawdust	SFOR (biomass) Kobayashi (coal)	Kinetic/diffusion-limited	[Undefined]	Finite rate/EDM	DO	(Bonefacic et al., 2015)
Sawdust	Global custom 5-step reaction mechanism based on first-order kinetics		k- ω -sst	EDM	DO	(Stroh et al., 2015)

2.7 *Jatropha curcas*

Currently, most research on *Jatropha curcas* focuses on the extraction and use of oil from the *Jatropha* seed as an alternative to diesel (Fernandes et al., 2015; Fernández et al., 2015; Go et al., 2016; Tambunan et al., 2012). The oil can be used directly in certain diesel engines, or it can be processed into conventional biodiesel (Sricharoenchaikul & Atong, 2009). Unprocessed *Jatropha* oil has seen successful use in diesel engine trials, and has shown low exhaust emissions compared to fuel-oil obtained from other vegetation sources, and has also shown favourable power outputs and fuel consumption figures when compared to conventional diesel. For use in higher-speed diesel engines (for instance, those used in road vehicles), the oil has to be transesterified by using methanol or ethanol (Gübitz et al., 1999).

However, the yield of fuel oil is only about 18% by mass of the dry *Jatropha* fruit. Approximately 38% by mass of the fruit consists of the shell, while 40% of the seed's mass comprises the husk. During the production of oil/diesel from *Jatropha*, a considerable amount of biomass is discarded as waste, and there is the potential to extract energy from this waste as well via other means. This would maximise the usage of the *Jatropha* fruit, and could possibly double or triple the total energy yield from the fruit (Singh et al., 2008).

It has been suggested that the seed cake can be used for biogas production via gasification (Basili & Fontini, 2012; Pandey et al., 2012). Laboratory- and pilot-scale studies using *Jatropha* seed cake as a gasification feedstock have been carried out by Christodoulou et al. (2014), KSrividhya et al. (2010) and Vyas & Singh (2007). Recently, Sharma & Sheth (2015) successfully applied pyrolysis to *Jatropha* seed cake to produce bio-oil using laboratory-scale apparatus. However, there is a dearth of information on using combustion as an energy conversion method for *Jatropha* seed

cake, particularly with respect to co-firing and electricity generation. Peng & Zhou (2014) proposed in their life cycle analysis that use of *Jatropha* outside biodiesel production – specifically, for bio-electricity generation – is necessary to make the total energy yield of the plant significant.

Characterization of a fuel is an important prerequisite to determining the feasibility of its application. Doshi et al. (2014) performed a characterisation study on the residue left after *Jatropha* whole seeds, kernels and hulls had been milled and de-oiled using solvent (hexane) extraction. The proximate and ultimate analyses, lignocellulosic content and the calorific value are reported in Table 2-12. For comparison, the available characterisation data of untreated (no oil extraction) *Jatropha* seed hulls from Singh et al. (2008) is also shown. Doshi et al. (2014) also performed an inorganic elemental analysis (using X-ray fluorescence spectrometry – XRF); based on the calculated base-to-acid ratio, it was suggested that the *Jatropha* seed residue would be prone to ash deposition problems such as slagging and fouling when combusted.

Table 2-12: Characterisation of Jatropha seeds (Doshi et. al, 2014; Singh et. al, 2008)

	No oil removed (Singh et al., 2008)	De-oiled (Doshi et al., 2014)		
	Hull	Whole seed	Kernel	Hull
Moisture (%)	10.75	9.4	8.7	10.2
Volatile matter (%)	71.01	61.3	66.7	60.2
Ash (%)	3.97	7.1	8.7	4.8
Fixed carbon (%)	24.99	22.3	16.0	24.9
Calorific value (MJ/kg)	16.93	18.61	18.96	17.68
Cellulose (%)	-	31.5	32.9	29.8
Hemicellulose (%)	-	22.7	24.9	17.2
Lignin (%)	-	4.8	3.5	8.3
C (%)	-	39.8	40.4	42.9
H (%)	-	6.2	6.5	5.4
O (%)	-	36.3	45.9	41.5
N (%)	-	4.0	7.2	0.9
S (%)	-	0.56	0.90	0.15

2.8 Concluding remarks

The importance of biomass as a fuel has been gaining increasing attention over the past decade. Fundamental characterisation of various types of biomass have been carried out; characterisation is a key initial step in determining the applicability of a specific biomass type as a feedstock for energy conversion.

Although several energy conversion methods are available for biomass, combustion is the most widely implemented energy conversion method for biomass at present. In the short- to medium-term, direct co-firing of biomass with coal is the most pragmatic approach since it employs the existing combustion facilities with minimal

modifications. However, studies have established the drawbacks of direct biomass co-firing in terms of ash deposition issues and problematic blending and co-combustion behaviour. These are caused primarily by the difference in chemical, physical and thermochemical characteristics between coal (for which the combustion plants were initially designed) and biomass. Torrefaction and leaching are biomass pre-treatment techniques have been identified in recent years as two of the most important methods of mitigating these problems. These two pre-treatment methods were hence selected as the focus of the present study; torrefaction and leaching aim to bridge the gap between coal and biomass in terms of thermochemical and chemical properties, respectively.

The application of CFD as a tool to predict biomass combustion and co-firing has been lagging relative to that of coal, caused in part by the fundamental differences between coal and biomass. However, increasing significance has been given in recent years to research in co-firing modelling. Although the limitations in some of the current models have been recognised, this avenue of research is an important step in understanding the underlying mechanisms and subsequently optimising the co-firing process.

It is evident that research into the use of *Jatropha curcas* seed cake as an energy source is still in its infancy. There is a substantial gap in the research with respect to its comprehensive characterisation and subsequent pre-treatment, and application of CFD to evaluate its combustion and co-firing behaviour. With the increasing recognition of *Jatropha* seed oil as a viable biodiesel feedstock, an in-depth investigation into utilising the resulting seed cake in this manner would be a worthwhile undertaking.

3 METHODOLOGY

3.1 Introduction

This chapter presents the experimental methods and apparatus which were used in this study. The chapter begins by outlining the biomass feedstock preparation (Section 3.2). This is followed by the detailed methodology of each experimental technique employed, i.e. the two pre-treatment methods (Section 3.3), characterisation methods (Section 3.4) and combustion tests using the drop tube furnace (Section 3.5).

Figure 3-1 shows the overall methodology utilised for this thesis. While the practical specifics of the individual techniques are described in this chapter, the experimental design for each phase is outlined in the relevant chapters (Chapters 4, 5, 6, 7). The four elements in UPPER CASE in Figure 3-1 refer to the main phases of the work, each described in detail in its corresponding chapter. This chapter is devoted only to the experimental methodology – the combustion modelling methodology is detailed in Chapter 7.

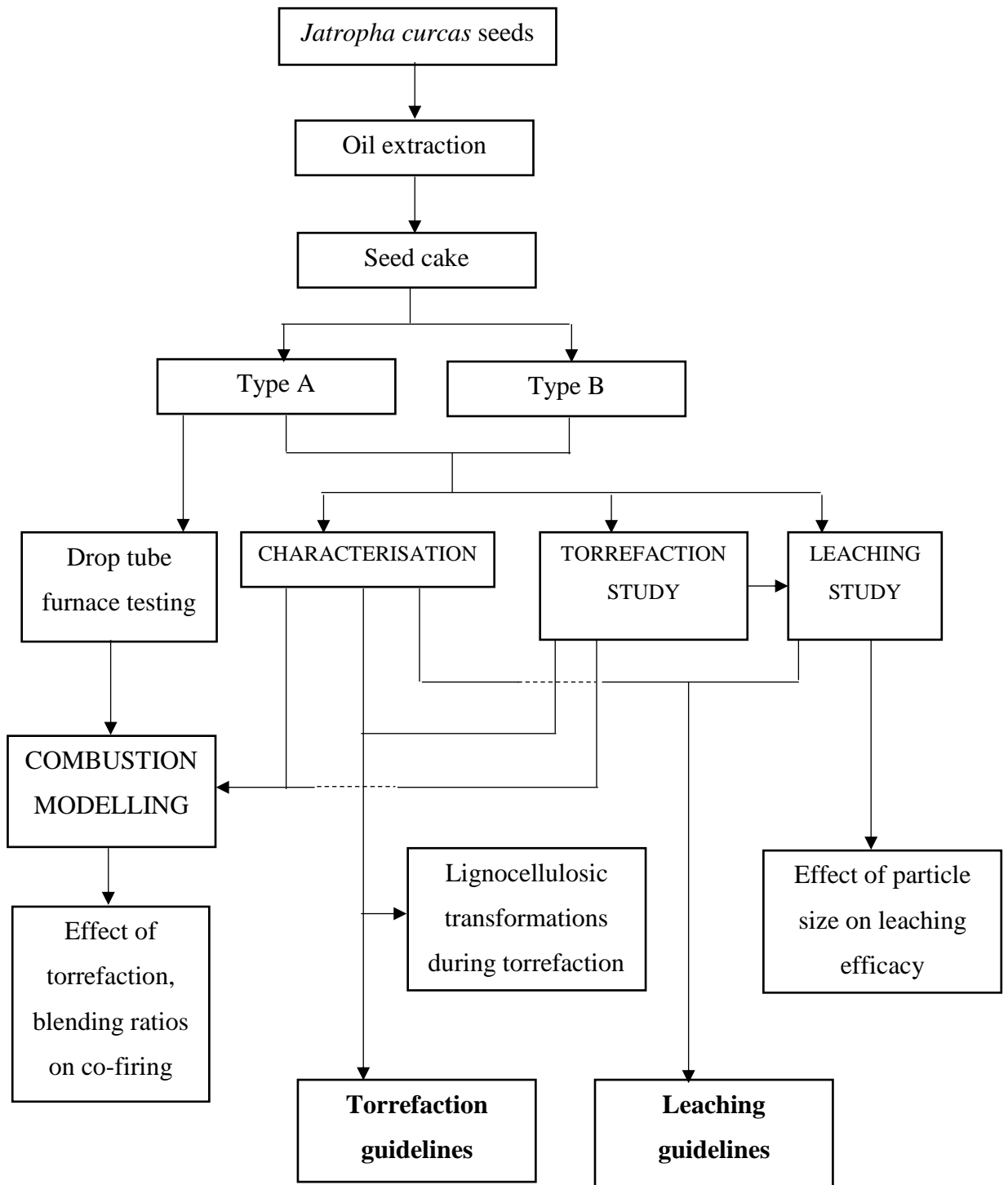


Figure 3-1: Overview of methodology used in this thesis.

3.2 Biomass feedstock

The *Jatropha curcas* seeds were sourced from a plantation in Sepang, Malaysia. They were dried for 24 h in an oven at 105°C, and double wrapped in large plastic bags before shipping to the UK. 55 kg of the seed were sent to an external facility (Statfold Seed Oil Ltd.) for oil extraction. The extraction was carried out by twin-screw, cold-pressing expellers (Statfold Seed Developments Ltd, 2016). 48.5 kg of solid residue (seed cake) were obtained, corresponding to an oil yield of 12%. This is lower than the oil yield of 28-29% reported in the literature (Singh et al., 2008).

The seed cake appeared to consist of two distinct components – hard, dark, rod-like structures (referred to as “type A” henceforth) in a soft, oily, loose soil-like matrix (“type B”). The type B comprised of approximately $\frac{3}{4}$ (by weight) of the total seed cake. Figure 3-2 (a), (b) and (c) illustrate the seed cake as received, type A only and type B only, respectively.

The Type A was milled using a Retsch PM100 ball mill (Figure 3-3 (a)). The ball mill consists of a steel bowl into which approximately 200 ml of the seed cake was loaded at a time, along with eight stainless steel balls (Figure 3-3 (b)). The securely closed and clamped bowl was spun inside the milling unit at 400 rpm for 60 s. The collisions between the steel balls and the seed cake pulverises the caked material. The milled seed cake was then separated into three particle size fractions. A Retsch AS200 sieve shaker (Figure 3-3 (c)) fitted with three sieves (ASTM standard sizes) were used for this purpose. The particle size fractions are listed below:

- < 1 mm (fine)
- 1 mm – 2.36 mm (medium)
- 2.36 mm – 4.75 mm (coarse)

Relatively coarse particle sizes had to be chosen, since using finer meshes proved problematic due to agglomerated particles clogging the meshes. The wide size fractions allowed a sufficient amount of type A seed cake to be available within at least two of the fractions (fine and medium). The type B biomass proved even more challenging to sieve using fine meshes due to its higher apparent oil content, and was used as received.



Figure 3-2: Jatropha curcas seed cake (a) as received, (b) type A, (c) type B.

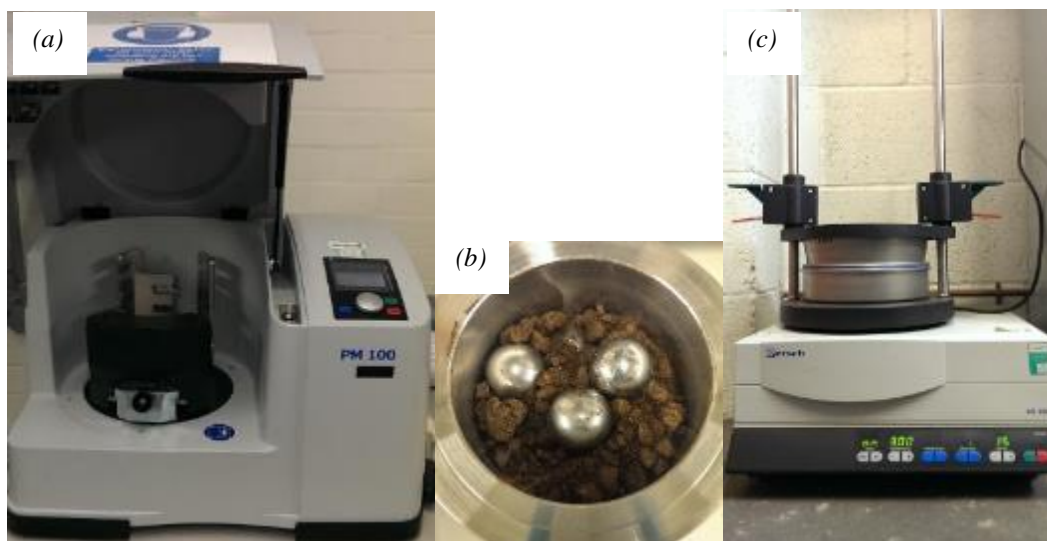


Figure 3-3: (a)(b) Ball mill, (c) sieve shaker used on type A biomass

3.3 Pre-treatment

3.3.1 Torrefaction

Torrefaction of the seed cake was carried out using a horizontal tube furnace (HTF). The HTF used was a TSHH 11/90/457 model manufactured by Elite Thermal Systems (Figure 3-4). It is a split-type furnace with a tube furnace of 90 mm and a heated zone length of 457 mm, which can reach a maximum temperature of 1100°C. A quartz reactor tube with an internal diameter of 60 mm was placed within the furnace. End seals were fitted to the two open ends of the reactor tube, and a N₂ gas supply was connected to one end. A rotameter enabled the gas flow rate to be controlled. The other end of the tube was connected to a gas scrubber unit filled with water, which was vented to a fume extractor unit. A schematic diagram of the HTF is shown in Figure 3-5.



Figure 3-4: Horizontal tube furnace used for torrefaction

For each torrefaction run, approximately 25 g (± 0.5 g) was measured into a ceramic “weighing boat”. The weighing boat was placed in the middle of the reactor tube and both ends of the tube were sealed using rubber bungs. The N₂ supply was switched on and set to 2 l/min (at room temperature). After the N₂ flow had been running for 5 min

(to ensure that O₂ is purged out of the reactor tube), the hood of the furnace was closed and its power supply switched on. The integrated PID controller was used to program the required temperature profile. For each run, a constant ramp of 10°C/min was used until the required torrefaction temperature was reached, followed by an isothermal period for the necessary holding time.

Immediately after the run was completed, the controller switches off the furnace and the hood of the furnace was opened to accelerate cooling. When the temperature readout reached 100°C, the N₂ supply is switched off and the sample was removed from the reactor tube. The sample was reweighed after it had cooled down to room temperature, and transferred to an airtight plastic bag for storage until subsequent analyses were carried out. The post-run procedure was standardised across all runs regardless of torrefaction temperature and holding time, since the pyrolysis process would continue to occur at the elevated temperatures during the cooling phase.

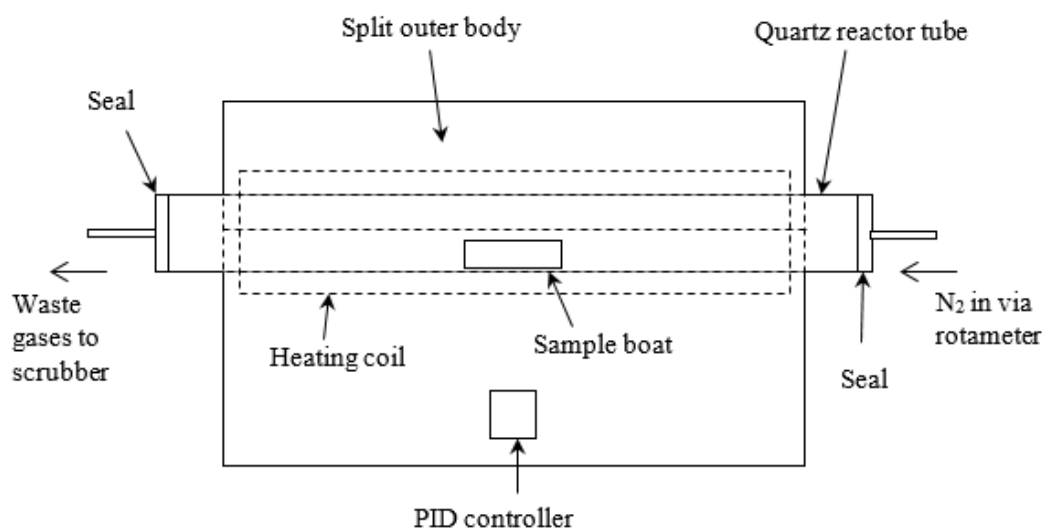


Figure 3-5: Schematic diagram of HTF used for torrefaction.

The mass and energy yields for each torrefaction run were calculated as follows:

$$\text{mass yield} = \frac{\text{final mass of sample (after torrefaction)}}{\text{initial mass of sample (before torrefaction)}} \times 100 \quad \text{Eqn 3-1}$$

$$\text{energy yield} = \frac{\text{HHV of torrefied sample} \times \text{final mass}}{\text{HHV of raw sample} \times \text{initial mass}} \times 100\% \quad \text{Eqn 3-2}$$

where the HHV (higher heating value) was measured using a bomb calorimeter (Section 3.4.2).

3.3.2 Leaching

The leaching process was carried out for 24 h in a Jeiotech BS-21 shaking water bath (Figure 3-6). For each leaching run, 3.0 g of biomass was weighed and set aside, and 300 ml of Milli-Q water (with resistivity <0.030 MΩ cm) was measured into a glass jar Figure 3-7. The jars were closed with their lids (to minimise evaporation at higher temperatures), and placed on the spring rack of the water bath Figure 3-8. The bath was topped up until its water level was higher than the water level inside the jars. The PID controller of the bath was then used to set the desired water temperature, residence time and vibrating speed. The vibrating speed was set to 40 rpm, as this was found by preliminary tests to provide satisfactory mixing without causing spillage. After the bath was switched on, a period of 45 min was allowed for the water temperature to stabilise at the set level. An electrical conductivity (EC) meter (Fisher Scientific Traceable pen) was used to measure the initial EC in each jar. The temperature readout of the meter was also used to ascertain that the desired water temperature had been reached inside the jars. The weighed biomass samples were then poured, one by one, into the corresponding jars and their lids replaced.



Figure 3-6: Shaking water bath used for the leaching runs.



Figure 3-7: Glass jars with Milli-Q water used for the leaching runs.



Figure 3-8: Jars with biomass loaded, secured in the water bath.

EC readings were then taken every hour for the first 6 h, and the last 3 h of the 24-h period. The loading of the samples into the jars and the taking of the EC measurements were carried out in the same sequence of jars, so that the time between measurements was kept approximately constant. The hood of the bath was kept closed throughout the leaching process, except when loading the samples and taking EC measurements. At the end of the 24-h period, leachate samples (10 ml) were extracted from each jar using a syringe and stored in glass vials for analysis.

Following this, the jars were removed from the bath and the solid separated out by decanting and filtration (Figure 3-9). The filter paper containing the solid was placed on a steel tray and dried in a vacuum oven at 60°C and a gauge pressure of -900 mbar for 2 h (Figure 3-10). The dried solid was then transferred to open glass vials and dried for a further 2 h under similar conditions. The vials were then closed and stored for analysis.



Figure 3-9: Filtration to separate biomass from leachate.

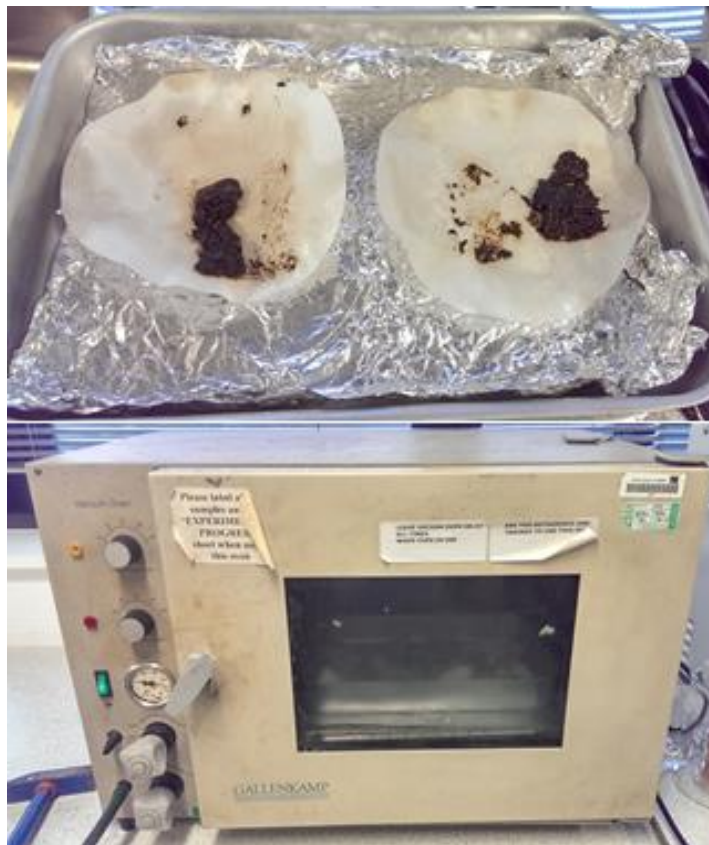


Figure 3-10: Drying of leached biomass samples in vacuum oven.

3.4 Characterisation

3.4.1 Thermogravimetric analysis

3.4.1.1 Proximate analysis

Thermogravimetric analysis (TGA) was used to determine the proximate composition of the seed cake, i.e. the moisture, volatile matter (VM), fixed carbon (FC) and ash content. The fundamental concept behind this technique is that the biomass sample undergoes a mass loss in several consecutive stages as it is heated. These stages correspond to the different proximate components of the biomass being lost (moisture, VM, FC in that order), with the residual mass being the ash content.

Figure 3-11 shows the TGA unit which was used – a TA Instruments Q500 with a 16-position autosampler (TA Instruments, 2016). It contains a vertical microbalance that can measure a sample up to 1 g, with a sensitivity of 1 µg. The balance is housed in a temperature-controlled environment. During operation, the sample is enclosed in a vertically-aligned furnace. A maximum temperature of 1000°C can be reached. Two thermocouples which are immediately adjacent to the sample are used to measure the sample temperature for feedback and control purposes. The TGA unit is interfaced with a PC with the TA Instruments control software. This software allows control over the TGA instrument, carries out data logging, and also allows post-processing of the output.

The empty platinum sample pans (up to 16 at a time) are placed on the autosampler tray and tared. The samples are then loaded on to the pans. The TGA profile and sample particulars are programmed into the software, which then manages the multiple runs automatically.



Figure 3-11: TA Instruments Q500 used for thermogravimetric analysis (TGA).

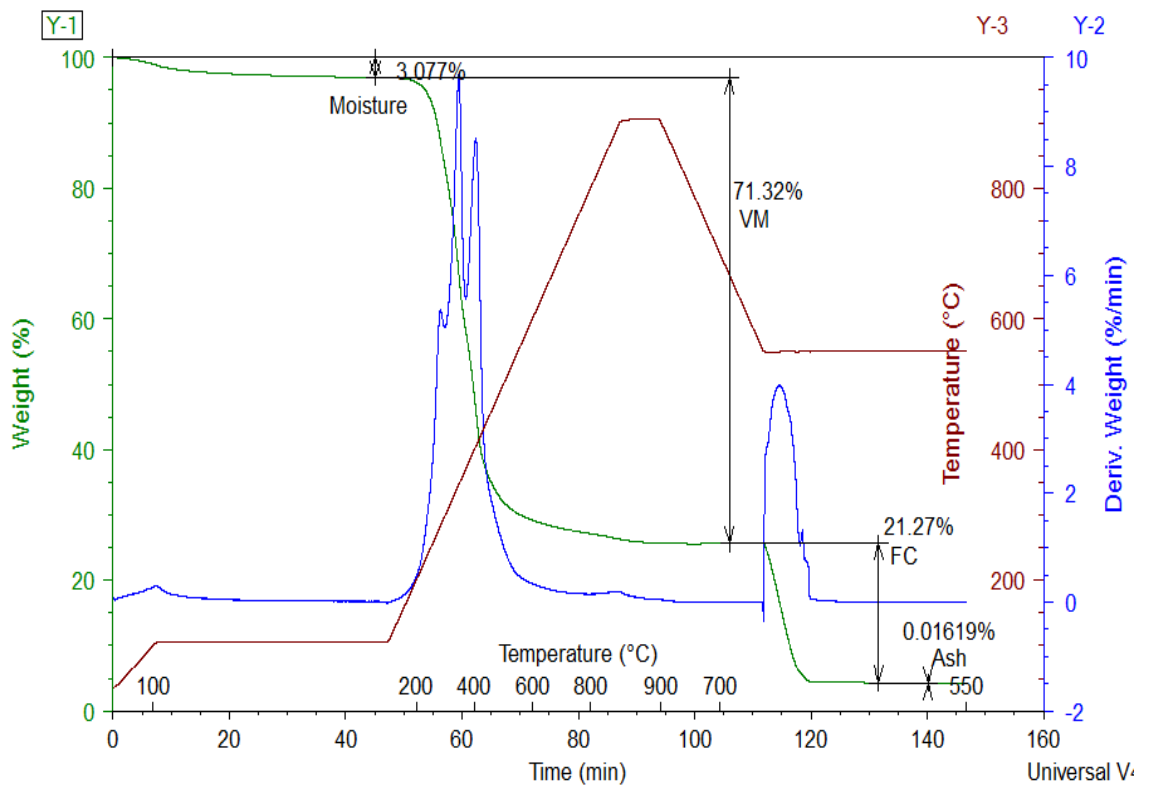


Figure 3-12: Typical TGA trace used for proximate analysis.

Figure 3-12 shows a typical TGA trace obtained from the instrument, processed using the TA Instruments Universal Analysis software. The distinct weight loss stages corresponding to each proximate component is shown – moisture, VM and FC in that order. The residual mass at the end of the run is the ash content.

The ash content was converted to dry basis, while the VM and FC content were converted to dry ash-free (DAF) basis:

$$dry\ ash\ (\%) = 100 \times \frac{ash\ (\%)}{100 - moisture\ (\%)} \quad \text{Eqn 3-3}$$

$$DAF\ VM\ (\%) = 100 \times \frac{VM\ (\%)}{100 - moisture\ (\%) - ash\ (\%)} \quad \text{Eqn 3-4}$$

$$DAF\ FC\ (\%) = 100 \times \frac{FC\ (\%)}{100 - moisture\ (\%) - ash\ (\%)} \quad \text{Eqn 3-5}$$

Optimisation of TGA profile for proximate analysis

Preliminary TGA runs were carried out employing the following TGA profile to determine the proximate composition. This profile was constructed based on the British Standards guidelines for proximate analysis of biomass (British Standards BS EN 14774-2:2009, BS EN 15148:2009, BS EN 14775:2009).

- N₂ flowing at 100 ml/min
 - Heating to 105°C at 10°C/min
 - Holding at 105°C for 40 min
 - Heating to 905°C at 20°C/min
 - Holding at 905°C for 7 min
 - Cooling to 550°C at 20°C/min
- Air flowing at 100 ml/min
 - Holding at 550°C for 120 min

Following this profile, the total time for each run was approximately 235 min. Due to the relatively large number of individual runs in the presently described main study, it was desirable to reduce the time taken per run without compromising the quality of

the results. This optimisation was done by analysing the weight loss curves from the preliminary TGA runs which employed the original full-length profile (Figure 3-13).

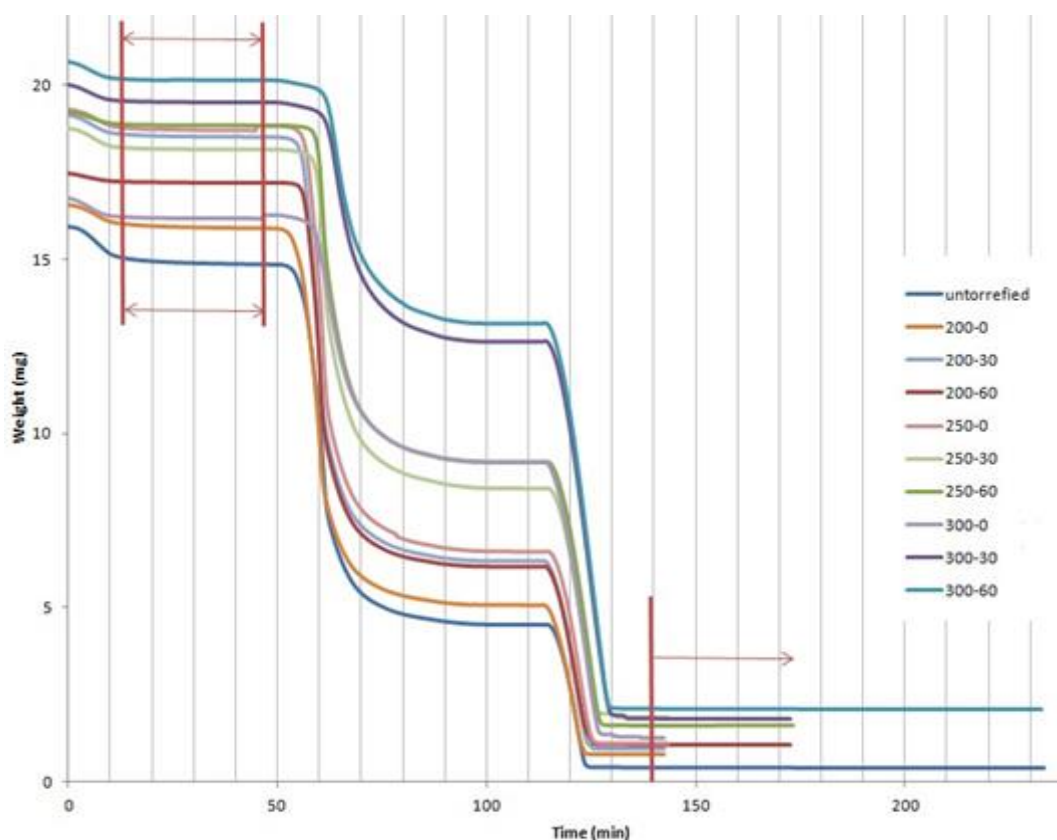


Figure 3-13: Weight loss profiles for preliminary TGA runs carried out with full-length temperature profile.

The sections marked by red arrows indicate isothermal regions of no weight loss. The first such region is in the drying segment of the run. Within 10 min, most of the moisture has been driven out of the torrefied samples. Leaving a safety margin, the isothermal stage at 105°C was reduced from 40 min to 20 min. However, it is possible that the untorrefied biomass can have higher levels of moisture. To ensure the reliability of the data, the duration of the isothermal drying stage was hence left unaltered for the untorrefied samples. The other isothermal region where there is a plateau in the weight loss is the final post-combustion segment of the run. It can be observed from the TGA outputs that complete combustion is always achieved in approximately 20-25 min. Hence, this segment was shortened from 120 min to 35 min.

Table 3-1 summarises the changes made to the proximate analysis TGA profile. The per-run time was reduced by 105 min and 85 min for the torrefied and untorrefied samples, respectively. This translates to a significant reduction in the total time required for the proximate analysis of all the samples.

Table 3-1: Summary of changes made to TGA profile.

Stage			Time interval (min)		
			Original	Modified (torrefied)	Modified (raw)
N ₂	Heat to 105°C @ 10°C/min	Drying	<10	10	10
	Hold @ 105°C		40	20	40
	Heat to 905°C @ 20°C/min	Devolatilisation	40	40	40
	Hold @ 905°C		7	7	7
	Cool to 550°C @ 20°C/min	-	18	18	18
O ₂	Hold @ 550°C	Combustion	120	35	35
Total time			235	130	150

3.4.1.2 Devolatilisation kinetics

The TGA was also used to measure the devolatilisation kinetics. The devolatilisation reaction can be described by the following the expression (Gil et al., 2010):

$$\frac{dx}{dt} = k(T).f(x) \quad \text{Eqn 3-6}$$

where x is the degree of conversion, t is time in s, $f(x)$ is the reaction model, and $k(T)$ is the rate constant which is a function of the absolute temperature T (K).

The degree of conversion is defined as:

$$x = \frac{m_0 - m}{m_0 - m_f} \quad \text{Eqn 3-7}$$

where m is the mass of the sample at time t , and m_0 and m_f are the mass at the beginning and end of the devolatilisation segment in question, respectively. In this study, m_0 was taken to be the dry mass of the sample, while m_f was the final mass of the sample at the end of the TGA run. The value of $(m_0 - m)$ gives the mass of volatiles released up to time t , while $(m_0 - m_f)$ is the total mass of volatiles released. The ratio x thus expresses the degree of conversion in terms of the volatiles released.

The rate constant is governed by the Arrhenius law:

$$k = A \cdot e^{-E/RT} \quad \text{Eqn 3-8}$$

where A is the pre-exponential factor, E is the activation energy and R is the universal gas constant of $8.314 \text{ J K}^{-1} \text{ mol}^{-1}$.

Substituting Equation 3-8 in Equation 3-6:

$$\frac{dx}{dt} = A \cdot f(x) \cdot e^{-E/RT} \quad \text{Eqn 3-9}$$

Also,

$$\frac{dx}{dt} = \frac{dx}{dT} \cdot \frac{dT}{dt} = \beta \cdot \frac{dx}{dT} \quad \text{Eqn 3-10}$$

where β is the heating rate.

Hence,

$$\frac{dx}{dT} = \frac{A}{\beta} \cdot f(x) \cdot e^{-E/RT} \quad \text{Eqn 3-11}$$

There are several methods present in the literature to solve Equation 3-11 and determine the activation energy, E . Model-fitting methods only require

thermogravimetric data at a single heating rate, but are dependent on the accurate determination of the reaction model $f(x)$ to which the measured data is statistically fitted. Model-free methods typically require thermogravimetric data from several heating rates (β), but are simpler to implement and are excluded from any errors introduced by an incorrect choice of reaction model. Regardless of the solution method employed to determine E , determination of the pre-exponential factor, A , requires a reaction model to be chosen.

The first-order chemical reaction assumption is typically used in devolatilisation studies (Gil et al., 2010):

$$f(x) = -\ln(1 - x) \quad \text{Eqn 3-12}$$

The method developed by Coats & Redfern (1964) is a widely-used model-fitting method used to calculate the kinetic parameters of devolatilisation. This method offers an approximate solution to Equation 3-11 as:

$$\ln\left(\frac{f(x)}{T^2}\right) = \ln\left(\frac{AR}{\beta E}\right)\left(1 - \frac{2RT}{E}\right) - \frac{E}{RT} \quad \text{Eqn 3-13}$$

It can be assumed that $2RT \ll E$ (Damartzis et al., 2011). Hence, Equation 3-13 can be simplified to:

$$\ln\left(\frac{-\ln(1 - x)}{T^2}\right) = \ln\left(\frac{AR}{\beta E}\right) - \frac{E}{RT} \quad \text{Eqn 3-14}$$

A straight line is fitted to a plot of $\ln(-\ln(1-x)/T^2)$ against $1/T$. From the gradient and y-intercept of the fitted line, the activation energy and pre-exponential factor, respectively, can be calculated.

The devolatilisation segment of the TGA traces used for proximate analysis was used to extract the devolatilisation kinetics using the Coats-Redfern method. A Matlab program was written (Appendix 1) to read the TGA data files, process them and calculate the kinetic parameters E and A .

3.4.2 Calorimetry

An IKA C5000 bomb calorimeter (Figure 3-14) was used to measure the higher heating value (HHV) of samples (IKA-Werke, n.d.). The C5000 is a modular system consisting of a controller, measurement cell and cooling system. A significant portion of the measurement procedure is automated.

The sample is placed in a combustible bag (to prevent dispersion of the sample when oxygen is pumped in under pressure later) with a known calorific value, as shown in Figure 3-15 (a); the mass of both the bag and the sample are measured (to the nearest 0.0001 g) and recorded. The sample bag is secured into a stainless steel combustion crucible, which is then suspended from the lid of the combustion vessel (Figure 3-15 (c)). Figure 3-15 (c) also shows the cotton ignition thread (with a known calorific content) which is tied to the ignition wire so that it is in contact with the sample bag. The lid/holder is then lowered into the combustion vessel and tightened shut. The C5010 combustion vessel (Figure 3-15 (b)) is rated for a maximum pressure of 230 bar.



Figure 3-14: IKA C5000 bomb calorimeter.

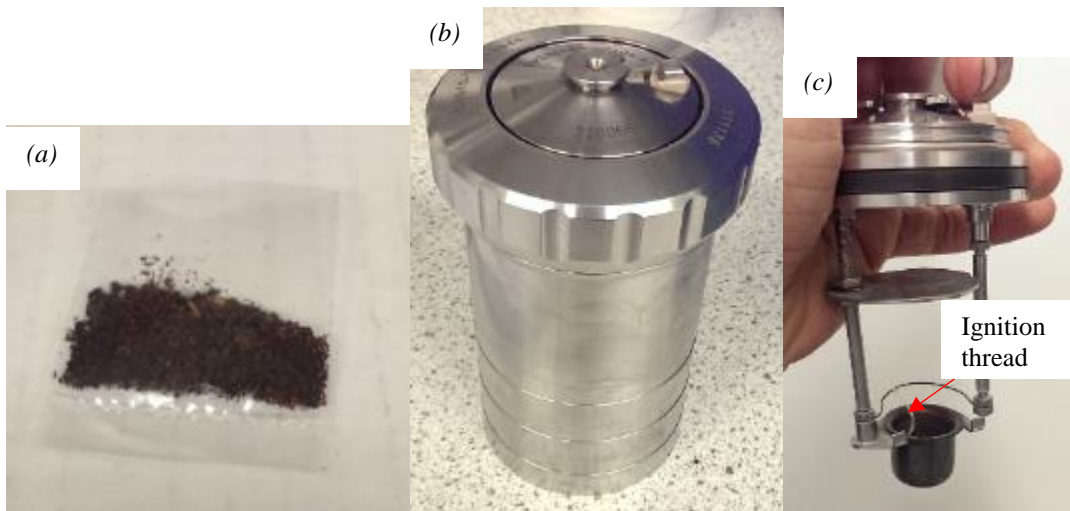


Figure 3-15: (a) Sample in combustible bag, (b) combustion vessel (c) suspended crucible.

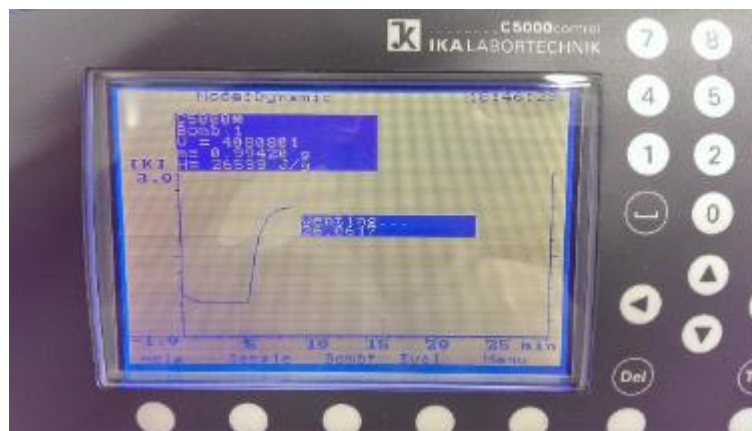


Figure 3-16: Control panel of calorimeter with display showing the progress of the run.

The following input parameters are entered into the controller: the mass of the sample, the calorific content of the cotton ignition thread, the calorific content of the combustible bag (calculated manually using the measured mass and specified calorific value of the bag). Once the combustion vessel is placed inside the measurement cell, the process is automated. The vessel is filled with oxygen from a 30 bar supply (99.95% pure), and the measurement cell is filled with water to submerge the vessel. Once the temperature of the water stabilises, an electric current is supplied to the ignition wire, which ignites the cotton ignition thread and in turn the sample (the cotton thread and sample bag are consumables). The progress of the run in terms of temperature rise is shown on the controller's display (Figure 3-16). The temperature rise is measured and used by the instrument, along with the previously entered input parameters, to calculate the HHV of the sample.

Standard runs using benzoic acid tablets are carried out at regular intervals to ascertain the calibration of the instrument, and hence the accuracy of the sample measurements. Two tablets (combined mass of approximately 1.0 g) are used for these runs; they are a recognised reference material with a known calorific value of 26.460 MJ/kg. The temperature rise caused by combusting this amount of benzoic acid is about 2.6 K, and that caused by combusting the biomass sample must also be roughly similar for the measurement to be accurate. Approximately 1.0 g of material was also used for the sample runs.

3.4.3 CHON elemental analysis

Ultimate analysis of the samples was carried out in line with the relevant British Standards guidelines (BS EN 15104). A Thermo Scientific FlashEA 1112 elemental analyser was used for the measurement (Figure 3-17) (Thermo Electron, 2004). The unit consists of a furnace where the sample is completely oxidised by applying a method known as “dynamic flash combustion”. This involves the tin capsule containing the sample undergoing an exothermic reaction which causes the sample to oxidise completely at temperatures up to 1800°C. A helium carrier gas transports the gaseous products of the oxidation through a copper reduction tube; elemental C, H, N, S are oxidised to CO₂, H₂O, NO_x, SO₂ respectively, and the NO_x is subsequently reduced to N₂. The gases are passed through a gas chromatography column which separates the component products. These components are then measured using a thermal conductivity detector. Figure 3-18 shows a typical chromatogram obtained from the instrument. Integration is performed on the chromatogram to determine the percentage by weight of C, H, N, S. The O content can then be calculated by difference.

The samples are prepared by placing a weighed quantity of material (approximately 2-3 mg, measured to the nearest 0.001 mg) in a tin container (Figure 3-19 (a)). The container is then folded to form a capsule from which the sample cannot escape (Figure 3-19 (b)). If S content is required to be measured, a V₂O₅ catalyst is also added; this step was omitted from the present analysis as S content was measured instead using XRF (Section 3.4.4). The prepared sample capsules are then loaded into the MAS 200 autosampler (Figure 3-17 (b)).

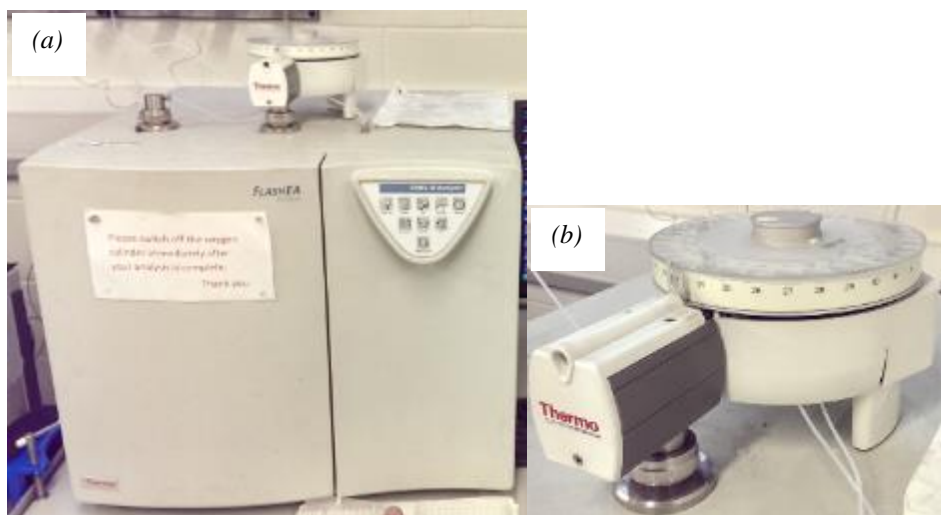


Figure 3-17 (a) FlashEA CHON analyser (b) MAS 200 autosampler.

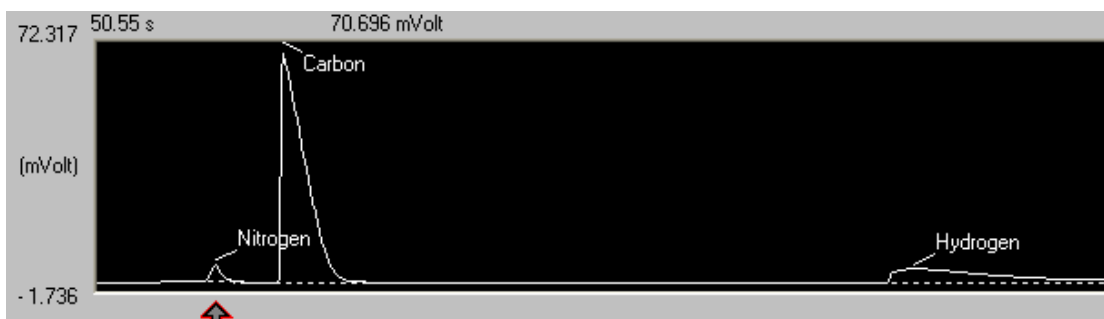


Figure 3-18: Typical chromatogram obtained from the EA instrument.

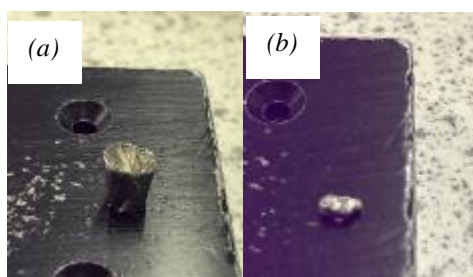


Figure 3-19: Tin container (a) before sample is loaded, (b) folded into capsule.

The Eager 300 software is used for controlling the instrument, data logging and subsequent analysis. The run sequence is programmed using this software, in the order in which the sample capsules were loaded into the autosampler. A typical sequence would include first a “blank” (an empty tin capsule which provides a baseline for measurement), a “bypass” (an unweighed sample of the standard reference material to “condition” the instrument), and one or more “standard” runs. The standard runs are

carried out with a weighed quantity of a reference material with known CHON composition. The reference material used was 2,5-Bis(5-tert-butyl-2-benzo-oxazol-2-yl)thiophene (“BBOT”) sourced from Elemental Microanalysis, which has an ultimate composition of 72.52% C, 6.09% H, 6.51% N, 7.43% O. The standard runs are used to plot a calibration curve using the k-factor method (Thermo Electron, 2004). The “unknown” runs follow the standard runs, employing the biomass samples which need to be analysed. “Unknown” runs using the reference material (BBOT) are carried out at regular intervals to ascertain the instrument calibration.

The moisture content of each sample, determined earlier by TGA, was used to calculate the C, H, N, content on dry basis, by using the following equations (BSI, 2011b):

$$C_{dry} = C_{measured} \times \frac{100}{100-M} \quad \text{Eqn 3-15}$$

$$H_{dry} = \left(H_{measured} - \frac{M}{8.937} \right) \times \frac{100}{100-M} \quad \text{Eqn 3-16}$$

$$N_{dry} = N_{measured} \times \frac{100}{100-M} \quad \text{Eqn 3-17}$$

where M is the moisture content (%).

The O content (dry basis) was then calculated using the following equation, based on the assumption that the C, H, N, O, moisture and ash content add up to 100%.

$$O_{dry} = 100 - C_{dry} - H_{dry} - N_{dry} - A \quad \text{Eqn 3-18}$$

where A is the ash content as determined by TGA.

3.4.4 XRF spectrometry

X-ray fluorescence (XRF) spectrometry was used to measure the inorganic content of the solid biomass samples, before and after leaching. The instrument used was a Bruker S8 Tiger (Figure 3-20)(Bruker Corporation, 2016). XRF relies on the principle of electron excitation from inner electron shells using X-ray beams. This in turn causes electron transitions from higher-energy states to lower-energy states, which results in energy being released as X-rays (“fluorescence”). The wavelength of this fluorescent radiation is characteristic to individual elements. By measuring the wavelength and intensity of this radiation, the individual elements and the concentrations in which they are present in the sample can be measured.

Since the electrons which are involved in the analytical process are from the inner shells which are not involved in chemical bonding, the measurement is independent of the compounds in which the elements are present. Hence, no chemical-based sample preparation is required prior to the analysis and the technique is non-destructive. This is an advantage compared to contemporary techniques such as ICP-MS (inductively charged plasma mass spectrometry) which require the sample to be undergo a hazardous and time-consuming acid digestion prior to the analysis.



Figure 3-20: Bruker S8 Tiger XRF spectrometer

The samples were loaded into cylindrical plastic containers which have a transparent Mylar® membrane at the base (Figure 3-21 (a), (b)). It was ensured that the sample is spread out evenly over the membrane with a depth of about 1 cm. The sample holders were then secured into steel holders (Figure 3-21 (c)) which are then loaded into the machine. They contain an orifice at the base, which together with the transparent membrane allows X-rays to enter and leave the sample freely. An autoloader mechanism is built-in, and up to 60 samples can be loaded at a given time.

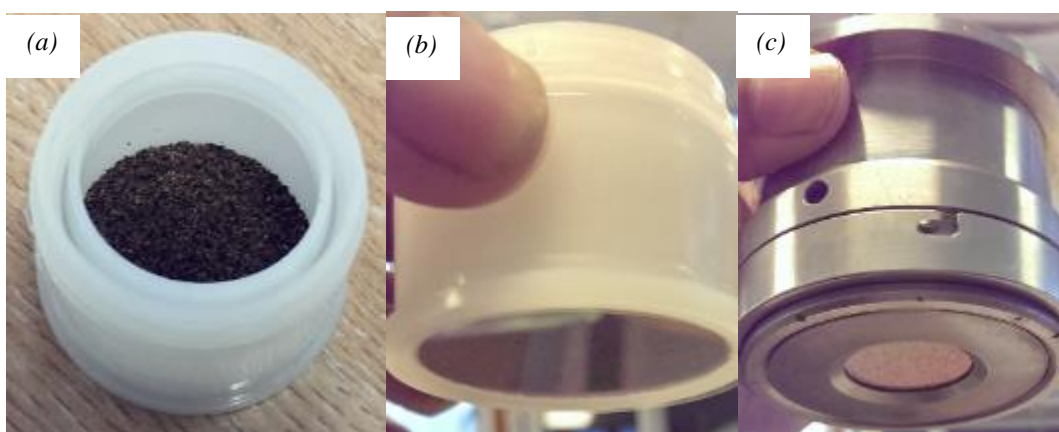


Figure 3-21: (a)(b) Plastic sample container, (c) steel holder with sample container within.

3.4.5 ^{13}C NMR spectroscopy

Solid-state ^{13}C nuclear magnetic resonance (NMR) spectroscopy was conducted on untorrefied and selected torrefied samples. It was used to identify the structural changes occurring within the biomass during the torrefaction process. These changes were related in particular to the three fundamental constituents of biomass – hemicellulose, cellulose and lignin. A high-power cross polarisation (CP) sequence was used along with proton decoupling on a Bruker Avance 200 NMR instrument (Figure 3-23). The resonance frequency for ^{13}C was 50 MHz. The sample was spun at approximately 5 kHz and 2500 scans were accumulated for each run. Tetrakis(trimethylsilyl)silane (TKS), which has a chemical shift of 3.5 ppm, was used with each sample run for calibration.

The cylindrical zirconia rotor (Figure 3-22 (a)) was filled with the biomass sample to be tested. A layer of TKS (which is supplied in a powdered form) was added on top of the sample. A metal tool (Figure 3-22 (b)) was used to compress the sample + TKS. This makes the TKS form a waxy seal on top of the biomass sample. This compression also caused much of the oil present in some samples (particularly the untreated type B) to be pressed out; this oil was wiped off, and the outside of the capsule cleaned before continuing. The rotor was then loaded into the machine.

The control panel on the unit shows the speed at which the rotor is spinning. This spin was increased to approximately 5 kHz by increasing the “drive pressure” and “bearing pressure”, with the bearing pressure being maintained at twice the drive pressure. Probe calibration was carried out, following which the analysis of the sample was initiated. The XWIN-NMR 3.5 software was used to control the acquisition of data, data logging and subsequent processing.

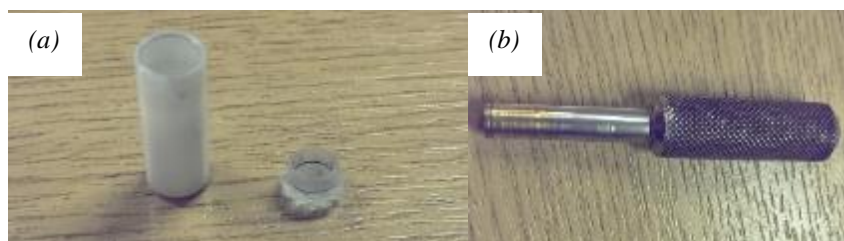


Figure 3-22: (a) Zirconia rotor for holding sample, (b) tool for compressing sample in rotor.



Figure 3-23: Bruker NMR system.

Figure 3-24 shows a typical unprocessed spectrum which was obtained. An exponential multiplication and Fourier transform, followed by phase and baseline correction were carried out to give the spectrum shown in Figure 3-25. A calibration along the horizontal axis (chemical shift) is also performed by setting the peak corresponding to TKS (a small, sharp peak close to 0 ppm) to 3.5 ppm.

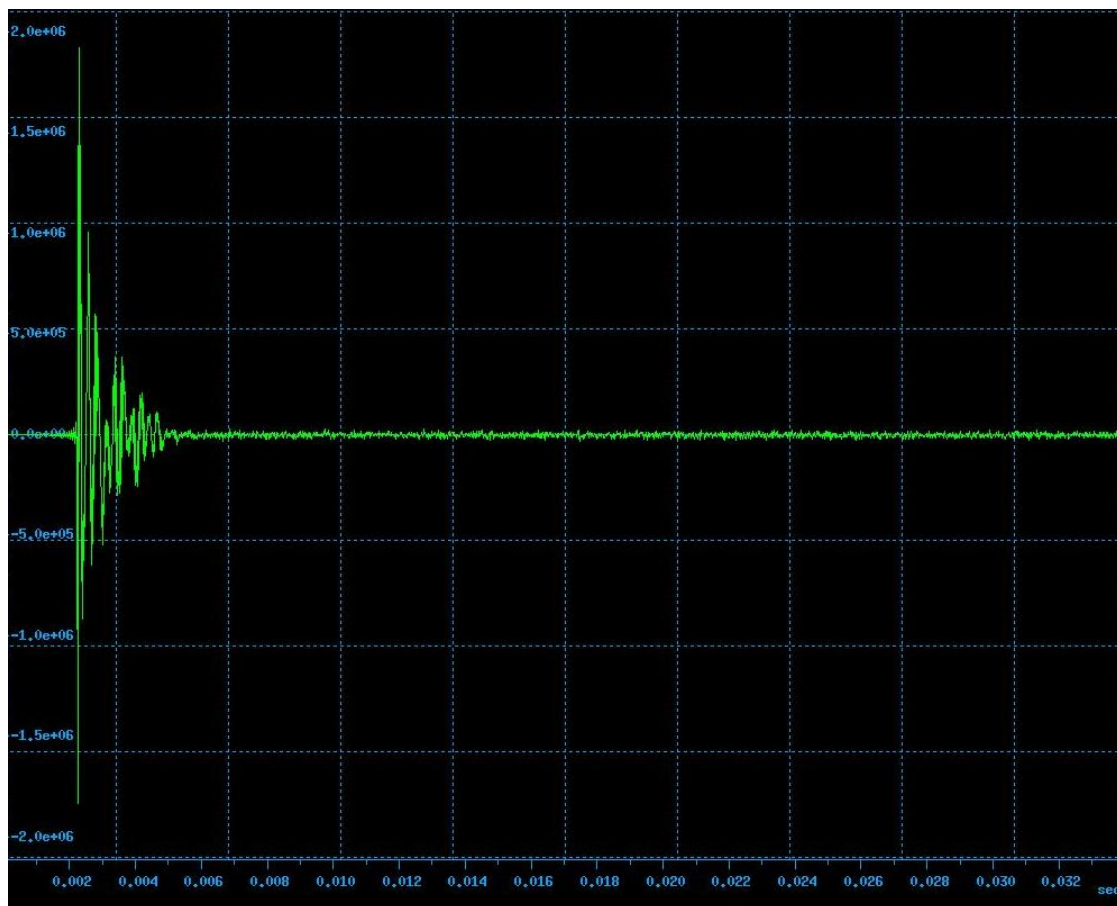


Figure 3-24: Unprocessed NMR spectrum.

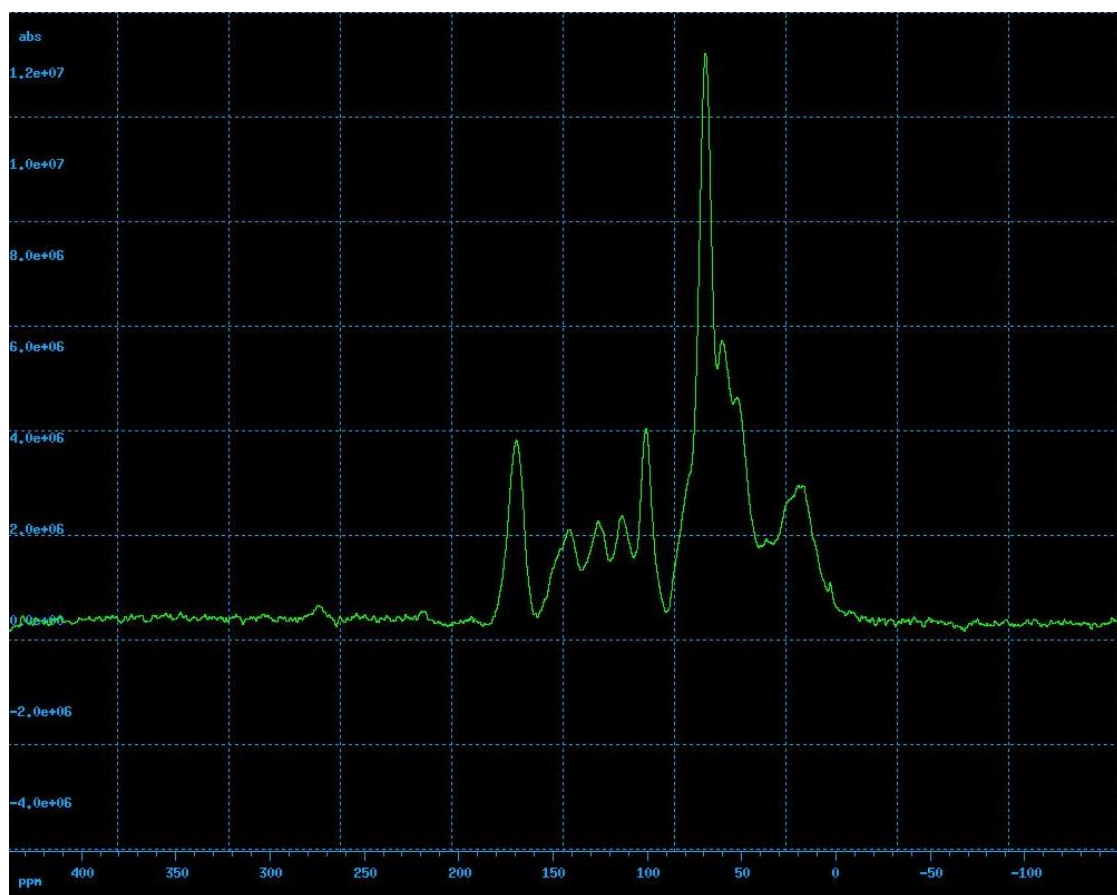


Figure 3-25: NMR spectrum after post-processin

3.4.6 ICP-MS

Inductively charged plasma mass spectroscopy (ICP-MS) was used to measure the inorganic content (cations) of the leachate samples throughout the leaching study. It was also used to measure the same of the solid leached biomass during the preliminary leaching study.

The solid samples had to be digested first since the analysis can only be carried out on liquids. The reagents used for the digestion was based on the relevant British Standards guidelines (BS EN 15290:2011), but the quantities of reagent and the procedure was modified to suit the available apparatus on a trial-and-error basis and visual inspection. 500 mg (\pm 3 mg, measured to the nearest 0.1 mg) of sample was weighed out into a conical flask. 5 ml of 30% hydrogen peroxide, and 13 ml of 65% nitric acid were added to the flask, and the mixture was heated using a hot plate until the volume in the flask had approximately halved (approximately 60 min) (Figure 3-26). The hot plate was switched off, and 10 ml of Milli-Q water was added to the flask to cool and dilute the mixture before it was filtered into a 50 ml volumetric flask. Milli-Q water was used to make up the volume to 50 ml. The mixture was filtered again and stored in vials, ready for analysis. Figure 3-27 shows the typical appearance of the solutions obtained after digestion of untorrefied and torrefied leached samples. A 1-in-10 dilution using 2% nitric acid was carried out on all samples (digests of solid samples and liquid leachate samples) prior to analysis. The ICP-MS analysis on the digested samples was performed by the School of Biosciences using a Thermo iCAP-Q spectrometer (Figure 3-28)(Thermo Fisher Scientific Inc., 2012).



Figure 3-26: Digestion of solid samples on hot plate.



Figure 3-27: Digested samples of (a) untorrefied, (b) torrefied biomass.



Figure 3-28: Thermo iCAP-Q ICP-MS unit.

3.4.7 Ion chromatography

Ion chromatography was used to measure the Cl content of the leachate samples throughout the leaching study. It was also used to measure the same of the solid leached biomass during the preliminary leaching study.

An aqueous extraction method was used for the solid samples, since Cl⁻ ions are easily dissolved in water. The sample was placed in a mortar and liquid nitrogen was poured on it. The freeze-dried sample was then ground into a fine powder using a pestle. 20 mg of the ground sample was weighed and transferred to 2.0 ml Eppendorf tube, and 1.5 ml of deionised water was added to it (Figure 3-29). The sample was then incubated at 4°C for 60 min while mixing, heated in a water bath at 90°C for 15 min, and then centrifuged for 15 mins to separate the solid sample from the liquid extract. A syringe was used to extract and transfer 0.5 ml of the extract to a sample tube. A 1-in-10 dilution using Milli-Q water was carried out on all samples (extracts from solid samples and liquid leachate samples). The ion chromatography was carried out on the sample by the School of Biosciences using a Thermo Dionex ICS-1000 instrument (Dionex Corporation, 2005).



Figure 3-29: Eppendorf tube with biomass sample and deionised water.

3.5 Drop tube furnace testing

The drop tube furnace (DTF) testing aimed to replicate the high heating rates found in industrial applications, for instance in pulverised fuel boilers (Ulloa et al., 2005). Figure 3-30 is a schematic representation of the DTF setup. The DTF consists of a vertically-aligned ceramic work tube which has an inner diameter of 50 mm and a length of 1.55 m. A water-cooled feeder probe with an internal diameter of 3 mm is present at the top of the work tube. At the base of the work tube is a water-cooled collector probe connected to a cyclone collector where the combusted material is deposited. The vertical position of the collector probe can be changed in order to vary the residence time; the probe separation was set to 22 cm in this case, which corresponds to a residence time of approximately 200 ms as calculated in the DTF's operating guidelines. The main gas inlet component flow rates (N_2 and O_2 in this case) and the feeder probe (carrier gas) gas flow rate (N_2 at 1 l/min) are controlled by rotameters. There are three heating units, all controlled via individual Eurotherm controllers (Figure 3-31) linked to thermocouples present along the work tube:

- Pre-heater – a spirally-wound silicon carbide element around the feeder probe which brings the temperature of incoming gases close to the desired operating temperature.
- Main heater – four vertical silicon carbide elements around the work tube.
- Trim heater – two smaller U-shaped elements at the base of the work tube, which compensate for the water-cooling of the collector probe.

The main gas component flow rates and temperature settings are set as per the guidelines in the standard operating procedure, and depend on the desired operating temperature, residence time, and volumetric gas makeup. For the respective settings of 1300°C, 200 ms and $N_2(90\%)/O_2(10\%)$ chosen for the runs, the N_2 and O_2 flow

rates were set to 11.1 l/min and 1.23 l/min, respectively. The temperature controllers were set to 100°C higher than the target temperature, i.e. to 1400°C.

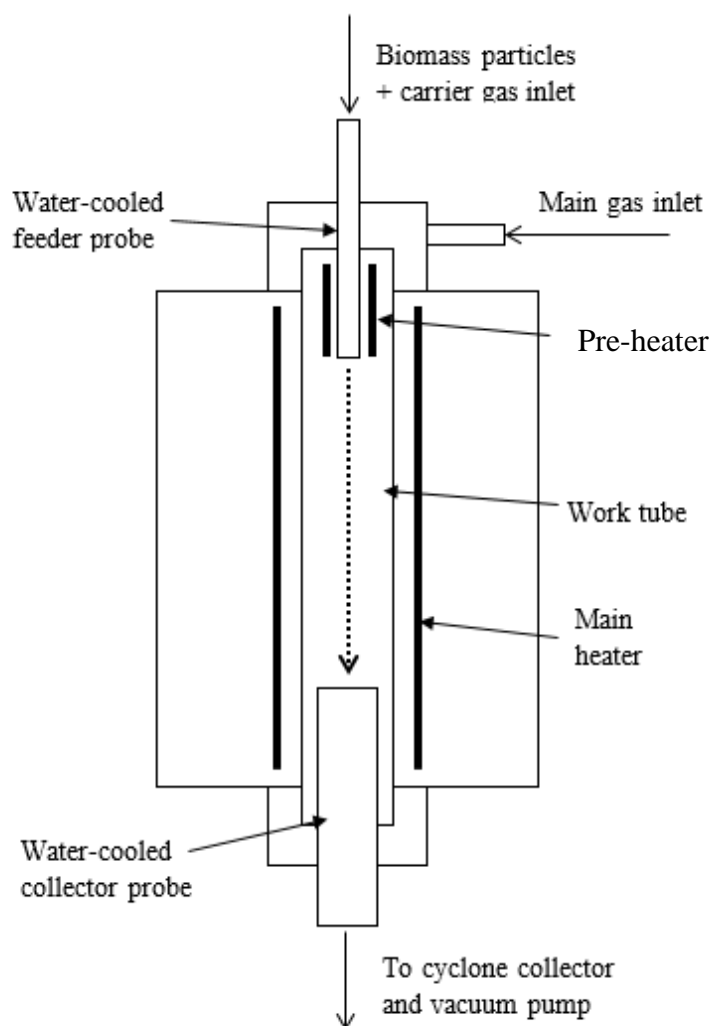


Figure 3-30: Schematic diagram of DTF.

A weighed biomass sample (3.0 g) was manually fed through the open end of the feeder probe, which has a funnel attached to it (Figure 3-32 (a)). Care was taken to make sure that the feeding is slow, controlled and at an even rate. The time taken to feed the entire sample was measured, allowing the average feed rate to be calculated. After the run was complete, the combusted sample (char) was collected from the removable sample pot attached to the cyclone collector, and stored in a glass vial for subsequent analysis by TGA.



Figure 3-31: Heater controls for the DTF.

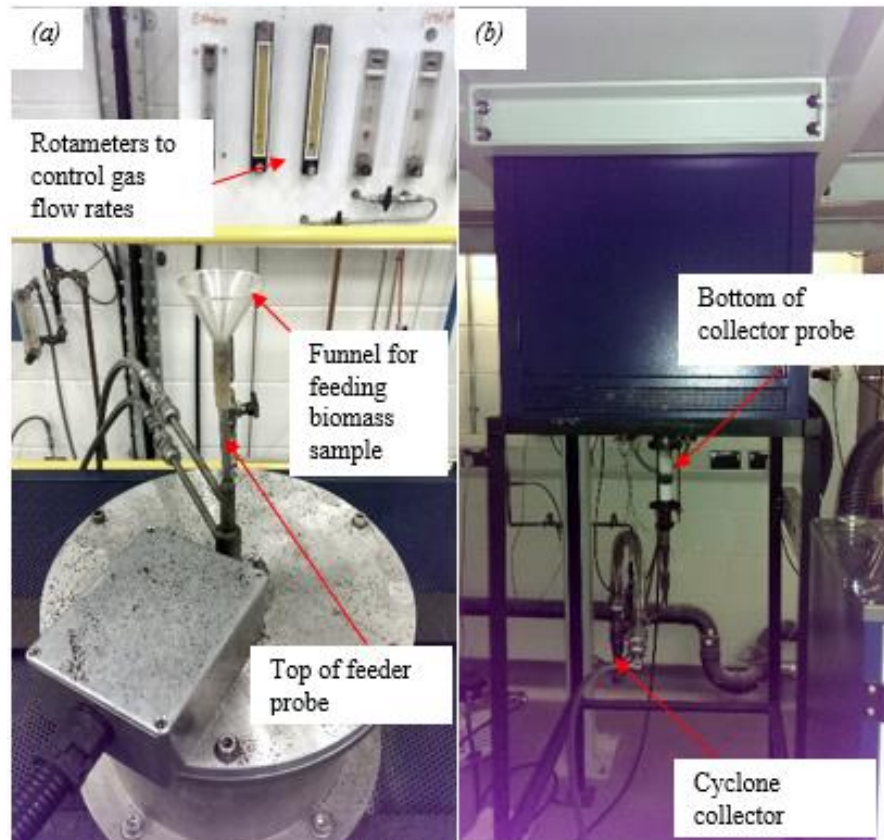


Figure 3-32: (a) Top of DTF showing feeder probe with funnel attached, (b) bottom section of DTF showing end of collector probe.

3.6 Concluding remarks

This chapter outlined the preparation of the *Jatropha curcas* seed cake and presented the experimental methods and apparatus utilised during the course of this research work. The subsequent chapters would present the experimental design and discuss the results obtained via the methods detailed in this chapter. Chapters 5 and 6 involve the pre-treatment procedures outlined in Sections 3.3.1 and 3.3.2, respectively. Chapters 4, 5 and 6 utilise the characterisation techniques detailed in Section 3.4. Chapter 7 would use the results obtained from drop tube furnace testing (Section 3.5).

4 BIOMASS CHARACTERISATION

4.1 Introduction

This chapter presents the fundamental fuel properties of the untreated type A (<1 mm size fraction) and type B *Jatropha curcas* seed cake. The data presented in this chapter establishes a baseline for the untreated biomass, while a more detailed discussion of how these properties change with pre-treatment, and the practical implications thereof, are presented in Chapters 5 and 6 accordingly.

The mean values for each property are presented, along with standard deviation (SD) and coefficient of variation (CV). The CV is the SD expressed as a percentage of the mean. Since the mean values for each element vary significantly, the CV provides a more useful representation of the relative variability.

4.2 Proximate analysis

The proximate composition of the seed cake as measured by TGA (six replicate measurements) is shown in Table 4-1. In addition to the as-measured values, those calculated on a dry and dry ash free (DAF) basis are also shown.

Comparing the type A and type B seed cake, it can be seen that the type B has a higher volatile matter (VM) content. Since the most conspicuous physical difference between the two types is the higher oil content in the type B, this suggests that the oil has a significant VM content. Among the proximate composition, the moisture content has the largest CV. Since the mean measured moisture levels are relatively low, even a variation which is small in absolute terms results in a relatively large CV. With a few exceptions, the CVs were generally lower for the type A material. This indicates that the higher compaction undergone by the type A during the pressing process (as suggested by the lower oil content) increases its homogeneity.

Table 4-1: Proximate analysis of Jatropha curcas seed cake.

		Type A	Type B
Moisture	Mean (% by weight)	3.62	3.92
	SD	0.53	0.44
	CV (%)	14.8	11.1
VM	Mean (% by weight)	69.26	75.71
	SD	0.65	1.88
	CV (%)	0.9	2.5
FC	Mean (% by weight)	21.39	16.15
	SD	0.96	1.63
	CV (%)	4.5	10.1
Ash	Mean (% by weight)	5.70	4.21
	SD	0.37	0.26
	CV (%)	6.5	6.1
Dry VM	Mean (% by weight)	70.87	78.80
	SD	1.00	1.93
	CV (%)	1.4	2.5
Dry FC	Mean (% by weight)	22.19	16.81
	SD	0.91	1.70
	CV (%)	4.1	10.1
Dry ash	Mean (% by weight)	5.91	4.38
	SD	0.36	0.26
	CV (%)	6.2	6.0
DAF VM	Mean (% by weight)	76.38	82.40
	SD	0.98	1.82
	CV (%)	1.3	2.2
DAF FC	Mean (% by weight)	23.58	17.58
	SD	0.97	1.82
	CV (%)	4.1	10.3

4.3 Ultimate analysis

Table 4-2 shows the ultimate analysis for the *Jatropha curcas* seed cake. Five replicate measurements were made for each seed cake type.

With respect to the dispersion of the ultimate analysis data, the CV is lowest for C (although this can partly be attributed to its relatively high mean value). The highest CV by a significant margin was for the N content. A possible explanation is that different parts of the seed would have a wide variation in N content due to the presence/absence of proteins in them, which contain a significant proportion of N. Even after milling and mixing, this variation would present itself as inhomogeneity within the seed cake. As with the proximate analysis, the CVs for the type B's ultimate analysis is consistently higher than those of type A's, demonstrating a greater inhomogeneity within the type B.

Table 4-3 shows the measured C, H, N along with their corresponding CV for both the untreated seed cake and BBOT (2,5-(Bis(5-tert-butyl-2-benzo-oxazol-2-yl)thiophene), which is the reference material used for calibration of the instrument. The measured value of the BBOT deviates from the reference value specified by its manufacturer by 0.2% or less, and its CV is below 1%. This confirms the accuracy and precision of the measurement technique for the ultimate analysis, leaving the inhomogeneity of the seed cake as the most plausible explanation for the variation in measured values.

Table 4-2: Ultimate analysis of *Jatropha curcas* seed cake.

		Type A	Type B
Dry C	Mean (% wt)	49.88	56.37
	SD	0.45	0.57
	CV (%)	0.9	1.0
Dry H	Mean (% wt)	6.57	8.05
	SD	0.09	0.39
	CV (%)	1.4	4.9
Dry N	Mean (% wt)	4.83	4.25
	SD	0.59	1.13
	CV (%)	12.2	26.6
Dry O	Mean (% wt)	32.81	26.96
	SD	0.26	1.63
	CV (%)	0.8	6.1
Dry H/C	Mean	0.13	0.14
Dry O/C	Mean	0.66	0.48
DAF C	Mean (% wt)	53.02	58.95
	SD	0.47	0.59
	CV (%)	0.9	1.0
DAF H	Mean (% wt)	6.99	8.42
	SD	0.09	0.41
	CV (%)	1.4	4.9
DAF N	Mean (% wt)	5.13	4.44
	SD	0.63	1.18
	CV (%)	12.2	26.6
DAF O	Mean (% wt)	34.87	28.19
	SD	0.28	1.71
	CV (%)	0.8	6.1

*Table 4-3: As-measured CHN content of *Jatropha curcas* seed cake and BBOT reference material.*

		Type A	Type B	BBOT (measured)	BBOT (reference)
C	Mean (% wt)	48.08	54.16	72.70	72.53
	SD	0.43	0.54	0.26	
	CV (%)	0.89	1.0	0.35	
H	Mean (% wt)	6.33	7.73	6.08	6.09
	SD	0.09	0.37	0.04	
	CV (%)	1.36	4.85	0.65	
N	Mean (% wt)	4.08	4.65	6.51	6.51
	SD	1.09	0.57	0.04	
	CV (%)	26.6	12.2	0.54	

4.4 HHV

Table 4-4 shows the HHV of the type A and type B biomass, based on three replicates each. A plausible explanation for the higher HHV of the type B seed cake is its higher apparent oil content. There was little variation in the HHV measurements among replicates, with a CV less than 0.5% in both cases. Table 4-4 also shows the measured HHV of benzoic acid tablets, which is the reference material used for calibrating the instrument. The deviation of the measured HHV from that specified by the reference material's manufacturer was ~0.1% with a CV of 0.3%, which demonstrates the accuracy and precision of the instrument.

Lower H/C and O/C ratios have been linked with a higher HHV, since C-C bonds are stronger than C-H and C-O bonds (as explained in detail in Section 2.5.2.2). The type B has a marginally higher H/C ratio, but a substantially lower O/C ratio as compared to type A, as seen in Table 4-2 (Section 4.3).

Table 4-4: HHV of *Jatropha curcas* seed cake and benzoic acid reference material.

		Type A	Type B	Benzoic acid (measured)	Benzoic acid (reference)
HHV	Mean (MJ/kg)	20.764	24.055	26.492	26.460
	SD	0.08	0.13	0.08	
	CV (%)	0.4	0.5	0.3	
Dry HHV	Mean (MJ/kg)	21.5	25.0		
	SD	0.09	0.13		
	CV (%)	0.4	0.5		

4.5 Inorganic content

Table 4-5 shows the inorganic content of the biomass. The most abundant inorganic element present, by a substantial margin, was potassium (K). Since K has been touted as a major contributor to ash-related issues in biomass combustion, this indicates that *Jatropha curcas* seed cake would be liable to these problems if combusted in its untreated form. With the exception of the XRF-measured P, the type A biomass has a consistently higher inorganic content than the type B. This corroborates the relatively higher ash content observed in the proximate analysis of type A (Table 4-1).

The inorganic composition was measured using two methods – XRF spectrometry and ICP-MS/IC (ICP-MS for cations and IC for Cl). The former is a non-destructive analytical method while the latter option requires digestion (ICP-MS) or aqueous extraction (IC) of the solid biomass sample. From Figure 4-1, it can be seen that with the exception of Mg, the elemental levels detected by the XRF are consistently higher. This can be attributed to the potentially incomplete digestion/aqueous extraction of the solid samples prior to ICP-MS/IC. However, the overall trends with respect to the

relative magnitudes of the inorganic elements and the differences between the type A and type B, are broadly similar. This suggests that either approach would be suitable as far as a comparative analysis is concerned. However, XRF would be preferred for its speed, ability to measure both cations and anions, and the lack of the additional experimental error introduced by a digestion/extraction step.

Table 4-5: Inorganic content of Jatropha curcas seed cake.

		ICP-MS/IC		XRF	
		Type A	Type B	Type A	Type B
K	Mean (% wt)	2.03	1.75	6.64	5.82
	SD	0.10	0.24	0.11	0.13
	CV (%)	4.9	13.9	1.7	2.3
Mg	Mean (% wt)	0.46	0.40	0.39	0.30
	SD	0.02	0.05	0.04	0.04
	CV (%)	5.19	12.6	9.2	11.6
Ca	Mean (% wt)	0.23	0.19	0.93	0.86
	SD	0.01	0.03	0.03	0.01
	CV (%)	4.6	13.9	3.7	0.7
S	Mean (% wt)	0.28	0.27	0.57	0.53
	SD	0.02	0.06	0.02	0.04
	CV (%)	7.79	22.3	3.0	7.7
P	Mean (% wt)	0.76	0.64	1.36	1.45
	SD	0.03	0.02	0.03	0.06
	CV (%)	4.3	3.7	2.4	4.0
Cl	Mean (% wt)	-	0.33	0.78	0.78
	SD	-	0.00	0.11	0.03
	CV (%)	-	0.9	14.1	3.8

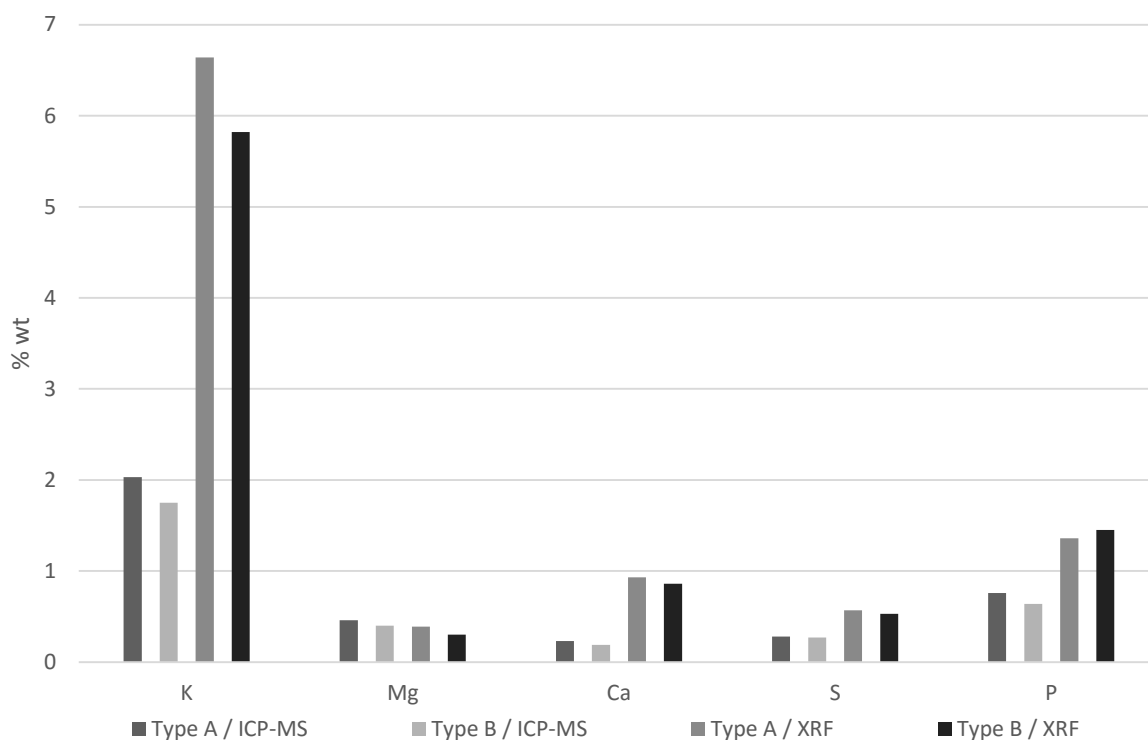


Figure 4-1: Inorganic content of Jatropa curcas seed cake.

4.6 Devolatilisation kinetics

Figure 4-2 and Figure 4-3 show the devolatilisation segments of the differential thermogravimetric (DTG) plots for type A and type B, respectively. An analysis of the significance of the peaks in these plots is presented in the Torrefaction chapter (Section 5.2.5).

Table 4-6 shows the devolatilisation kinetic parameters obtained from the Coats-Redfern method (Section 3.4.1.2). Figure 4-4 and Figure 4-5 show the linear regression plots generated by the Matlab program written to implement the method. The mean R^2 value for the regression is also shown in Table 4-6 (values closer to 1 show a good fit of the data). Four TGA curves were used for each seed cake type, and the mean values calculated.

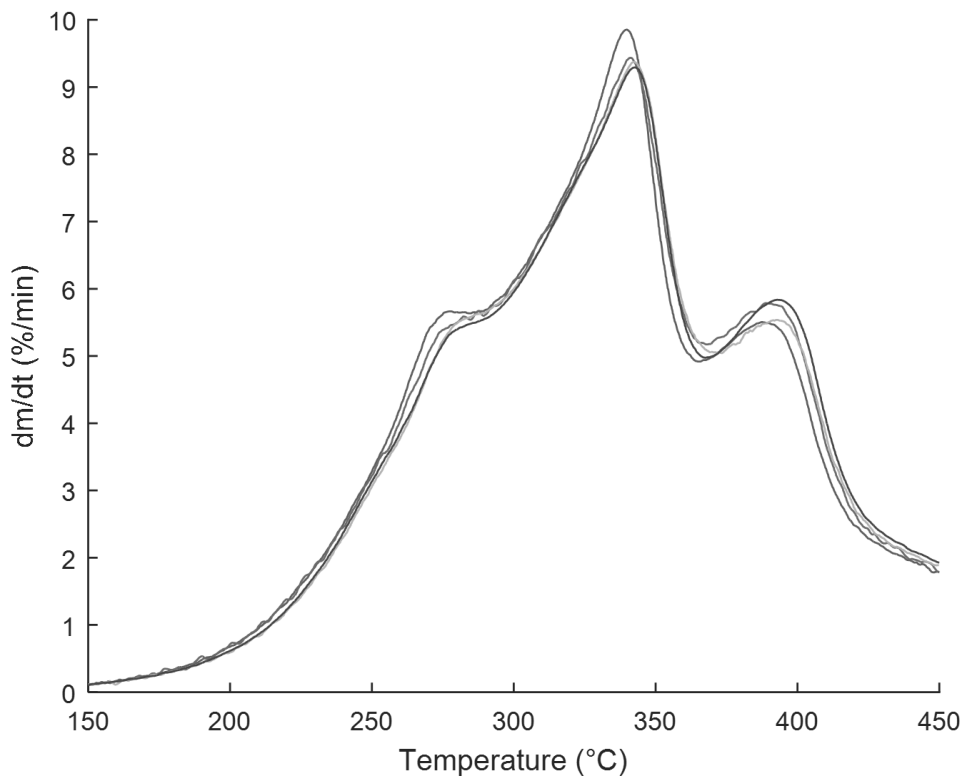


Figure 4-2: Devolatilisation DTG curves of type A seed cake.

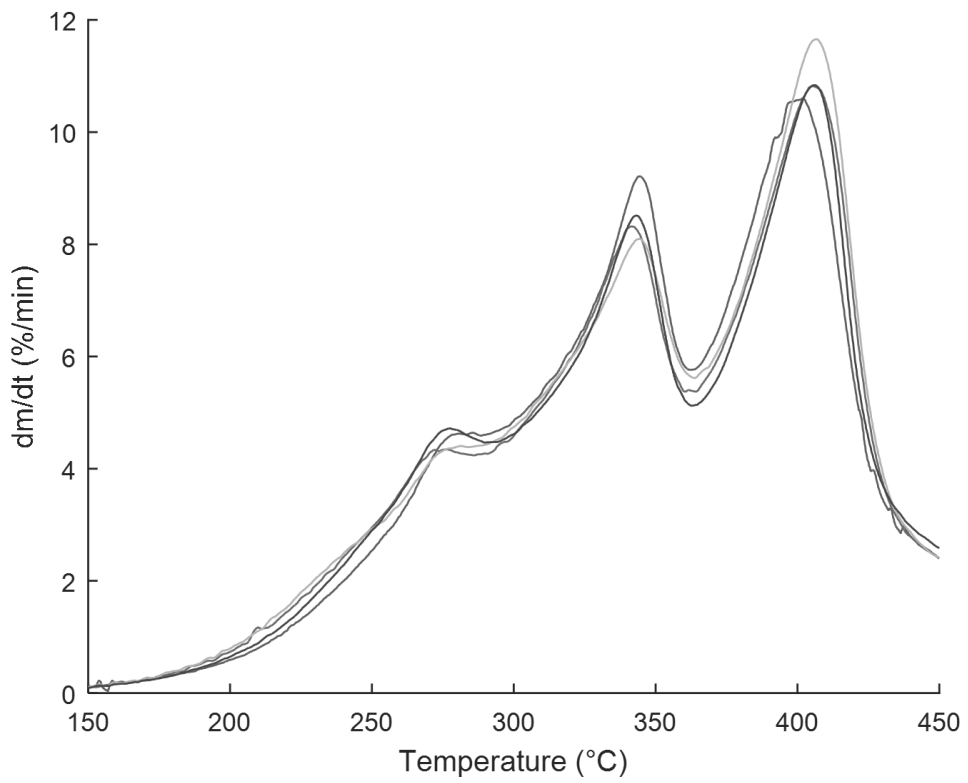


Figure 4-3: Devolatilisation DTG curves of type B seed cake.

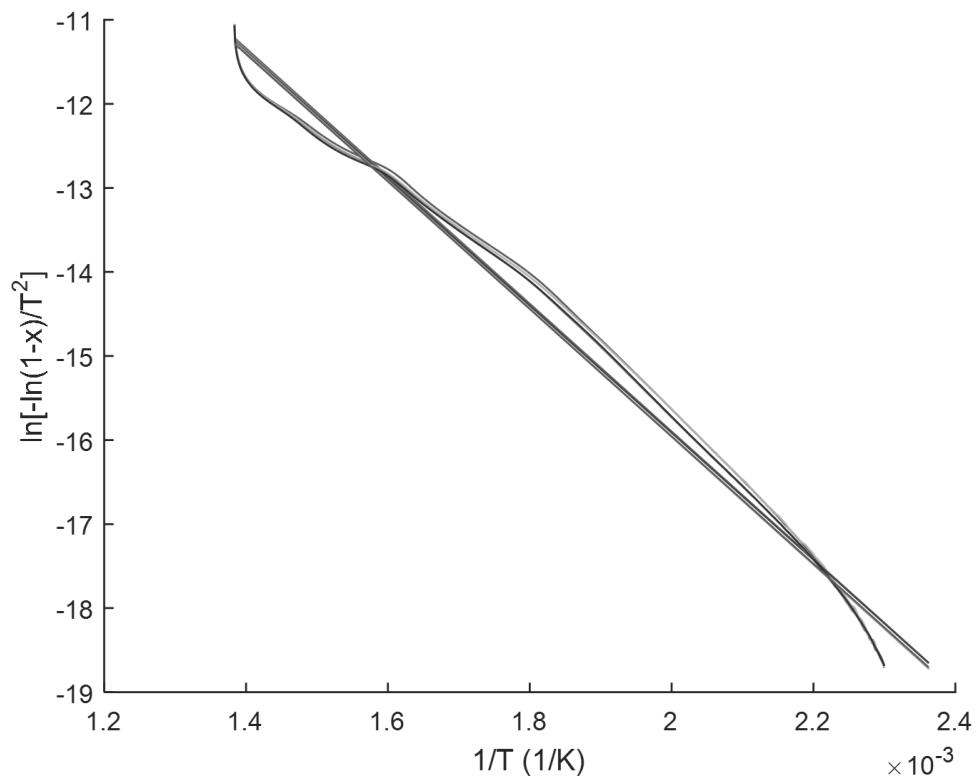


Figure 4-4: Coats-Redfern plots for type A seed cake.

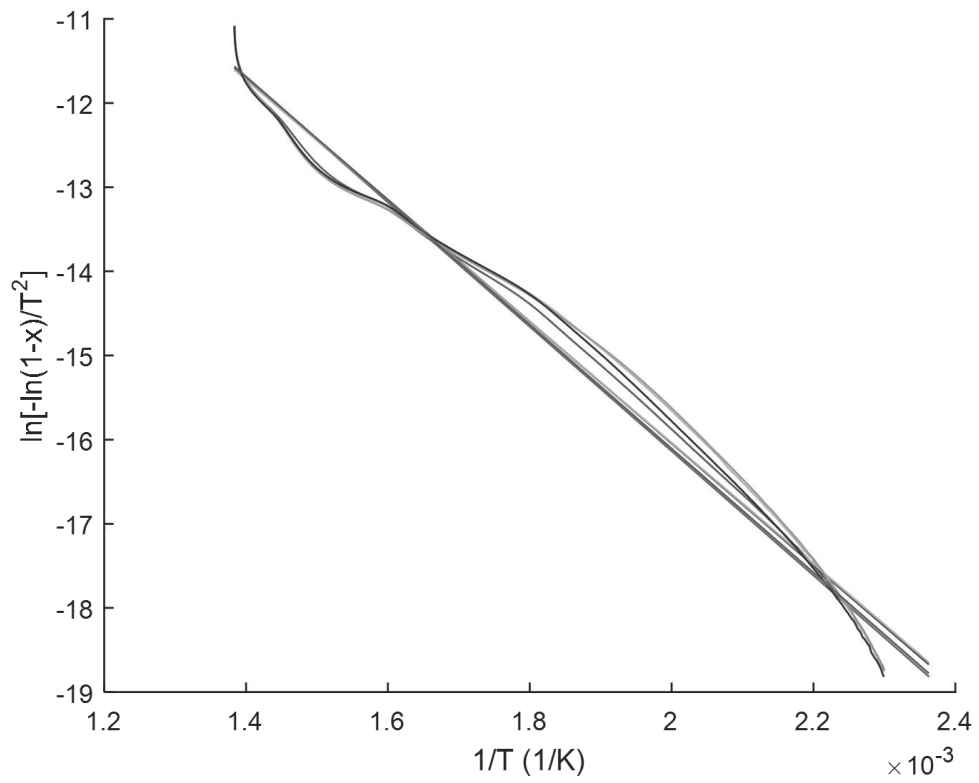


Figure 4-5: Coats-Redfern plots for type B seed cake

Table 4-6: Devolatilisation kinetic parameters of Jatropha curcas seed cake.

		Type A	Type B
<i>E</i> (kJ/mol)	Mean (% wt)	63.1	60.7
	SD	185	784
	CV (%)	0.29	1.29
<i>A</i> (s ⁻¹)	Mean (% wt)	1193	557
	SD	55	85
	CV (%)	4.6	15.3
Mean R ²		0.967	0.961

The activation energy *E* of the type A is higher than that of type B, albeit by a small margin (~4%). However, the pre-exponential factor *A* is significantly higher in the type A, indicating that the overall reactivity is higher in the type A seed cake. In line with the trends observed throughout this chapter, the CVs are higher for the type B indicating its inhomogeneity.

The devolatilisation kinetics calculated for the type A biomass were used later in the combustion modelling study (Chapter 7).

4.7 Comparison with other biomass varieties

Table 4-7 is a compilation of the thermochemical properties of some commonly-studied biomass varieties for comparison with *Jatropha curcas* seed cake.

Table 4-7: Comparison of thermochemical properties of common biomass varieties.

Biomass	(% wt) dry basis							HHV (MJ/kg)	Reference
	VM	FC	Ash	C	H	N	O		
<i>Jatropha curcas</i> seed cake, type A	70.87	22.19	5.91	49.88	6.57	4.83	32.81	21.5	This study
<i>Jatropha curcas</i> seed cake, type B	78.80	16.81	4.38	56.37	8.05	4.25	26.96	25.0	This study
Pine chips	72.40	21.65	5.95	49.66	5.67	0.51	38.07	19.8	(Tortosa Masiá et al., 2007)
Olive residue	67.35	25.48	7.17	54.18	5.37	1.28	31.7	21.7	
Palm kernel	77.28	17.59	5.14	48.34	6.2	2.62	37.44	20.7	
Sugarcane bagasse	83.66	13.15	3.20	45.48	5.96	0.15	45.21	18.7	(Channiwala & Parikh, 2002)
Miscanthus	79.30	15.54	5.16	48.87	5.38	0.65	39.82	20.0	(Khodier et al., 2012)
Straw	79.50	15.60	4.91	47.30	5.68	0.54	41.60	18.5	(Yin et al., 2010)

Figure 4-6 shows the HHVs of the biomass varieties presented in, plotted against their O/C ratio. A clear negative trend is observed, as expected (Section 2.5.2.2). A regular trend was not observed for the H/C ratio. Together with the results from Section 4.4, this suggests that the O/C ratio has a stronger influence on the HHV of biomass than the H/C ratio.

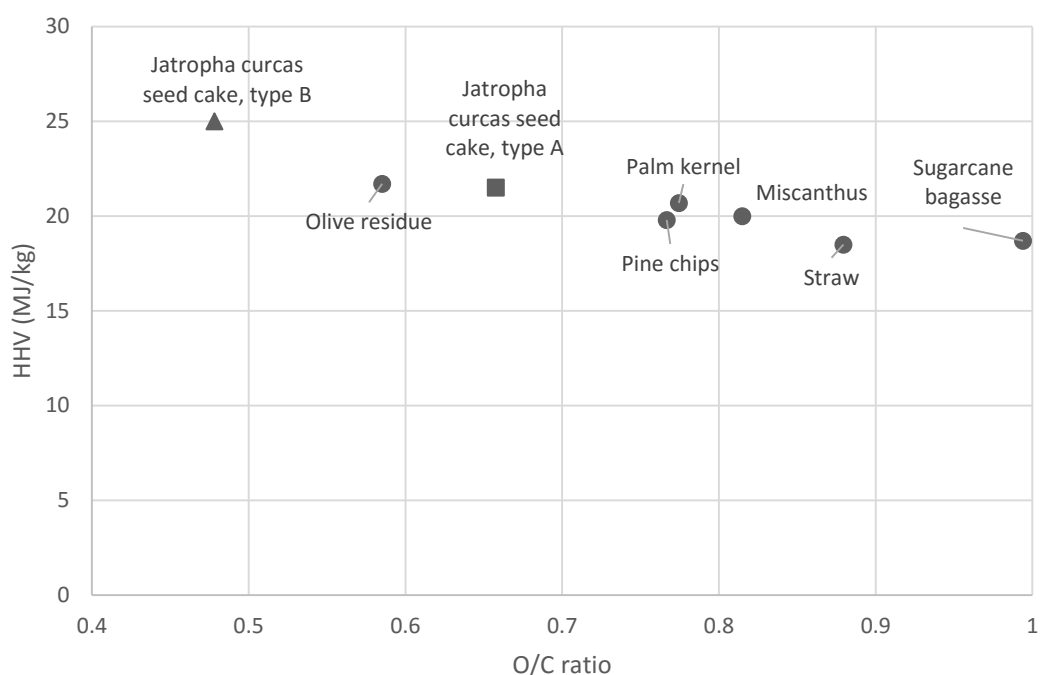


Figure 4-6: Variation of HHV with O/C ratio for different types of biomass

The HHV of the type A seed cake is among the top within the range of biomass taken from literature. The type B seed cake has an even higher HHV, which is 15% higher than the second-highest (that of olive cake). The ash content of the type A is slightly higher than the median value, while that of the type B is towards the lower end of the range. A high HHV (one that is closer to coal) and a low ash content are desirable characteristics for a biomass being considered for co-firing.

The thermochemical properties suggest that both types of untreated *Jatropha curcas* seed cake considered in this study compare favourably as a fuel to other types of biomass, with the type B seed cake being relatively more desirable than the type A in terms of HHV and ash content.

4.8 Concluding remarks

This chapter presented the key characterisation data for the untreated *Jatropha curcas* seed cake, both type A and type B. This included the proximate analysis, ultimate analysis, HHV, inorganic content and devolatilisation kinetics.

The proximate and ultimate analyses were presented as-measured, in dry basis as well as dry, ash-free (DAF) basis. The type A and type B had a HHV of 20.76 MJ/kg and 24.06 MJ/kg, respectively. The changes in proximate and ultimate analyses and the HHV are further explored in the torrefaction phase of the study (Chapter 5).

The inorganic content was measured using both ICP-MS/IC and XRF spectrometry. The type A had a consistently higher inorganic content, while K was the most abundant inorganic element in both types of seed cake. The inorganic content presented in this chapter provides a baseline for comparison with the leached *Jatropha curcas* seed cake (Chapter 6).

The devolatilisation kinetics were calculated using the Coats-Redfern method. This kinetics data, along with the proximate and ultimate analyses and the HHV, would be used as model inputs for the combustion modelling study (Chapter 7).

The CV was calculated throughout to give an indication of the variability in the results. The type B seed cake was observed to have a higher variability throughout most of the characterisation data, indicating a higher degree of inhomogeneity.

5 TORREFACTION

5.1 Introduction

The aim of this chapter is to investigate the effects of torrefaction on *Jatropha curcas* seed cake and establish a set of recommended guidelines for this pre-treatment process.

Figure 5-1 shows the overall workflow of the torrefaction study. As can be seen, the torrefaction study was carried out in two phases, primary and secondary. A section of this chapter is devoted to each phase – Section 5.2 and Section 5.3 for primary and secondary, respectively. Each section presents the experimental design and results for each phase. The practical details of the experimental procedures were outlined in Chapter 3. Since approximately 75% wt of the biomass was of type B, this was the feedstock used for the primary torrefaction study. A five-level full-factorial parametric investigation was carried out. The secondary torrefaction study was a less extensive 3-level full-factorial design utilising the type A seed cake (<1 mm size fraction). Both studies analysed the fundamental factors of mass yield, HHV, energy yield. The fixed carbon content was also analysed. However, the primary study also involved a deeper investigation into the intricacies of the torrefaction process by way of ultimate analysis, ¹³C NMR and differential thermogravimetry. The subsequent Section 5.4 discusses the practical implications of the results, and derives a set of guidelines for the torrefaction of *Jatropha curcas* seed cake.

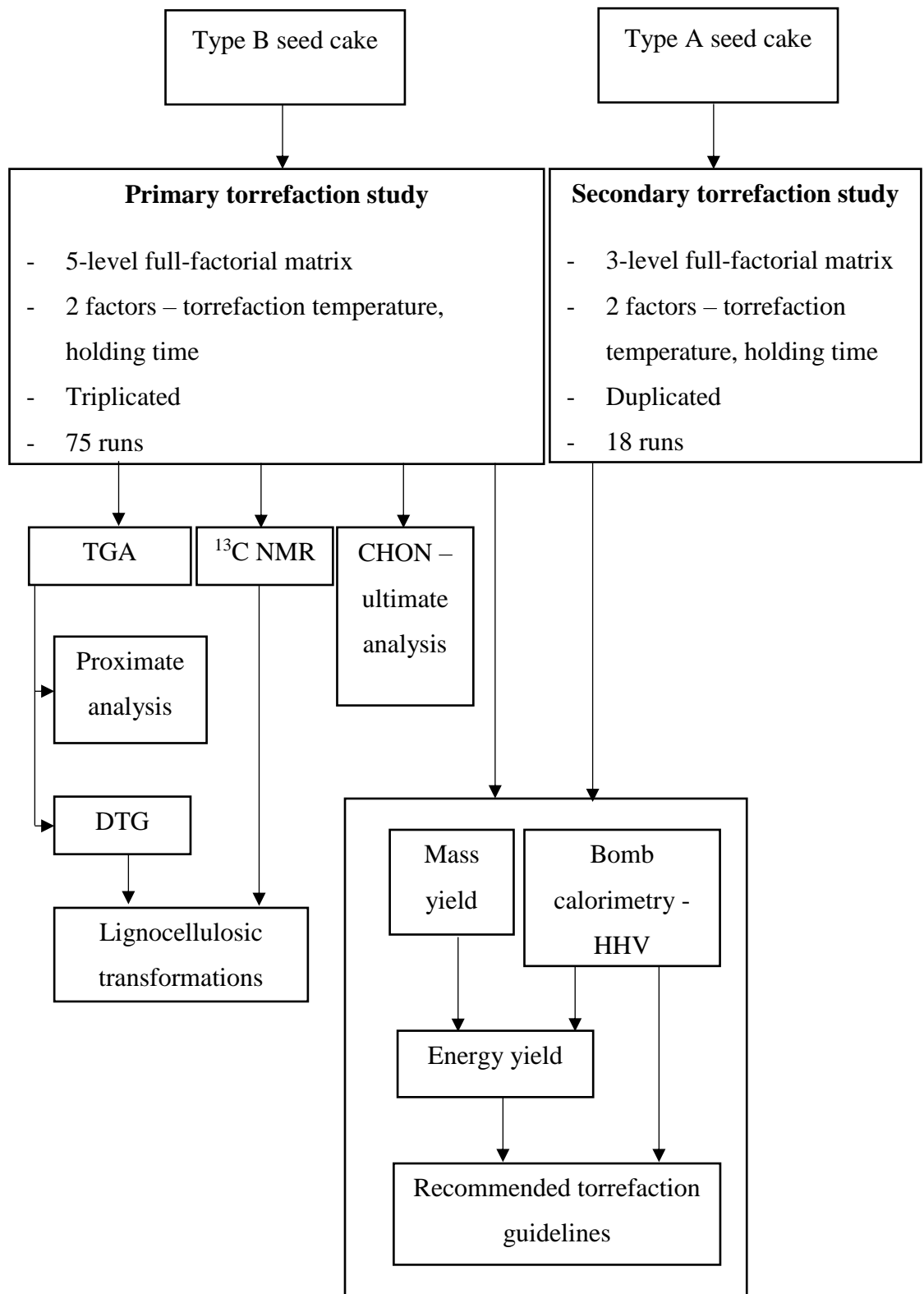


Figure 5-1: Flowchart of overall methodology of torrefaction study.

5.2 Primary torrefaction study

The primary torrefaction study was carried out on the type B seed cake, since the bulk of the seed cake obtained after oil extraction was of this type. A 5-level full-factorial (triplicated) design of experiment was used. The tested torrefaction temperatures were 200°C, 225°C, 250°C, 275°C and 300°C, while the tested holding times used were 0 min, 15 min, 30 min, 45 min and 60 min. The run order was randomised using Minitab 17 statistical software, which was also used for the subsequent data analysis. Including the replicates, a total of 75 torrefaction runs were carried out.

The fundamental analysis of the torrefied material was on the basis of the HHV and the energy yield. The mass yield was calculated using the sample mass before and after torrefaction. The HHV (higher heating value) was measured using a bomb calorimeter. The energy yield was calculated using the mass yield and the HHV. The HHV and energy yield are the main responses used to optimise the torrefaction process.

Additionally, proximate analysis using TGA (thermogravimetric analysis), CHON elemental analysis, ¹³C NMR (nuclear magnetic resonance) spectroscopy and DTG (differential thermogravimetry) was also carried out on the torrefied type B biomass. The objective of these additional analyses was to investigate the details and mechanics of the torrefaction process and how it is affected by the torrefaction temperature and holding time.

5.2.1 Mass yield, HHV, energy yield

Figure 5-2 and Figure 5-3 show the variation of the mass yield with torrefaction temperature and holding time, respectively. The error bars for these as well as all subsequent figures represent the standard error in the means. The mass yield decreases with increasing torrefaction intensity, i.e. increasing torrefaction temperature and holding time. This would be the expected observation, since more moisture and volatiles would be lost as the sample is exposed to a higher temperature for a longer time. It can be seen that discounting the 0 min holding time, the mass yield shows an approximately linear decrease with increasing temperature; as the temperature is increased from 200°C to 300°C, the mass yield drops by an average of 35% in these runs. A linear regression model for the non-0 min mass yield data resulted in an R^2 value of 0.941 (best-fit for all non-0 points). For the holding time of 0 min however, a different trend is seen. Here, the mass yield decreases at a much lower rate than the non-0 min runs as the temperature is increased. However, the trend is non-linear with the rate increasing at higher torrefaction temperatures. The 0 min holding time reflects the torrefaction occurring during the heating and cooling segments of each run, since the “holding time” variable only represents the isothermal residence time. Since a constant heating rate was used for all runs, the sample is exposed to elevated temperatures for a longer time when the torrefaction temperature is higher. This would result in a greater mass loss due to moisture or volatiles, and result in a curve with an increasing negative gradient.

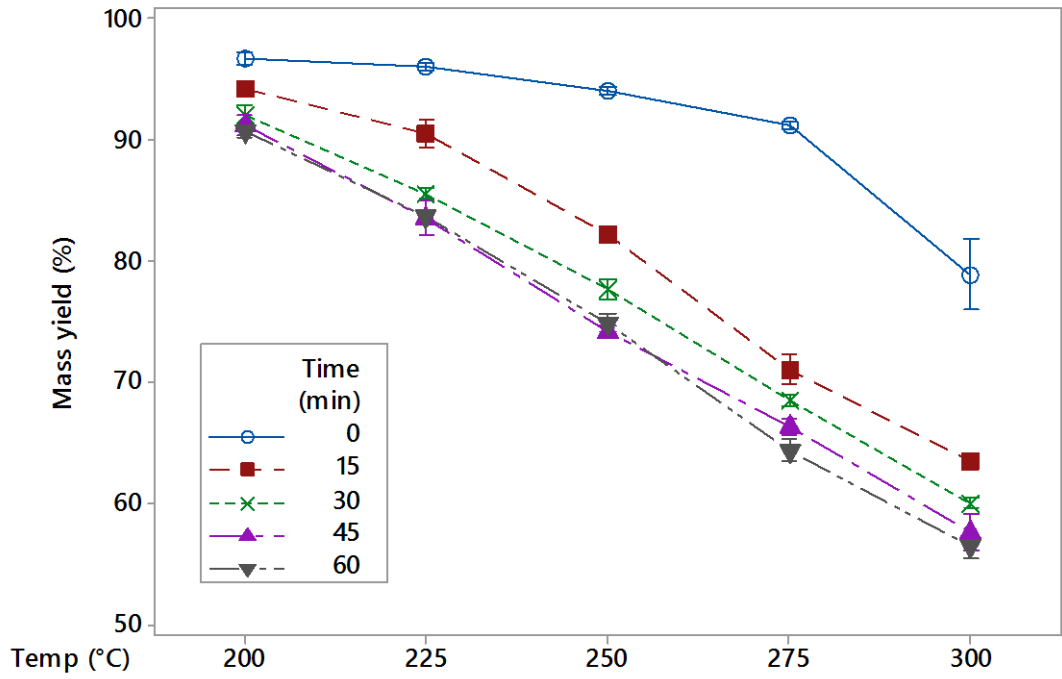


Figure 5-2: Interaction plot for the mass yield, grouped by holding time.

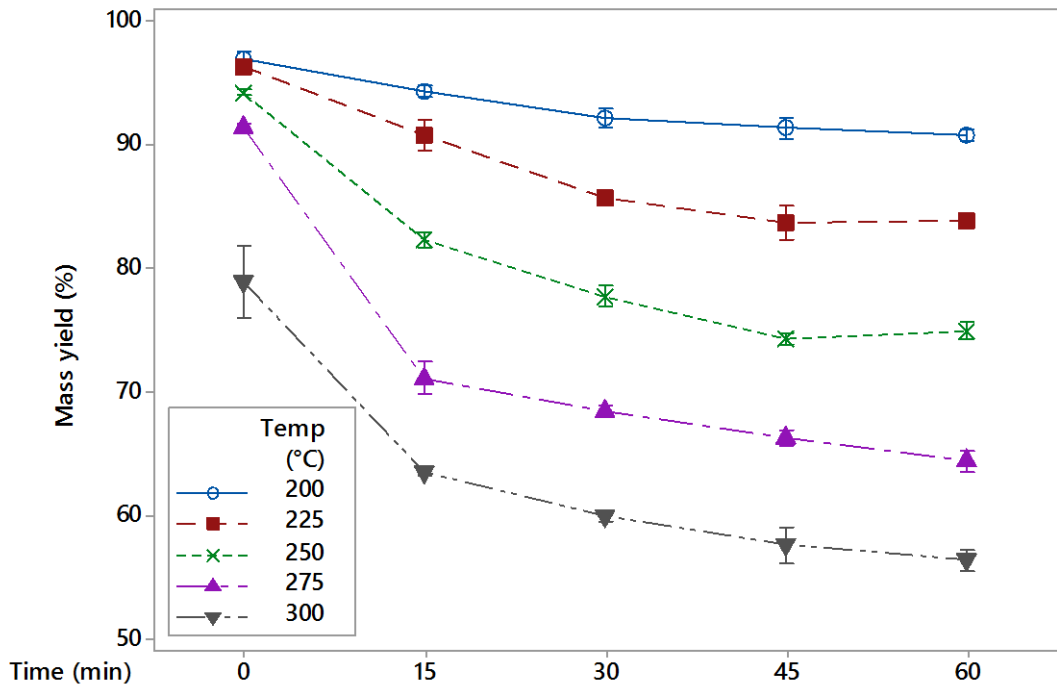


Figure 5-3: Interaction plot for the mass yield, grouped by torrefaction temperature.

Figure 5-4 and Figure 5-5 show the variation of HHV with torrefaction temperature and holding time, respectively.

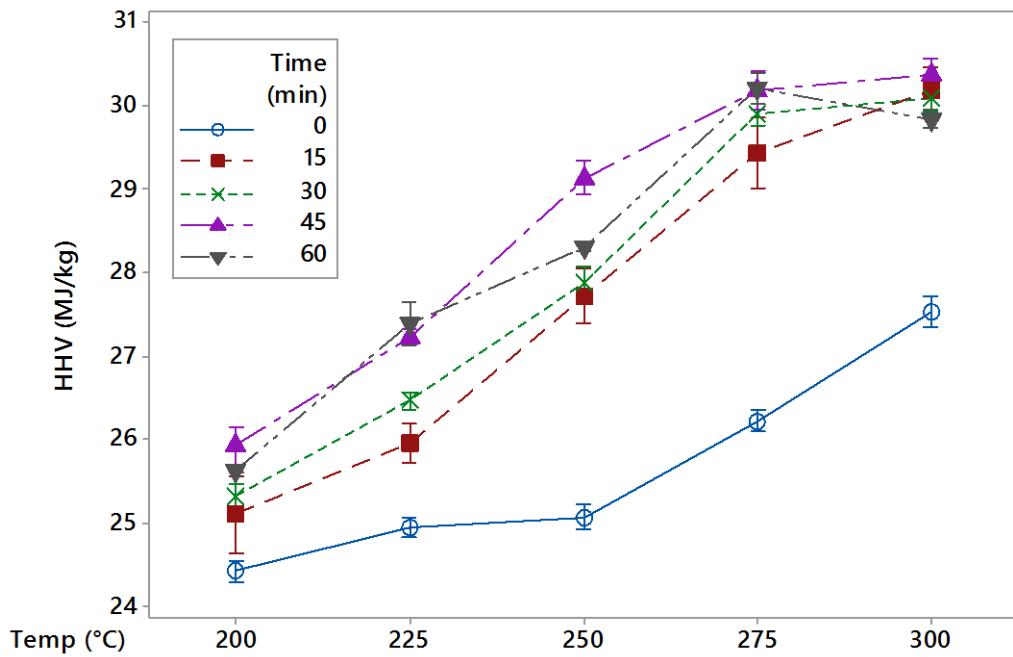


Figure 5-4: Interaction plot for the HHV, grouped by holding time.

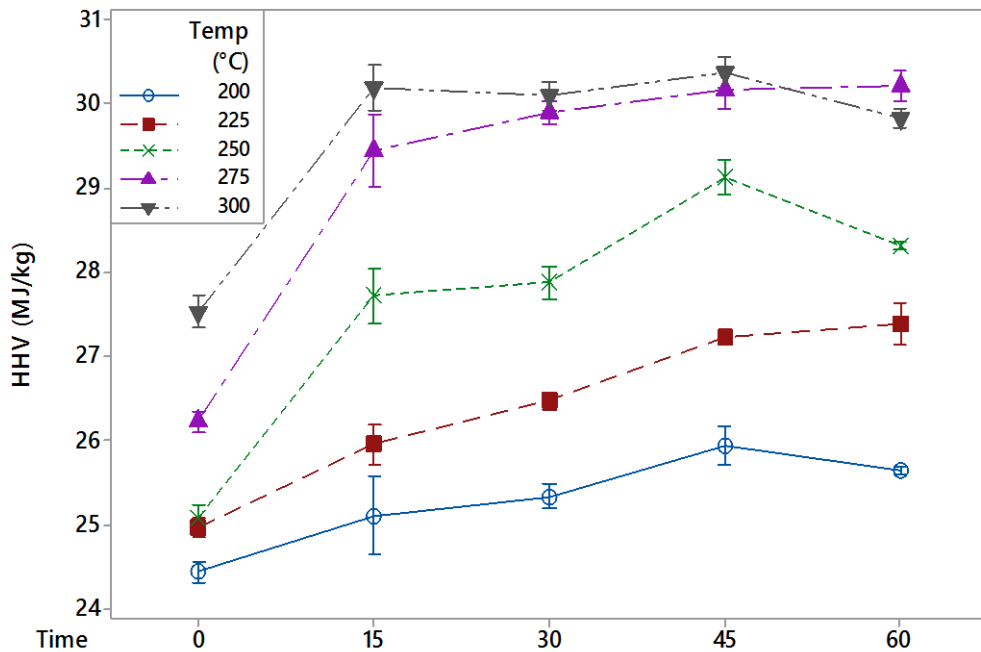


Figure 5-5: Interaction plot for the HHV, grouped by torrefaction temperature.

The HHV responds inversely to the mass yield, i.e. the HHV increases with escalating torrefaction intensity. This is in fact a primary driver for the consideration

of torrefaction as a biomass pre-treatment technique. This increase has been explained in literature on the basis that torrefaction results in a loss of VM. VM lost from biomass consists of hydrogen gas and light hydrocarbons which have a low C content compared to H (Vassilev et al., 2010). Hence, there is a substantially greater amount of H and O lost during torrefaction than there is C (Chen & Kuo, 2010; Chen et al., 2012). This is reflected in the increased FC and elemental C content observed in the proximate and ultimate analyses of torrefied *Jatropha* which will be discussed subsequently in Sections 5.2.2 and 5.3.3. There is a reduction in the H/C and O/C ratios, and since the C-H and C-O bond energies are lower than that of C-C, this results in an increase in the calorific value of the biomass (McKendry, 2002a; Narvaez & Orio, 1996).

Excluding the 0 min runs, the HHV shows an approximate direct proportionality to the temperature up to $\sim 275^{\circ}\text{C}$. A linear regression fit in this segment resulted in an R^2 value of 0.892 (best-fit for all non-0 points). The curves flatten beyond this temperature; this effect becomes more pronounced as the holding time increases. The mean HHV (taking into account all holding times excluding 0 min) increases by only 0.64% when the temperature is increased from 275°C to 300°C . Hence, using temperatures in excess of 275°C would not be beneficial as far as the HHV is concerned.

Table 5-1 shows how the enhancement of the HHV of *Jatropha curcas* seed cake compares with that of some other types of biomass (Ohm et al., 2015; Wannapeera et al., 2011; Chen et al., 2011b; Phanphanich & Mani, 2011; Deng et al., 2009). All results are at conditions of 250°C and 30 min. Although other variables such as heating rate and particle size make a direct comparison less meaningful, the results in Table 5-1 illustrate the range of possible outcomes of the torrefaction process on different

biomass types at seemingly similar conditions – the HHV enhancement varies from 1% to as much as 30% while that of *Jatropha* is 16%.

Table 5-1: Comparison of HHV enhancement obtained in recent torrefaction studies.

Biomass	HHV enhancement	Reference
<i>Jatropha curcas</i> seed cake (type B)	16%	This thesis
Waste wood	2%	(Ohm et al., 2015)
<i>Leucaena leucocephala</i> (woody biomass)	1%	(Wannapeera et al., 2011)
Lauan (woody biomass)	30%	(Chen et al., 2011b)
Pine chips	9%	(Phanphanich & Mani, 2011)
Logging residue	13%	
Rice straw	5%	(Deng et al., 2009)
Rape stalk	7%	

A regression analysis of the measured HHV in terms of the mass loss – obtained by subtracting the mass yield from unity – showed a linear fit with an R^2 value of 0.919. The following regression equation was obtained:

$$HHV (MJ/kg) = 24.55 + (0.15 \times \text{mass loss } (\%)) \quad \text{Eqn 5-1}$$

Similar linear trends were reported by Almeida et al. (2010) and Peng et al. (2013b) following the torrefaction of softwood and Eucalyptus wood and bark, respectively . The corresponding regression coefficients obtained by Peng et al. were 19.48 and 0.15, which are similar to those presented in Equation 5-1. Carrying out the regression using the mass loss instead of the mass yield results in an equation in which the constant is

approximately equal to the HHV of the untorrefied biomass, which is 24.06 MJ/kg (see Section 4.4). This feature of the regression equation was highlighted by Almeida et al. (2010).

Figure 5-6 and Figure 5-7 show the variation of the energy yield with torrefaction temperature and holding time, respectively.

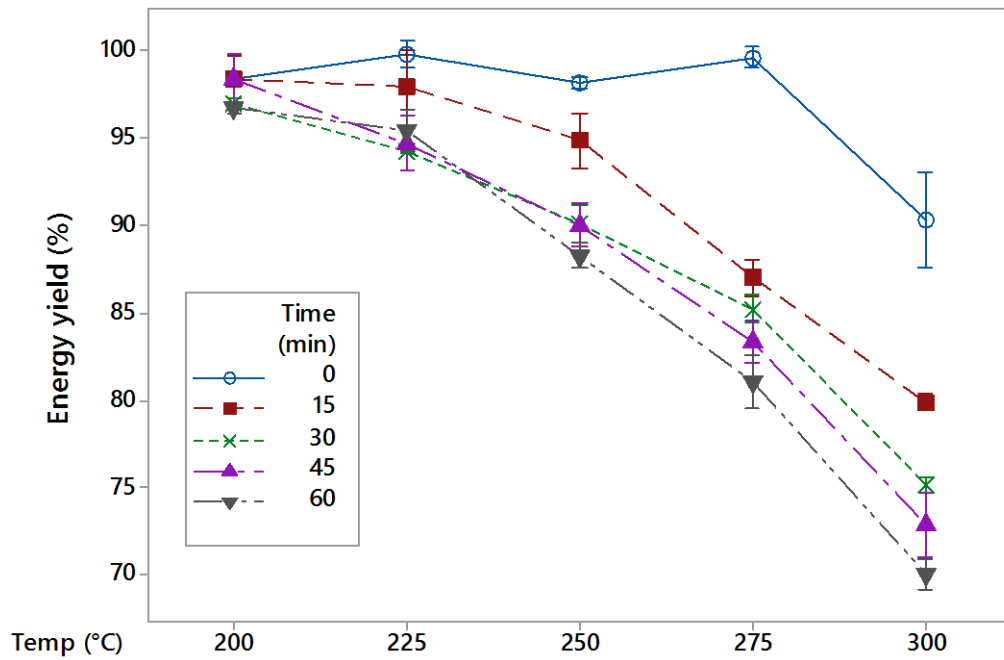


Figure 5-6: Interaction plot for the energy yield, grouped by holding time.

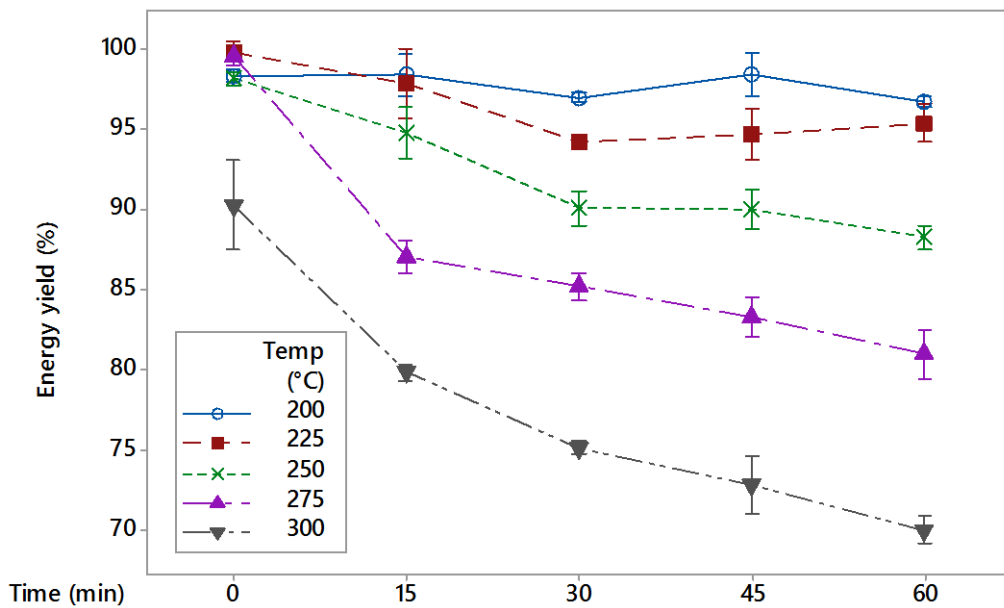


Figure 5-7: Interaction plot for the energy yield, grouped by torrefaction temperature.

The energy yield is a function of the mass yield and the HHVs of the untorrefied and torrefied biomass; the energy yield is directly proportional to both the mass yield and the HHV of the torrefied biomass since the HHV of the untorrefied biomass is considered a constant. As the torrefaction intensity is increased, the drop in the energy yield implies that the enhancement in the HHV is insufficient to compensate for the decreasing mass yield. For all non-0 holding times, the energy yield drops at a higher rate as the temperature is increased. When the holding time is 0 min, the trend shows a higher degree of irregularity; the energy yield shows a marked drop only when the torrefaction temperature is increased beyond 275°C. The mean energy yield (calculated from all non-0 holding times) decreases by 5.5 % when the temperature is increased from 200°C to 250°C, but drops by a further 14.6 % when the temperature is increased to 300°C.

Table 5-2 shows the results from an ANOVA (analysis of variance) test that was carried out on the mass and energy yields as well as the HHV. The 0 min holding time was excluded from the analysis. A p-value less than 0.05 indicates that a factor or interaction between factors has a statistically significant effect on the response, i.e. mass yield, HHV, energy yield. For all three responses, the interaction between temperature and time is not significant, i.e. the effect of the temperature on the response is not dependent on the holding time, and vice versa. This is reflected in the interaction plots, where the non-0 min curves are approximately parallel to each other.

Table 5-2: p- and F-values from ANOVA test of mass yield, HHV, energy yield data.

	p-value			F-value	
	temp	time	temp*time interaction	temp	time
Mass yield	0.000	0.000	0.221	1039.51	60.48
HHV	0.000	0.000	0.060	305.33	14.43
Energy yield	0.000	0.000	0.327	231.62	22.54

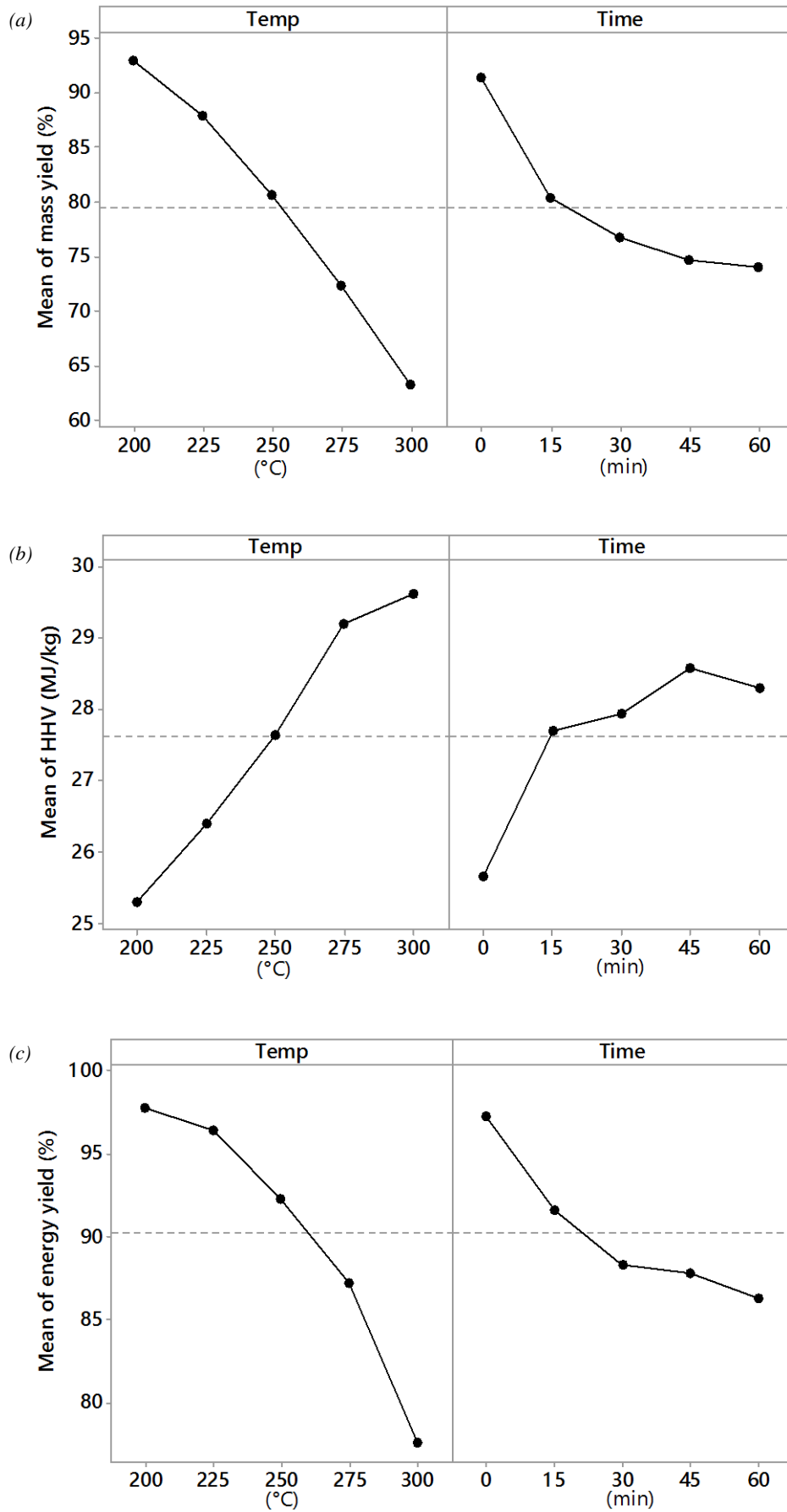


Figure 5-8: Main effects plots for (a) mass yield, (b) HHV, (c) energy yield.

The p-values for the temperature and time (main effects) are all 0.000. This indicates that when considered independently, both factors have a significant effect on the responses. This independent effect is illustrated in the main effects plots for the three responses in Figure 5-8, which show the mean response for each value of one factor, irrespective of the other factor. A striking feature of the plots is that the temperature has a substantially larger effect than the holding time; this is true for all three responses, i.e. the mass yield, HHV and energy yield. This is evident in Table 5-3, which shows the percentage change in the mean responses when each factor is increased (independently of the other) from the lower limit to the upper limit. This observation is corroborated by the F-values in Table 5-2, since a larger F-value is indicative of a more dominant factor.

Table 5-3: Main effects changes in mean mass yield, HHV, energy yield over full range of factors.

Change in	Temperature increased from 200°C to 300°C	Holding time increased from 0 min to 60 min
Mass yield	-31.9 %	-19.0 %
HHV	+17.1 %	+10.3 %
Energy yield	-20.6 %	-11.3 %

5.2.2 Fixed carbon (FC) content

The proximate analysis from the TGA yielded the moisture, VM, FC and ash contents of the samples. The VM and FC measurements were converted to DAF basis so to eliminate the variability introduced by the moisture and ash content. Since the DAF VM and DAF FC are by definition inversely proportional to each other (since the four components of the proximate analysis should add up to unity), only the DAF FC is presented.

Figure 5-9 and Figure 5-10 show the variation of the DAF FC with torrefaction temperature and holding time, respectively.

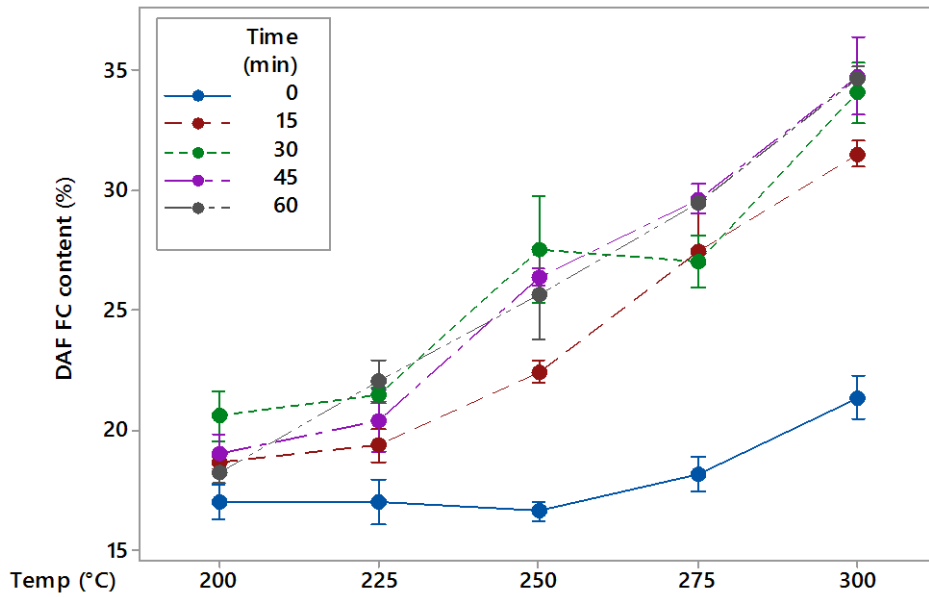


Figure 5-9: Interaction plot for the DAF FC content, grouped by holding time.

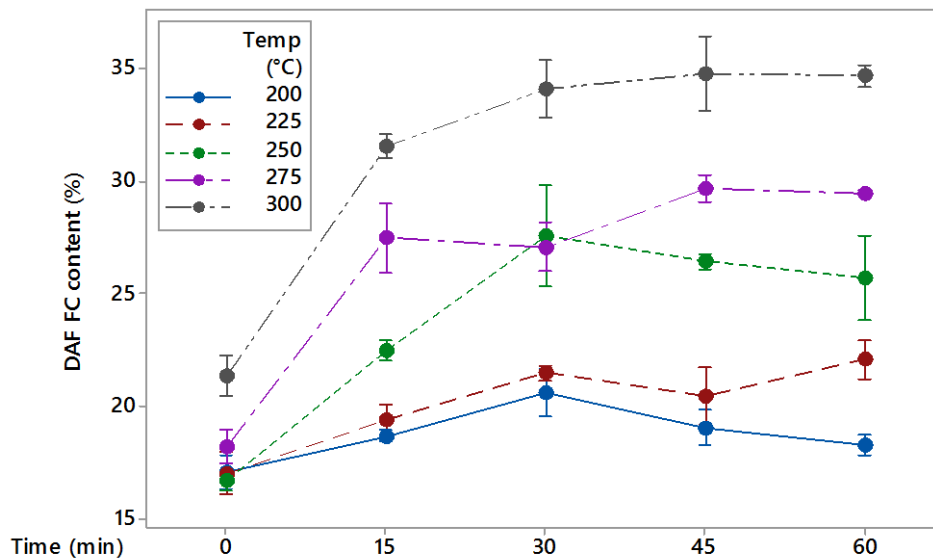


Figure 5-10: Interaction plot for the DAF FC content, grouped by torrefaction temperature.

Referring to Figure 5-9 and Figure 5-10, torrefaction at higher intensities causes the DAF FC to increase. At the median holding time of 30 min, the DAF FC content increases by 65% as the temperature is increased from 200°C to 300°C. At the extreme holding times of 0 min and 60 min, it increases by 25% and 90%, respectively. At higher temperatures, there is a greater loss in the VM; it can be postulated that this is due to the initiation of certain decomposition pathways which require higher activation energies. As stated in Section 5.2.1, the lost volatiles consist mostly of low-C

molecules, and hence a lower fraction of C is lost from the biomass compared to other elements. This would lead to an increase in the FC content. When comparing Figures, it can be seen that the effect of holding time on the DAF FC content is less significant than that of the temperature.

A method to estimate the HHV of solid fuels using their proximate analysis can prove to be useful tool; proximate analysis using TGA is a common initial characterisation of a fuel while accurate measurement of the HHV requires additional equipment. The scatter plot in Figure 5-11 indicates that there is a likely correlation between the DAF FC content and the HHV. There have been several past studies which have derived expressions for carrying this out (Demirbas, 1997; Nhuchhen & Abdul Salam, 2012; Yin, 2011; Sheng & Azevedo, 2005). In the present case, four regression models were applied to investigate the relationship between the DAF FC content and HHV, and the predicted R-square (pred-R²) value and standard error of regression (S value) were used to determine the efficacy of each model. The higher pred-R² value is desirable, as it is an indicator of how well the model can predict a removed observation. Compared to the standard R² value, the pred-R² prevents over-fitting noise into the model. The S value indicates the average distance from the observed points to the fitted line, and a lower value is preferred in this case. Table 5-4 shows the pred-R² and S values corresponding to the four models, along with the equation coefficients (a, b, c, d). The four models were:

- Linear: $HHV = a + b*(DAF_FC)$ **Eqn 5-2**
- Linear logarithmic: $HHV = a + b*\ln(DAF_FC)$ **Eqn 5-3**
- Quadratic: $HHV = a + b*(DAF_FC) + c*(DAF_FC)^2$ **Eqn 5-4**
- Cubic: $HHV = a + b*(DAF_FC) + c*(DAF_FC)^2 + d*(DAF_FC)^3$ **Eqn 5-5**

The quadratic and cubic functions possess the best pred-R² and S values. However, the quadratic function would be the more desirable option since it contains one less term and is the less complex equation of the two. The four regression models are graphically represented in Appendix 6 (Figure A6-1).

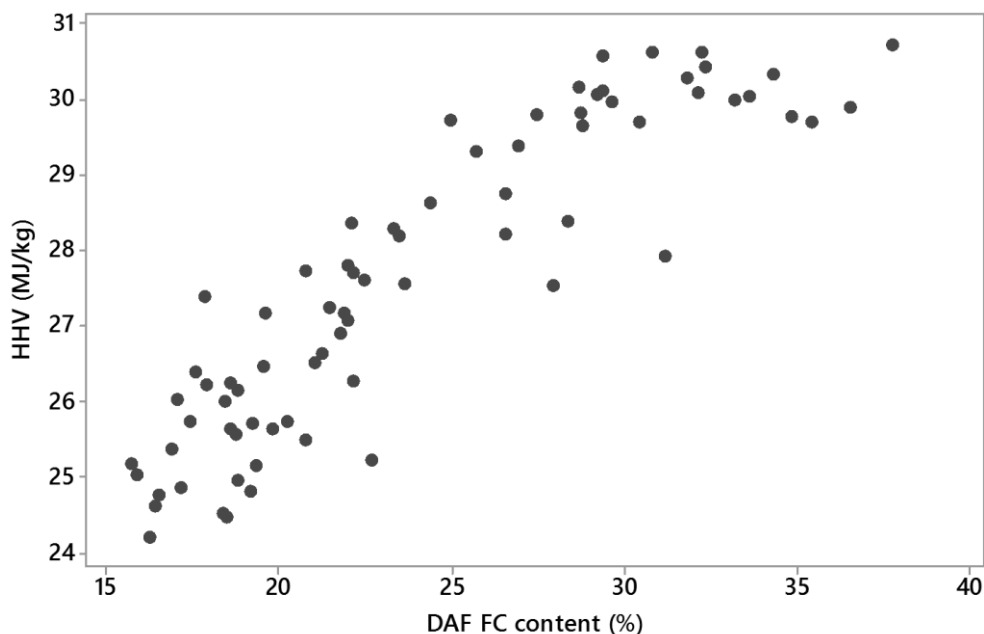


Figure 5-11: Scatter plot of HHV against DAF FC content.

Table 5-4: Regression coefficients and statistics for HHV vs DAF FC.

	Linear	Linear logarithmic	Quadratic	Cubic
pred-R ²	0.7998	0.8269	0.8377	0.8362
S	0.8834	0.8240	0.7968	0.7846
a	20.30	3.723	12.80	26.11
b	0.3046	7.587	0.9274	-0.7096
c	-	-	-0.01219	0.05258
d	-	-	-	-0.0008260

5.2.3 Ultimate analysis

Figure 5-12 shows the variation with torrefaction temperature of C, H, N, O content (% by weight, dry basis) of the torrefied seed cake. The error bars illustrate the standard errors associated with the calculated means. A clear pattern cannot be identified in the variation of the N and H content. There is a significant overlap in the error bars due to the large variation between the replicates. This could be attributed to the inherent

inhomogeneity in the biomass samples, coupled with the relatively low amounts of H and N measured (relative to C and O). A similarly large variability was observed in the N content of the untorrefied biomass and an explanation for this was discussed earlier in Section 4.3.

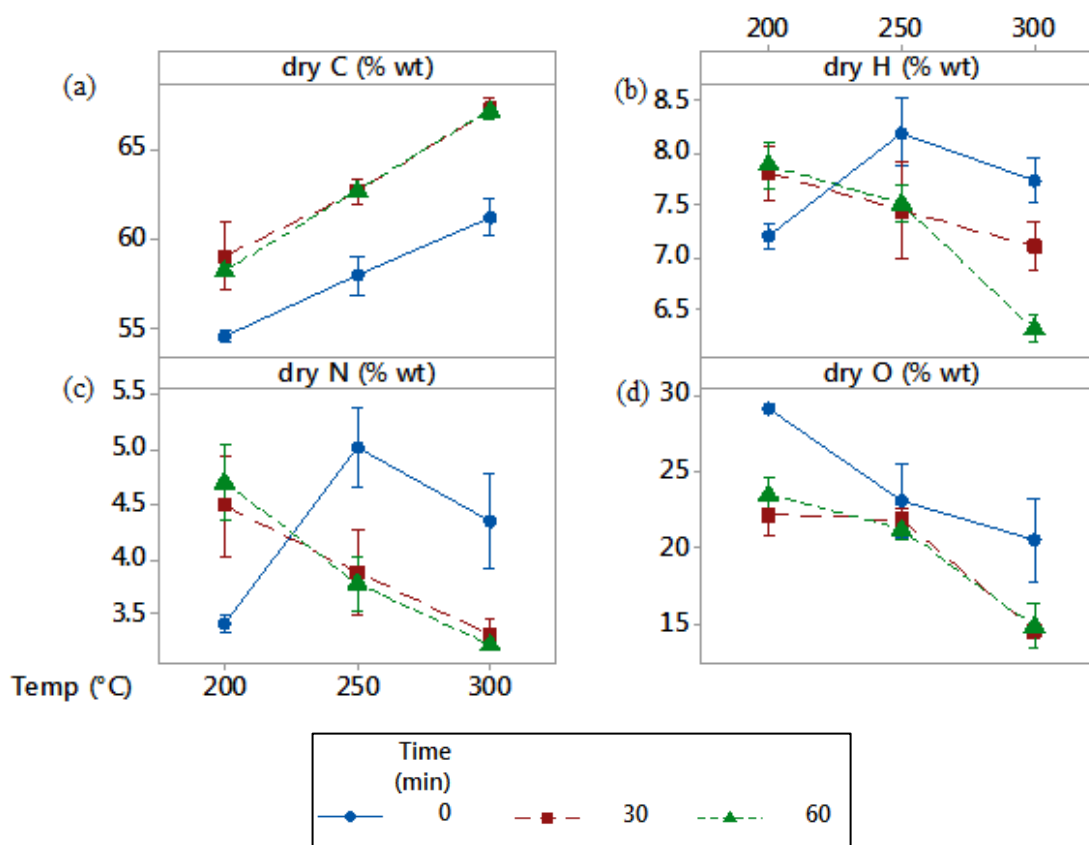


Figure 5-12: Interaction plots for elemental (a) dry C, (b) dry H, (c) dry N, (d) dry O.

This overlap is also observed in the C and O content, albeit to a lesser degree. However, some distinct trends can be observed in this case. With increasing torrefaction intensity, the C content increases while the O content decreases. As the temperature is increased from 200°C to 300°C, there is an approximately linear increase in the C content by 14%, while the O content decreases by 33%. The trend in C content confirms previous findings of increasing FC content (from the proximate analysis obtained from TGA, Section 5.2.2), and can be traced to the loss of low-C volatiles during the torrefaction process. However, the reducing O content indicates

that the volatiles lost also contain a significant proportion of O in their molecular structure. Another observation is that the torrefaction temperature has a more pronounced effect on both the C and O content than the holding time; there is substantial overlapping between the 30 min and 60 min curves. This observation is expected since it is a trend that has been observed throughout the study (mass and energy yields, HHV, DAF FC content).

Table 5-5: p-values from ANOVA of dry CHON

	p-value		
	temperature	time	temperature*time interaction
C	0.000	0.000	0.747
H	0.012	0.114	0.009
N	0.051	0.293	0.002
O	0.000	0.002	0.372

Table 5-5 shows the p-values from the ANOVA test. These values confirm that the torrefaction temperature and holding time have a statistically significant effect on the C and O content. The high p-values for the temperature and time factors (individually) for H and N further strengthen the conclusion that the dispersion among the data is too great to extract a statistically reliable trend from it. Meanwhile, the high p-values for the temperature*time interaction for C and O indicate a statistically insignificant interaction between the two factors, i.e. a change in the holding time does not change how the temperature influences the response (C or O content). This is reflected in the relatively parallel gradients observed in Figure 5-12(a) and (d).

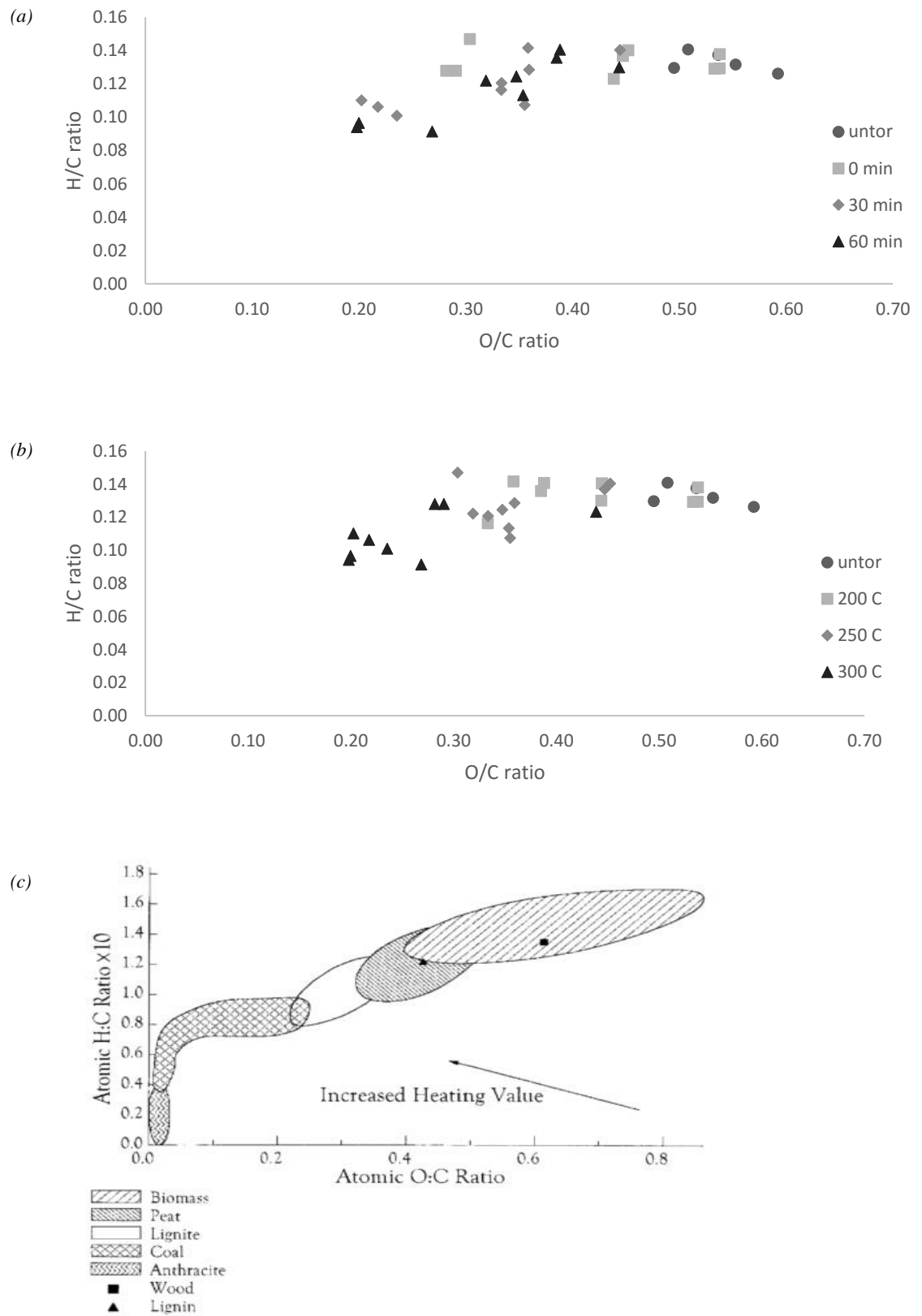


Figure 5-13: van Krevelen diagrams of (a) torrefied Jatropha seed cake grouped by holding time, (b) torrefied Jatropha seed cake grouped by temperature, (c) various solid fuels (McKendry, 2002).

Figure 5-13(a) and (b) are van Krevelen diagrams which show the H/C ratio plotted against the O/C ratio; the torrefied and untorrefied seed cakes have been included, grouped by holding time and temperature in Figure 5-13(a) and (b), respectively. These diagrams have been used in literature as a tool to characterise the thermochemical properties of fuels. Figure 5-13(c) shows the typical positions of biomass and coal on such a diagram (McKendry, 2002a). Coal occupies the lower-left section of the diagram, and it is desirable for the biomass in question to be in this vicinity since it indicates similar thermochemical properties to coal (which would be beneficial for the ultimate aim of co-firing). It can be seen from Figure 5-13(a) that increasing the torrefaction temperature causes the points to shift towards the lower-left direction, which is the required outcome of the torrefaction process. However, Figure 5-13(b) shows a wide dispersion of points when grouped according to holding time, further reinforcing the conclusion that holding time has a less significant effect on the properties of the biomass than the torrefaction temperature.

5.2.4 ^{13}C NMR spectroscopy

Figure 5-14 shows the NMR spectra for the untorrefied and torrefied biomass, with that of one sample selected from each level of torrefaction. Assignment of the peaks was done using the existing literature while taking into account the fact that an uncertainty of ± 2 ppm can exist. The sharp peak at 3.5 ppm is caused by the standard TKS which was used for calibration of the spectrum. A typical ^{13}C biomass spectrum can be broadly grouped into four sections (Fründ & Lüdemann, 1989):

- >160 ppm : carboxylic C
- 110 ppm – 160 ppm : aromatic C
- 46 ppm – 110 ppm : carbohydrate C
- <46 ppm : aliphatic C

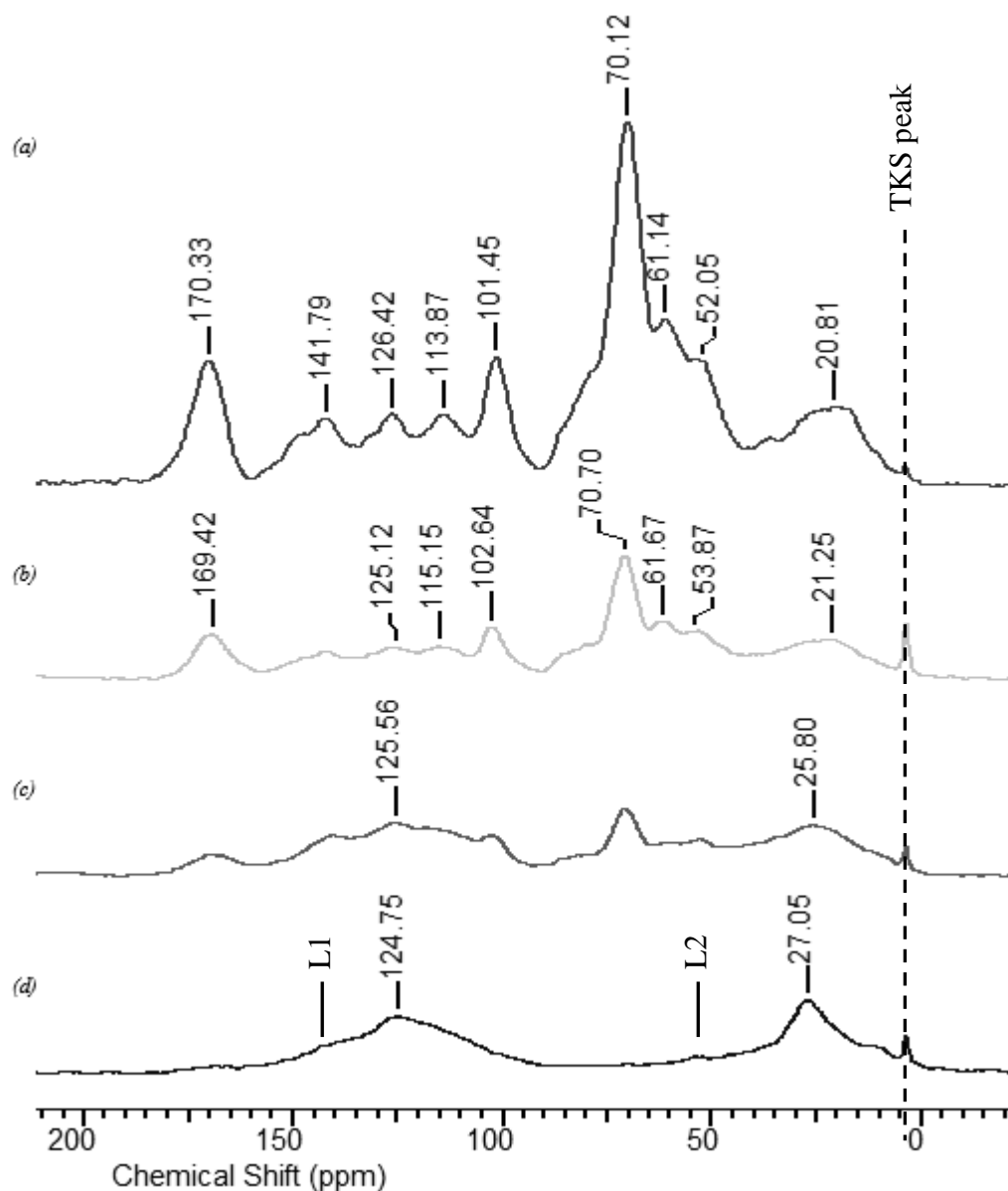


Figure 5-14: ^{13}C NMR spectra for (a) untoasted *Jatropha* seed cake and *Jatropha* seed cake toasted for 60 min at (b) 200°C, (c) 250°C, (d) 300°C.

The peaks at approximately 21 ppm and 171 ppm are assigned to acetyl groups in hemicellulose (Li et al., 2015; Neupane et al., 2015; Sievers et al., 2009). The group of peaks between 62 ppm and 103 ppm are due to C1 to C6 atoms, predominantly of cellulose although hemicellulose also makes a contribution (Bernardinelli et al., 2015; Neupane et al., 2015). The cluster of peaks between 110 ppm and 160 ppm are attributed to aromatic rings in lignin (Bernardinelli et al., 2015; Gilardi et al., 1995) while the broad shoulder at approximately 52–56 ppm is assigned to the methoxyl

group of lignin (Bernardinelli et al., 2015; Park et al., 2013). In the untreated biomass, cellulose appears to be the most abundant component, followed by hemicellulose and lignin.

Following torrefaction at the lowest temperature of 200°C, degradation can be observed across the spectrum. The most significant losses are of the hemicellulose-only peaks (acetyl groups) and the carbohydrate region. Due to the overlap of hemicellulose and cellulose signals in the carbohydrate region (62—110 ppm), the extent of individual cellulose and hemicellulose decomposition cannot be determined with certainty; however, Neupane et al. (Neupane et al., 2015) attributed most of this decomposition to hemicellulose. A flattening is observed in the 110—160 ppm region, indicating that lignin decomposition has occurred; methoxyl lignin has also undergone degradation. Despite these changes in intensity, the overall shape of the spectrum is still comparable to that of the untorrefied biomass.

After torrefaction at 250°C, more significant changes have occurred. The hemicellulose has almost completely decomposed, although a degree of cellulose is still present. The most noteworthy observations are the appearance of two new broad peaks centred around 26 ppm (aliphatic region) and 125—126 ppm (aromatic region). Overall, lignin decomposition has not progressed drastically since the 200°C torrefaction.

It is evident that torrefaction at 300°C has changed the structure of the biomass comprehensively. Both hemicellulose and cellulose have undergone complete decomposition. The spectrum is now dominated by the aforementioned two broad peaks; these represent the aliphatic and aromatic products of the torrefaction reaction, since their growth occurred parallel to the decomposition of the cellulose peaks.

Although not immediately evident due to the overlap by the aromatic product peak around 125—126 ppm, the shoulder at approximately 140 ppm (L1 on Figure 5-14) and the slight bump at approximately 54 ppm (L2 on Figure 5-14) indicates that the lignin has still not completely decomposed.

From this analysis, it can be seen that hemicellulose is the most volatile component present and undergoes significant decomposition between torrefaction temperatures of 200°C and 250°C. Cellulose is comparatively more stable, and although it starts degrading below 250°C, complete decomposition only occurs between 250°C and 300°C. Lignin undergoes decomposition over a wide range of temperatures, starting from as low as 200°C and continuing beyond 300°C. These results are in line with other ¹³C NMR studies carried out on other types of torrefied biomass including bamboo (Wen et al., 2014), beech wood (Melkior et al., 2012) and loblolly pine (Neupane et al., 2015). The phenomenon of decreasing aliphatic and aromatic signals under mild conditions, followed by the increase thereof at higher temperatures was also reported by Neupane et al. (Neupane et al., 2015). This study proposed that this was due to aliphatic and aromatic C-C and C-H bonds being formed from the decomposition products by way of polymerisation and recondensation products (Ben & Ragauskas, 2012; Neupane et al., 2015; Zawadzki & Wisnewiski, 2002).

5.2.5 Differential thermogravimetry

Differential thermogravimetric (DTG) plots were obtained from the TGA runs which were originally utilised for the proximate analysis. The segment of the TGA run that is of interest here is the devolatilisation stage, i.e. when the temperature is ramped up at a constant rate of 20°C/min after drying at 105°C. Figure 5-15 shows a typical DTG plot for this segment for the untreated type B biomass. The derivative of the mass with respect to time is plotted against the temperature. Two distinct peaks are

observed, with a “shoulder” on the first peak. The shoulder at $\sim <300^{\circ}\text{C}$, the peak at $\sim 320\text{-}350^{\circ}\text{C}$ and the peak at $\sim 400^{\circ}\text{C}$ will be referred to as peak P0, peak P1 and peak P2, respectively. A trailing edge is also observed after peak P2.

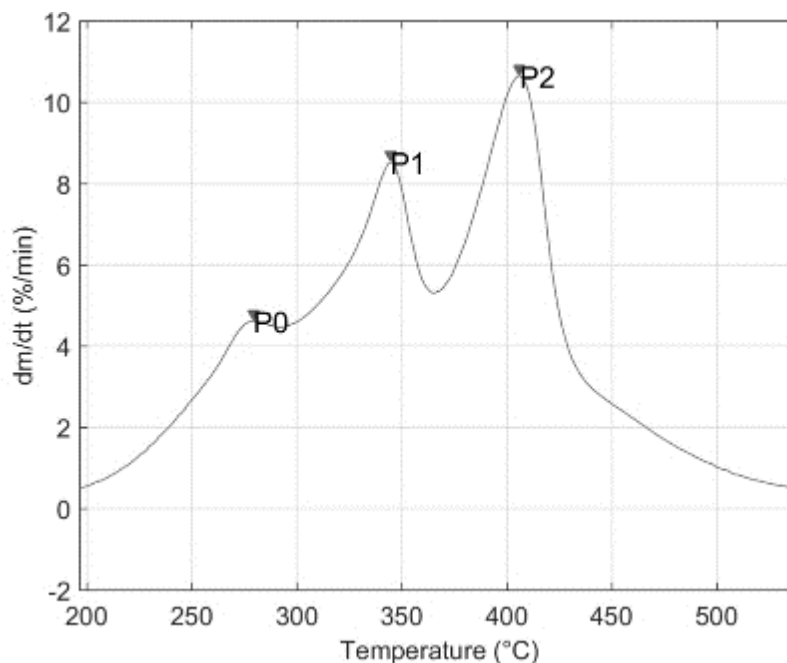


Figure 5-15: DTG plot of untreated type B.

Table 5-6 shows the typical temperatures at which the generic individual components of biomass – hemicellulose, cellulose, lignin – undergo decomposition. Based on this data, peaks P0 and P1 were assigned to hemicellulose and cellulose decomposition, respectively. The cause of the P2 peak will be discussed later in this section. The trailing edge following P2 was regarded as representing lignin decomposition since lignin decomposition typically occurs at a low rate over a wide range of temperatures up to 900°C (Gašparovič et al., 2010).

Table 5-6: Temperatures at which lignocellulosic components undergo decomposition.

Biomass	Hemicellulose	Cellulose	Lignin	Reference
Bamboo	275°C	275-350°C	250-500°C	(Wu & Lin, 2012)
Wood chips	200-380°C	250-380°C	180-900°C	(Gašparovič et al., 2010)
Individual components, synthetic mixtures	220-315°C	315-400°C	>400°C	(Yang et al., 2006)

Figure 5-16 and Figure 5-17 show the DTG plots for the torrefied type B biomass, sorted by holding time and torrefaction temperature, respectively. Representative single replicates were chosen for each temperature-time combination. TA Instruments Universal Analysis 2000 software was used to process the raw TGA data and obtain the DTG signal. A Matlab program was written to further process this DTG data, including generating the plots shown (Appendix 2).

From Figure 5-16(a), it can be seen that hemicellulose is completely decomposed after torrefaction at 300°C even when the holding time is 0 min, indicating the sensitivity of hemicellulose to high temperatures; there is no significant decomposition observed in the 200°C and 250°C plots. The effect of the torrefaction temperature can be seen more clearly in the 30 min and 60 min plots (Figure 5-16(b) and (c)). After torrefaction at 250°C, hemicellulose has decomposed completely while a significant amount of cellulose has also undergone degradation. At 300°C, cellulose also has undergone virtually complete decomposition. With the exception of the highest torrefaction temperature, the holding time does not appear to have a significant effect, especially beyond 30 min (Figure 5-17).

Lignin decomposition is known to be spread over a wide range of temperatures, well exceeding the maximum torrefaction temperature of 300°C. Hence, any lignin molecules which were partially-degraded during the torrefaction process would undergo decomposition at the relatively higher temperatures during the TGA run. This would explain the enhancement of the “bulge” after the P2 peak at higher torrefaction temperatures (Figure 5-16), as there would be more partially-degraded lignin molecules at higher torrefaction intensities.

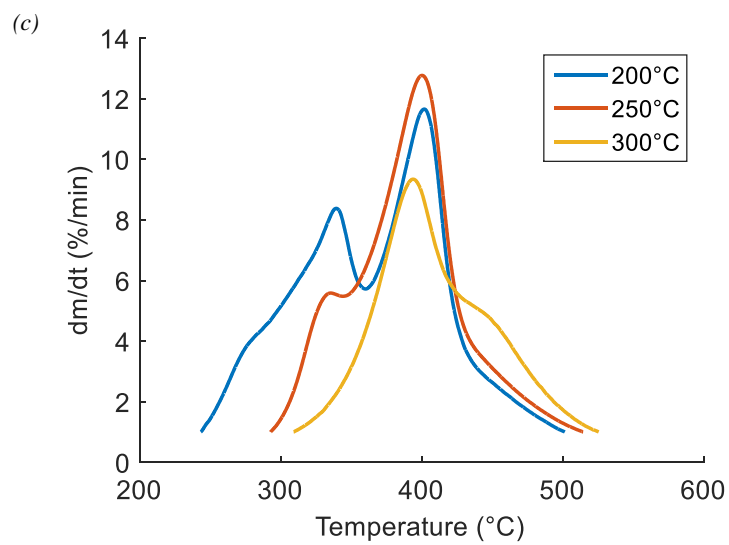
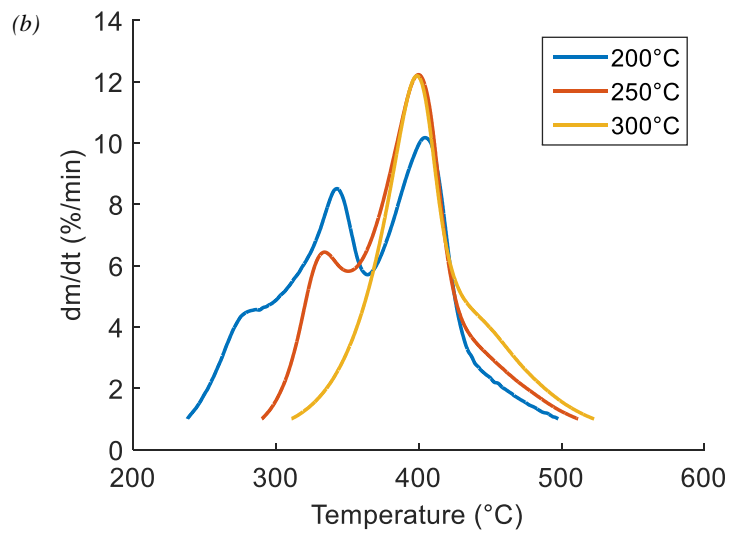
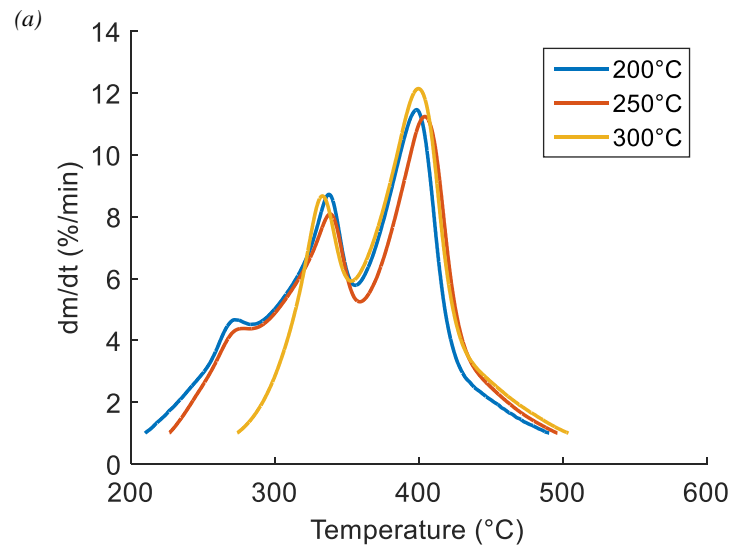


Figure 5-16: DTG plots for type B biomass torrefied for (a) 0 min, (b) 30 min, (c) 60 min.

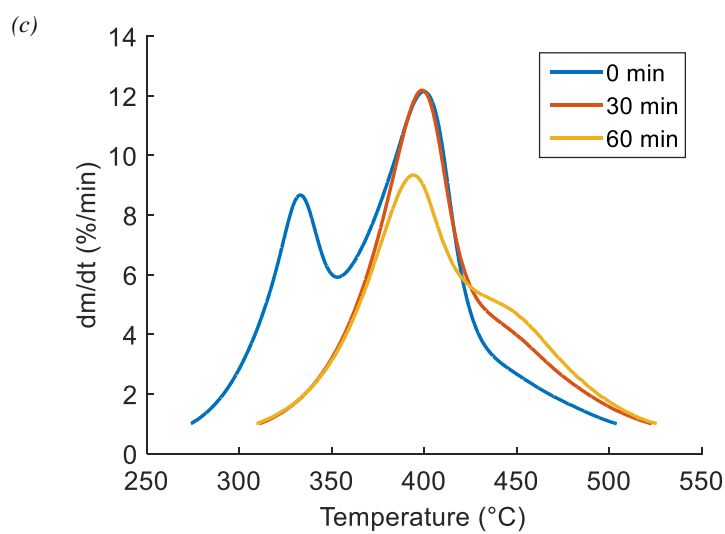
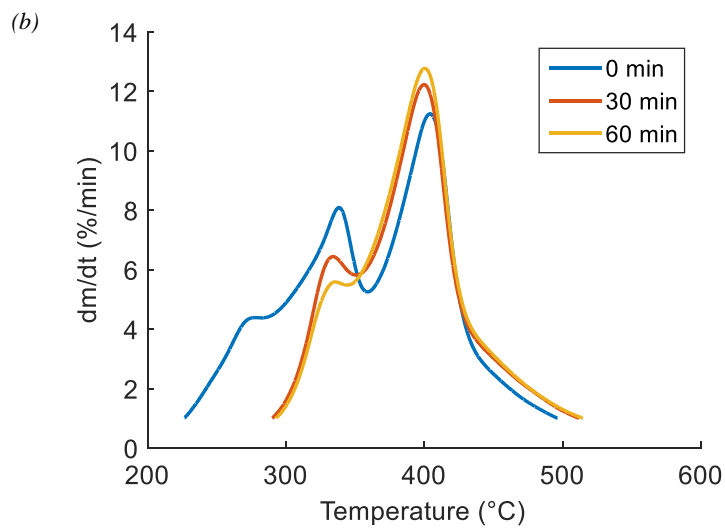
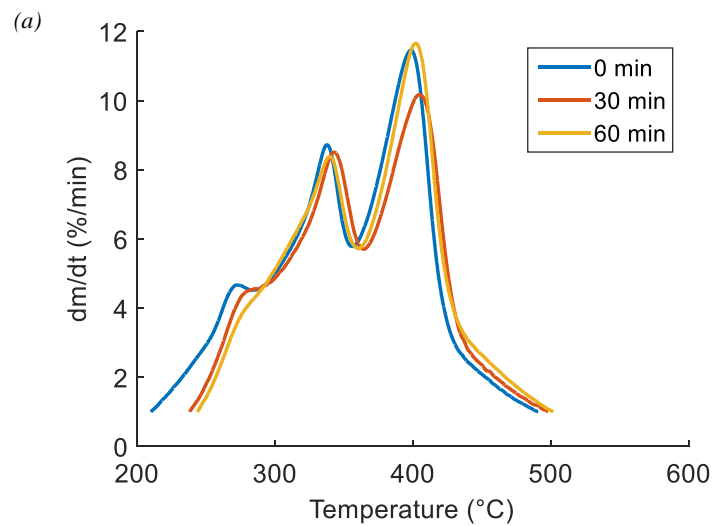


Figure 5-17: DTG plots for type B biomass torrefied at (a) 200°C, (b) 250°C, (c) 300°C.

The Matlab program which generated the DTG plots in Figure 5-16 and Figure 5-17 also picks out the peaks and records the temperature and peak height. In order to quantify the observed trends, an ANOVA test was carried out on the heights of the P1 and P2 peaks. The resulting p-values are given in Table 5-7, while Figure 5-18 and Figure 5-19 show the corresponding interaction plots. For the non-0 holding times, the height of P1 drops by 23-34% when the torrefaction temperature is increased from 200°C to 250°C; there is no P1 peak at 300°C. This corresponds to a greater degree of cellulose decomposition occurring when torrefied at higher temperatures. The p-values of 0.000 confirm that the effect on the height of P1 of temperature and holding time as well as their interaction are statistically significant.

Table 5-7: p-values from ANOVA test of P1 and P2 peak heights.

Peak	Temperature	Time	Interaction
P1	0.000	0.000	0.000
P2	0.123	0.979	0.005

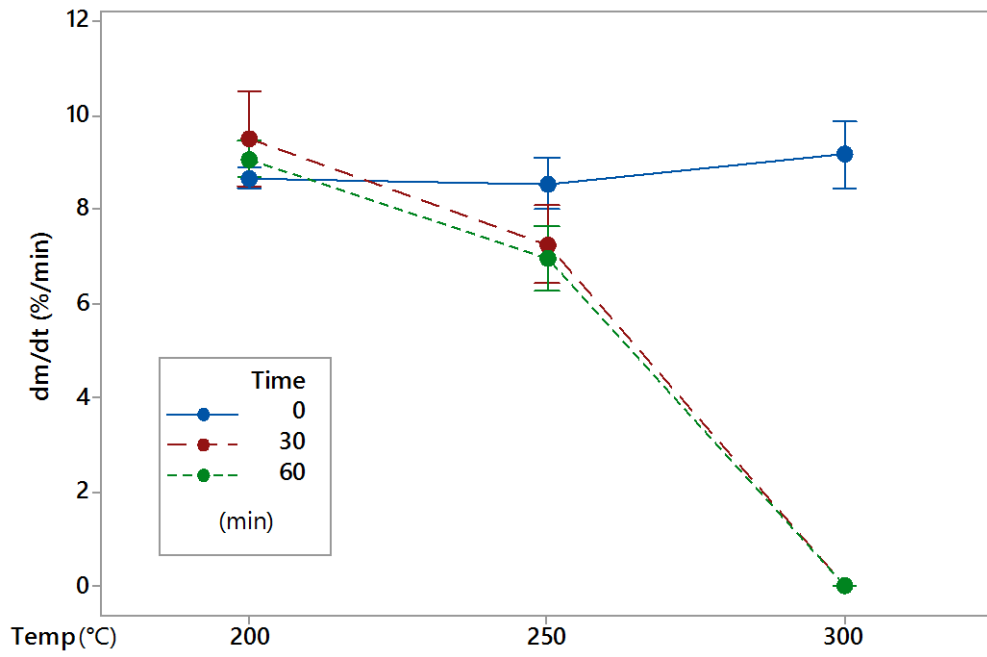


Figure 5-18: Interaction plot for the P1 peak height.

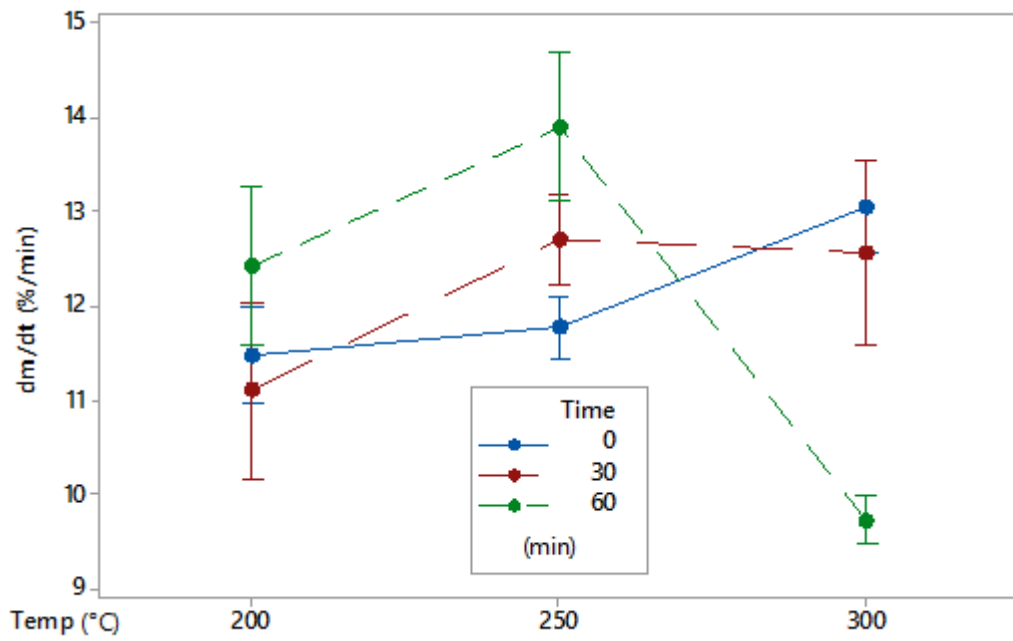


Figure 5-19: Interaction plot for the P2 peak heights.

A possible explanation for the presence of peak P2 is the decomposition of the oil present in the seed cake. One piece of evidence supporting this theory is the lack of a signal in the NMR spectra which correspond to the trends observed in P2 height in the DTG plots; most of the oil is pressed out of the sample when it is compacted into the sample capsule in preparation for the NMR analysis. To explore the plausibility of this explanation further, the Matlab program was used to analyse the DTG data of three samples each of untorrefied type A and type B. Overlaid DTG plots of representative single replicates are shown in Figure 5-20. It can be seen that the height of P2 is significantly lower in the case of type A. The mean P2 height (calculated from the three samples) for the type A was 48% lower, i.e. approximately half the height of the type B. A two-sample t-test confirmed the results, with a P-value less than 0.05 ($P=0.000$) indicating that the P2 heights of type A and type B are significantly different. Since the type A material has a lower apparent oil content than the type B (Section 3.2), the significant fall in the P2 height strongly suggests that this peak is caused by the oil still present in the seed cake.

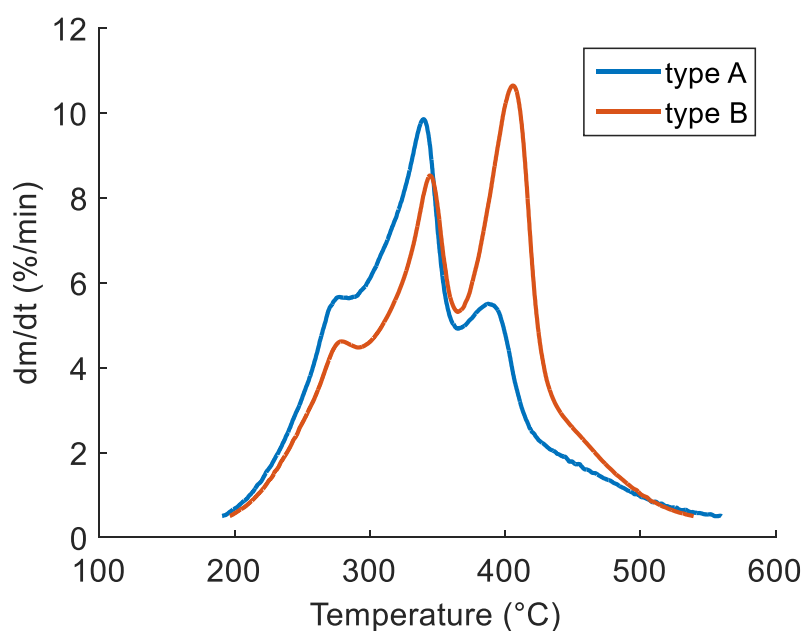


Figure 5-20: DTG plots of untreated type A and type B biomass.

The p-values for P2 (Table 5-7) indicate that the main effects of temperature and time are not significant, while the interaction between the variables is on the margin of statistical significance. Considering the overlapping of the error bars, no clear trend can be observed in either direction. The exception is the sharp fall of the peak height at the most intense torrefaction conditions, i.e. 300°C for 60 min. This indicates that the oil in the seed cake resists degradation more than the hemicellulose and cellulose, and only decomposes at the high torrefaction temperatures and holding times.

The NMR results (Section 5.2.4) were compared with Figure 5-16(c) (since the NMR runs were carried out on samples torrefied at 60 min). The NMR analysis corroborated the trends observed in the DTG. Hemicellulose and cellulose undergo complete decomposition when torrefied at 250°C and 300°C, respectively. Lignin decomposes over a range of temperatures starting from as low as 200°C, as indicated by the “trail” after P2 being present in the 200°C DTG plots (Figure 5-17(a)). Lignin continues to decompose at temperatures beyond 300°C.

5.3 Secondary torrefaction study

A limited study was carried out on the type A seed cake. The finest size fraction (<1 mm) was used since this was the most abundant by mass. A 3-level full-factorial (duplicated) matrix was used. The tested torrefaction temperatures were 200°C, 250°C and 300°C, while the tested holding times used were 0 min, 30 min and 60 min. A total of 18 runs were carried out. Again, Minitab was used to randomise the run order and analyse the collected data.

As with the primary study (type B), the HHV and energy yield were the fundamental responses which were used to optimise the torrefaction factors. Additionally, the proximate analysis was carried out using TGA.

5.3.1 Mass yield, HHV, energy yield

Figure 5-21 and Figure 5-22 show the variation of the mass yield with torrefaction temperature and holding time, respectively.

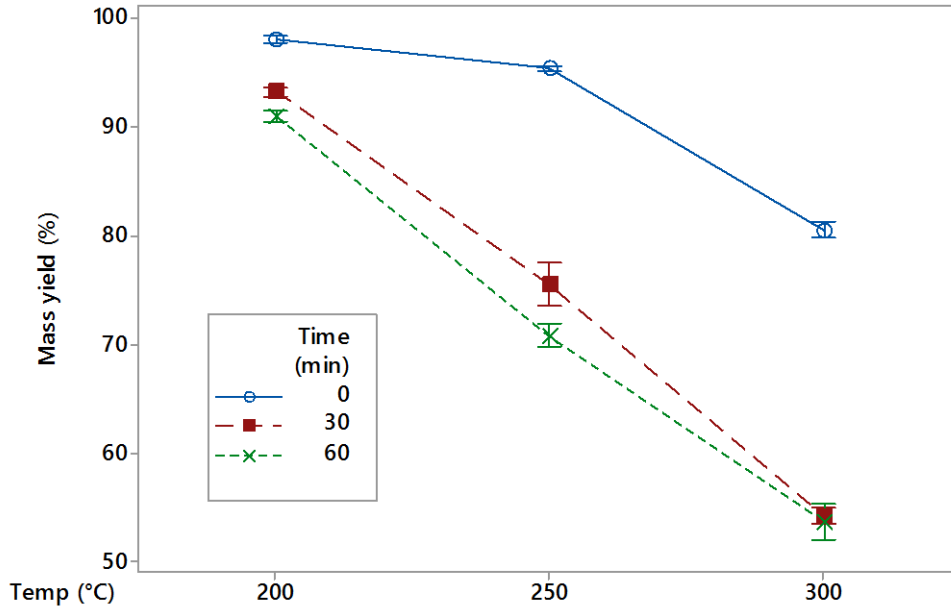


Figure 5-21: Interaction plot for mass yield, grouped by holding time.

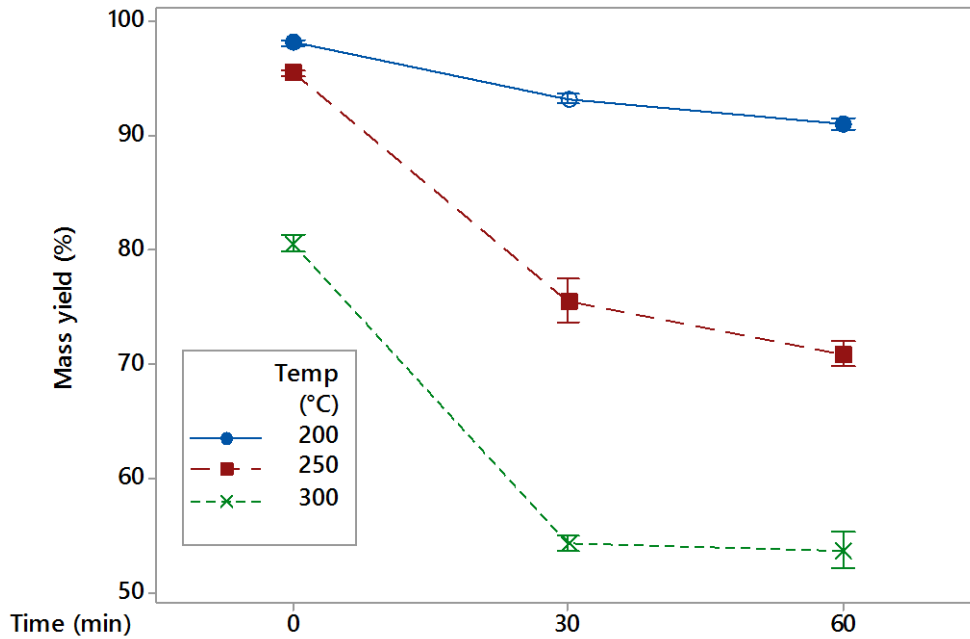


Figure 5-22: Interaction plot for the mass yield, grouped by torrefaction temperature.

As is the case for type B, the mass yield for the type A torrefaction shows an approximately linear decrease with increasing torrefaction temperature for the non-0 min runs; linear regression of the non-0 min data yielded an R^2 value of 0.985. The

mass yield decreases by 41-42% when the torrefaction temperature is increased from 200°C to 300°C, compared to a corresponding decrease of 35% in the case of the type B. For the 0 min runs, the mass yield drops at a slower rate from 200°C to 250°C; this non-linearity in the 0 min runs which was also observed in the type B is caused by the biomass undergoing torrefaction in the heating and cooling stages of the run (see Section 5.2.1).

The general trends in the HHV (Figure 5-23 and Figure 5-24) and energy yield (Figure 5-25 and Figure 5-26) of the type A biomass are similar to those observed with the type B, i.e. the HHV increases and the energy yield decreases as the torrefaction intensity is increased.

At the median torrefaction conditions of 250°C and 30 min, the HHV of the type A seed cake is enhanced by 17%. This is similar to the enhancement of 16% that was recorded for the type B seed cake at similar conditions (Table 5-1). The maximum HHV enhancements are also similar at 27% and 26% for type A and type B, respectively. However, since the HHV of the untreated type A is lower than that of untreated type B (20.76 MJ/kg vs 24.06 MJ/kg), the highest post-torrefaction HHV achieved for the type A biomass is lower at ~26 MJ/kg compared to ~30 MJ/kg for type B. A linear regression of HHV with respect to the mass loss (mass yield subtracted from unity) resulted in the following equation, with an R² value of 0.966:

$$HHV (MJ/kg) = 20.84 + (0.1224 \times \text{mass loss} (\%)) \quad \text{Eqn 5-6}$$

The constant of the regression equation is approximately equal to the HHV of the untreated biomass. This result, which was suggested by Almeida et al. (2010), was also observed in the case of the type B biomass (Equation 5-1).

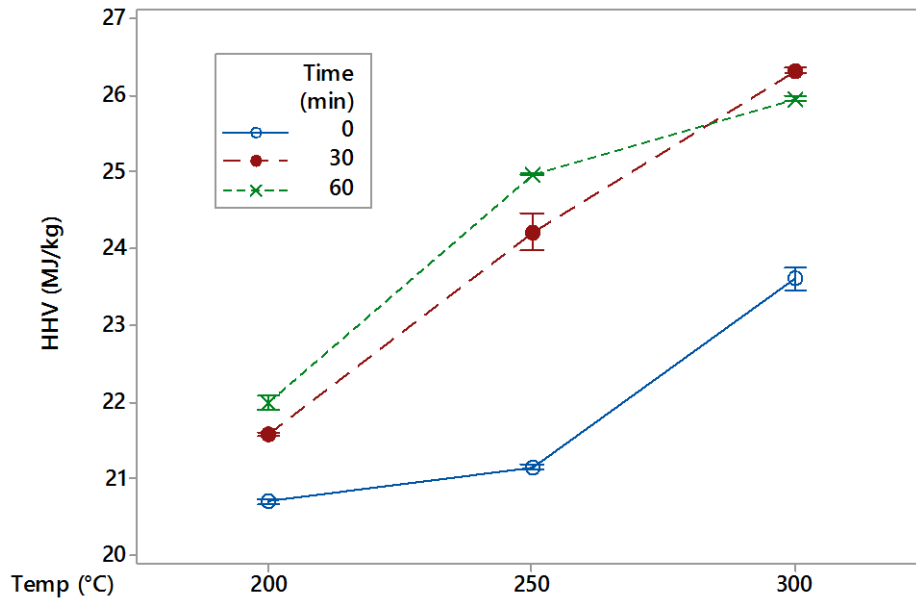


Figure 5-23: Interaction plot for the HHV, grouped by holding time.

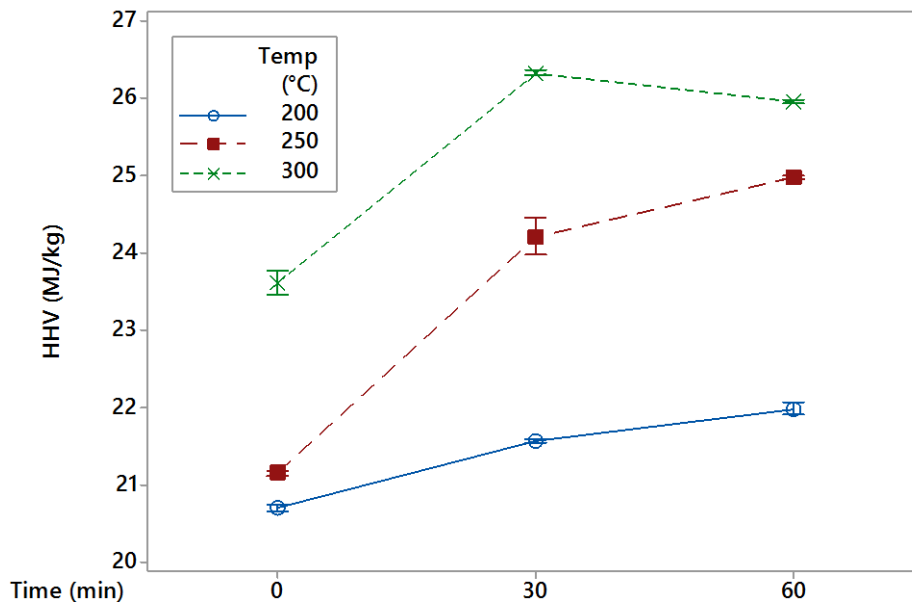


Figure 5-24: Interaction plot for the HHV, grouped by torrefaction temperature.

The energy yield drops at a higher rate when the torrefaction temperature is increased. The mean energy yield for the non-0 min runs decreases by 10% when the torrefaction temperature is increased from 200°C to 250°C, and by a further 22% from 250°C to 300°C. The corresponding values for the type B biomass are 6% and 15%. Although the trends in both types A and B are similar, the magnitude of the energy yield drop is greater in type A, i.e. the type A biomass is more sensitive to the torrefaction temperature. The energy yield at the median (250°C, 30 min) and most

intense (300°C, 60 min) torrefaction conditions are 88.01% and 67.04%, respectively, in the case of type A. The corresponding energy yields for type B are 90.02% and 70.02%. Hence, torrefaction of type A biomass results in relatively lower energy yields than that of type B, although the margin is not substantial.

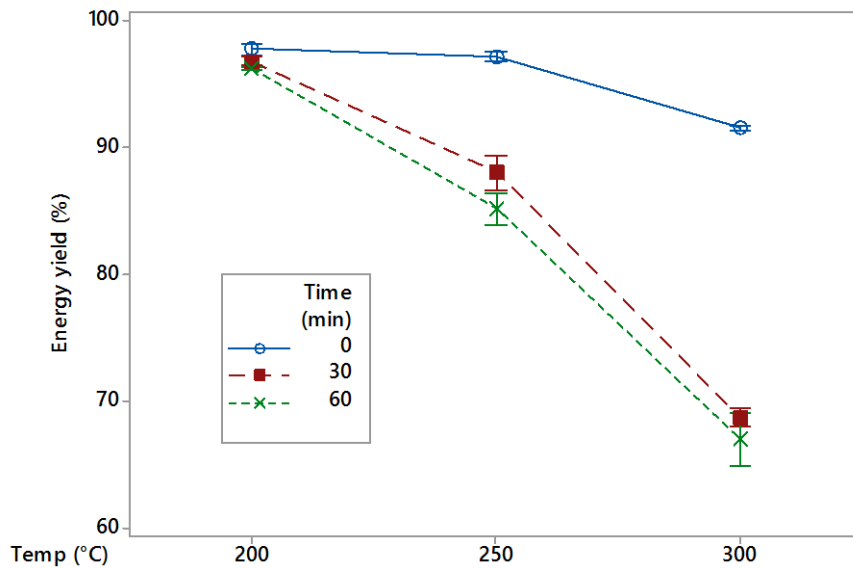


Figure 5-25: Interaction plot for the energy yield, grouped by holding time.

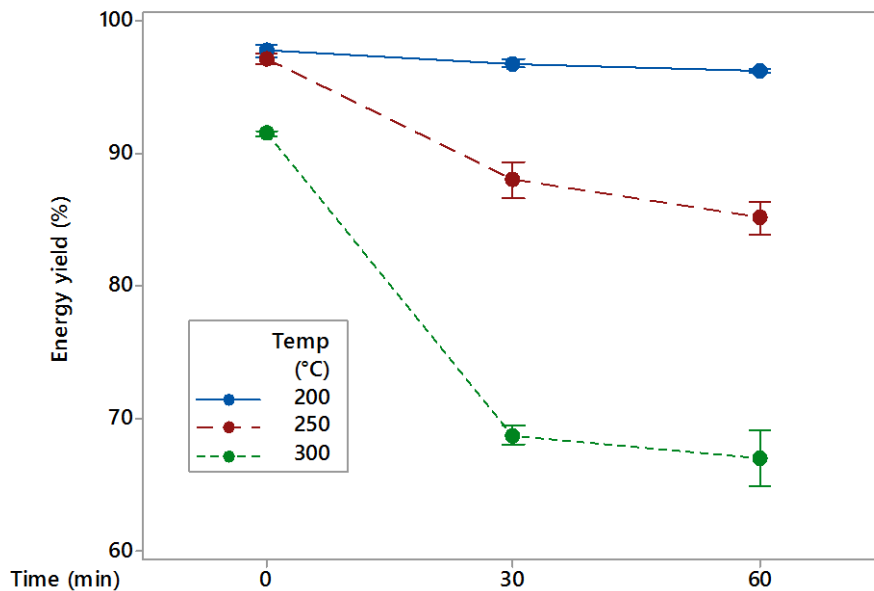


Figure 5-26: Interaction plot for the energy yield, grouped by torrefaction temperature.

Table 5-8 shows the p-values obtained from the ANOVA test carried out on the type A mass yield, HHV and energy yield data. For all three responses, the temperature, time and temperature-time interaction are statistically significant, i.e. $p < 0.05$.

Table 5-8: p- and F-values obtained from ANOVA test on mass yield, HHV, energy yield data.

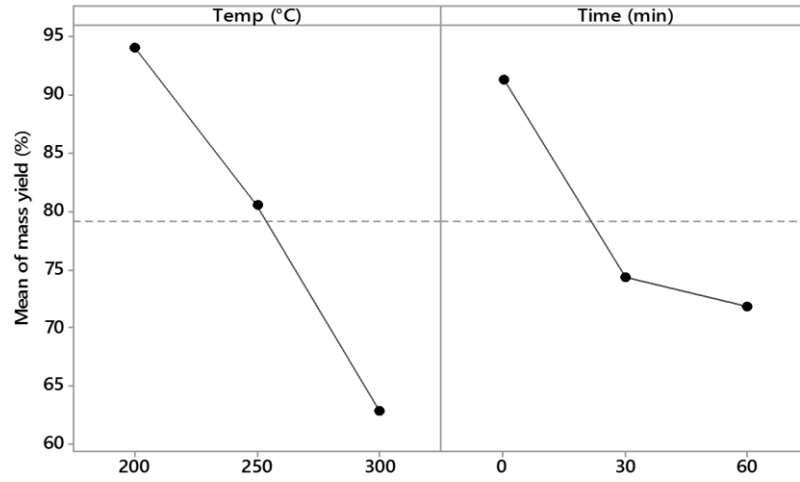
	p-value (type A)			F-value			
				type A		Type B	
	temp	time	temp*time interaction	temp	time	temp	time
Mass yield	0.000	0.000	0.000	737.56	339.18	1039.51	60.48
HHV	0.000	0.000	0.000	1067.10	528.72	305.33	14.43
Energy yield	0.000	0.000	0.000	352.69	142.97	231.62	22.54

The F-values from the statistical analysis are also given in Table 5-8; larger F-values indicate a greater effect on the response. The corresponding F-values from the type B analysis are also tabulated for comparison. In both type A and type B, the torrefaction temperature was the more dominant factor in affecting the mass yield, HHV and energy yield. Table 5-9 gives the percentage change in the mean responses when each factor is increased (independently of the other) from the lower limit to the upper limit. Comparing with the corresponding results for type B in Table 5-3, it can be seen that relative changes are broadly similar between the two types. The main effects for type A are illustrated graphically in Figure 5-27.

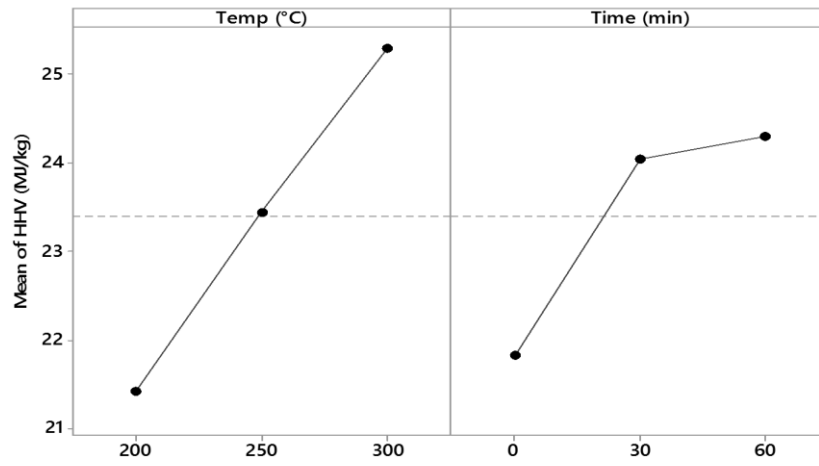
Table 5-9: Main effects changes in mean mass yield, HHV, energy yield over full range of factors.

Change in	Temperature increased from 200°C to 300°C	Holding time increased from 0 min to 60 min
Mass yield	-33.2 %	-21.4%
HHV	+18.1 %	+11.4 %
Energy yield	-21.8 %	-13. 3%

(a)



(b)



(c)

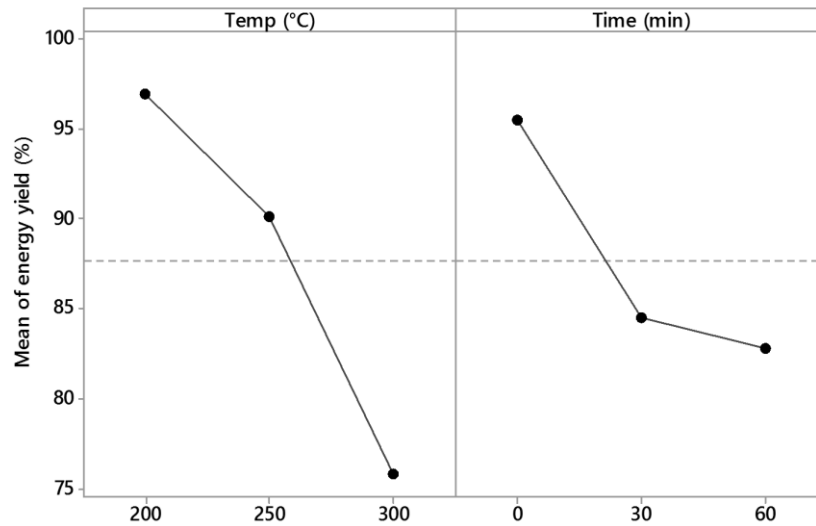


Figure 5-27: Main effects plots for (a) mass yield, (b) HHV, (c) energy yield.

5.3.2 Fixed carbon (FC) content

Figure 5-28 and Figure 5-29 show the variation of the DAF FC with torrefaction temperature and holding time, respectively. Similarly to the type B material, the DAF FC content increases with increasing torrefaction intensity. For the non-0 min runs, the DAF FC content increases by ~32% when the torrefaction temperature is increased from 200°C to 250°C, and by a further ~45% when the temperature is increased from 250°C to 300°C. Increasing the holding time from 30 min to 60 min appears to have a relatively insignificant effect.

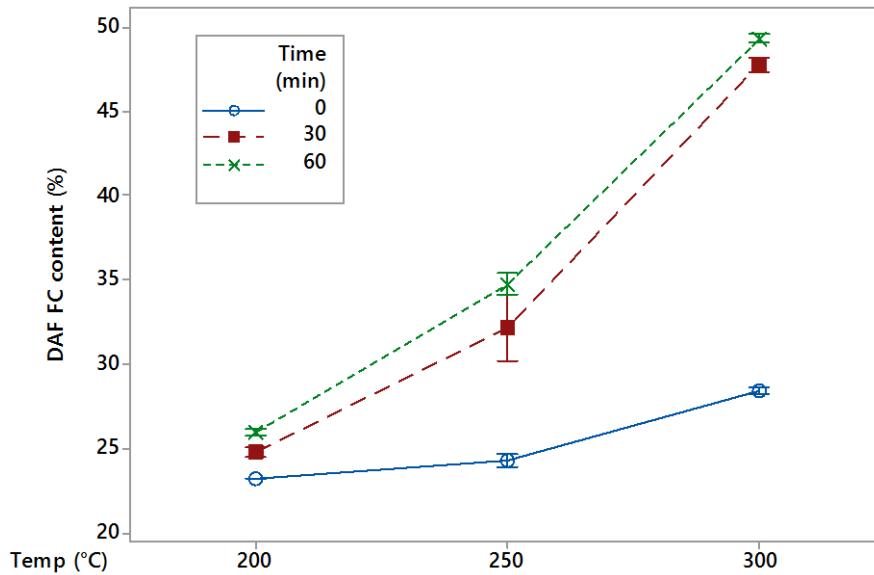


Figure 5-28: Interaction plot for the DAF FC content, grouped by holding time.

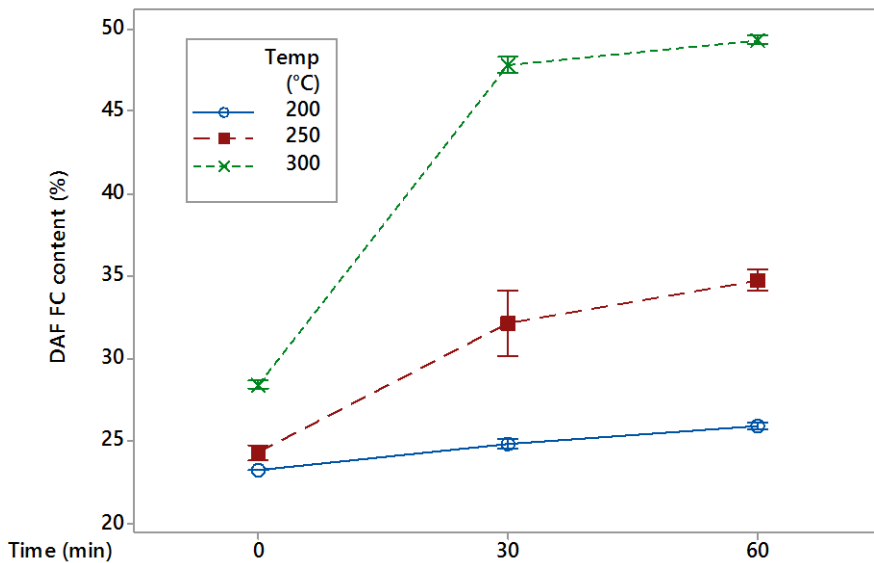


Figure 5-29: Interaction plot for the DAF FC content, grouped by torrefaction temperature.

The link between the DAF FC content and the HHV has been explained earlier in Sections 5.2.1 and 5.2.2. From the scatter plot in Figure 5-30, it is immediately apparent that there is a correlation between the DAF FC content and HHV in the case of the type A as well.

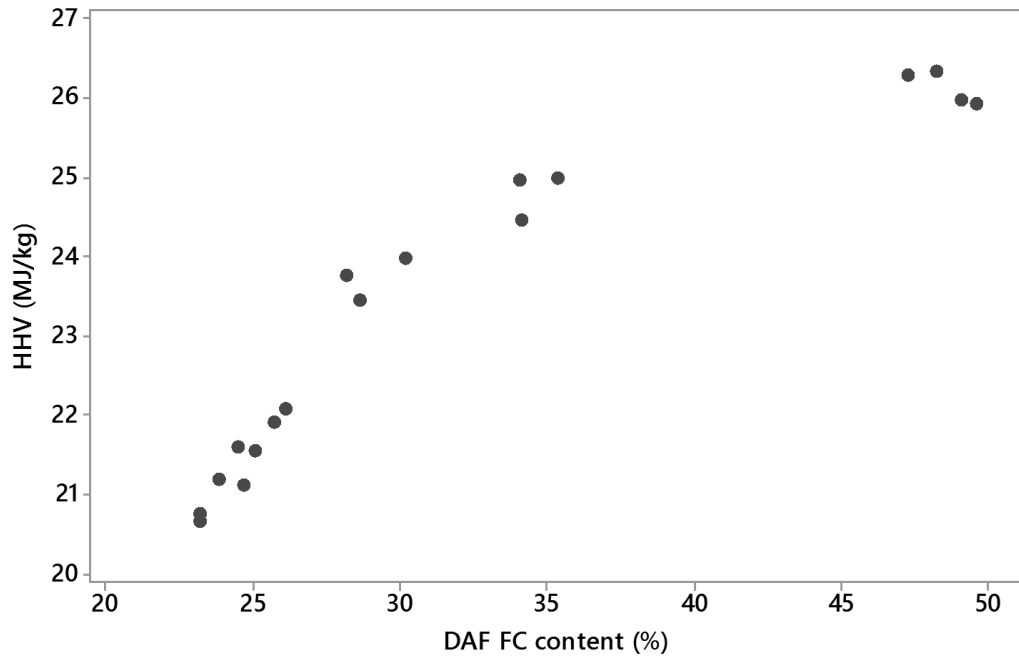


Figure 5-30: Scatter plot of HHV vs DAF FC content.

A regression analysis was carried out, where the data was fitted into the models shown in Equations 5-7 to 5-10. The coefficients and regression statistics are shown in Table 5-10.

- Linear: $HHV = a + b \cdot (DAF_FC)$ **Eqn 5-7**
- Linear logarithmic: $HHV = a + b \cdot \ln(DAF_FC)$ **Eqn 5-8**
- Quadratic: $HHV = a + b \cdot (DAF_FC) + c \cdot (DAF_FC)^2$ **Eqn 5-9**
- Cubic: $HHV = a + b \cdot (DAF_FC) + c \cdot (DAF_FC)^2 + d \cdot (DAF_FC)^3$ **Eqn 5-10**

Table 5-10: Regression coefficients and statistics for HHV vs DAF FC.

	Linear	Linear logarithmic	Quadratic	Cubic
pred-R²	0.8274	0.8940	0.9764	0.9749
S	0.7923	0.6172	0.2889	0.2806
a	17.02	-1.02	2.534	-11.05
b	0.1971	7.103	1.061	2.305
c	-	-	-0.01184	-0.04849
d	-	-	-	-0.000345

From the pred-R² (which have to be maximised) and S (which have to be minimised) in Table 5-10, the cubic model would be the most reliable equation to use to predict the HHV. However, there is very little difference between the regression statistics of the quadratic and cubic model. The quadratic model would also be an acceptable equation to use, particularly when considering its lower complexity compared to the cubic model. The four regression models are graphically represented in Appendix 6 (Figure A6-2).

5.4 Discussion

The key driver behind torrefaction in the context of this study is the enhancement of the HHV. Coal used in power plants would typically have a HHV in the range of 27-32 MJ/kg (Mardon & Hower, 2004). To support co-firing, it would be desirable to bring the HHV of the biomass to within this range. A higher HHV also implies that the energy density is higher, and this is advantageous in terms of storage and transport. When carried out at higher intensities, the torrefaction process was able to increase the HHV of the type B *Jatropha* seed cake to ~30 MJ/kg. However, the energy yields at these torrefaction conditions are less than 80% (see Figure 5-31(a) and (b)). A low energy yield would be undesirable from an energy efficiency standpoint and could potentially make the process economically unviable. Hence, the torrefaction conditions should be chosen so that neither the HHV nor the energy yield is excessively compromised.

Figure 5-31(c) was generated by overlaying the selected regions of the two contour plots in Figure 5-31(a) and (b), with an energy yield greater than 90% and a HHV greater than 27 MJ/kg. The unshaded region depicts the range of torrefaction conditions which would satisfy both these conditions. The possible combinations of torrefaction temperature and holding times range from <5 min at >280°C to longer holding times (~45 to 60 min) at lower temperatures (220°C to 250°C). These guidelines are valid for the conditions under which the torrefaction was performed, most significantly the heating rate of 10°C/min.

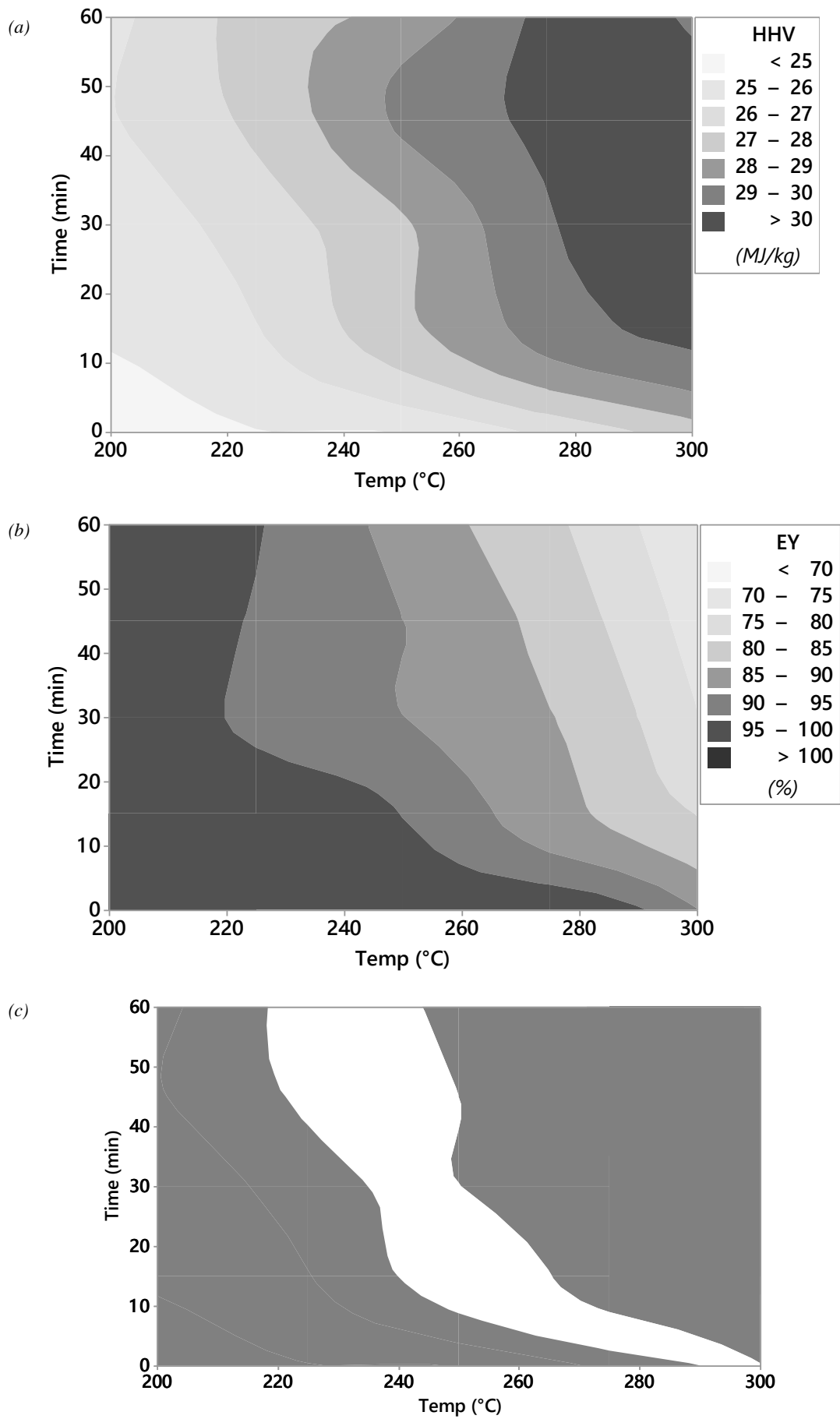


Figure 5-31: Contour plots of (a) HHV, (b) energy yield (EY), (c) overlay of HHV and EY for type B.

Similar plots for the type A *Jatropha* seed cake are given in Figure 5-32. However, the lower absolute HHV's recorded in the type A (see Section 5.3.1) means that intense torrefaction conditions, i.e. 300°C for 30-60 min, are required to raise the HHV to ~26 MJ/kg. However, the energy yield is only ~68% at these conditions. Hence, a greater compromise had to be made in the case of the type A; the overlaid contour plot in Figure 5-32(c) shows the range of torrefaction conditions where the energy yield is >85% and the HHV is >24.5 MJ/kg. The envelope of conditions was narrower than in the type B, with the aforementioned conditions being satisfied when the torrefaction temperature is ~250°C and the holding time is 45-60 min.

The cost of the torrefaction process in terms of energy required by the furnace and the cost of the N₂ supply should also be taken into account in a practical implementation of the process. The cost implications of using low temperature/long holding time versus high temperature/short holding time have to be investigated further, and would be dependent on the torrefaction rig used. This would allow the desirable parameter range to be narrowed down further, and the process to be optimised in a more comprehensive manner. Measurement of energy expenditure was considered beyond the scope of this study, particularly because it is at a laboratory scale and any results thus obtained would not be scalable to a full-scale torrefaction plant. A few studies focusing on the economic aspects of torrefaction have been conducted in the recent past (Agar et al., 2015; Topell Energy BV, 2015). Typically, the energy cost of the torrefaction process is offset by the improvement in grindability and energy density which in turn reduce milling and transport costs. However, this would depend on a careful design and implementation of the system taking into account factors such as the transport distances, mode of transport and the energy source for the pre-treatment processes.

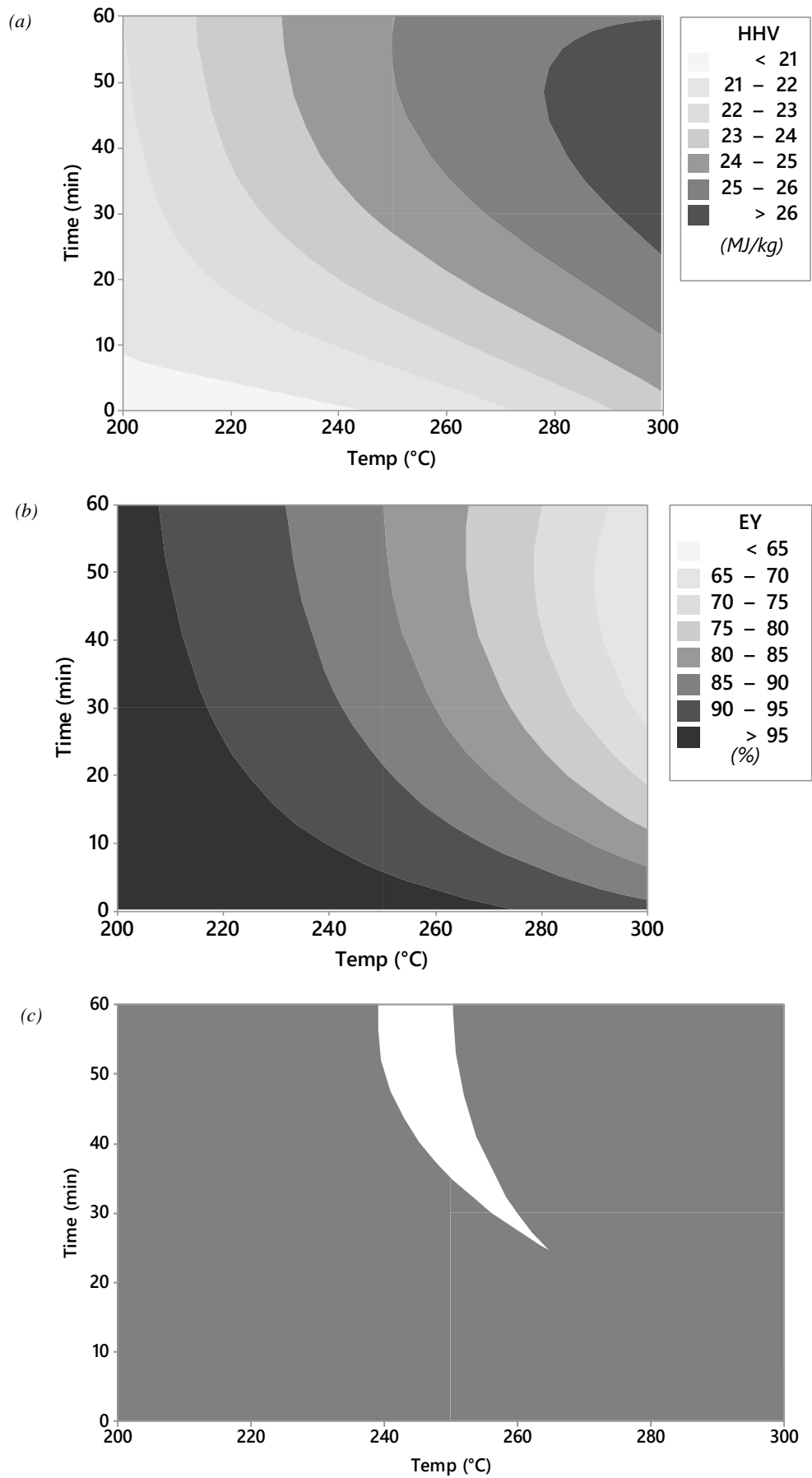


Figure 5-32: Contour plots of (a) HHV, (b) energy yield (EY), (c) overlay of HHV and EY for type A.

It is important to adopt a holistic approach when assessing the suitability of a certain type of biomass for co-firing. Torrefaction aims to improve the thermophysical and physical characteristics of the fuel. However, there are other considerations as well, chief among which is chemical composition of the biomass. The typically high inorganic content of biomass is one of the major detractors to biomass combustion as it is responsible for a host of ash-related problems. Leaching is touted as a pre-treatment option to mitigate these issues. Another aspect that has to be explored is the combustion behaviour of *Jatropha curcas* seed cake, including devolatilisation and char combustion characteristics.

5.5 Concluding remarks

The fundamental parameters used for the optimisation of the torrefaction process are the HHV and energy yield, which respond inversely to each other. For the type B seed cake, an envelope of torrefaction conditions exists – ranging from <5 min at >280°C to >45 min at 220°C-250°C when a heating rate of 10°C/min is used – where a HHV greater than 27 MJ/kg can be obtained while maintaining an energy yield greater than 90%. A tighter envelope of ~250°C for 45-60 min was determined for the type A seed cake; in this case however, the range was for a HHV greater than 24.5 MJ/kg and an energy yield no less than 85%. From the point of view of the HHV and energy yield, the type B material is a more versatile feedstock for torrefaction; a relatively wide envelope of conditions exists which can cause the required HHV enhancement without compromising excessively on the energy yield.

The increase in measured elemental C content and proximate DAF FC content corroborated the theoretical explanation for the increase in HHV as the torrefaction intensity was increased. The ¹³C NMR and DTG analysis provided insight into the structural changes occurring during the torrefaction process, with hemicellulose proving to be the most volatile lignocellulosic component followed by cellulose and lignin. Complete decomposition of hemicellulose and cellulose occurred by 250°C and 300°C, respectively, while lignin continued to decompose beyond 300°C. Throughout the study, the torrefaction temperature was demonstrated to be a more dominant factor than the holding time.

6 LEACHING

6.1 Introduction

This chapter aims to investigate how both untorrefied and torrefied *Jatropha curcas* seed cake reacts to leaching, and establish a set of recommended guidelines for this pre-treatment process. Figure 6-1 illustrates the overall workflow for the leaching study. The leaching study was conducted in three phases – preliminary, primary and secondary. The experimental design and results for each phase are presented in this chapter, while the specific details relating to the experimental procedures were outlined in Chapter 3.

The preliminary study (Section 6.2) established a broad picture of how *Jatropha curcas* seed cake (type B) reacts to leaching. The most significant factors were identified using these results. The inorganic content of the biomass was measured using two approaches – ICP-MS/IC and XRF – and the trends compared. The primary study (Section 6.3) expanded on the preliminary study; a more extensive 3x4 experimental matrix (with triplicate runs) was created for the two most significant factors identified in the preliminary study. Electrical conductivity and ionic content of the leachate, the individual inorganic elemental levels in the solid biomass, the VM content and the HHV were all analysed. The effects of leaching temperature and torrefaction on the leachability of the type B seed cake was investigated.

While both the preliminary and primary studies involved the more abundant type B biomass, a less-extensive secondary study using the type A biomass was also carried out (Section 6.4). All other variables were fixed, and two particle size fractions were used. The inorganic content of the leached biomass was used to gauge the effect that the particle size has on the leachability.

Sections 6.5 and 6.6 discuss the practical implications of the results, and recommend guidelines to be followed when leaching untoasted or toasted *Jatropha curcas* seed cake.

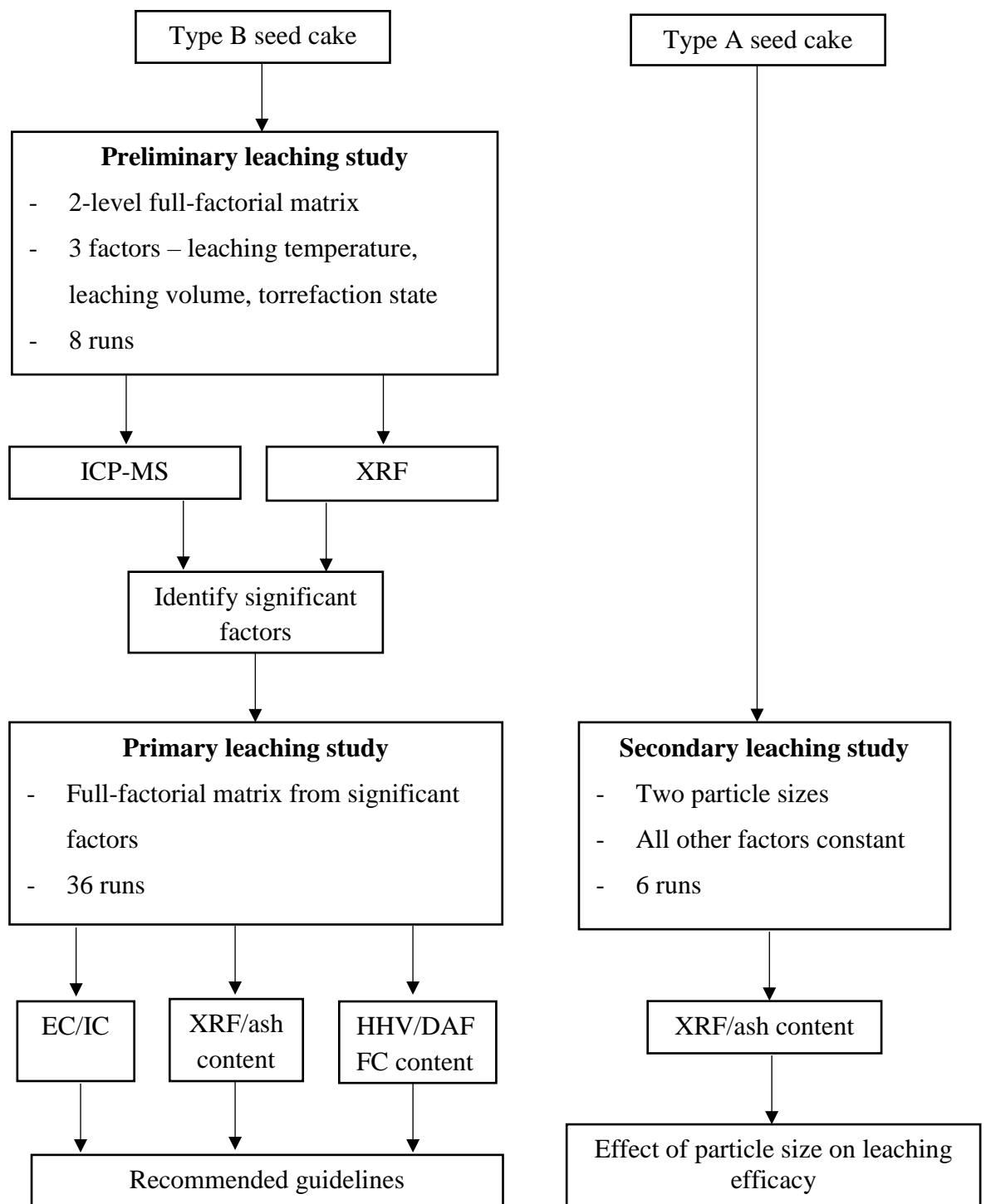


Figure 6-1: Flowchart of overall methodology of leaching study.

6.2 Preliminary leaching study

Three variables (factors) were identified – volume of water used, temperature of the water and torrefaction state of the biomass. An initial screening study was carried out to ascertain which factors had a significant effect on the inorganic content of the biomass and hence warranted a more detailed investigation.

A two-level factorial matrix was devised. The leaching temperatures used were 20°C and 50°C, while the leaching volumes were 100 ml/g and 200 ml/g. Both untorrefied type B biomass (referred henceforth as “UT”) and type B seed cake torrefied for 60 min at 300°C (“HT”) were used.

Hence, eight leaching runs were carried out. The leached material was analysed using two approaches. The first involved a combination of inductively coupled plasma mass spectroscopy (ICP-MS) and ion chromatography (IC); ICP-MS was used to measure the K, Mg, Ca, S and P content, while IC was used to measure the Cl content. The second method utilised X-ray fluorescence spectroscopy (XRF).

6.2.1 Inorganic content – ICP-MS/IC

Figure 6-2 shows the mean levels of each inorganic element in the untorrefied samples, and illustrates the efficacy of the leaching process in removing each element. For the leached samples, the “xxxx-yy” labels represent the leaching conditions, with “xxxx” denoting the volume of water used in ml and “yy” representing the temperature in °C. It can be seen that Cl undergoes the most drastic reduction, by almost 100%. This is followed by K and P – only 5%-17% of the original elemental content remains in the leached samples. Mg and S show a moderate decrease – between 42% and 63% of the original content remains. Ca levels are the least affected – there is no effect at 20°C (the values slightly above 100% can be attributed to experimental error and

variation within digests), while at 50°C there appears to be a low degree of leaching out.

Figure 6-3 shows the same data while omitting the columns for the unleached biomass, so that the differences between the different leaching conditions can be distinguished. For K, Mg and Ca, temperature is the most significant factor affecting the leaching efficacy. This is particularly evident in the case of K. The P content appears to be marginally more affected by the volume, although the statistical significance of this cannot be determined using this chart alone. The S content shows an uneven trend and it is possible that this is caused due to variation between digests, as evident in the high degree of overlapping of the error bars. In the case of Cl, the only detectable post-leaching levels of the element are found with the lower volume and lower leaching temperature.

Figure 6-4 is a similar graph that illustrates the elemental levels for the leached/torrefied biomass. Once again, the effect of increasing the temperature can be observed clearly. However, there are irregular trends with respect to the volume; a slight increase in the content observed at the higher volume, which is not the expected result. Again the overlapping of error bars suggests that this could be caused by the variation between digests.

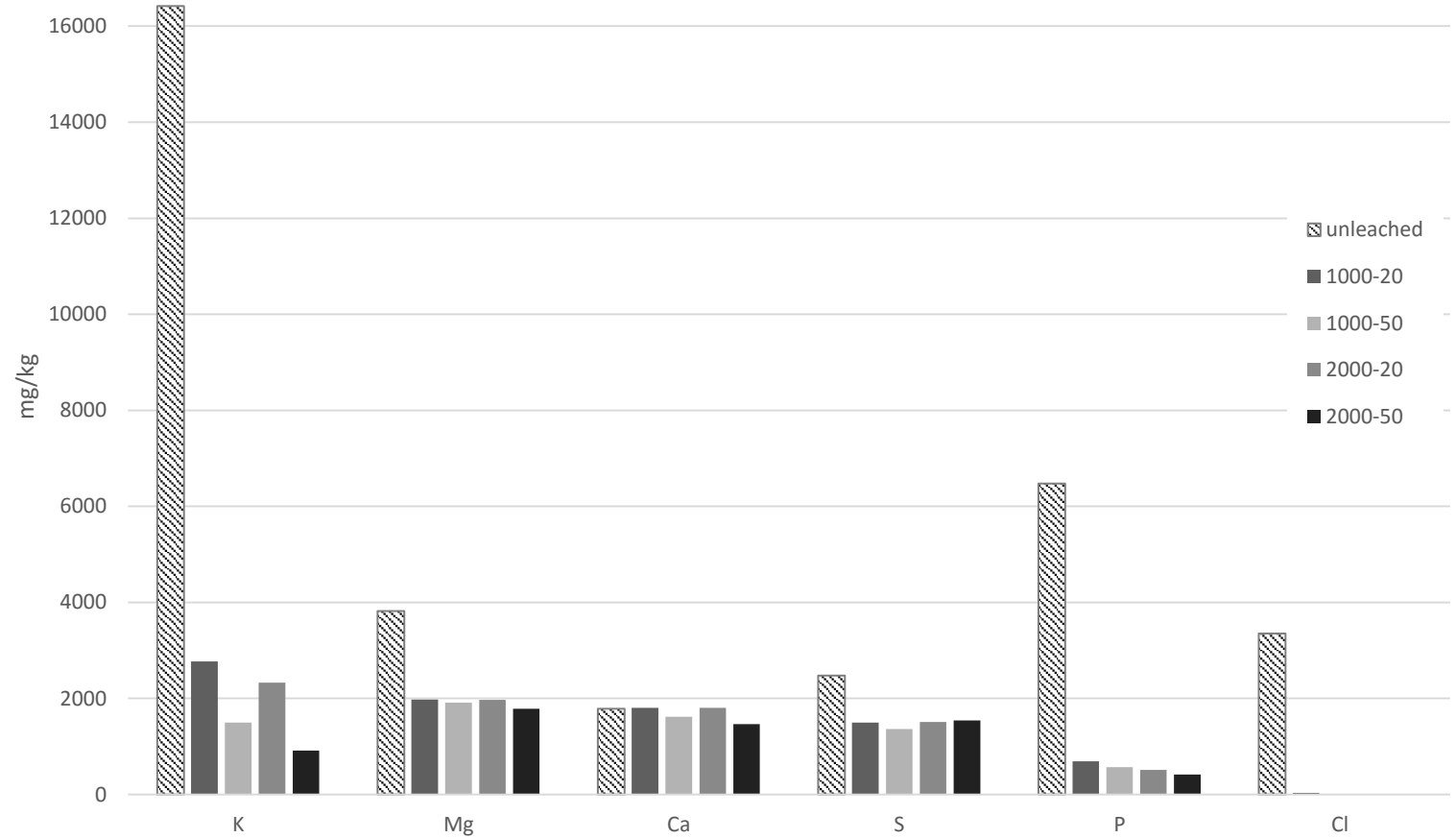


Figure 6-2: Inorganic content of untorrefied type B biomass, measured by ICP-MS/IC

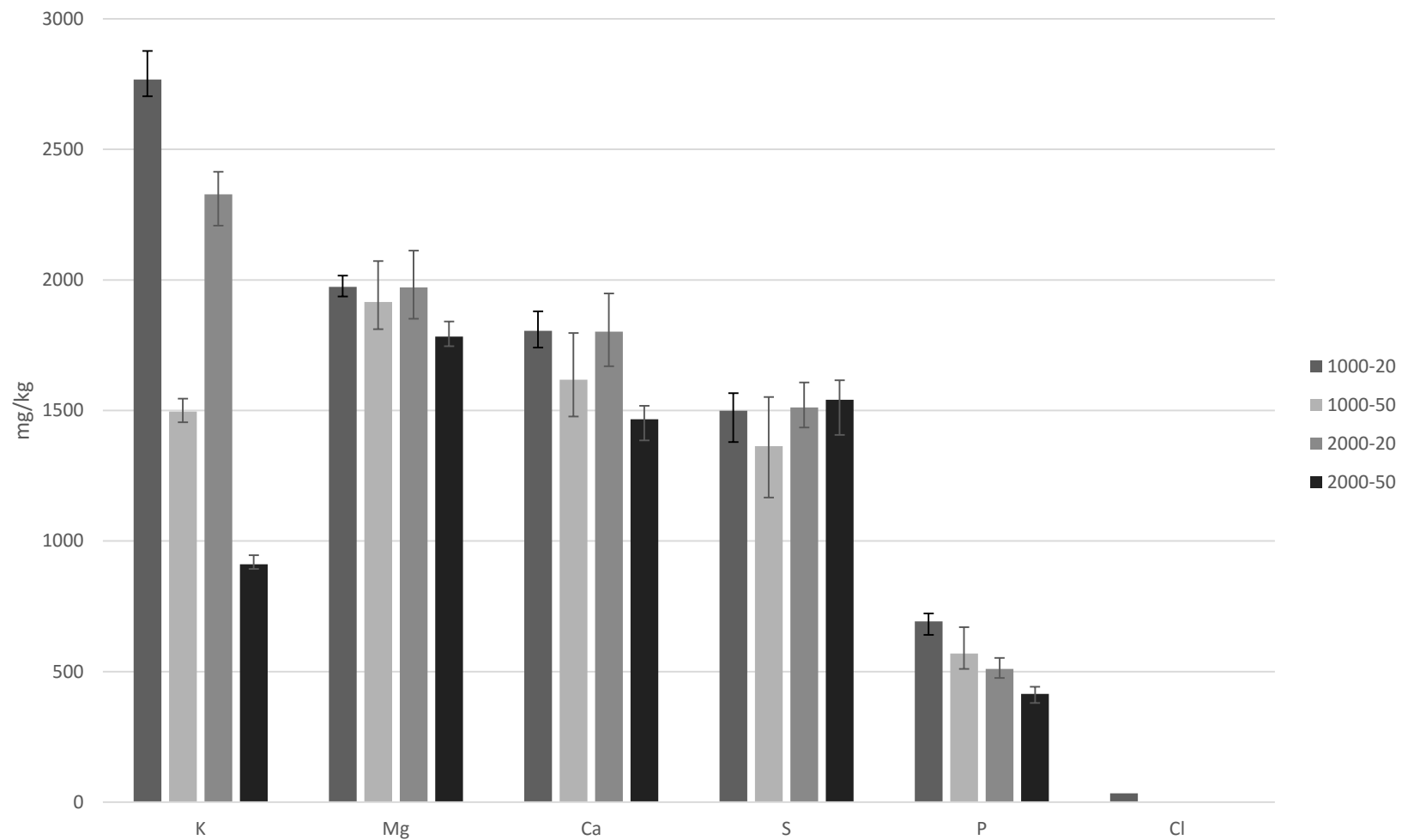


Figure 6-3: Inorganic content of untorrefied, leached type B biomass, measured by ICP-MS/IC

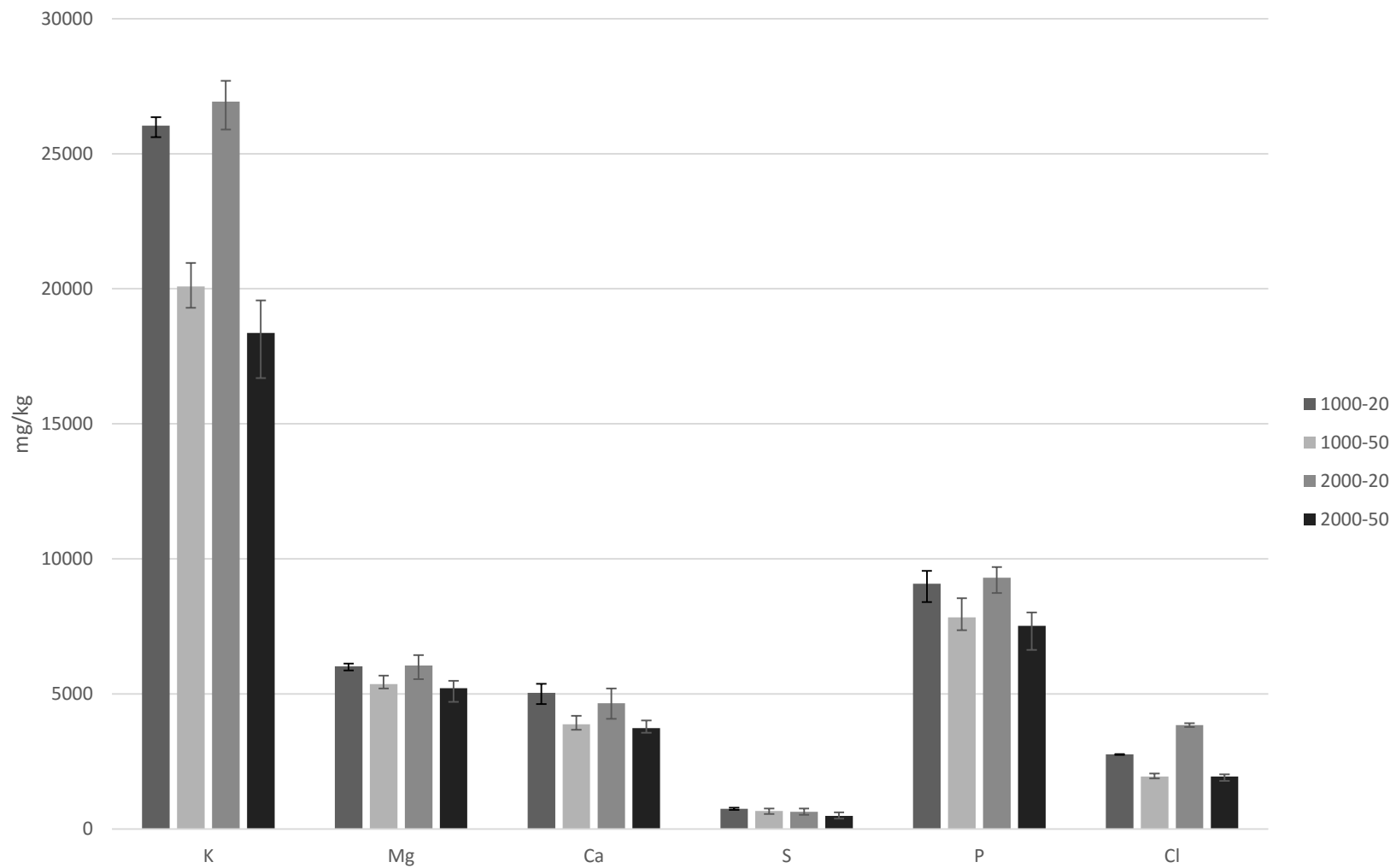


Figure 6-4: Inorganic content of torrefied, leached type B biomass, measured by ICP-MS/IC

Taking into account the variance observed in some of the readings and the few irregularities observed, a statistical analysis using Minitab was carried out to further ascertain the effects of the leaching parameters on the inorganic content. Table 6-1 summarises the p-values obtained from the analysis of variance (ANOVA) analysis of the data. A low p-value (<0.05) indicates the factor or interaction between factors has a statistically significant effect on the dependent variable (in this case the level of each element).

Table 6-1: p-values from ANOVA of type B ICP-MS/IC data

	p-value					
	volume (vol)	temperature (temp)	torrefaction state (tor)	vol*temp interaction	vol*tor interaction	temp*tor interaction
K	0.127	0.000	0.000	0.029	0.865	0.000
Mg	0.557	0.001	0.000	0.468	0.968	0.009
Ca	0.162	0.000	0.000	0.841	0.433	0.004
S	0.614	0.096	0.000	0.635	0.023	0.519
P	0.561	0.000	0.000	0.507	0.750	0.002
Cl	0.000	0.000	0.000	0.000	0.000	0.000

It can be seen from Table 6-1 that temperature is a significant factor in determining the levels of all the elements except for S. The torrefaction state also shows a low p-value throughout, indicating that it is a significant factor. Low p-values are also observed for the temp*tor interaction (again, with the exception of S). This shows that the interaction between the temperature and the torrefaction state has a statistically significant effect on the levels of these elements. In other words, the effect that the temperature has on the element levels is dependent on whether the biomass is torrefied or not. This was an expected result from an early stage, when a visual inspection showed that the untorrefied biomass caused discolouration of the leaching water at both temperatures, while discolouration only occurred at the higher temperature with

the torrefied biomass. The only element where the volume or interaction involving volume was significant was Cl. With the exception of this, the analysis of the ICP-MS/IC data indicates that the leaching temperature and torrefaction state are the most significant factors which warrant a more detailed investigation.

6.2.2 Inorganic content - XRF

Figure 6-5 and Figure 6-6 show the inorganic content of the leached untorrefied and torrefied type B, respectively, as measured by XRF spectrometry.

The XRF data was also processed using Minitab 17. Since no replicate runs were carried out in the preliminary leaching study, Pareto charts (Figure 6-7) were used as a statistical tool. Pareto charts offer a means to determine which factors and interactions between factors are statistically significant. In the figures, “Temp”, “Vol” and “Tor_state” represent the leaching volume, leaching temperature and torrefaction state, respectively. The absolute values of the unstandardised effects are shown, along with a reference line. In the absence of replicates, the software uses Lenth’s pseudo-standard error (LSE) to determine the location of the reference line (Lenth, 1989) (see Appendix 7). If the magnitude of an effect is larger than the LSE, it can be considered that the corresponding factor or interaction is statistically significant. The significance of the factors and/or interactions determined using this approach are summarised in Table 6-2.

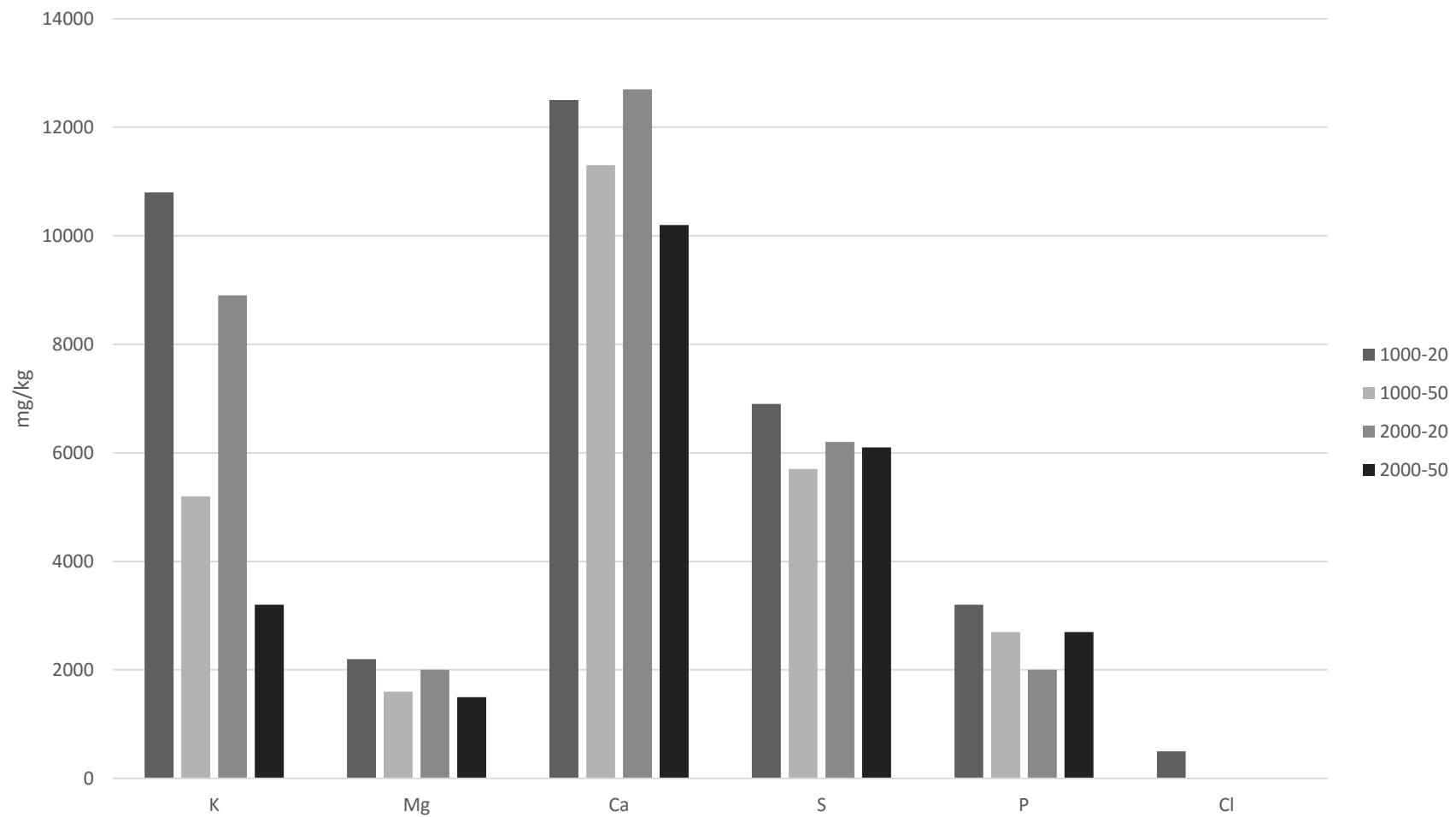


Figure 6-5: Inorganic content of untorrefied, leached type B biomass, measured by XRF spectrometry

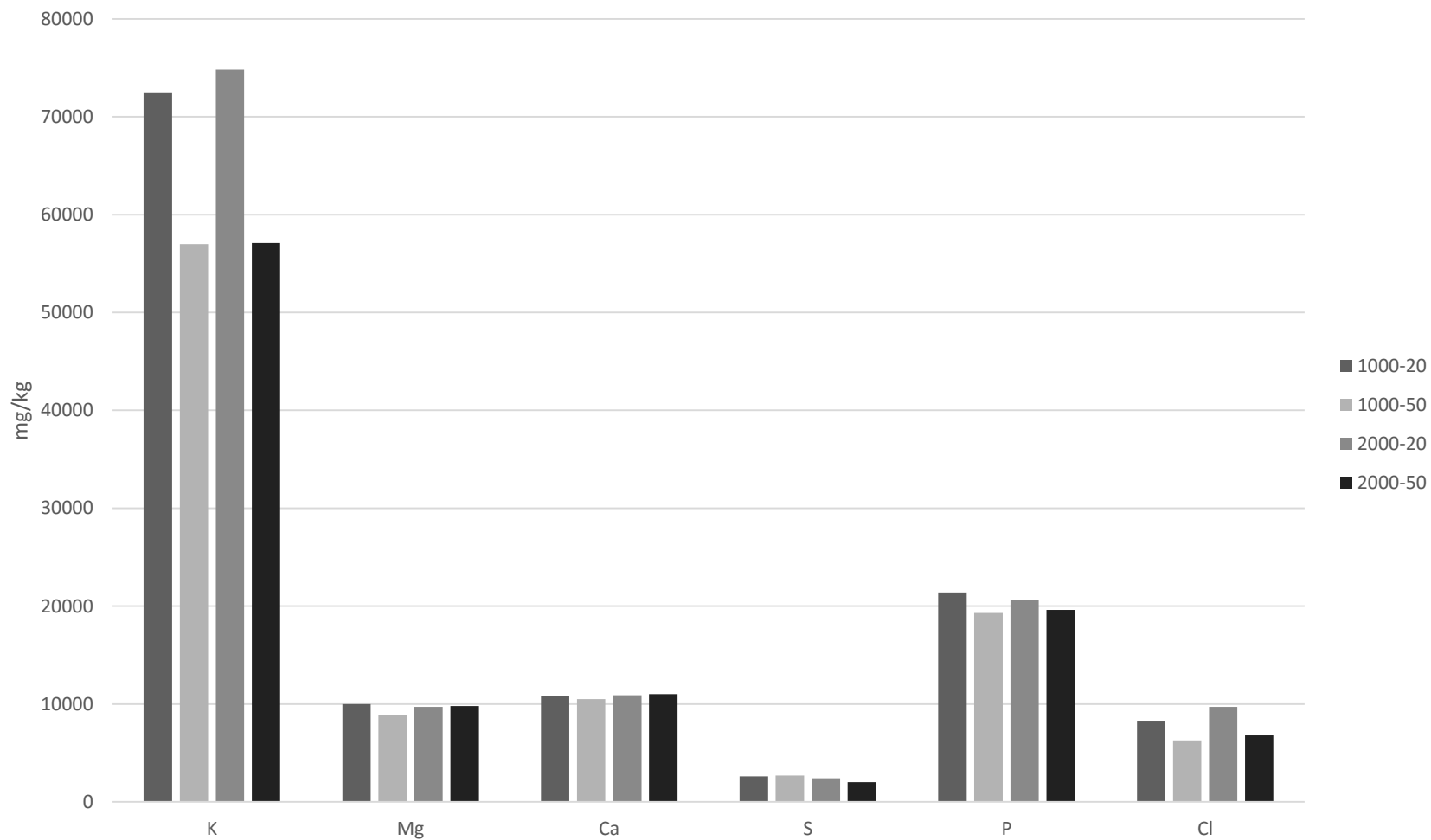


Figure 6-6: Inorganic content of torrefied, leached type B biomass, measured by XRF spectrometry

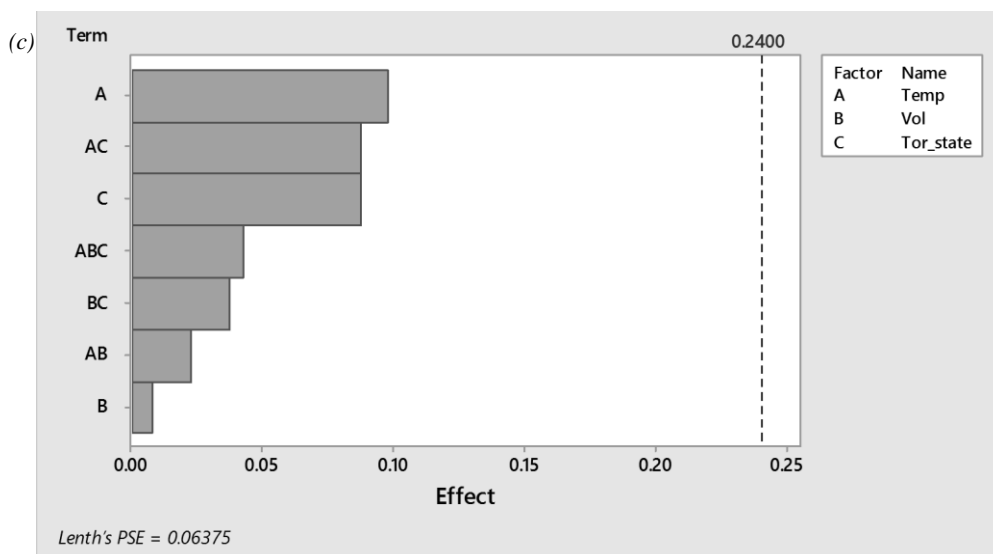
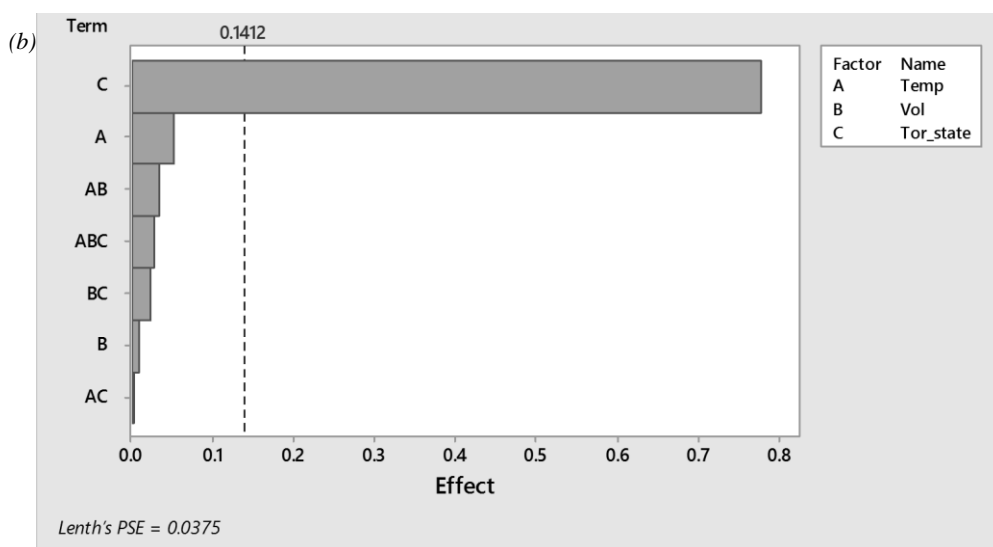
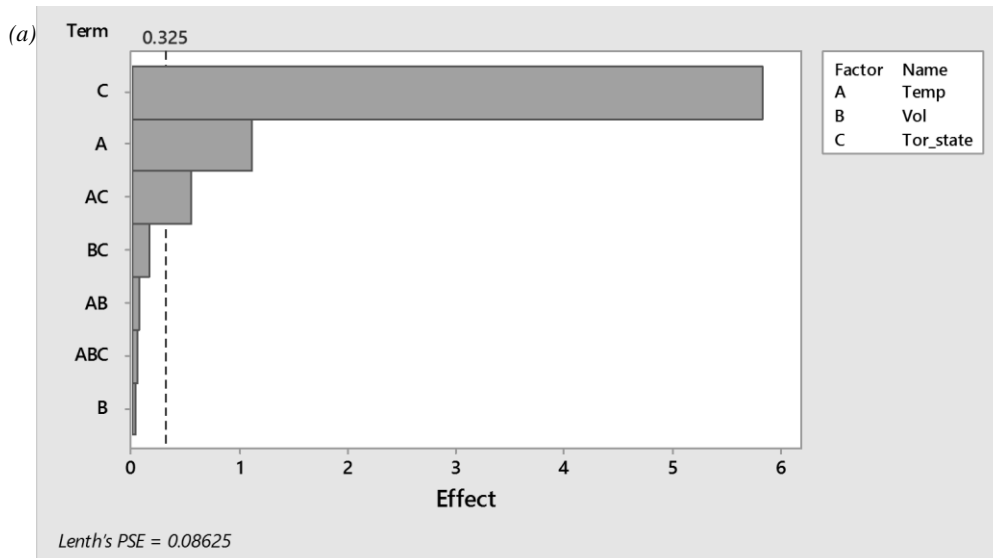


Figure 6-7: Pareto charts of XRF-measured (a) K, (b) Mg, (c) Ca.

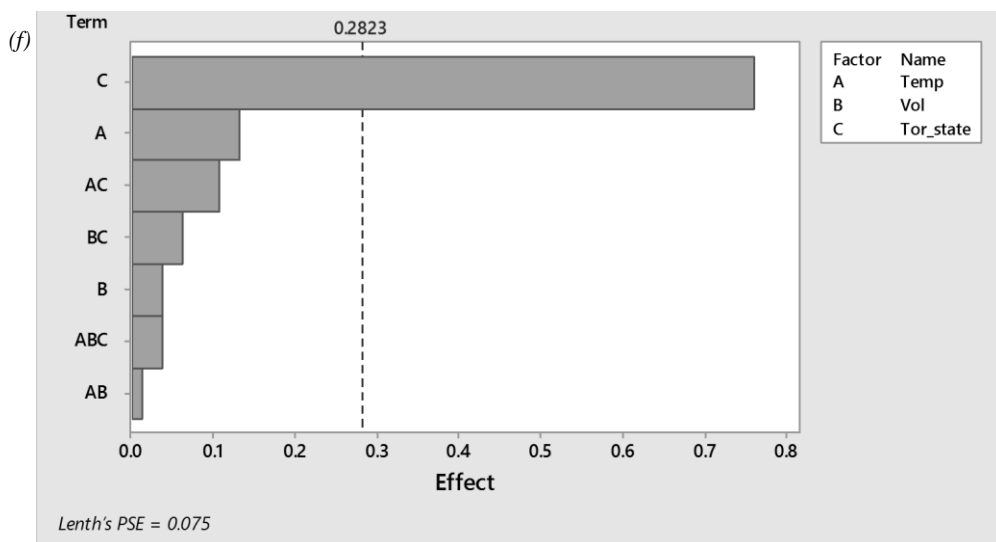
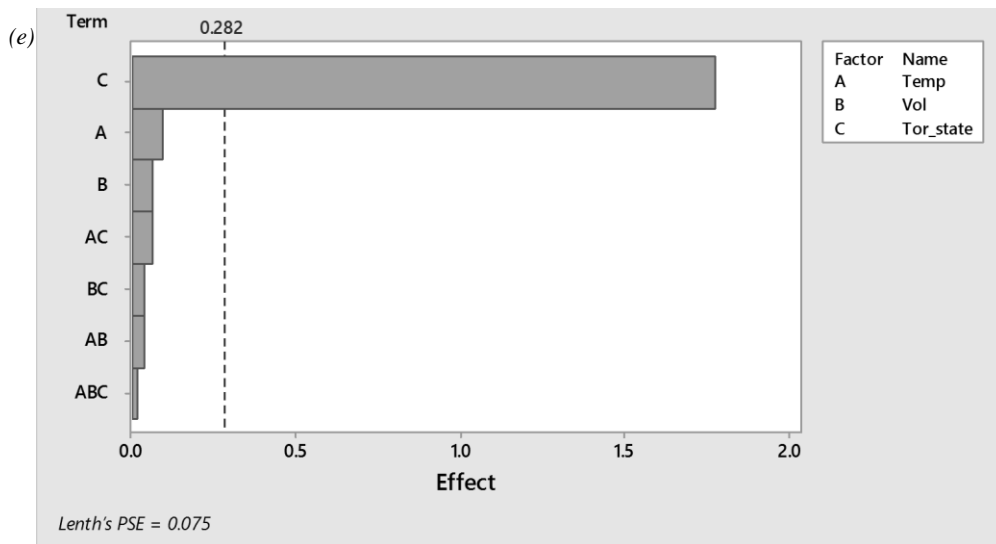
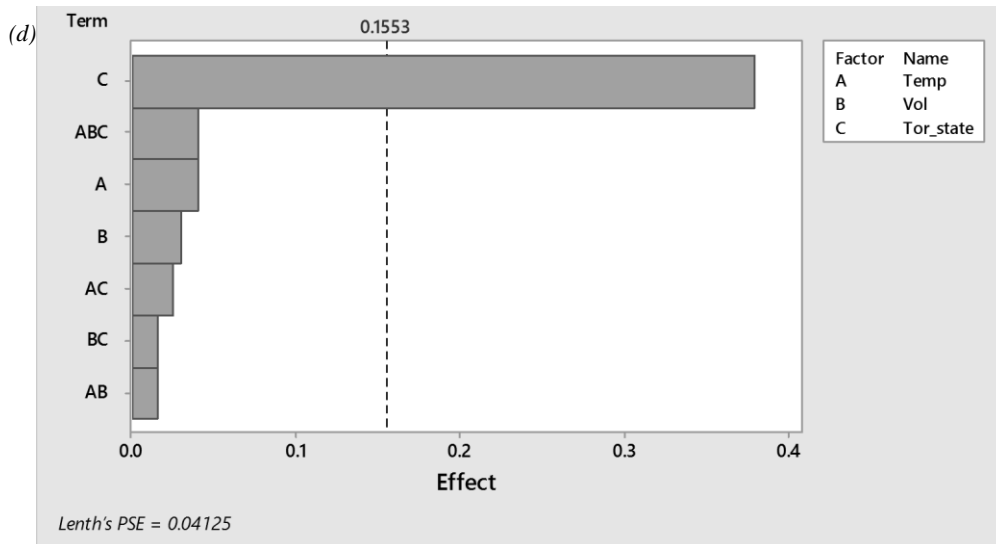


Figure 6-7 (contd.): Pareto charts of XRF-measured (d) S, (e) P, (f) Cl.

Table 6-2: Significance of factors and interactions obtained from Pareto charts.

Element	Significant factors and interactions
K	Temperature, torrefaction state, interaction between temperature and torrefaction state.
Mg	Torrefaction state.
Ca	None.
S	Torrefaction state.
P	Torrefaction state.
Cl	Torrefaction state.

From Table 6-2, it can be seen that with the exception of Ca, the torrefaction state is a common significant factor. For K, the leaching temperature and torrefaction state are both significant factors. Additionally, the interaction between these two factors is also significant in the case of K, i.e. how the K content varies with the leaching temperature is dependent on whether it is torrefied.

6.2.3 Summary of preliminary results

The main aim of the preliminary study was to identify the most significant factors which can then be explored in more detail in the primary study. Considering Table 6-1 and Table 6-2, it can be seen that the leaching temperature and torrefaction state are broadly the most significant factors affecting the leaching process. This was corroborated by both methods; the only exception was the Cl content measured by the ICP-MS/IC method, which was also affected by the leaching volume.

The trends in the inorganic content as measured by the two approaches are broadly similar. However, their corresponding absolute values vary significantly. The ICP-MS/IC method has consistently lower measurements compared to the XRF method. This can be attributed to the potentially incomplete digestion (for ICP-MS) or ion extraction (for IC) of the samples prior to analysis. This step introduces an additional possibility for experimental error. In contrast, XRF spectrometry is a non-destructive method which eliminates this preparatory step and hence the error associated with it.

This, coupled with the faster overall analysis speed, made XRF spectrometry the preferred solid inorganic analysis method for the rest of the study. However, the results from the ICP-MS/IC approach provided additional confirmation of the trends in the measured inorganic content of the leached biomass.

6.3 Primary leaching study

The major leaching study involved the type B seed cake. Two factors were varied, the leaching temperature of the water and the torrefaction state. The three leaching temperatures used were 20°C, 35°C and 50°C. There were four torrefaction states – untorrefied (“UT”), and samples torrefied at temperatures of 200, 250 and 300 °C for a period of 30 min each (“LT”, “MT” and “HT”, respectively). For each of the 12 points in the full-factorial matrix (excluding the unleached samples), three replicate runs were carried out, resulting in a total of 36 leached samples. The leaching was carried out in batches of 12 for each leaching temperature. An additional run with identical conditions, but with no biomass added was also carried out for each temperature as a control.

6.3.1 Physical appearance

The leachate samples of the UT and mildly torrefied (LT) runs have a more cloudy appearance since the oily nature of the seed cake is reduced following the more intense torrefaction treatments. The solutions become darker as the torrefaction temperature is increased up to 250°C, and this matches the increasing darkness of the solid seed cake. The exception is the HT leachate, which is almost transparent. This indicates that the most intensely torrefied biomass might be resistant to leaching. There is no apparent change in the colour of the seed cake following the leaching process. However, the leached seed cakes have a harder and less oily texture compared to the corresponding

unleached samples, with a reduced tendency to clump up (this was especially true of the untorrefied type B samples).

6.3.2 Electrical conductivity (EC)

Figure 6-8 shows the variation of the EC during the course of leaching of type B seed cake. Since EC of a solution is a function of the concentration of ions in it and can be measured instantly using an EC meter, it provides a useful method of monitoring the progress of the leaching process with time. Additionally, since EC is also a function of the solution temperature, the EC meter was set to automatically calibrate all measurements to those of a solution at 25°C. The mean EC has been calculated from the three simultaneous replicate runs for each point. The mean EC for the final 3 h are approximately constant. Thus, it can be assumed that by this time, the leaching process is complete.

The distinguishing feature of the graph is the separation between the sample types, i.e. torrefaction level. The final EC of the HT runs are the lowest, followed by that of the MT runs. There is a degree of overlap between the LT and UT runs. The observed trends indicate that increasing the torrefaction intensity makes the biomass more resistant to the leaching process. This is also reflected in the initial gradients of the curves, which are indicative of the rate at which the ions are leached out of the seed cake. The lowest gradient is in the HT samples, followed by the MT samples. Again, there is some overlap between the LT and UT samples.

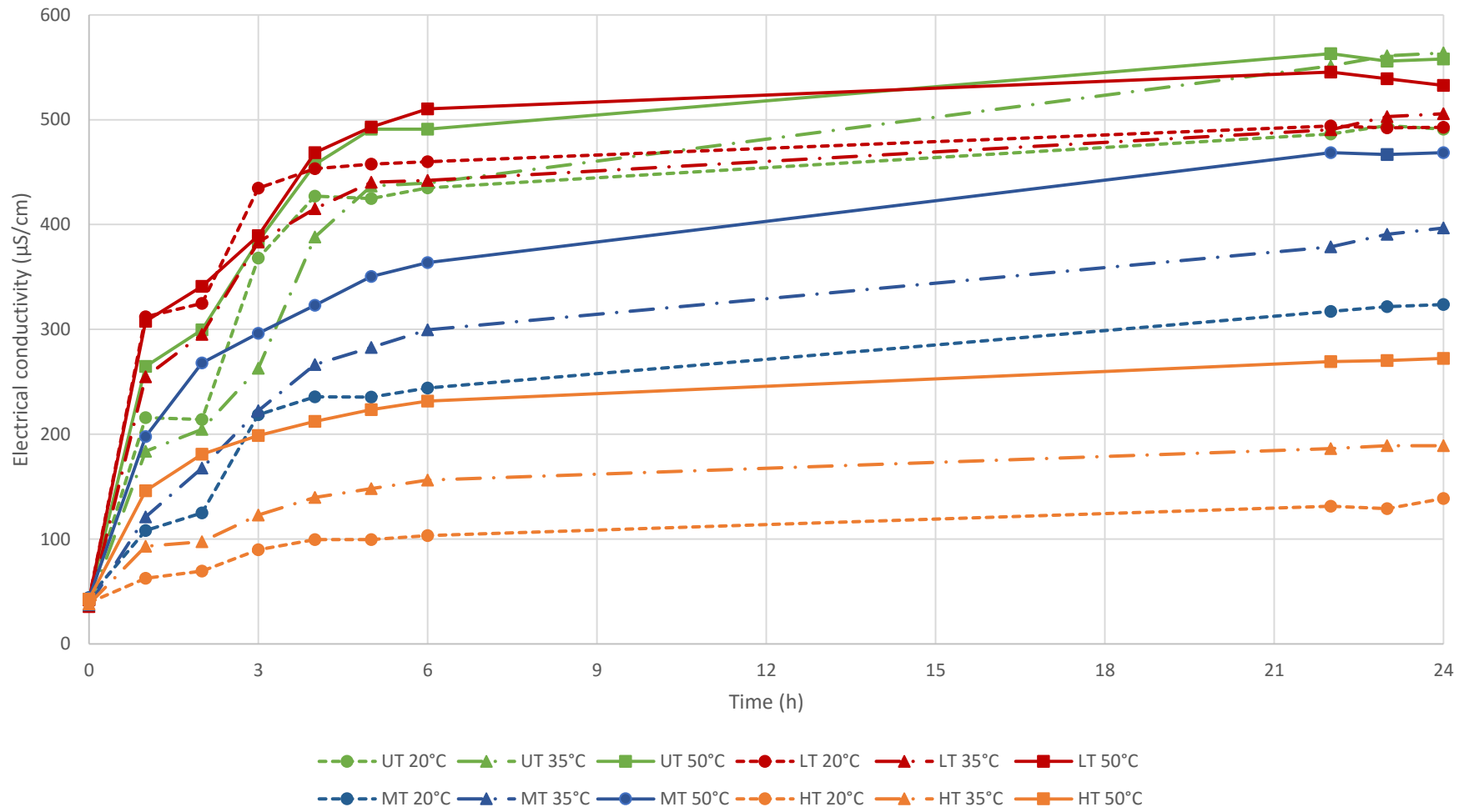


Figure 6-8: Progression of mean EC with time

When looking at the effect of the leaching temperature, in general there is an increase in the leaching rate as well as the final EC. However, the effect of the temperature appears to be highly dependent on the torrefaction state. The separation of the respective curves is significantly greater for the HT and MT samples. Increasing the leaching temperature is much more effective in increasing the leachability of the more intensely torrefied samples.

To illustrate these trends more clearly, the final EC after 24 h and the initial leaching rate were plotted in Figure 6-9 and Figure 6-10, respectively. The leaching rate is the average rate calculated over the first 6 h of leaching, assuming a linear rate for the purposes of comparison. There is no significant effect of increasing the leaching temperature in UT and LT samples, especially considering the overlap of the error bars. In the MT samples however, the final EC increases by 45% while the 6 h leaching rate increases by 61%, when the leaching temperature is increased from 20°C to 50°C. For the HT samples, the hikes are even more substantial at 96% and 191%, respectively. This enhancing of the leachability of the more intensely-torrefied material is potentially a very useful observation since it is these samples that proved most resistant to the leaching process.

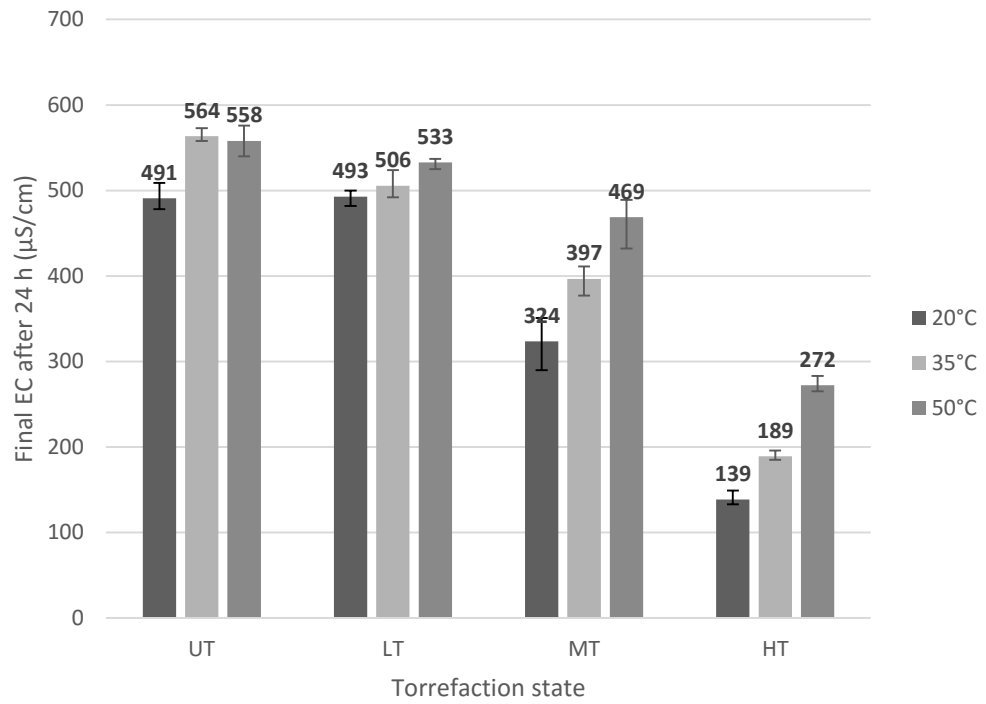


Figure 6-9: Final EC after 24 h (type B).

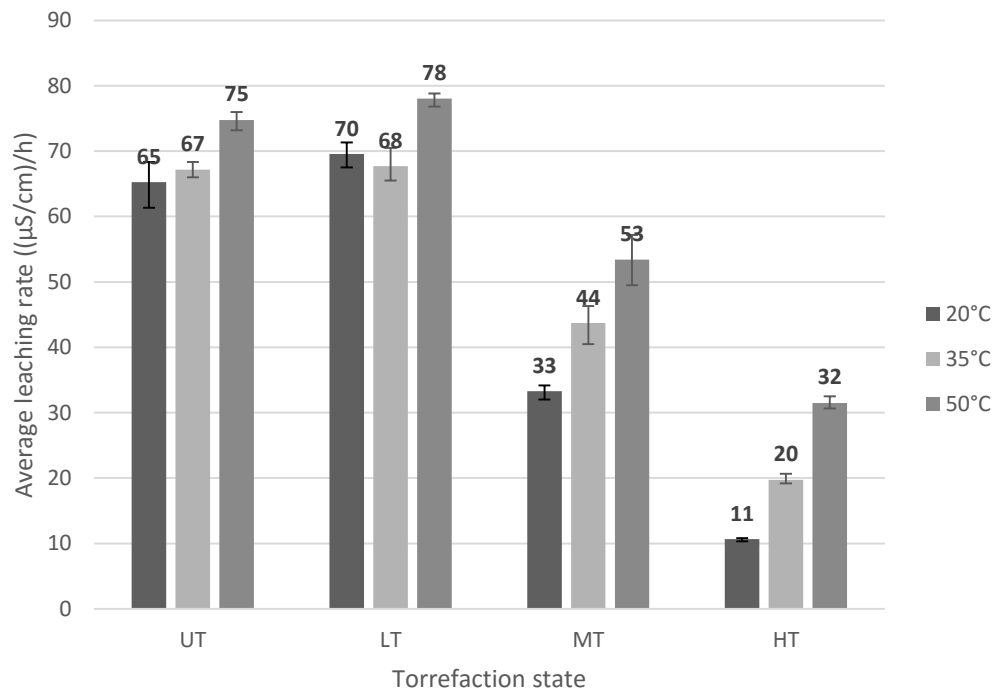


Figure 6-10: Average leaching rate of type B biomass.

6.3.3 Ion analysis of leachate

Figure 6-11 shows the final concentration of the major cations and anions present in the leachate as measured by ICP-MS and IC, respectively. The ions in question are K, Cl, magnesium (Mg) and phosphate (PO_4). The illustrated values are those obtained after subtracting the corresponding concentrations in the control sample which had no biomass added. The EC of the solution is superimposed; this value is the difference between the EC after 24 h and the initial EC. Although not exact, a correlation can be observed as expected between the total ion concentration and the EC.

From Figure 6-11, a clear positive trend can be observed in the effect of the leaching temperature on the K levels in the type B leachate. Once again, the torrefaction state plays a role in this correlation. When the leaching temperature is increased from 20°C to 50°C, the K levels in the UT and LT samples increase by 10.2% and 15.1%, respectively. For the MT sample, the increase is a more substantial 33.6%. However, for the HT sample, the increase is 164.3%, i.e. more than doubled. Since the most prominent ion present in the leachate by a significant margin is K, the trends observed in the total ion levels are comparable to those of K.

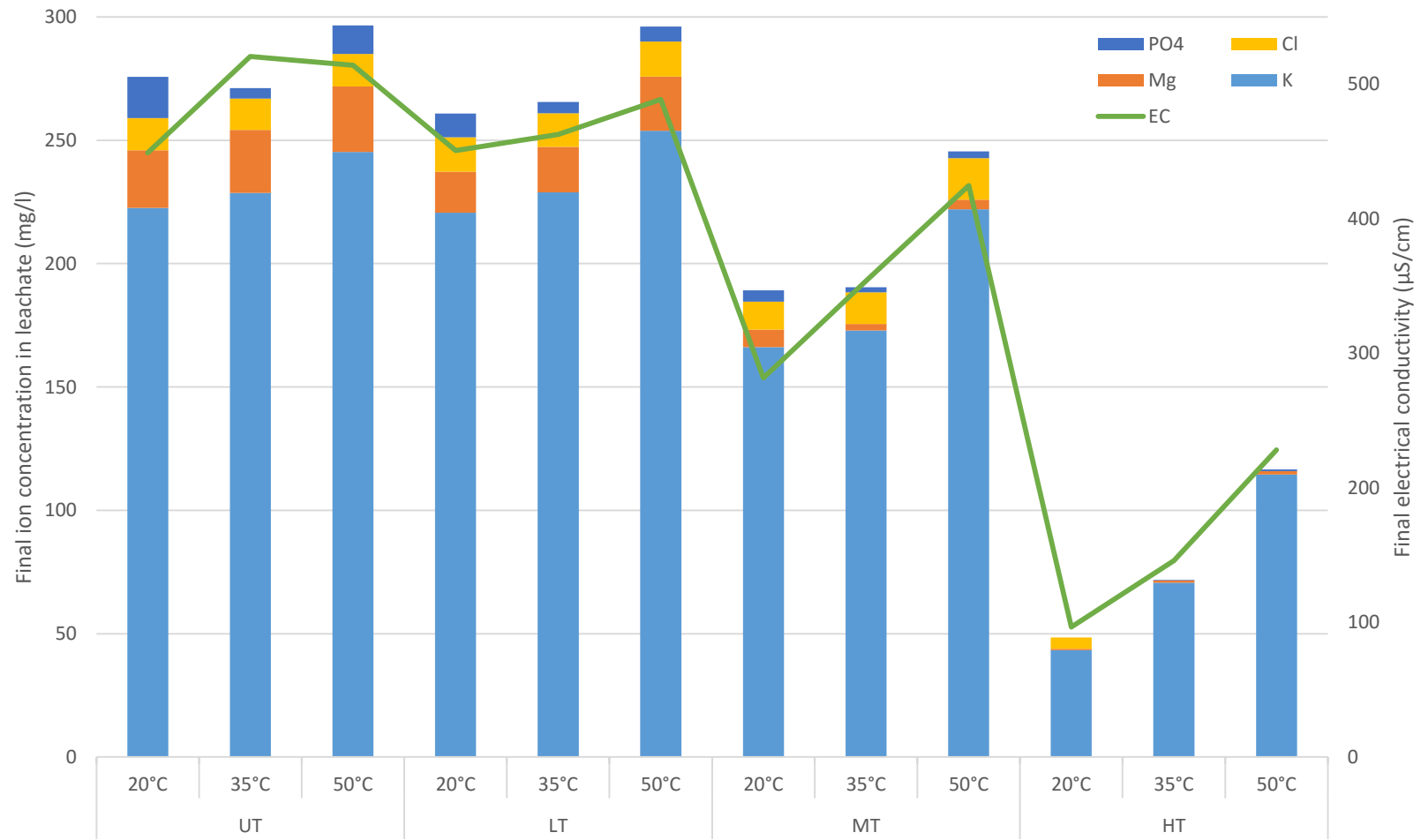


Figure 6-11: Net ion concentration and EC after 24 h (type B).

6.3.4 Inorganic content - XRF

Figure 6-12 shows the elemental inorganic composition of the solid biomass, both before and after leaching. These are the mean levels of the most abundant inorganic elements measured using XRF spectroscopy –K, Ca, Mg, Cl, S and phosphorous (P). The mean values for the unleached biomass was calculated from the replicate torrefaction runs, while those for the leached biomass was from the replicate leaching runs. The sum of the values of these elements is shown next to each column on the chart. The dry ash content obtained from TGA has been superimposed on the graph as well to illustrate the expected correlation between the inorganic content and the ash content.

The XRF results of the type B corroborate the previous observation that the more intensely torrefied biomass is more resistant to the leaching process. For instance, following leaching at 35°C, the sum of the inorganics (the numerical values displayed in the figure) decreases by 71% and 66% for the UT and LT samples, respectively. The decrease is 34% for the MT sample while the decrease is only by 7.5% in the case of the HT sample. These figure illustrate a substantial increase observed in the inorganic levels as higher temperatures are used for the torrefaction. This can be attributed to the correspondingly decreasing mass yield as more volatiles are lost during the torrefaction process; the overall mass of the sample decreases while there is minimal loss in the inorganic content, resulting in an increase in the percentage weight of the inorganic elements.

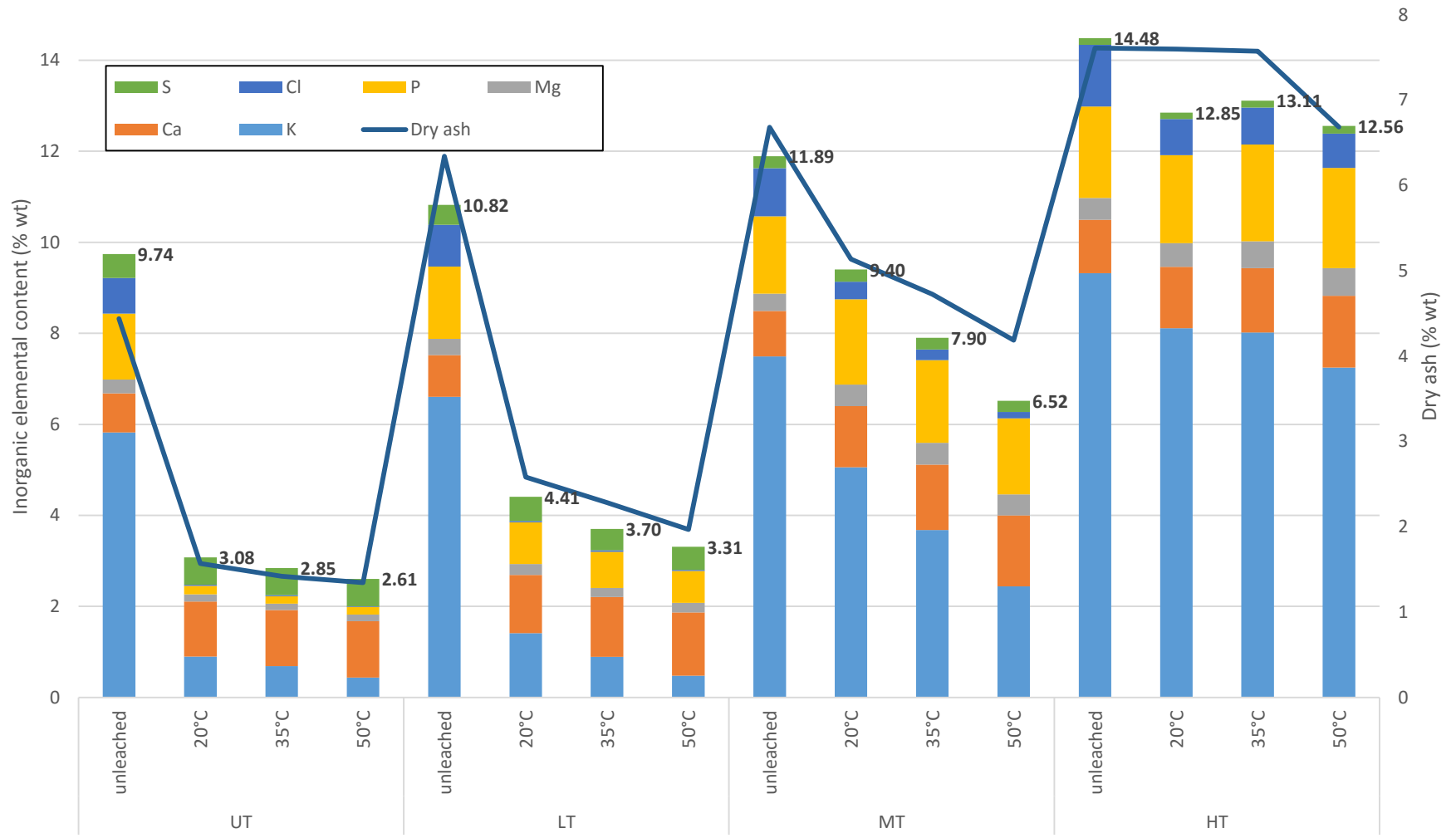


Figure 6-12: Total inorganic content from XRF for leached and unleached type B

To obtain a more rigorous analysis of the XRF data, a statistical analysis was carried out using Minitab 17. A low p-value (<0.05) for a particular variable indicates that the variable in question has a statistically significant effect on the response. This would be reflected in the main effects plot as a non-parallel line – the higher the effect, the steeper the line. A low p-value for the interaction indicates that there is a statistically significant interaction between the two variables, i.e. the effect of the leaching state on the response (for instance, the K content) is affected by the torrefaction state. This is graphically illustrated in the interaction plot. The stronger the interaction, the more the lines deviate from being parallel to each other. If there is a statistically significant interaction, this interaction should be taken into account when interpreting the main effects. Typically, the main effects plots and p-value are meaningful only if the interaction is negligible (interaction $p > 0.05$).

Figure 6-13 show the main effects plots and interaction plots (whichever is relevant) for the XRF data generated by Minitab for type B. Table 6-3 shows the p-values obtained from the analysis of variance (ANOVA) carried out by the software. Throughout the Minitab analysis, the variable “LeachState” shows the leaching temperature in degrees Celsius or “UL” if unleached, while “TorrState” refers to the temperature in degrees Celsius at which the sample has been torrefied (all at 30 min holding time) or “UT” if untorrefied.

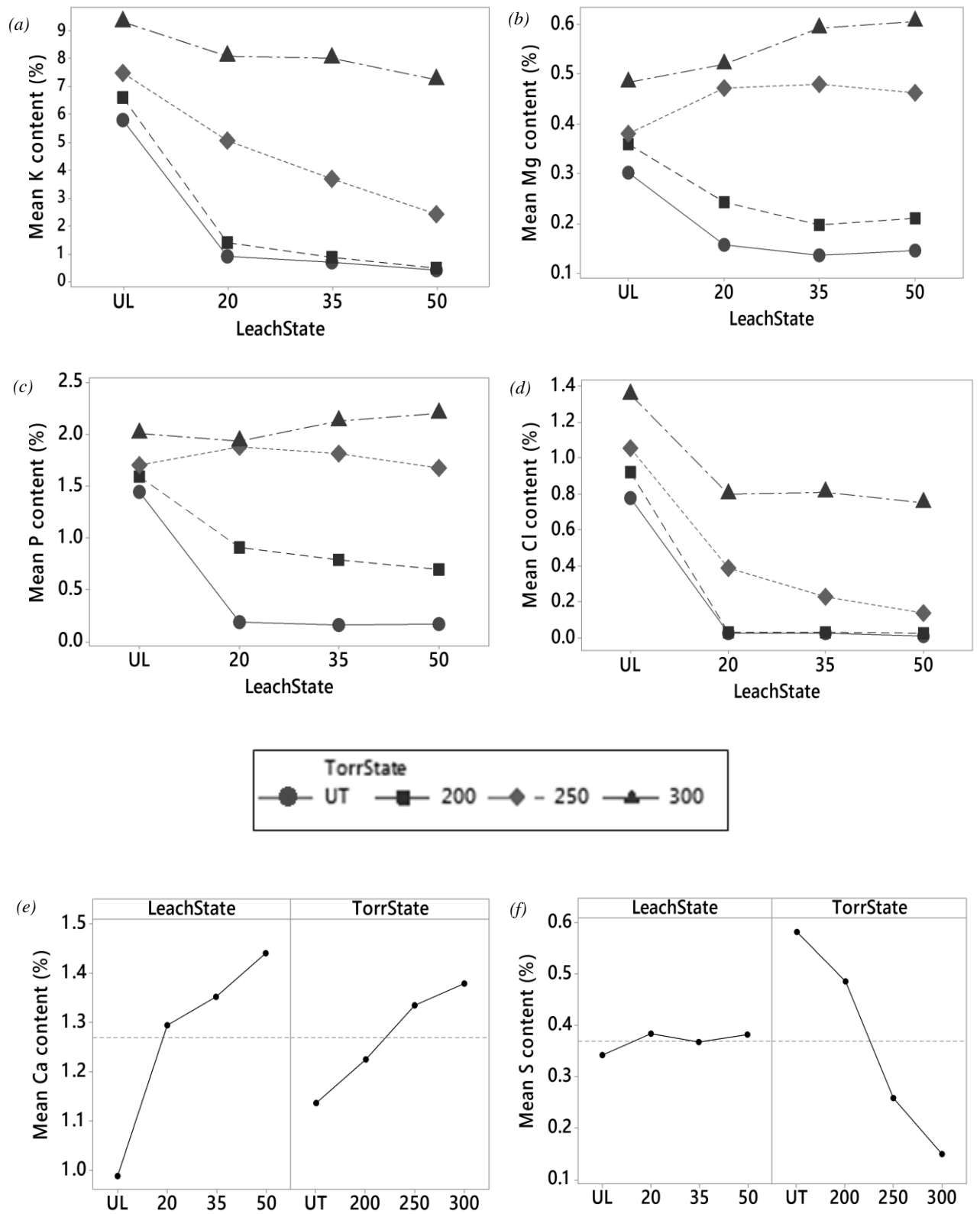


Figure 6-13: Factorial plots for XRF content of type B (a) K interaction, (b) Mg interaction, (c) P interaction, (d) Cl interaction, (e) Ca main effects and (f) S main effects.

Table 6-3: p-values from ANOVA of type B XRF data

	Type B (unleached and leached)			Type B (leached)		
	LeachState	TorrState	Interaction	LeachState	TorrState	Interaction
K	0.000	0.000	0.000	0.000	0.000	0.000
Ca	0.000	0.000	0.168	0.001	0.000	0.394
Mg	0.015	0.000	0.000	0.748	0.000	0.007
P	0.000	0.000	0.000	0.420	0.000	0.001
Cl	0.000	0.000	0.000	0.000	0.000	0.000
S	0.004	0.000	0.053	0.345	0.000	0.347

For K, Mg, P and Cl, there is a highly significant interaction between the variables, meaning that the samples torrefied at different temperatures react to the leaching in different ways where these elements are concerned. When examining the interaction plots for these elements, it can be seen that the UT and mildly torrefied (LT) seed cake undergo a larger decrease in the levels of these elements following the leaching process.

The relative ease of leaching of K and Cl from the untorrefied *Jatropha* is consistent with results from leaching studies conducted on other types of biomass – wheat straw (Deng et al., 2013), rice straw (Jenkins et al., 1995; Deng et al., 2013; Yu et al., 2014), olive-derived biomass (Vamvuka et al., 2008), grassland herbage (Tonn et al., 2011), switchgrass (Ravichandran et al., 2013). The extent to which these elements are removed by leaching is related to the mode in which they occur in the structure of the biomass. K is typically found as K⁺ ions which are either dissolved in water present in the plant tissue or organically bound (Zevenhoven et al., 2012). Cl is also found as free Cl⁻ ions or as part of organic compounds (Deng et al., 2013). The high water-leachability of K and Cl from the untorrefied *Jatropha* suggests that these

elements are present as simple ions which readily dissolve in water. The decrease in their extraction as the torrefaction intensity is increased indicates that the structural changes occurring in the biomass during the torrefaction process has an effect on the mode of occurrence of K and Cl within the biomass structure, causing the free ions to be bound more rigidly to the organic compounds. It follows that a higher energy input would be required to break these bonds, hence the enhancement of the leachability of the torrefied biomass that was observed at higher water temperatures.

When examining the interaction plots for Mg and P, it can be seen that the UT and mildly torrefied (LT) seed cake undergo a decrease in the levels of these elements following the leaching process; the Mg content undergoes a slight increase and the P content remains approximately unchanged in the highly-torrefied (MT and HT) biomass. The irregularities in the Mg content can be attributed to inhomogeneity and measurement uncertainty introduced by the instrument, compounded by the very low levels detected (less than 0.6% wt). While the measured P content does not exceed 2.5% wt, the levels fall to <0.25% wt and <1% wt in the untreated and LT samples, respectively; there is no appreciable effect of increasing the leaching water temperature. P in biomass can occur as soluble phosphate salts or as P-containing organic molecules (Zevenhoven et al., 2012). The results suggest that they occur as the former in the untreated *Jatropha* seed cake, but undergoes a transformation to the latter during the torrefaction process. Since even the high-temperature leaching (which was effective in the case of the K content) did not reduce the P content of the torrefied biomass, it appears that the P atoms become more rigidly bonded to the organic molecules than the K atoms. Owing to the fact that P can occur in both water-soluble and water-insoluble forms in biomass, there is a wide range of P leachability that is

reported in the literature, from as much as >50% (Zhang et al., 2015) to non-detectable (Said et al., 2013) and even slightly increased levels (Carrillo et al., 2014).

Since the interaction is statistically insignificant for Ca and S, the main effects plots are considered here. The Ca levels show a clear increase following leaching. The S levels show an increase as well, although the trend is more irregular in this case. The low p-values ($p < 0.05$) also reflect this. Since the leaching process cannot increase the levels of any element, the conclusion derived from these observations is that there is a very high degree of inhomogeneity in the Ca and S levels (more so than the other major inorganic elements) throughout the type B seed cake. The problem is aggravated by the fact that the measured quantities of these elements are relatively low (less than 1.5%), which increases the uncertainty of the measurement.

To analyse the effect of the leaching temperature more closely, the statistical analysis was repeated with the data for the unleached samples omitted. The Ca and S concentrations were not considered since it was shown previously that the observations are too irregular. From the p-values shown in Table 6-3, it can be seen that the rest of the inorganic elements – K, Mg, P and Cl – show a statistically significant interaction. The efficacy of the leaching is represented by the gradient of the lines in the interaction plots (Figure 5-13); a steeper negative gradient implies a greater fall in the concentration of that element as the leaching temperature is increased.

Mg and P show irregular trends but with small positive/negative gradients, indicating that although the torrefaction intensity causes the biomass to behave differently (a statistically significant difference) as the leaching temperature increases, the measured absolute quantities are still too low to ascertain any practical effect of increasing the leaching temperature. Looking at the plots for K and Cl, it can be seen

that for the torrefied and mildly torrefied (LT) seed cake, there is no appreciable effect of using higher leaching temperatures; leaching at 20°C appears to be sufficient. For the MT seed cake, there is a more profound effect; a linear drop of the K level is observed as the water temperature is increased. For the HT seed cake, the drop is only observed after 35°C. This indicates that as far as K and Cl are concerned, a higher torrefaction temperature increases the resistance of the biomass to leaching, and consequently, a higher leaching temperature is required.

6.3.5 Dry ash free volatile matter (DAF VM) content and higher heating value (HHV)

Figure 6-14 show the main effects plot and the interaction plot for the DAF VM content of type B. The p-value for the interaction is 0.032; looking at the interaction plot, it can be seen that there is a marked difference between the behaviour of the UT and torrefied seed cake. The torrefied samples all show irregular behaviour, while the UT case shows an appreciable decrease in the DAF VM. The leaching process would be expected to remove some of volatiles from the seed cake, which is what is observed in the UT samples. However, torrefaction (even mildly) appears to reduce the leachability of the volatiles. A possible explanation is that the light volatiles that are driven off in the torrefaction process are the ones that are more readily soluble in water and are hence removed from the UT biomass during leaching. The volatiles that are left following torrefaction process are heavier and are either insoluble in water or adsorbed onto the structure of the biomass, and are thus impervious to the leaching process.

The relationship between the DAF VM content and the higher heating value (HHV) has been demonstrated in literature. A decreasing DAF VM content corresponds to an increasing DAF fixed carbon (FC) content as the volatiles lost

contain less carbon (C) atoms than hydrogen (H) and oxygen (O) atoms. This leads to a reduction in the H/C and O/C ratios, and since C-H and C-O bond energies are weaker than those of C-C, the calorific value increases (McKendry, 2002b; Narvaez & Orio, 1996). This relationship is reflected in the factorial plot for the HHV of the leached samples, shown in Figure 6-15. A p-value of 0.004 indicates a statistically significant interaction and this is illustrated in the interaction plot by the non-parallel lines. The highly-torrefied seed cake shows an irregular trend, while the UT case shows a clear increase in the HHV after the sample is leached. As explained earlier, this agrees with the trends observed in the DAF VM content. The mean HHV increases from 24.06 MJ/kg to 25.32 MJ/kg (by 5%) and 26.47 MJ/kg (by 10%) after leaching at 20°C and 50°C, respectively.

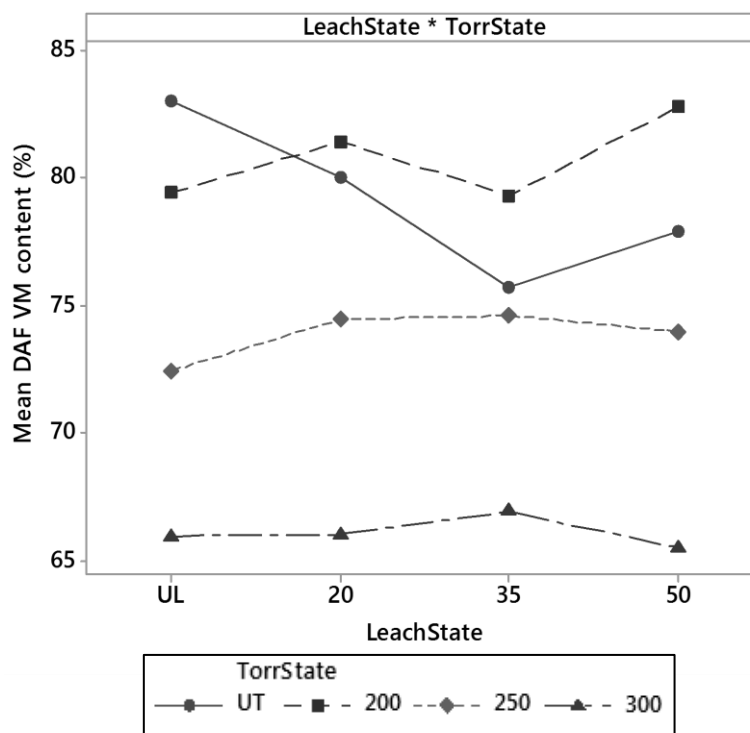


Figure 6-14: Interaction plot of type B DAF VM content.

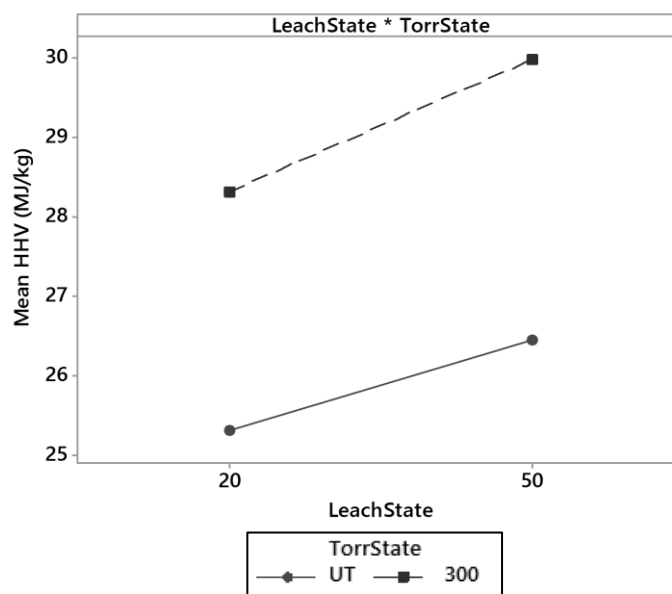


Figure 6-15: Interaction plot of type B HHV.

6.4 Secondary leaching study

A smaller study was carried out on the type A seed cake. Here, only untorrefied samples were leached at a temperature of 35°C and the variation was in the particle size fraction. Two particle size fractions were used – <1 mm (“fine”) and 1–2.36 mm (“medium”). Again, the runs were triplicated for a total of 6 runs.

Figure 6-16 shows the inorganic content of the solid biomass, with the sum of the measured inorganic content shown on top of each column. Comparing the two categories of type A, the effect of particle size can be determined; the smaller particles undergo a decrease of 80% compared to the 77% reduction in the larger particle size. Although the magnitude of the difference is not substantial, this would be the expected direction of change since the larger particle size would have less overall surface area exposed to the water for the same mass of seed cake. Type B sees a decrease by an even smaller 71% after leaching at 35°C. A possible explanation for this is that the oil content of the type B seed cake interferes with the mechanism by which the ions leave the structure of the biomass.

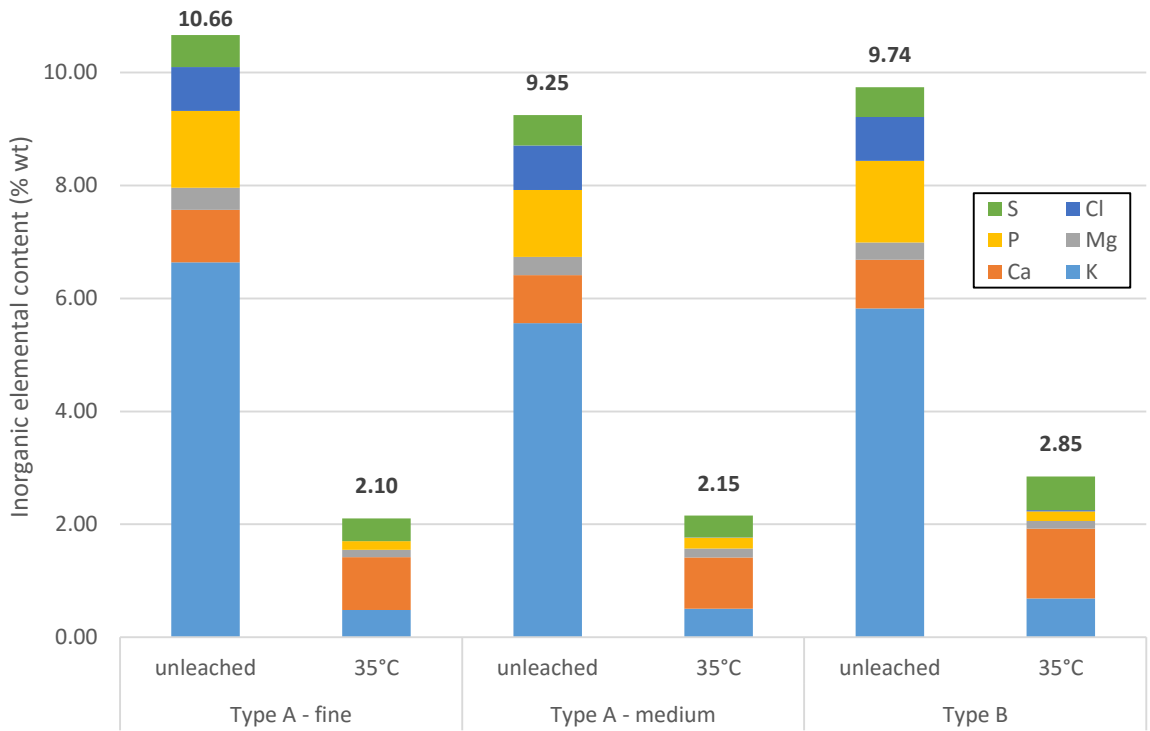


Figure 6-16: Inorganic content from XRF (untorrefied type A and type B)

Table 6-4 shows the p-values obtained from the ANOVA of the type A data. From the p-values, it can be seen that there is a significant interaction between the factors for all elements except Cl. In other words, the different types of seed cake respond differently to the leaching, with respect to the levels of these elements.

Table 6-4: p-values from ANOVA of type A XRF data

	Type	LeachState	Interaction
K	0.000	0.000	0.000
Ca	0.011	0.003	0.005
Mg	0.038	0.000	0.004
P	0.000	0.000	0.000
Cl	0.910	0.000	0.920
S	0.000	0.000	0.000

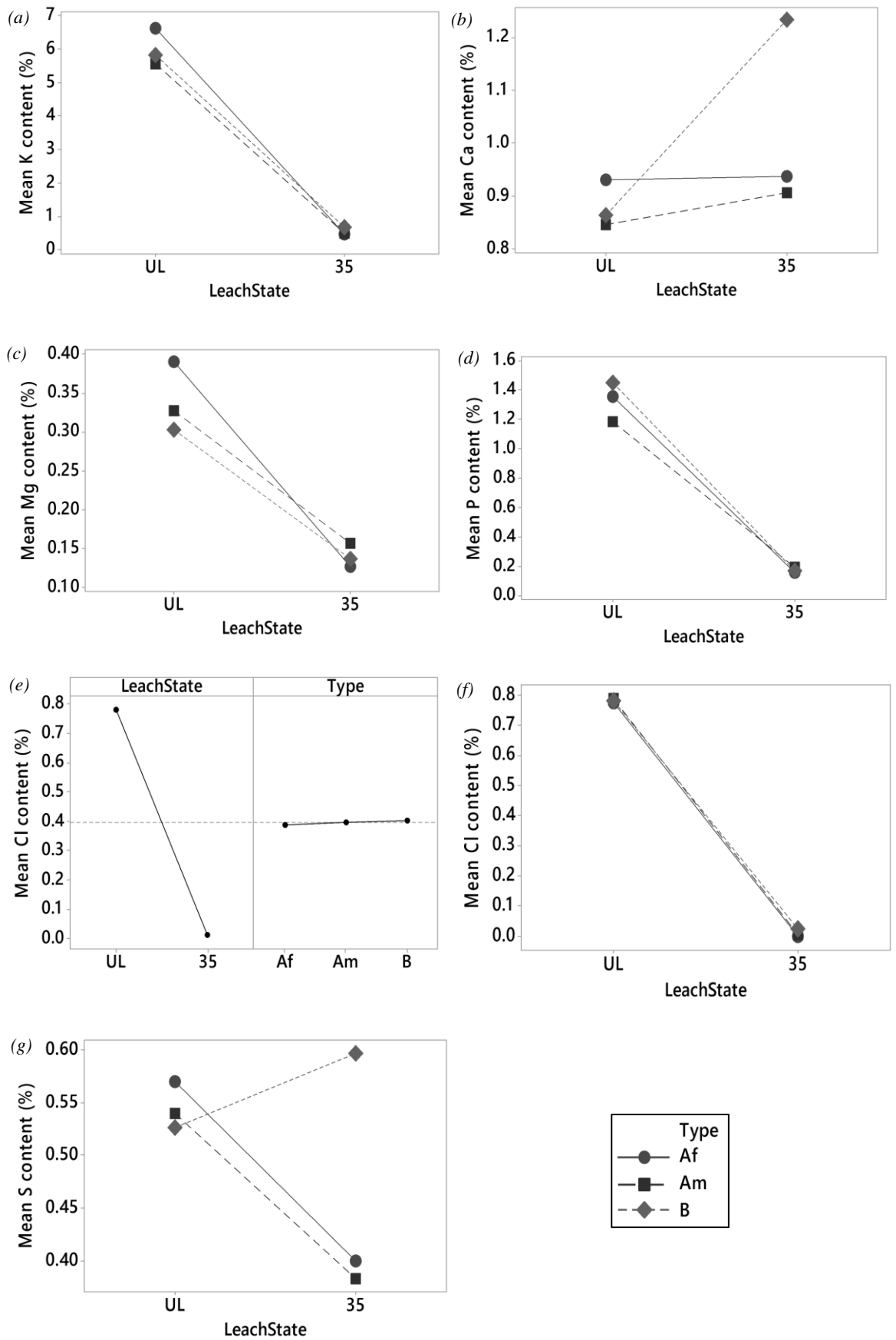


Figure 6-17: Factorial plots for XRF content of type A (a) K interaction, (b) Ca interaction, (c) Mg interaction, (d) P interaction, (e) Cl main effects, (f) Cl interaction and (g) S interaction.

The nature of this variation can be seen by examining the interaction plots in Figure 6-17, where a steeper gradient indicates a greater change in the level of the element after leaching. K, Mg, P and Cl see falling levels during leaching, in all three types of seed cake. The type A (fine) undergoes a greater decrease in the K, Mg and P content compared to the type A (medium). All 3 types of seed cake show a similar response to leaching where Cl is concerned, as reflected in the high p-value for the interaction ($p = 0.920 > 0.05$) and the “type” variable ($p = 0.910 > 0.05$); this is also illustrated in the parallel lines in the interaction plot and the near-horizontal line in the “type” main effects plot. Irregular trends are observed in the S and Ca content (with the Ca content even appearing to increase) and these are attributed to the inhomogeneity in the biomass and uncertainty of the instrument when measuring small quantities.

6.5 Discussion

The major drawbacks of biomass firing include deposit formation and corrosion, and these are direct consequences of the high inorganic content of biomass. There are two modes of deposit formation – slagging and fouling – and both deposits are composed of the sulphates, chlorides, hydroxides and silicates of alkali and alkaline earth metals. Slagging is caused by molten ashes in the high-temperature radiative sections of the boiler, while fouling is caused by ash deposits formed during cooling in the lower-temperature convective sections (Bryers, 1996; Savolainen, 2003; Teixeira et al., 2012). K and Cl have been considered in previous studies to be the critical inorganic elements which are responsible for ash deposit formation and corrosion (Hansen & Nielsen, 2000; Sander, 1997; Wieck-Hansen et al., 2000; Yin et al., 2008). Nielsen et al. (2000) proposed several mechanisms by which Cl is responsible for corrosion in combustion systems, including those involving gaseous Cl species, Cl species in solid deposits and Cl species in the molten state. It was

observed that the presence of K aggravates the corrosion problem since K species are part of certain reaction mechanisms related to corrosion.

Of the inorganic elements investigated, K and Cl show a definite decrease following leaching. This is consistent with the results from leaching studies conducted on other types of biomass – rice straw (Jenkins et al., 1995), banagrass (Turn et al., 1997), olive-derived biomass (Vamvuka et al., 2008), grassland herbage (Tonn et al., 2011). At 20°C, the K and Cl content of the untorrefied type B *Jatropha* biomass decreased by 85% and 97%, respectively. K is the dominant inorganic component of *Jatropha* seed cake, and hence its reduction is a vital outcome of the leaching process. In the case of the untorrefied biomass, the K content is reduced to less than 1 wt%, while Cl is reduced to approximately 0.02 wt%. In comparison, the K and Cl range of typical coals is 0.01-0.09 wt% and 0.01-0.03 wt%, respectively (Oleschko et al., 2007). The leaching process is hence effective in bringing down the levels of these crucial inorganic elements in the untorrefied biomass closer to those of coal. This implies that leached *Jatropha* seed cake could be co-fired with coal without a significant increase in the possibility of slagging, fouling or corrosion.

The increase in the HHV that was observed was not one of the primary aims behind leaching; instead, torrefaction is the pre-treatment process that aims to enhance the HHV. However, the mild increase in HHV following leaching is a welcome secondary benefit, since a higher HHV is a desirable characteristic for a biofuel. Enhancement of the HHV following leaching has been reported previously as well (Said et al., 2013; Yu et al., 2014). Although the higher HHV following leaching is advantageous, it should be noted that it is at the cost of the total energy content of the biomass, as some organic content is being lost via the leachate. Quantification of the relative energy loss is beyond the scope of this study, but is suggested as an area for

future investigations. Relative energy losses ranging from 1% to 28% have been reported in the literature, with increasing leaching temperature having a detrimental effect on the loss value (Deng et al., 2013).

In the UT type B samples, the K content decreased from 0.90 wt% to 0.69 wt% when the leaching temperature was increased from 20°C to 35°C, a reduction of only 0.21 wt%. Increasing the leaching temperature to 50°C caused a further reduction in the K content by 0.25 wt%. A similar minute decrease was observed in the LT samples. However, the MT samples saw a more substantial reduction of 1.38 wt% and 2.62 wt% when the temperature was increased from 20°C to 35°C and 50°C, respectively. These figures are significant when considering that the difference between the unleached and 20°C-leached samples is only 2.44 wt%, compared to 4.92 wt% and 5.19 wt% in the case of the UT and LT samples, respectively. Leaching at room temperature is hence adequate in the case of untoasted or mildly toasted samples. More intensely-toasted seed cake sees an appreciable benefit from higher leaching temperatures.

In the HT type B samples however, the K content decreases by only 0.09 wt% when the temperature is increased from 20°C to 35°C, and by a further 0.86 wt% when increased to 50°C. This trend indicates that at this degree of toasting, a much higher water temperature would be required to cause any appreciable leaching. Although further experimental work can be done to ascertain this, using very high water temperatures have negative practical implications such as controlling evaporation and a higher energy expenditure to maintain the temperature for extended periods of time.

The inorganic content of the untreated type A seed cake was higher than that of the untreated type B. However, after leaching at the median temperature of 35°C, the total inorganic content of the type A falls to lower than that of the type B. Comparing the

two particle size fractions, K, Mg and P showed an improvement in leachability when the particle size was smaller. However, the change in the overall inorganic content is not substantially larger with the finer particles. Since the initial (unleached) inorganic levels of the finer size fraction was higher, the inorganic composition of the two leached type A size fractions appear to be similar. Hence, using a finer particle size merely for the purpose of improving leachability of the type A biomass would not be justified. The higher leachability of the type A vis-à-vis the type B at 35°C also suggests that leaching at 20°C would be sufficient for the untorrefied type A seed cake, irrespective of the particle size (for particles <2.36 mm).

6.6 Concluding remarks

This study is that of the second stage of a two-step pre-treatment process, the first stage being torrefaction. Invariably, the optimum leaching parameters cannot be recommended without reference to the corresponding torrefaction parameters; the final form of the fuel is the culmination of the optimisation of both processes. The torrefaction study carried out on the type B seed cake determined an envelope of optimum torrefaction parameters, i.e. torrefaction temperature and holding time – for a holding time of 30 min, the optimum torrefaction temperature was approximately 240-250°C (see Section 5.4).

These conditions correspond to the MT samples in the present study. As discussed earlier in this section, a leaching temperature of 50°C can be recommended for these samples since it would offer a significant increase in leaching efficiency over lower temperatures – 67% of K was leached out compared to 51% at 35°C and 32% at 20°C. For this combination of torrefaction and leaching conditions, the leaching process has plateaued before 22 h with respect to the EC readings (Figure 6-8). However, 75% of the leaching has occurred by the end of the 6th hour. A more narrowed-down study,

which is beyond the scope of the current work can be conducted in future with more regular intermediate EC readings to optimise the leaching time. Consideration of the energy costs of keeping the leaching water at 50°C by exploring options such as solar heating is also suggested.

7 COMBUSTION MODELLING

7.1 Introduction

The fundamental aim of this research work is to ascertain the suitability of pre-treated *Jatropha curcas* seed cake for co-firing. Combustion of solid fuels is a complex process. This is even more so when two fuels, i.e. biomass and coal, are fired together. The fundamental differences between biomass and coal in properties such as reactivity, HHV, proximate and ultimate analysis, and particle characteristics can have a profound effect on their combustion characteristics. This is further compounded by the possibility of interaction effects between the two fuels.

This section of the study focused on the use of CFD as a tool to analyse the behaviour of *Jatropha curcas* seed cake when co-fired with a typical bituminous coal. Figure 7-1 shows the overall workflow followed for the combustion modelling study. The CFD model was developed in Ansys Fluent 14.0 (ANSYS Inc., 2011b) for a drop tube furnace (DTF), and DTF runs are used to validate the model (Section 7.4). The accuracy of the model depends on the model inputs; although the fundamental fuel characteristics could be measured, there are several uncertainties in the model inputs resulting from limited experimental data and the lack of such data in the literature (as *Jatropha curcas* seed cake is still a novel source of energy). The model was adapted to fit the DTF data. However, these limitations mean that the extraction of detailed quantitative data cannot be justified. Hence, the objective of this study would be to analyse the effect of torrefaction and co-firing from a qualitative/semi-quantitative standpoint, and establish an understanding of the mechanisms.

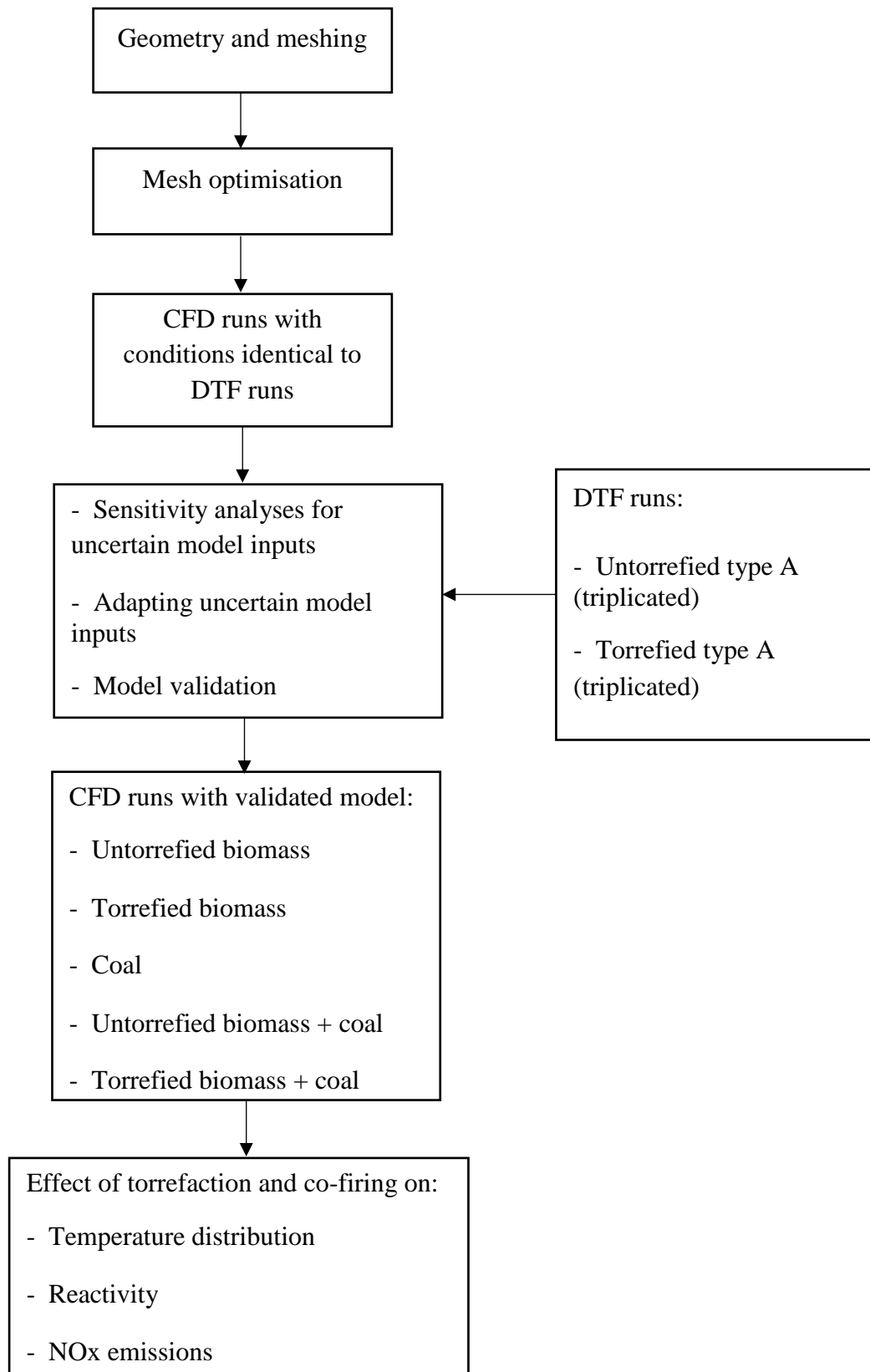


Figure 7-1: Overall workflow for combustion modelling study

7.2 Geometry and meshing

A 2D axi-symmetric mesh was used for the CFD modelling. A 2D mesh in axi-symmetric mode cuts down on computational time compared to a full 3D mesh. Since the domain is truly axi-symmetric, 2D modelling of a “slice” of this cylinder is sufficient as this can then be rotated around the axis. Figure 7-2 (Sarroza et al., 2014) shows the section of the DTF that is represented in the mesh (marked out by the dashed line). Table 7-1 gives a summary of the fundamental settings and dimensions of the DTF, while a detailed methodology of the DTF operation is discussed in Chapter 3 (Section 3.5).

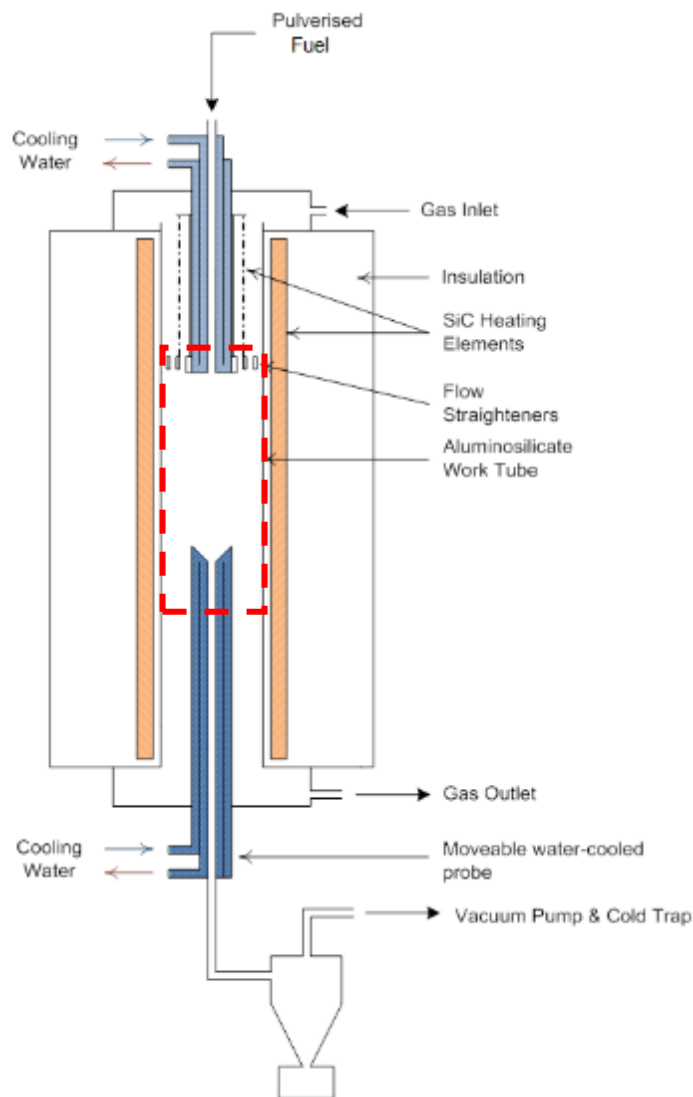


Figure 7-2: Schematic of DTF, showing the volume that is modelled (Sarroza et al., 2014).

Table 7-1: Summary of fundamental DTF settings and dimensions

Target temperature	1300°C
Carrier gas flow rate	1 l/min
Main gas flow rate	11.1 l/min N ₂ + 1.2 l/min O ₂
Feeder probe diameter	3 mm
Collector probe diameter	15 mm
Probe separation*	0.22 m
Work tube diameter	50 mm

*Distance between exit of feeder probe and inlet of collector probe, i.e. shortest distance travelled by particle between the two probes.

The initial geometry was created in Ansys DesignModeler, as shown in Figure 7-3.

A combination of rectangular sketches were used to generate a 2D surface.

Ansys Meshing was then used to generate the mesh from the geometry. The “mapped meshing” and “fixed advanced sizing” features were used to obtain a grid of uniformly-sized quadrilateral faces (Figure 7-4). This method was chosen to minimise the orthogonal skew and maximise the orthogonal quality. These two mesh statistics are indicators of a high-quality mesh (ANSYS Inc., 2011b). A summary of the boundary conditions is shown in Table 7-2, while the names of the boundaries are shown in Figure 7-4.

Table 7-2: Summary of boundary conditions used.

air_in	Mass flow inlet; 2.35×10^{-4} kg/s; 1300°C
fuel_in	Mass flow inlet; 1.94×10^{-5} kg/s; 20°C
air_out	Wall; 30°C *
fuel_out	Outflow
inlet_wall	Wall; 1300°C
collector_wall	Wall; 30°C
furnace_wall	Wall; 1300°C
symmetry	Axis

* Wall assumption made since this outlet is blocked and all outflow is through the collector probe.

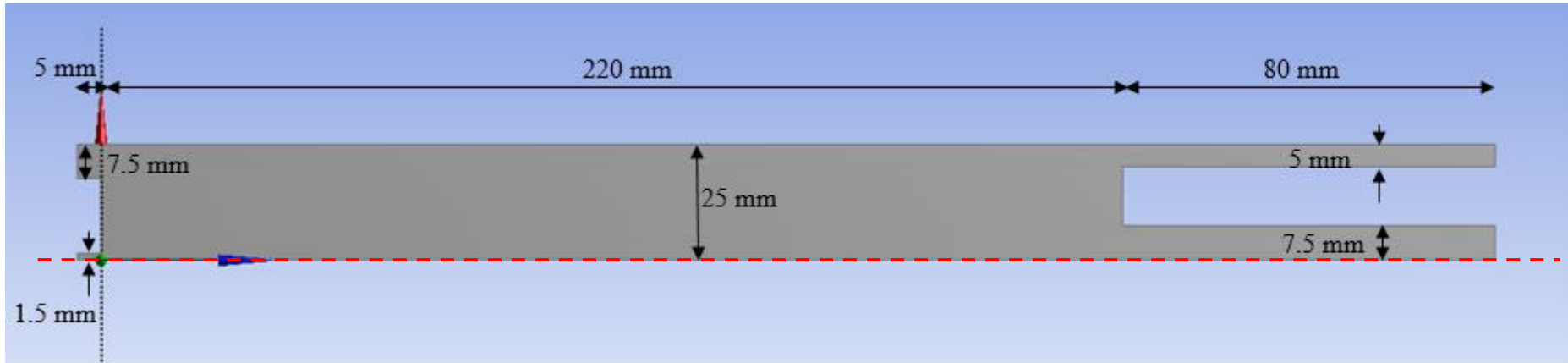


Figure 7-3: Geometry created in Ansys DesignModeler.

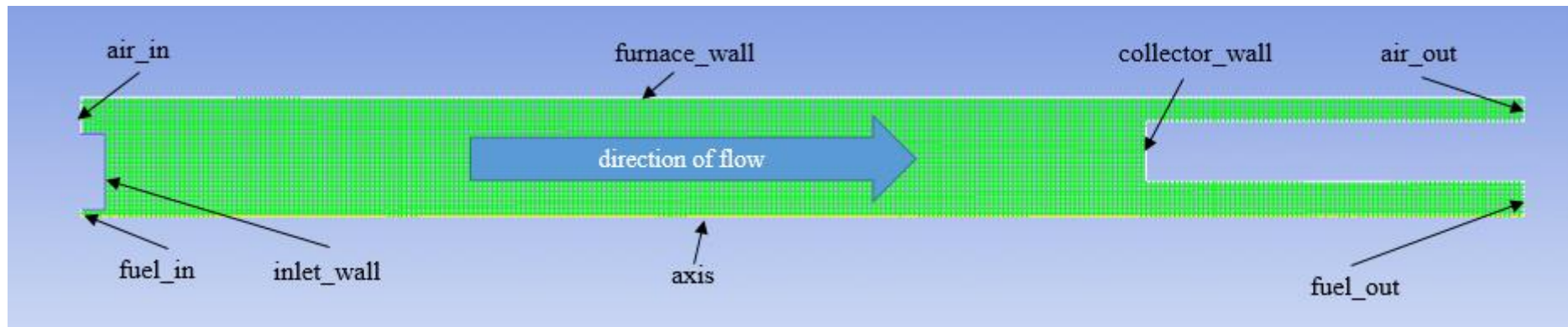


Figure 7-4: Generated mesh (mesh no. 3) showing boundary names and flow direction.

7.2.1 Mesh optimisation

A mesh-independence study was carried out to ascertain that the mesh size (how fine the mesh is) does not have a significant effect on the results, and to determine the optimum mesh size. By varying the maximum face size, six meshes were generated, as shown in Table 7-3. This table also shows the minimum orthogonal quality and the maximum orthogonal skewness of the generated meshes obtained from the “mesh statistics” feature, the former being closer to 1 and the latter being closer to 0 indicates a mesh with good quality (ANSYS Inc., 2011b).

Table 7-3: Mesh properties

Mesh no.	1	2	3	4	5	6
Max. face size (mm)	1.5	1.25	1.0	0.5	0.4	0.3
No. of cells	2791	4188	6810	26180	41349	72296
No. of particle streams	1	1	2	3	4	5
Min. orthogonal quality	0.950	1.00	1.00	1.00	0.992	0.998
Max. orthogonal skew	0.202	1.30×10^{-3}	8.63×10^{-3}	1.31×10^{-10}	8.47×10^{-3}	2.14×10^{-3}

An identical case was run on all six meshes, and three measured outputs (monitors) were chosen for comparison – the temperature integrals at two x-positions along the mesh (0.15 m and 0.25 m), and the particle volatile matter conversion (Figure 7-5). The volatile matter conversion (VMC) is particularly important since it is used to validate the model against empirical data from the DTF (Section 7.4.1). Also, there was some concern that the number of particle streams could have an effect on the VMC; since a surface injection is used (Section 7.3.3) the number of particle streams is dependent on the number of faces on the injection surface, and this varies with the mesh density (Table 7-3).

Excluding the coarsest mesh, a reasonable level of mesh-independence was seen. The maximum variation among the VMC and the temperature integrals were 4.2% and 1.4%, respectively. It is also noteworthy that although the variation of the monitors was small, the number of cells in the mesh (and hence the computational cost) increases exponentially as the maximum face size is decreased (Figure 7-6). The computational cost was measured using the average time per iteration reported by Fluent; a PC with an Intel Core-i5 3.1 GHz processor and 4GB of RAM was used for the CFD work. Taking into consideration these factors, mesh 3 was chosen to be used for the rest of the study.

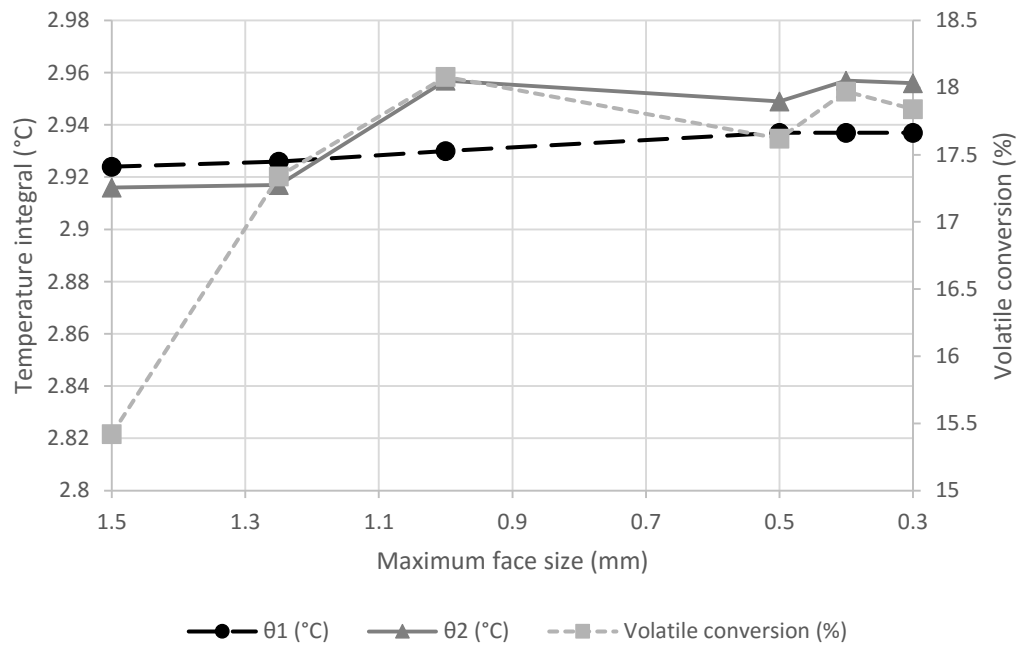


Figure 7-5: Variation of monitors with maximum face size

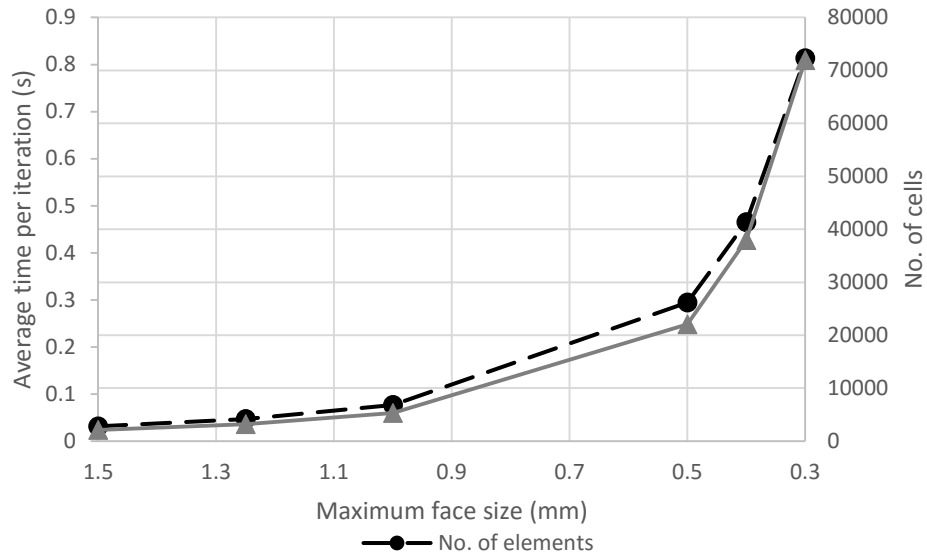


Figure 7-6: Variation of no. of cells and average time per iteration with maximum face size.

7.3 Sub-models

The combustion process inside the DTF was modelled as a two-phase flow. The continuous phase (or fluid phase) consists of the gases inside the work tube, i.e. the primary (N₂) and secondary (N₂ and O₂ mixture) inlet flows, volatiles evolved, reaction intermediates and products. The discrete phase (or solid phase) consists of the solid fuel (biomass and/or coal) particles. Fluent uses an Euler-Lagrangian approach, where the continuous phase is modelled using Navier-Stokes equations and the discrete phase is modelled by tracking the particles through the flow field. The system was modelled as steady state, since the DTF setup aims to achieve a steady, laminar-regime flow with minimum fluctuations. Table 7-4 summarises the sub-models used and the key parameters for each sub-model. Unless specified, the default parameters have been used.

7.3.1 Turbulence

The most commonly-used approach to modelling turbulence in co-firing applications is the $k-\epsilon$ model and its two variants, i.e. RNG and realisable (Tabet & Gökalp, 2015; Wang & Yan, 2008). The realisable $k-\epsilon$ model was implemented in this

case, since this model has been favoured in recent studies due to its pragmatic compromise between accuracy and computational demand, and better solution convergence (Black et al., 2013; Li et al., 2009; Park et al., 2015a; Rezeau et al., 2012).

7.3.2 Chemistry and turbulence-chemistry interaction

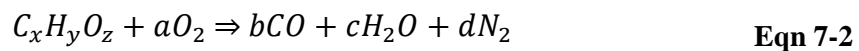
The chemistry model to be used is dependent on the turbulence-chemistry interaction model. The turbulence-chemistry interaction was modelled using the Eddy-Dissipation model (EDM) (Magnussen & Hjertager, 1977). EDM is a commonly-used interaction models for biomass combustion studies, and is appropriate for one-step or two-step reaction chemistries. The EDM assumes that reaction rates are limited by turbulent mixing (as is the case with fast-burning fuels) and hence avoids computationally-expensive Arrhenius chemical kinetics calculations.

The volumetric combustion chemistry, i.e. the reactions occurring in the gaseous phase, was modelled using the Species Transport model. This model involves solving conservation equations for each chemical species, i . Equation 7-1 is the general form of the conservation equation:

$$\frac{\partial}{\partial t}(\rho Y_i) + \nabla \cdot (\rho \vec{v} Y_i) = -\nabla \cdot \vec{J}_i + R_i + S_i \quad \text{Eqn 7-1}$$

where Y_i is the local mass fraction of a species i , S_i is its rate of addition from the dispersed phase and J_i is its diffusion flux (modelled by Fick's Law). R_i is the net rate of production of i by chemical reaction, and is calculated by the EDM (ANSYS Inc., 2011a).

A two-step mechanism was used for the gaseous phase reaction, as follows:



Hence, the volatiles in the gaseous phase (which are represented by $C_xH_yO_z$) undergo oxidation via an intermediate CO species.

The Coal Calculator is a tool available within Fluent. The proximate and ultimate analyses (measured by the TGA and CHON analyser respectively), the HHV (measured by the bomb calorimeter) and the desired reaction mechanism (two-step) are entered into the calculator. Fluent then uses this data to calculate and set the relevant input parameters for the Species Transport and Discrete Phase (Sections 7.3.2 and 7.3.3) models for each case.

7.3.3 Discrete phase

The Discrete Phase Model (DPM) treats the fuel particles using a Lagrangian approach. The DPM calculates the particles' motion through the continuous phase, as well as their heat and mass exchange with the continuous phase. The particle injections were defined as shown in Table 7-4. A surface injection from the fuel inlet was specified; a particle stream is emitted from each face on this surface. The velocity magnitude was calculated from the carrier gas flow rate (2.36 m/s), and the average flow rate was calculated from the time taken to feed a measured quantity of sample. The continuous and discrete phase calculations were coupled, i.e. the discrete phase affects the continuous phase (two-way coupling), with 10 continuous phase iterations being performed for every DPM iteration. This number was chosen by trial and error, based on solution convergence and stability.

7.3.3.1 Particle motion

The particle trajectory is governed by the following force balance:

$$\frac{du_p}{dt} = F_D(u - u_p) + \frac{g_x(\rho_p - \rho)}{\rho_p} \quad \text{Eqn 7-4}$$

where u_p is the particle component velocity, u is the fluid velocity, F_D is the drag force, g_x is the gravitational force component, ρ_p is the particle density and ρ is the fluid density. The drag force is calculated by:

$$F_D = \frac{18\mu C_D Re}{\rho_p d_p^2} \frac{1}{24} \quad \text{Eqn 7-5}$$

where μ is the fluid viscosity, d_p is the particle diameter, C_D is the drag coefficient and Re is the Reynold's number. The drag coefficient is calculated using the non-spherical drag law developed by Haider & Levenspiel (1989). This model uses a shape factor to account for non-spherical nature of the particle. The shape factor is the ratio of the surface area of a sphere having the same volume of the particle, to the actual surface area of the particle.

7.3.3.2 Particle heat and mass exchange

For the case of a combusting particle, the heat and mass exchange of the particle are governed by four laws, which are activated in succession:

Inert heating

This models the heating of the particle until it reaches its vaporisation temperature. A simple heat balance is used to calculate the particle temperature by taking into account the convective and radiative heat transfer.

Devolatilisation

The devolatilisation of the particle was modelled in this case by the single first-order reaction:

$$-\frac{dm_p}{dt} = k[m_p - (1 - f_{v,0})m_{p,0}] \quad \text{Eqn 7-6}$$

where m_p is the particle mass, $m_{p,0}$ is the initial particle mass, and $f_{v,0}$ is the initial volatile fraction. k is the rate constant, which is given by:

$$k = Ae^{\frac{-E}{RT}} \quad \text{Eqn 7-7}$$

where A is the pre-exponential factor, E is the activation energy, R is the universal gas constant, and T is the particle temperature. The kinetic parameters A and E were calculated from TGA runs (using the method detailed in Section 3.4.1.2) and entered into the model. The values of A and E are given in Table 7-6.

Surface combustion

Surface combustion of the char is initiated after complete devolatilisation has taken place. A simple diffusion-limited model was used in this case, since accurate surface combustion kinetics were not available. The diffusion-limited model has been used in previous biomass co-firing studies (Yin et al., 2004; Yin et al., 2010). Complete devolatilisation was not expected in the present case due to the low particle residence time in the DTF. Hence, accurate modelling of the char combustion was not considered vital.

Inert cooling

This is similar to the inert heating law, in that the heat balance is used to calculate the particle temperature after complete devolatilisation.

7.3.4 Radiation

The discrete ordinates (DO) model was used to model the radiative heat transfer. This is a widely-used radiation model in biomass combustion and co-firing studies (Álvarez et al., 2014; Bonafacic et al., 2015; Gubba et al., 2012; Stroh et al., 2015). The DO model solves the radiative transfer equation for a number of discrete solid angles (angular discretisation). Each solid angle is associated with a vector direction

fixed in the global Cartesian coordinate system. The radiative transfer equation accounts for the absorption, emitting and scattering of radiation in the different direction vectors (ANSYS Inc., 2011a).

7.3.5 NO_x

The formation of NO was modelled by using the Thermal model. This mechanism is temperature dependent and calculates the NO formed from the cracking of atmospheric N₂ at very high temperatures. It is based on the following equilibrium reactions:



Other NO formation models that are available include the Prompt NO model and the Fuel NO model. However, these were not activated since they require inputs which were not known for this case and would introduce further uncertainty. For instance, the Fuel NO model requires the ratio to which the N content was split with the volatiles and the char.

Table 7-4: Summary of models and model parameters used

Viscous (Turbulence)	
Model	Realisable k-epsilon
Near-wall treatment	Standard wall functions
C2-Epsilon	1.9
TKE Prandtl number	1
TDR Prandtl number	1.2
Energy Prandtl number	0.85
Wall prandtl number	0.85
Turbulent Schmidt number	0.7
Species (Chemistry)	
Model	Species transport
Reactions	Volumetric
Turbulence-Chemistry interaction	Eddy-dissipation
DPM	
Particle treatment	Steady state
No. of continuous phase iterations per DPM iteration	10
Injection type	Surface (fuel_in)
Particle type	Combusting
Material	Varies with case
Diameter distribution	Uniform
Diameter	Varies with case
Temperature	300 K
Velocity magnitude	2.36 m/s
Total flow rate	1.2×10^{-4} kg/s
Turbulent dispersion	Disabled
Drag law	Non-spherical (shape factor varies with case)
Devolatilisation	Single first order reaction
Char combustion	Diffusion-limited
Radiation	
Model	Discrete Ordinates
Angular discretisation	3 pheta divisions 3 phi divisions 1 theta pixel 1 phi pixel
NOx	
Model	Thermal

7.4 Model validation

7.4.1 Drop tube furnace testing

Samples of both untorrefied and torrefied type A material were combusted in the DTF. The untorrefied type B runs on the DTF were unsuccessful since the relatively high oil content caused clumping and blocking of the feeder probe, which is only 3 mm in diameter. In order for the runs to be effective, the DTF requires a relatively fine particle size. Hence, the fine particle size fraction (<1 mm) of the type A was used. The torrefied samples used were from the median torrefaction intensity - 250°C for 30 min. The key material properties of both the untorrefied and torrefied biomass are included in Table 7-6 (Section 7.5.1).

Triplicate runs were carried out in each case. After passing through the DTF, the proximate analysis of the samples was carried out using TGA. In order to determine the fraction of the original volatile matter content which had been lost (volatile matter conversion, VMC), it is necessary to know the total weight loss of the sample as it passes through the DTF. However, direct measurement of the weight loss is not possible since the collection efficiency of the DTF is low; particles can stick to the feeder and collector probes. Hence an indirect method known as the ash tracer method was used (Shuangning et al., 2006). This is widely-used in DTF testing, and relies on the assumption that the ash content does not undergo any change within the DTF. Using the ash tracer method, ΔW , the mass loss of the sample as a percentage of the original mass, is given by:

$$\Delta W = 100 \times \left(1 - \frac{A}{A'}\right) \quad \text{Eqn 7-11}$$

where A and A' are the dry ash contents of the original sample and the char (after passing through the DTF), respectively.

V_c , the VM content of the char as a percentage of the original mass, was then calculated as follows:

$$V_c = V' \times \frac{100 - \Delta W}{100} \quad \text{Eqn 7-12}$$

where V' is the dry VM content of the char measured by proximate analysis.

The VMC is then calculated:

$$VMC = 100 \times \frac{V - V_c}{V} \quad \text{Eqn 7-13}$$

where V is the dry VM content of the original sample measured by proximate analysis.

The VMCs for each DTF run, along with the calculation steps, are shown in Table 7-5. It was observed that the mean VMC of the torrefied material was higher than that of the untorrefied samples. However, it should be noted that there is a degree of overlap between the untorrefied and torrefied samples, as illustrated in Figure 7-7. A larger coefficient of variation (CV) was obtained in the untorrefied case. A significant degree of uncertainty would be expected considering the several variables that affect the operation of the DTF, in addition to the unique challenges posed by biomass testing such as the low collection efficiency and inhomogeneity within the biomass itself (especially in the untorrefied samples).

The empirical VMCs thus obtained would be used to validate the CFD model. However, taking the above-mentioned sources of error should be taken into account when interpreting the results from the CFD model.

Table 7-5: Calculation of volatile matter conversion % (VMC)

	Untorrefied type A (<1 mm)			Torrefied type A (<1 mm)		
V (%)	70.9			63.1		
V' (%)	60.8	57.2	49.6	36.9	38.9	43.2
A (%)	5.9			7.6		
A' (%)	13.9	11.8	18.4	20.0	17.3	16.3
ΔW (%)	57.3	50.1	67.9	62.2	56.2	53.5
V _c (%)	25.9	28.6	15.9	14.0	17.0	20.1
VMC (%)	63.4	59.7	77.5	77.9	73.0	68.2
mean VMC (%)	66.9			73.0		
CV of VMC (%)	14.1			6.6		

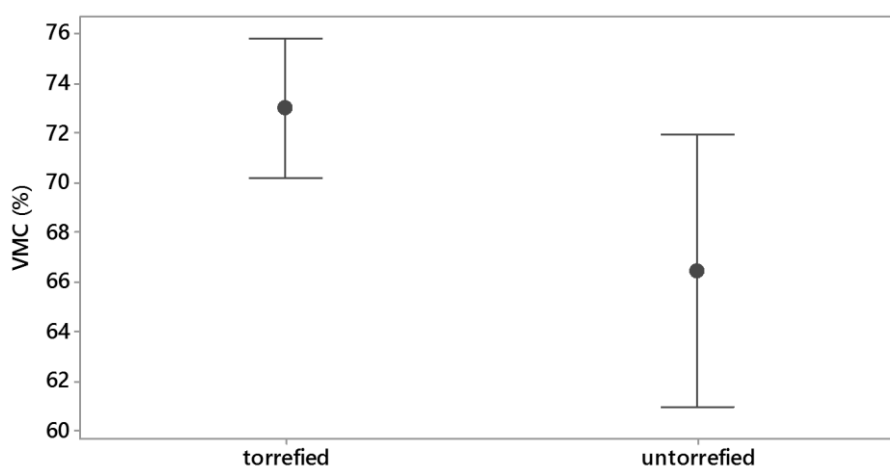


Figure 7-7: Interval plot of the empirical VMCs, error bars show the standard error.

7.4.2 Sensitivity analyses

The basic fuel properties such as the proximate analysis, ultimate analysis, HHV and devolatilisation kinetics were measured and input into the CFD model. However, there were several gaps in the required inputs where empirical measurements could not be made. Furthermore, the novelty of the use of *Jatropha curcas* seed cake as a fuel means that these unknown properties are unavailable in literature as well, as limited characterisation work has been done to date. The estimates used as inputs in these cases introduce uncertainties in the results; therefore, sensitivity analyses were conducted to quantify these effects. In each case, the uncertain property in question was

varied while all other model parameters were fixed; the effect of this variation on the volatile matter conversion % (VMC) was studied.

7.4.2.1 Devolatilisation kinetics and particle size

The most fundamental uncertainties were with respect to the particle size and the devolatilisation kinetics.

Although the samples used in the DTF had been sieved to less than 1 mm, an accurate distribution within this size fraction could not be determined. A tendency of the particles to agglomerate resulted in ineffective sieving at fine mesh sizes, and hence a sieve analysis could not be performed. This issue also meant that an optical particle analysis using a Retsch Camsizer (Retsch Technology, 2016) also did not yield reliable data; Figure 7-8 (a) and (b) shows the clumping of untorrefied type A particles as seen through the Camsizer unit and SEM (scanning electron microscopy), respectively. Figure 7-9 is the particle size distribution for the untorrefied type A, obtained from the Camsizer. The normal-like distribution which would be expected is observed in the 0-300 μm range, with a centre of approximately 200 μm . A small peak is observed at approximately 400 μm , followed by a much larger peak centred at ~600-700 μm . It can be postulated that these latter peaks are the result of the agglomeration of two or more 0-300 μm particles. The fact that the latter peaks occur approximately at multiples of 200 μm further supports this. Hence, although the Camsizer results are far from conclusive, they support the possibility that the majority of the individual particles are in the 200 ± 50 μm range.

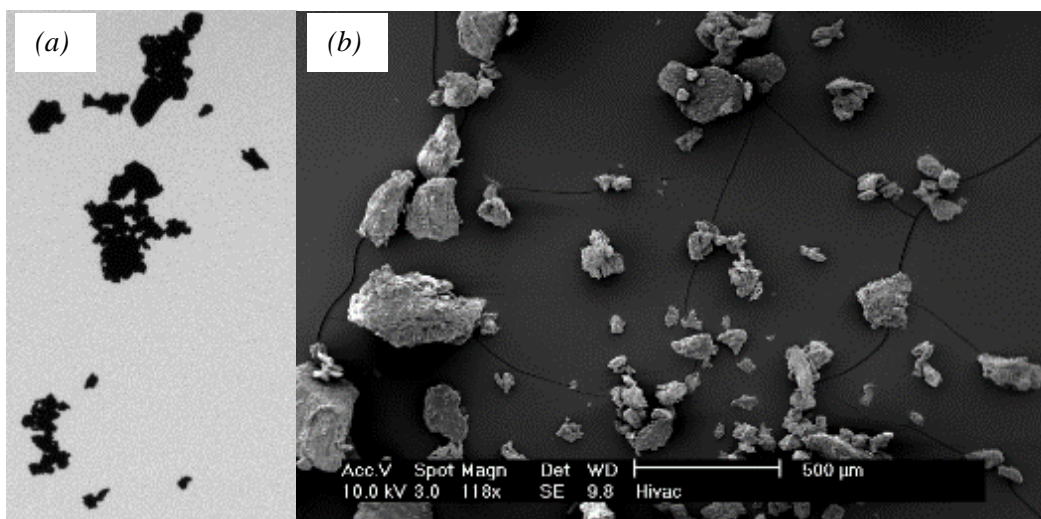


Figure 7-8: Type A particles as observed by (a) Camsizer, (b) SEM.

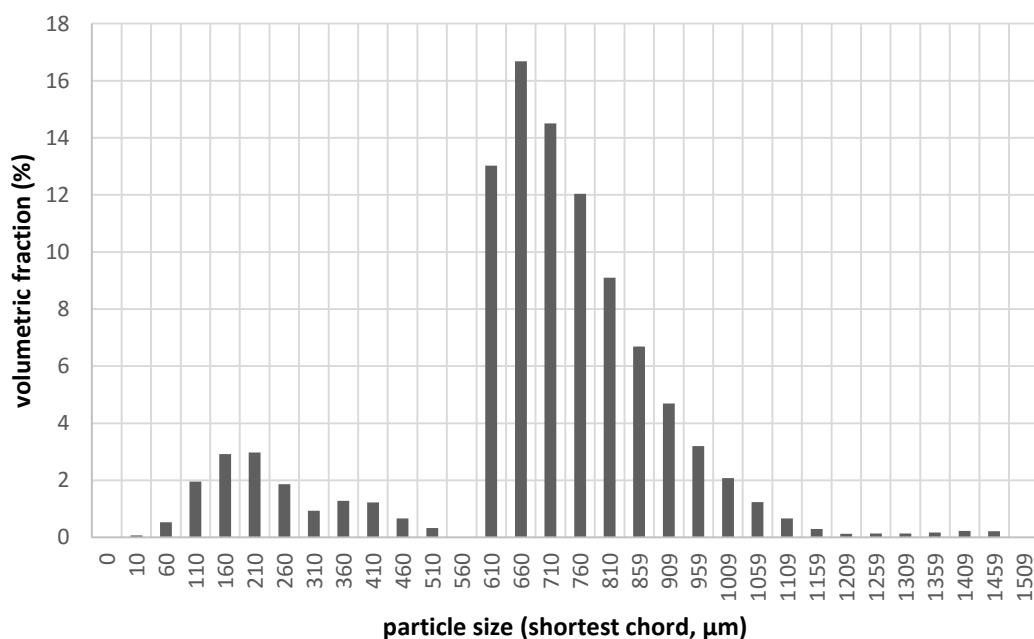


Figure 7-9: Particle distribution for untorrefied type A, measured by Camsizer

The devolatilisation kinetics were measured using TGA data. This method is acceptable to compare the kinetics between different materials. However, data obtained from the TGA cannot be reliably applied to the DTF as there is a vast difference in the heating rate between the two instruments – a heating rate of 15°C/min was used in the TGA runs, while that in the DTF is in the order of 10⁴-10⁵ °C/min.

Hence, the approach taken was to carry out the CFD runs with the devolatilisation kinetics obtained from the TGA (as given in Table 7-6 in Section 7.5.1), along with constant particle diameter injections (this was specified in the DPM settings). The VMC calculated by the model was compared with that obtained from the DTF, and the impact of particle size on the VMC was gauged.

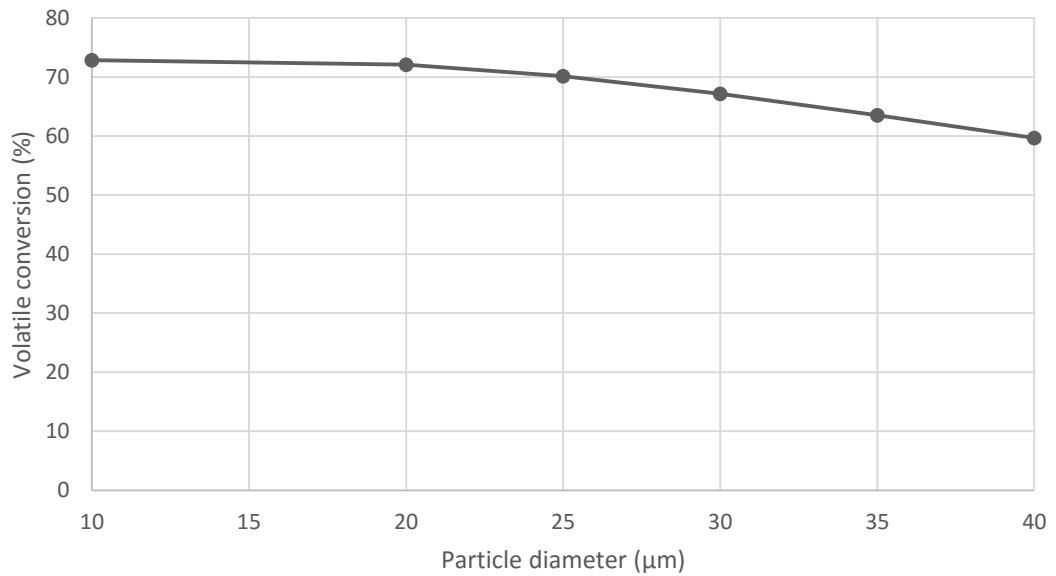


Figure 7-10: Variation of VMC with particle diameter (untorrefied case)

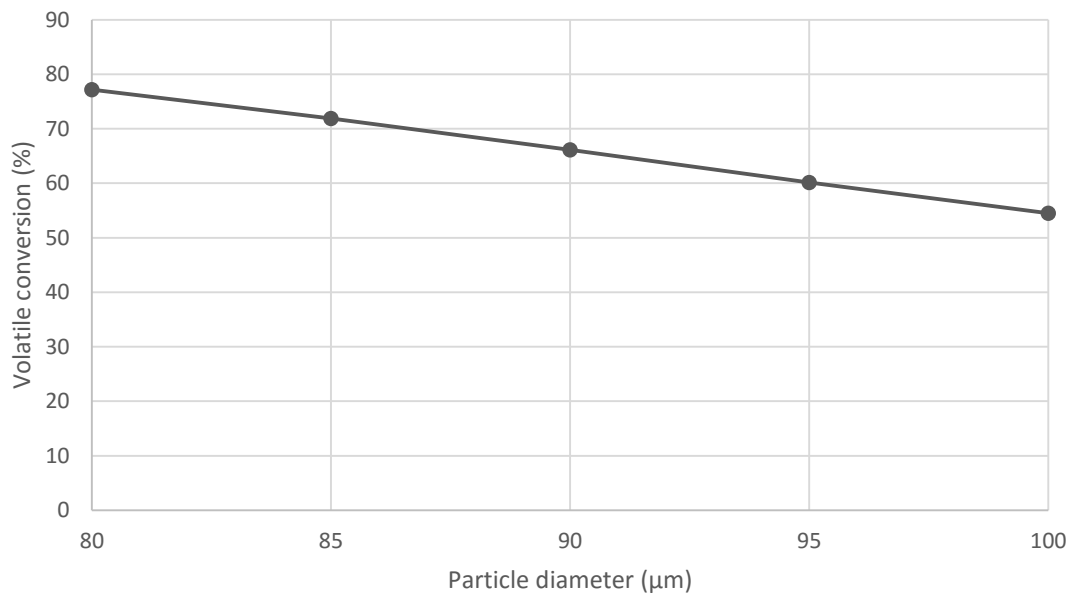


Figure 7-11: Variation of VMC with particle diameter (torrefied case)

Figure 7-10 and Figure 7-11 show the effect of the particle diameter on the VMC for the untorrefied and torrefied cases, respectively. The VMC range obtained from the DTF is 59.7%-77.5% and 68.2%-77.9% for the untorrefied and torrefied samples, respectively (Table 7-5). For the untorrefied case, this corresponds to a particle diameter of <40 μm . The corresponding diameter is higher for the torrefied case, at approximately 80-90 μm . A possible reason for this apparent increase is that particles have undergone agglomeration after torrefaction. Another factor is the possibility of particle swelling during the torrefaction process. This phenomenon has been observed before in a different type of biomass by Dufour et al. (2012) – Miscanthus biomass underwent swelling at torrefaction temperatures up to 250°C. However, the uncertainty of the TGA kinetics would be a definite and significant contributor to this difference in particle size.

Overall, the particle size range obtained is at the low end of the possible spectrum of 0 to 1000 μm . Although an accurate particle size distribution could not be measured empirically, as explained earlier in this section, the tentative empirical measurements indicate a mean particle size higher than 150 μm . The lower particle diameter predicted by the CFD runs is a reflection on the unreliable applicability of the TGA kinetics to the DTF due to the substantial difference in heating rates.

Single first order reaction (SFOR) devolatilisation kinetics parameters do not take into account heat transfer effects to and within the particle; they are based on the assumption that the particle is at a uniform temperature. TGA runs which are performed at relatively low heating rates allow larger particle sizes to be used while satisfying this assumption, but this assumption is no longer valid within the DTF. , As the reaction kinetics are dependent on the heating rate, the TGA kinetics cannot be directly applied to the DTF to make accurate predictions of absolute values. However,

considering the lack of high-heating rate kinetic data, the TGA kinetics were deemed suitable enough to make a comparative analysis between untorrefied biomass, torrefied biomass and coal (see Section 7.5.1) as long as the kinetics for all the cases were derived under similar TGA conditions. Previous studies by Stroh et al., (2015) and Zhang et al., (2013) have also utilised TGA kinetics in combustion modelling cases.

For the rest of the validation CFD runs, it was assumed that the biomass injection can be modelled by a single particle diameter of 30 μm and 85 μm (based on the mean VMC obtained from the DTF) for the untorrefied and torrefied cases, respectively, while using the TGA kinetics

7.4.2.2 Density

The particle density affects its velocity through the fluid phase and hence its residence time in the high-temperature zone. This in turn would change the VMC.

Although the bulk density of *Jatropha curcas* has been reported in literature as 670 kg/m^3 (Kavalek et al., 2013), this is not indicative of the particle density which is what has to be input in to Fluent. The particle density would depend on the pressing process used to extract the oil out of the seeds. Since pelletisation would also require the material to be pressed, the typical density of biomass pellets was considered to be representative of the particle density of the seed cake. The density of biomass pellets can be in the range of 1000-1400 kg/m^3 (Bergström et al., 2008; Stelte et al., 2011b); since the type A seed cake easily sinks in water, a density range of 1200-1500 kg/m^3 was used for the sensitivity analysis (Figure 7-12). The VMC shows a mild sensitivity to the density – the VMC decreased by 17% as the density was increased by 25% - in the torrefied case, with negligible change in the untorrefied case.

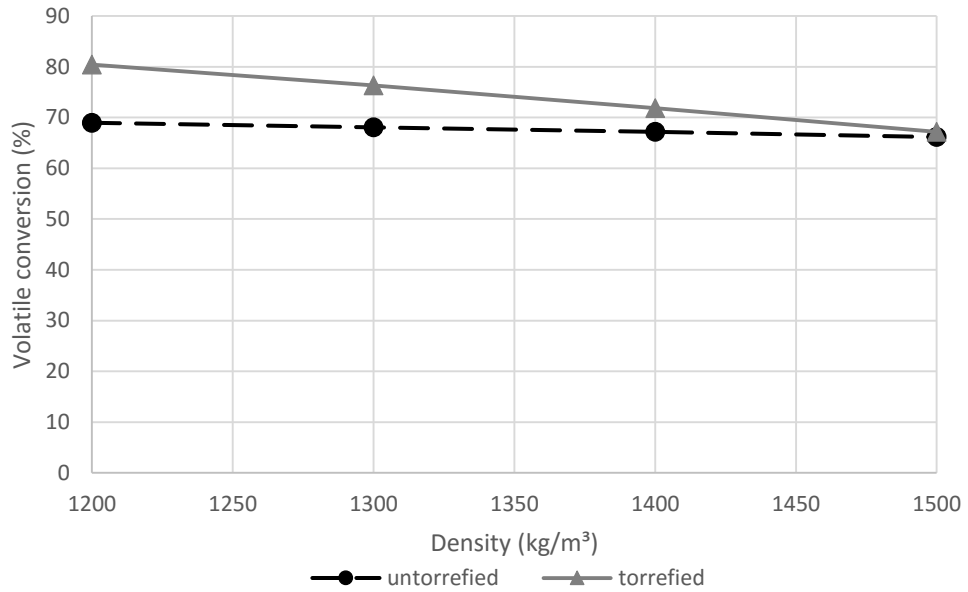


Figure 7-12: Variation of VMC with particle density

7.4.2.3 Shape factor

Figure 7-13 illustrates the sensitivity of the VMC to the shape factor. The shape factor is a parameter used to account for the non-spherical nature of particles. A shape factor of 1 would be the simplest case, where the particle is modelled as a perfect sphere. A shape factor of 0.5 means that the particle has a surface area twice that of a sphere of the same volume. The shape factor has a negligible effect on the VMC in the case of the untorrefied biomass. For the torrefied case, the VMC increased by 8% when the shape factor is decreased by 60%, indicating a mild sensitivity. Coal particles can typically be modelled as simple perfect spheres, i.e. shape factor of 1 (Ma et al., 2009). However, the fibrous nature and irregular shape of biomass particles means that a lower shape factor would be more suitable. The shape factor of the untorrefied biomass was assumed to be 0.7. It has been reported in literature that the torrefaction process causes particles to become more spherical (Arias et al., 2008). Hence, a shape factor of 1 was assumed for the torrefied case.

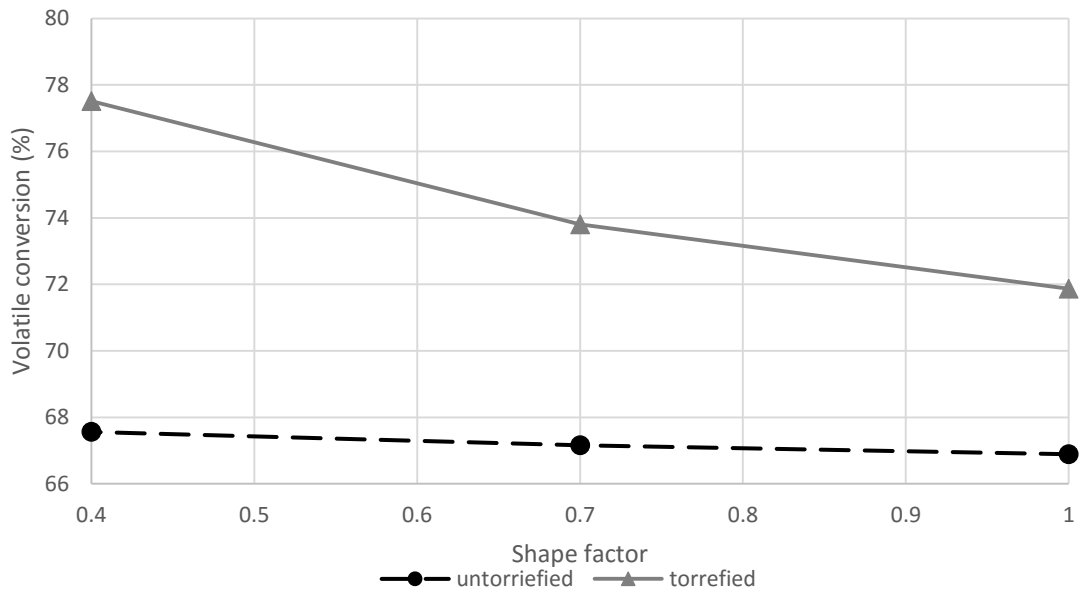


Figure 7-13: Variation of VMC with shape factor

7.4.2.4 Emissivity

Emissivity is a measure of the how effectively radiative heat is transferred to the particle. The baseline value of 0.9 is the default value used in Fluent. Although 0.9 is commonly used in biomass studies, values as low as 0.75 have also been reported (Gupta et al., 2003; Ma et al., 2009; Pokothoane, 2010). Figure 7-14 shows the variation of the VMC with the emissivity. There is a linear positive relationship between the emissivity and the VMC, as higher heat transfer to the particle would result in a higher particle temperature and hence more devolatilisation. The sensitivity is moderate in the case of the torrefied biomass – VMC drops by 11% when the emissivity is decreased by 22% from the baseline of 0.9 to 0.7. There is a relatively negligible effect in the untorrefied case.

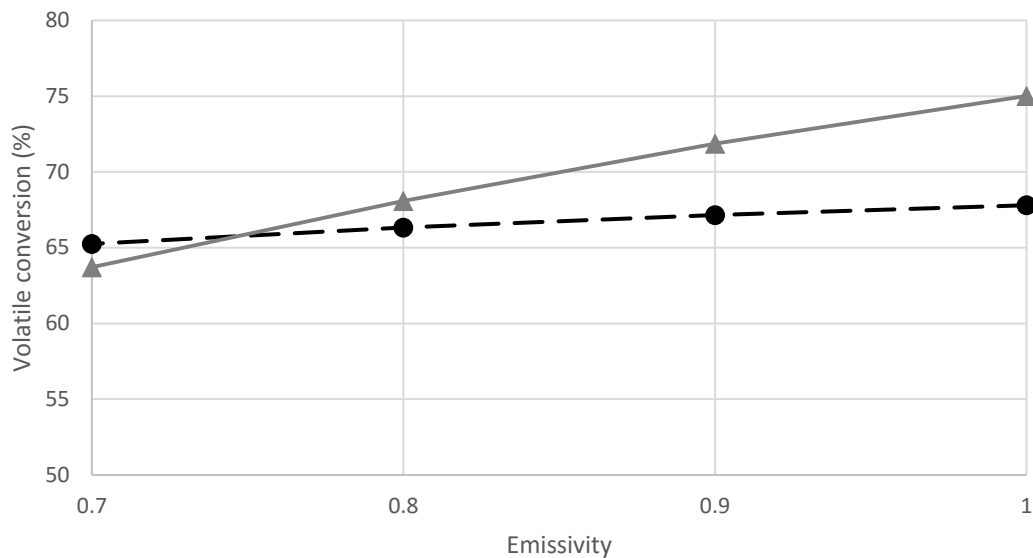


Figure 7-14: Variation of VMC with emissivity

7.4.2.5 Overview of sensitivity analyses

The particle size and kinetics were considered the most significant uncertainties. The TGA kinetics were fixed and the effect of varying the particle size was analysed. Based on the VMCs thus predicted from the model, and the empirical VMCs obtained from the DTF, representative particle diameters of 30 μm and 85 μm were chosen for the untorrefied and torrefied cases, respectively. These assumptions were considered sufficient for a comparative study without a detailed quantitative aspect.

The density and shape factor had a mild effect on the VMC in the case of the torrefied biomass, while the emissivity had a more significant effect. However, the sensitivity of the untorrefied biomass to these three factors was relatively negligible.

7.4.3 Stochastic tracking

Stochastic tracking (ST) uses the discrete random walk (DRW) model to model the effects of turbulence on the particle trajectories, i.e. the turbulent dispersion. ST was not performed on the sensitivity analyses and co-firing cases in order to reduce

computational time and improve convergence. However, two simulations with ST enabled were carried out for the baseline untorrefied and torrefied cases, in order to determine if there is a change in solution. 10 stochastic “tries” were performed for each particle track that is injected at the fuel inlet, i.e. 10 particle trajectories per non-ST track. This results in a total of 20 different particle trajectories per symmetric half of the 2D mesh.

Figure 7-15 shows the particle tracks coloured by particle temperature. In both cases, the majority of the particles (approximately 90%, as calculated from the particle mass flow rates at the inlet and outlet) exit the furnace through the collector probe. This indicates that the entrained flow conditions remain valid to a significant degree even with very small particles in the order of 20 μm .

The VMCs obtained with ST enabled were 67.2% and 71.9% for the untorrefied and torrefied cases, respectively. The corresponding values without ST were 74.8% and 77.4%. Despite the difference in VMCs between non-ST and ST cases, they all fall within the corresponding ranges of empirical VMCs obtained from the DTF runs. The particle size would have an effect on the turbulent dispersion modelled by ST. Since the particle sizes used in the CFD are not an accurate representation of the actual particle size used in the DTF runs (as they were adjusted to fit the TGA kinetics, see Section 7.4.2.1), it is possible that an additional degree of error is introduced by enabling ST. Furthermore, the present CFD study is comparative in nature. Considering these factors, using ST could not be justified for the subsequent CFD runs, and the simpler non-ST approach was chosen.

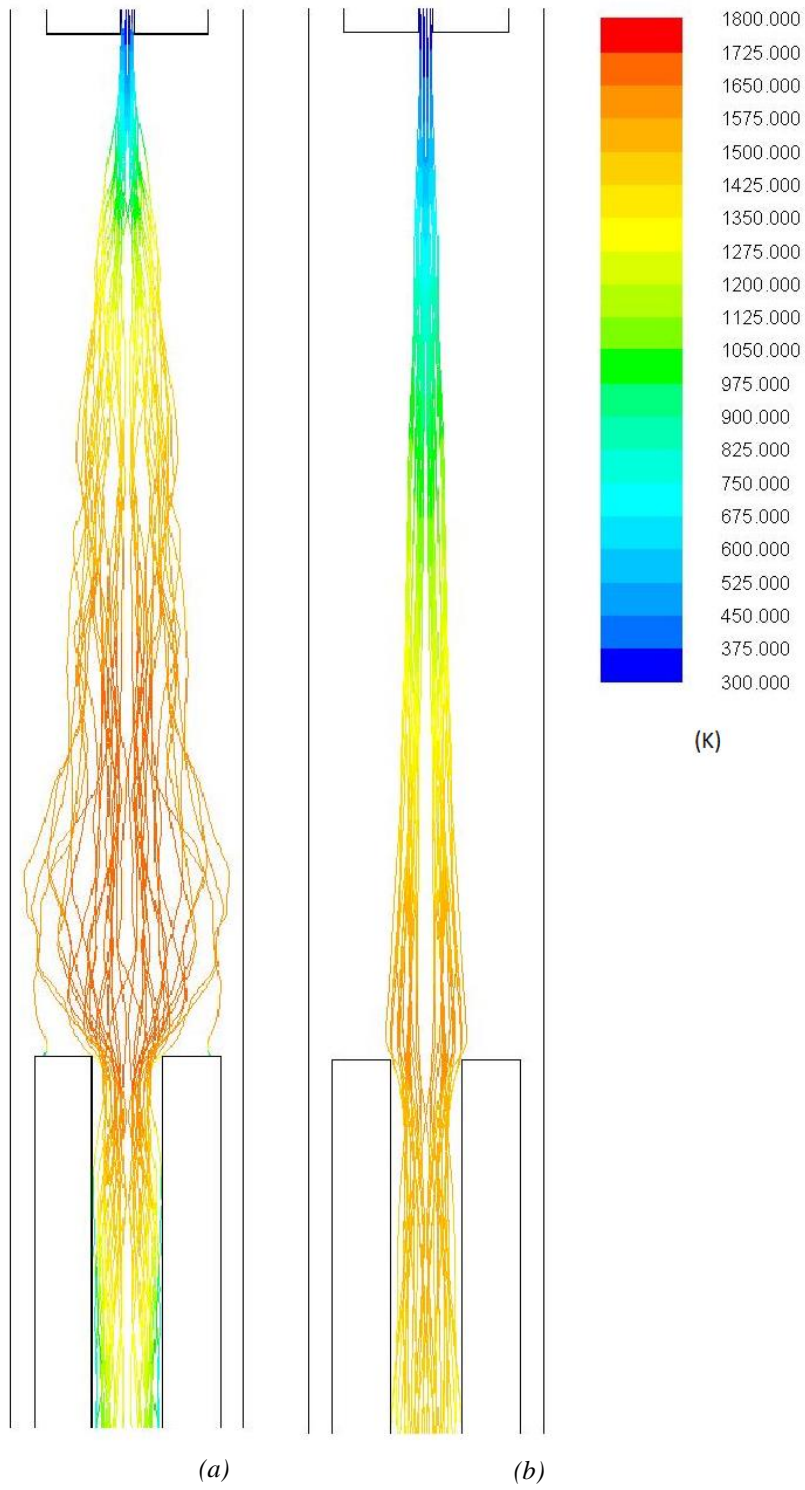


Figure 7-15: Particle tracks with stochastic tracking enabled for (a) untorrefied, (b) torrefied biomass

7.5 Finalised model and results

7.5.1 Material properties

Table 7-6 presents the material/particle properties that were used in the main study. Experimental measurements were made of the fundamental properties of the untorrefied and torrefied biomass, while the selection of uncertain or estimated properties was justified in Section 7.4. The properties of a typical coal (a high-volatile bituminous coal) was taken from literature (Biagini et al., 2002). This source was chosen since the devolatilisation kinetics were measured in similar conditions to those of the *Jatropha* seed cake (20°C/min in an N₂ flow).

Table 7-6: Key material/particle properties used in the finalised model

	<i>Jatropha curcas</i> seed cake (type A, <1 mm)		Bituminous coal
	Untorrefied	Torrefied	
Moisture (%)	3.62	3.06	2 ¹
Volatile matter (%)	69.26	61.18	32.6 ¹
Fixed carbon (%)	21.39	28.41	58.0 ¹
Ash (%)	5.70	7.33	7.4 ¹
DAF C (%)	53.02	58.31	81.8
DAF H (%)	6.99	5.72	5.6
DAF N (%)	5.13	4.55	1.3
DAF O (%)	34.87	31.42	11.3
HHV (MJ/kg)	20.76	24.22	29
<i>E</i> (kJ/mol)	63.1	79.2	91.2
<i>A</i> (s⁻¹)	1190	13800	955
Density (kg/m³)	1400 ²	1400 ²	1400 ³
Shape factor	0.7 ⁴	1.0 ⁴	1.0 ⁴
Emissivity	0.9 ⁵	0.9 ⁵	0.9 ⁵

¹ Since the proximate analysis was presented in the source in dry basis, a nominal moisture value of 2% was assumed, and the proximate analysis re-calculated to as-received basis.

² See Section 7.4.2.2.

³ Estimated value.

⁴ See Section 7.4.2.3.

⁵ See Section 7.4.2.4

7.5.2 Individual biomass/coal combustion

Figure 7-16 (c) and (d) shows the temperature distribution for the untorrefied and torrefied cases, respectively. Both cases have a similar VMC (30 μm and 85 μm particle diameter for the untorrefied and torrefied cases, respectively). The “flame” can be considered the areas where the temperature is greater than the 1490-1580 K band (as the DTF temperature was set to 1573 K). For comparison, Figure 7-16 (a) shows the temperature distribution with no combustion (inert particle). The distinct shape of the flame is visible in both biomass cases (c & d). However, there is a difference seen in the size and position of the flame. In the untorrefied case, the flame starts closer to the top of the furnace, and is more widely distributed.

This difference can be attributed to the devolatilisation characteristics of the two materials. The untorrefied biomass has a lower activation energy. Hence, the reaction can commence at a lower particle temperature (closer to the top of the furnace). However, the pre-exponential factor is higher in the torrefied biomass by an order of magnitude. The pre-exponential factor determines the overall magnitude of the reaction rate. Hence, although the devolatilisation is delayed in the case of the torrefied biomass, it is more intense when it starts. This allows the torrefied case to achieve a VMC similar to that of the untorrefied biomass, even though the activation energy is higher. This effect is graphically illustrated in Figure 7-17 (a) and (b), which are contour plots of the devolatilisation rate for the untorrefied and torrefied cases, respectively. Although the onset of devolatilisation is delayed, a higher devolatilisation rate of 5.1×10^{-9} kg/s is obtained in the torrefied case, compared to 3.6×10^{-9} kg/s for the untorrefied biomass.

However, the delayed onset of devolatilisation in the torrefied case means that more volatiles combustion occurs within the collector probe. Since the collector probe

is cooled, the temperature of the flame is controlled. This explains the lower-than-expected peak temperatures observed with the torrefied biomass – the peak temperatures recorded within the modelled volume was 1785°C and 1720°C for the untorrefied and torrefied cases, respectively. The lower temperatures obtained with the torrefied biomass are hence not a result of a lower energy release from the combustion reaction itself – the heats of reaction calculated over the modelled volume was higher for the torrefied case at 127 W, compared to 104 W for the untorrefied biomass (as expected because of the torrefied biomass' higher HHV).

In a practical sense, this difference in devolatilisation characteristics and flame temperatures is important since it can affect the formation of NO_x pollutants. The maximum NO formation rates were $1.3 \times 10^{-4} \text{ mol m}^{-3} \text{ s}^{-1}$ and 3.4×10^{-5} for the untorrefied and torrefied cases, respectively. The NO flow rates at the outlet were $4.9 \times 10^{-11} \text{ kg/s}$ and $1.3 \times 10^{-11} \text{ kg/s}$ for the untorrefied and torrefied cases, respectively. These results demonstrate the link between the temperature distribution and the NO formation, with higher NO levels being formed with larger, higher-temperature flames.

A distinct flame was not observed in the case of the coal (Figure 7-16 (b)). This is reflected in the very low VMC of 7%. As expected from the kinetic parameters, the coal is significantly less reactive than both untorrefied and torrefied *Jatropha* seed cake.

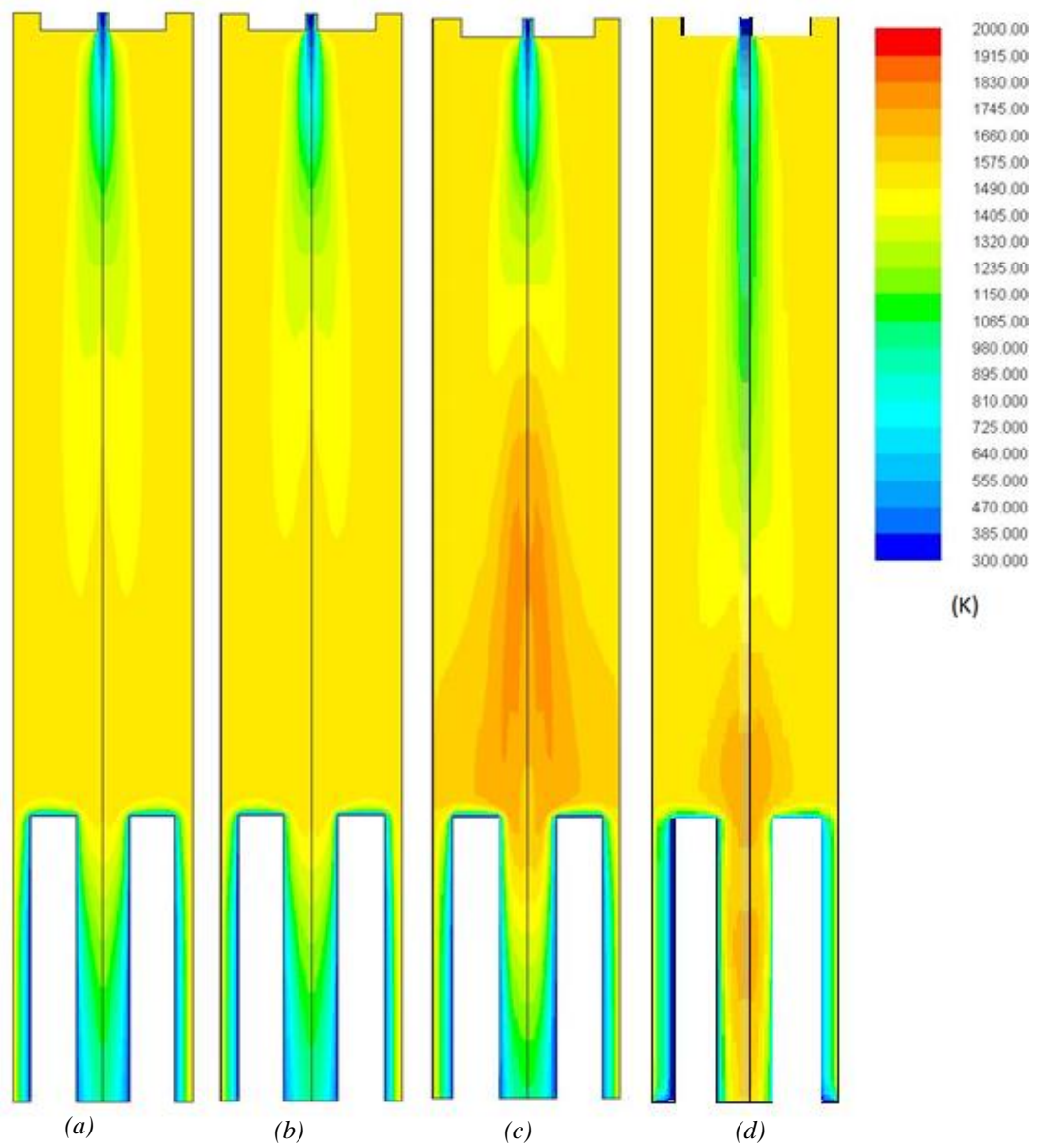


Figure 7-16: Temperature distributions for (a) inert particle, (b) coal, (c) untorrefied biomass, (d) torrefied biomass.

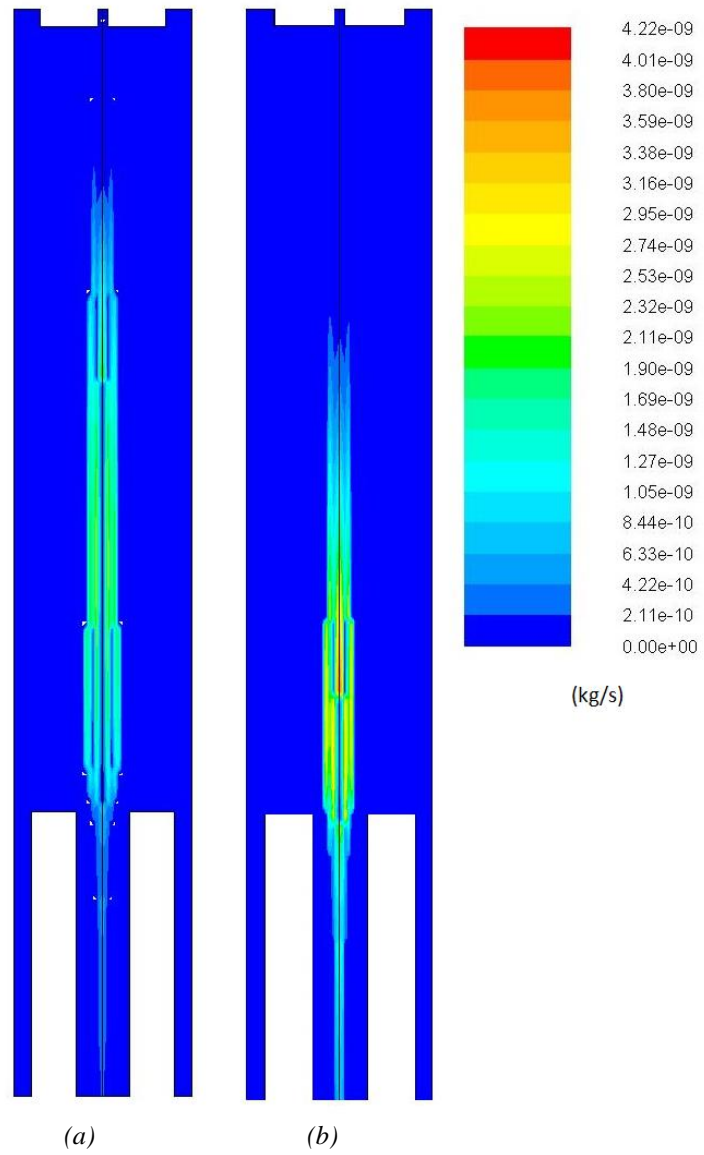


Figure 7-17: Devolatilisation rate for (a) untorrefied, (b) torrefied biomass.

7.5.3 Coal co-firing

7.5.3.1 Reactivity

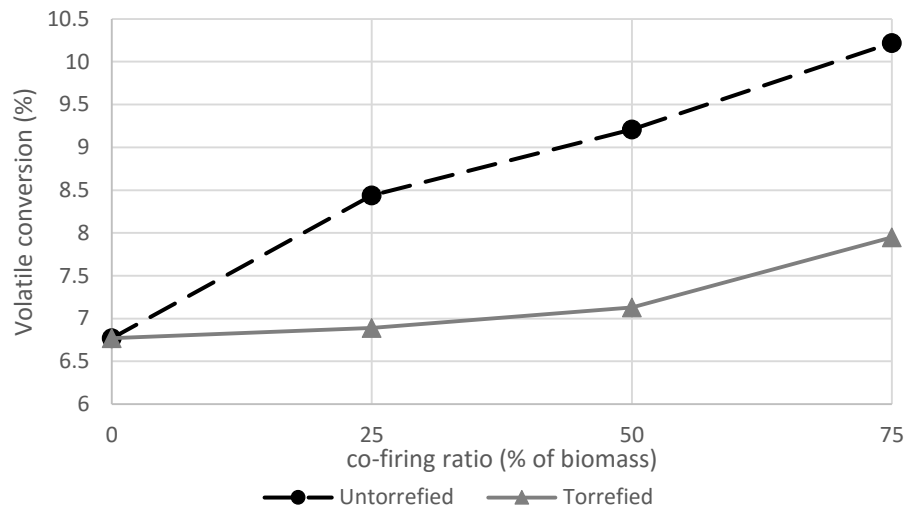


Figure 7-18: Effect of co-firing ratio on coal VMC

Coal co-firing cases were run with both untorrefied and torrefied seed cake. Two DPM injections were defined, one with the properties of the biomass and the other with those of the coal. The biomass % by mass was varied through 25%, 50% and 75% by changing the flow rates of each injection, while keeping the overall flow rate constant. Figure 7-18 shows the variation of the coal VMC with the co-firing ratio. As the biomass % is increased, the VMC of the coal increases as well. Although the increase is marginal in the case of the torrefied biomass, an increase by 51% is observed when the coal is co-fired with untorrefied biomass. The more reactive biomass undergoes combustion, and causes the temperature to rise (the flame region). As the coal particles enter this flame region, their temperature increases and this results in the coal undergoing faster devolatilisation. There was no regular trend in the change in VMC of the biomass under co-firing conditions, and the magnitude of the change was not significant.

This effect is graphically illustrated in Figure 7-19, which shows the temperature distribution for the three co-firing ratios for the untorrefied case. As the biomass %

increases, the flame region grows in size and intensity. Hence, the coal particles are subjected to both increasingly higher temperatures and longer residence times within the flame, thus experiencing significantly faster devolatilisation.

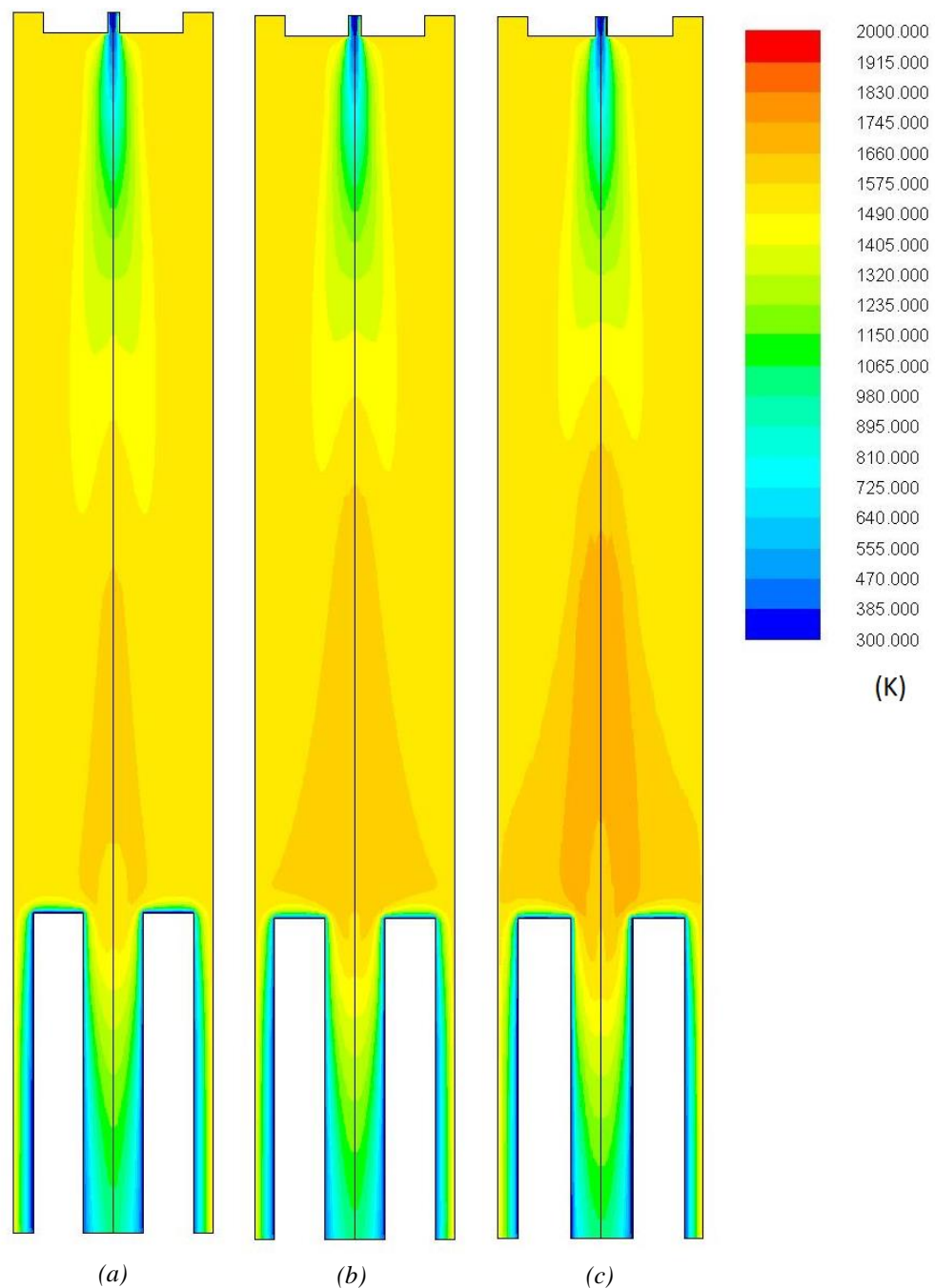


Figure 7-19: Temperature distribution for co-firing with (a) 25%, (b) 50%, (c) 75% untorrefied biomass .

The temperature distributions for the torrefied biomass co-firing is shown in Figure 7-20. Here, it can be seen that due to the delayed devolatilisation of the torrefied biomass (Section 7.5.2), the region of the flame is relatively small, even with the highest biomass fraction. Hence, the boost given to the coal devolatilisation is much less substantial than in the untorrefied co-firing case. This is reflected in the less significant increase in the coal VMC seen in Figure 7-18.

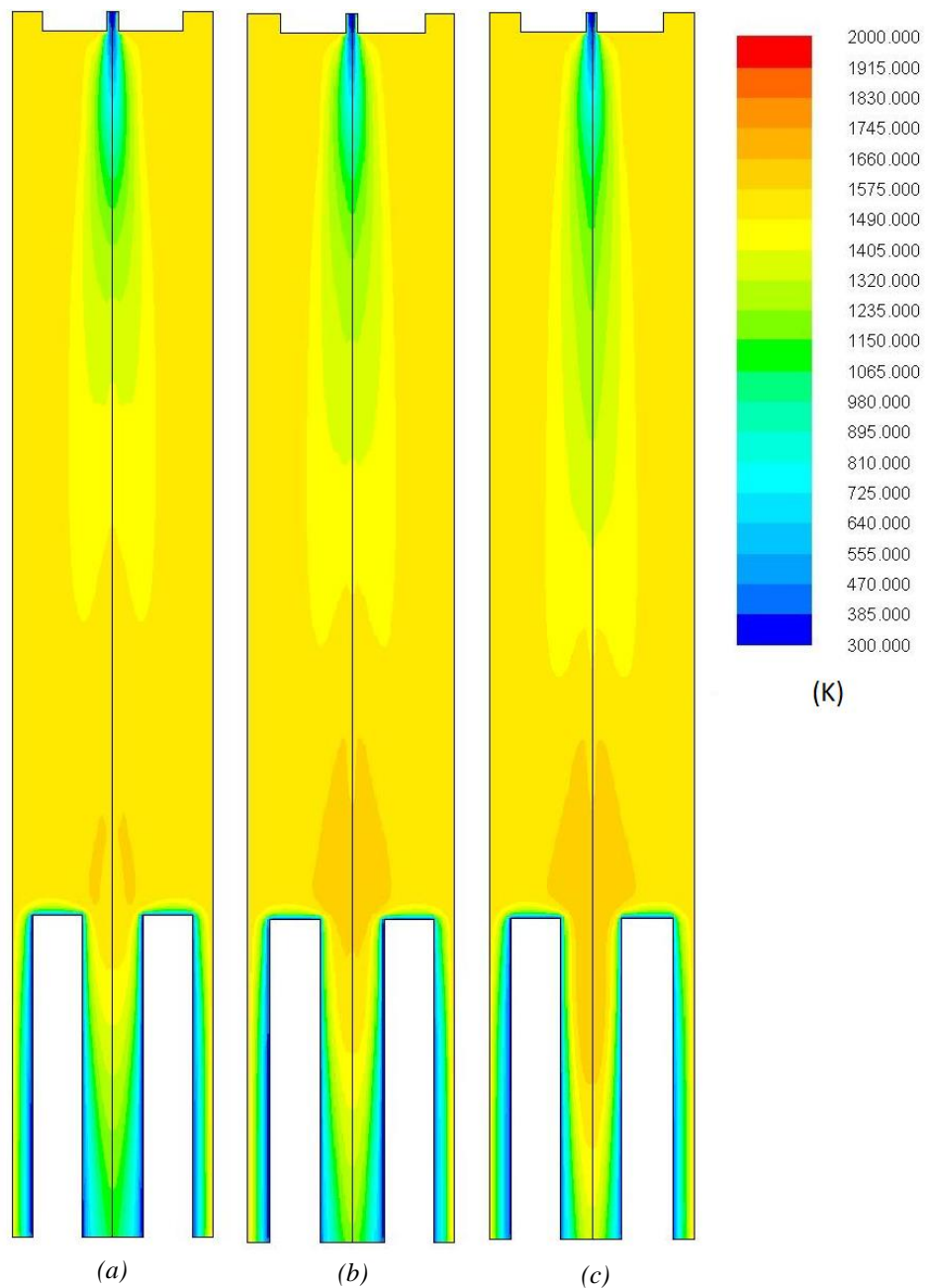


Figure 7-20: Temperature distribution for co-firing with (a) 25%, (b) 50%, (c) 75% torrefied biomass

7.5.3.2 NO_x emissions

Since there was a significant difference in the volatile conversion between the biomass and coal particles, a direct comparison in the NO emission is not meaningful. Hence, the NO flow rate at the outlet was normalised by the total heat of reaction summed over the entire volume. This gives an indication of the efficiency of the co-firing in terms of NO reduction.

Figure 7-21 and Figure 7-22 show the normalised NO emissions when the coal is co-fired with the untorrefied and torrefied biomass, respectively. Although the uncertainties in the model do not justify detailed conclusions being drawn, the overall trends indicate that co-firing reduces the NO emissions when compared to combusting only coal. However, it should be noted that only a small fraction of the coal has reacted. If the coal and biomass combustion continues to a greater extent (for instance with a longer residence time), the results from the model are liable to change.

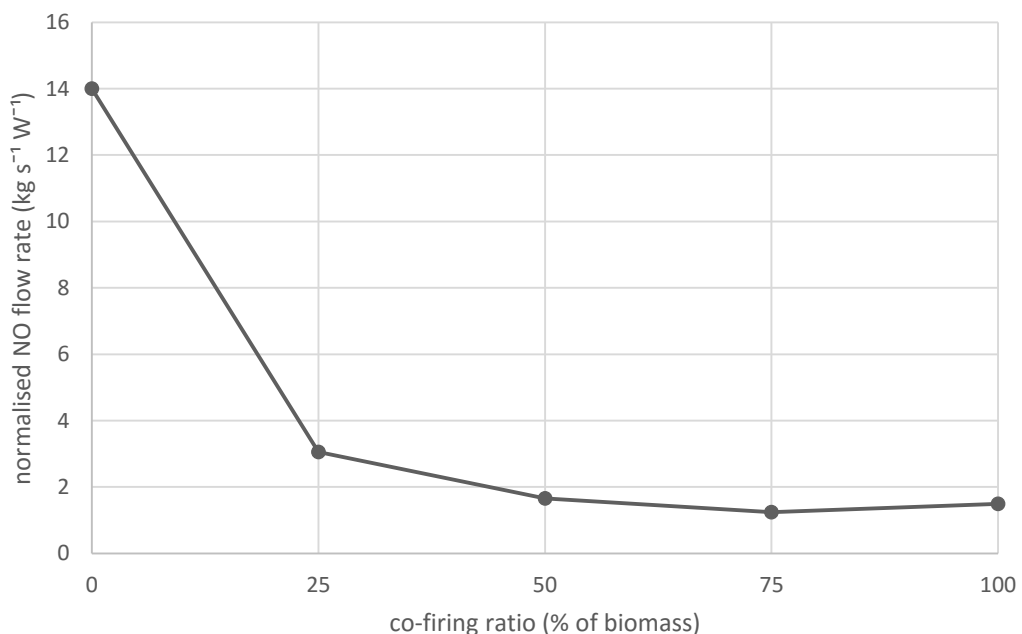


Figure 7-21: Effect of co-firing ratio on normalised NO emissions (untorrefied biomass)

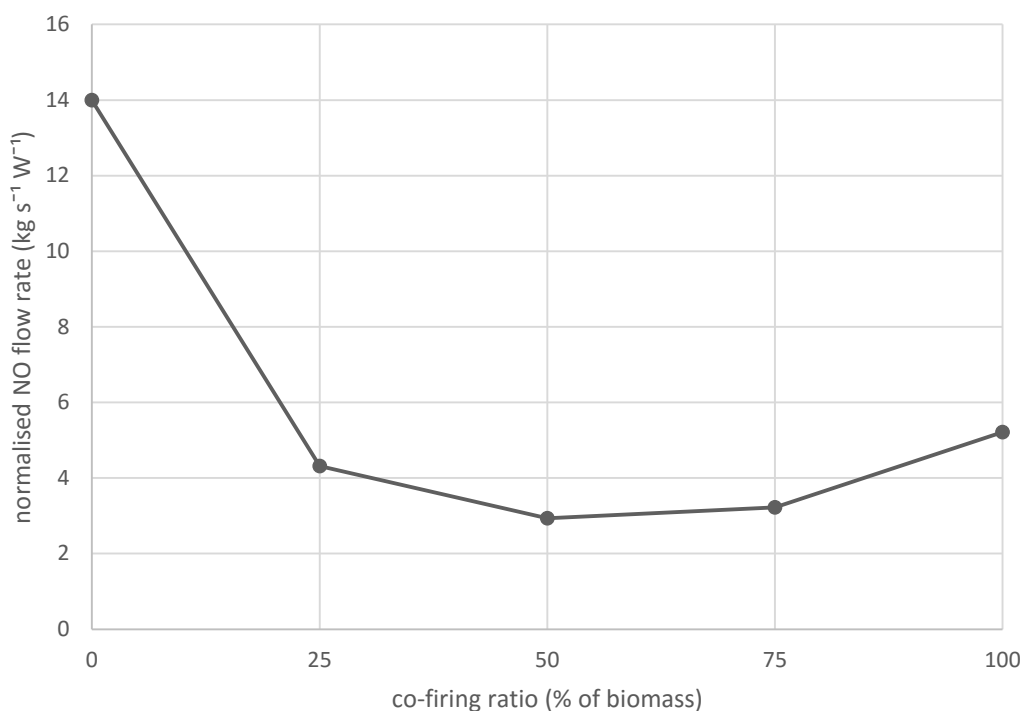


Figure 7-22: Effect of co-firing ratio on normalised NO emissions (torrefied biomass)

7.6 Concluding remarks

A CFD model was developed to investigate the combustion behaviour of the *Jatropha curcas* seed cake in a DTF, where conditions which are close to real-world applications, i.e. high temperature (up to 1300°C) and heating rate (in the order of 10⁴-10⁵ °C/min). However, a model's accuracy is dependent on the accuracy of the inputs given to the model. Several properties of the biomass had to be estimated in the light of limited experimental resources and a dearth of detailed characterisation of *Jatropha curcas* seed cake in the literature. The most significant uncertainties were the lack of accurate particle size data, and the devolatilisation kinetics obtained from low-heating rate TGA. An approach was adopted where the TGA kinetics were used but the particle size used in the model was reduced until the volatile conversion predicted by the model matched that measured by from the DTF runs. Sensitivity analyses were also carried out to ascertain the potential inaccuracy introduced by other estimated inputs.

Significant differences in the temperature distribution were observed between the untorrefied and torrefied combustion. The untorrefied biomass resulted in a more dispersed flame. This was reflected in the significant differences in NO emissions that were observed, as NO production is heavily temperature-dependent at the high temperatures present in the furnace.

The co-firing cases demonstrated an interaction between the coal and biomass in terms of reactivity. The higher reactivity of the biomass has the effect of boosting the reaction rate of the coal particles as well due to the extra heat generated by the biomass combustion. This effect was most profoundly seen with the untorrefied biomass.

In the light of the model input uncertainties, detailed quantitative analysis of the combustion modelling results cannot be justified. However, this study has highlighted some important distinctions between coal and biomass combustion, untorrefied and torrefied biomass combustion, and the interaction effects between the two fuels that occur during co-firing. The importance of using CFD as a tool to investigate and optimise the co-firing of torrefied *Jatropha curcas* seed cake was established.

From this baseline, the model can be further developed in the future to include more accurate model inputs (for example, using kinetic data obtained under high heating rates, use of the Fuel NO and Prompt NO mechanisms as well) and longer residence times so that the coal and biomass undergo a greater degree of conversion.

8 CONCLUSIONS AND FUTURE WORK

The aim of this research work was to investigate the effective utilization of *Jatropha curcas* seed cake as a solid fuel to be co-fired with coal. The study was carried out in four phases – characterisation, torrefaction, leaching and combustion modelling – with each phase aiming to achieve 1-2 of the objectives that were outlined in Section 1.2. A chapter was allocated to each phase, to present its experimental design, results and discussion. This chapter presents the key findings from the research and also makes recommendations for future work.

8.1 Conclusions

The following list presents a response to each of the numbered objectives listed in Section 1.2, demonstrating how they were achieved. The corresponding chapter is also referenced.

1. The fundamental fuel properties of the untreated *Jatropha curcas* seed cake were measured, establishing a baseline for subsequent work and a comparison with literature. This included the proximate analysis, ultimate analysis, HHV and inorganic content. HHV (20.76 MJ/kg and 24.06 MJ/kg for type A and type B, respectively) and ash content (5.9% and 4.4% for type A and type B, respectively, dry basis) compared favourably with other varieties of biomass. K was the most abundant inorganic element, with type A having a higher inorganic content than type B.

(Chapter 4)

2. Increasing torrefaction intensity, i.e. torrefaction temperature and holding time, resulted in lower mass and energy yields, but an enhanced higher HHV. The need to arrive at a compromise in terms of HHV and energy yield was

recognised. The torrefaction temperature was observed to be the more dominant of the two factors.

An envelope of torrefaction conditions was recommended for each type of seed cake on the basis of a favourable balance between HHV and energy yield. For the type A biomass, torrefaction at ~250°C for 45-60 min resulted in the HHV being enhanced to more than 24.5 MJ/kg while maintaining an energy yield no less than 85%. For the type B, a wider range of conditions – ranging from <5 min at >280°C to >45 min at 220°C-250°C – was identified where the HHV was higher than 27 MJ/kg while the energy yield remained greater than 90%. A typical coal used for power generation would have a HHV of 27-32 MJ/kg. The type B is the better feedstock for torrefaction because of the wide envelope of suitable torrefaction conditions which allow the enhancement of the HHV to the range of that of coal.

(Chapter 5)

3. The increasing HHV was linked to the rising FC content and decreasing O/C content measured by proximate and ultimate analysis, respectively. Taking advantage of the correlation, an expression was derived to estimate the HHV using the DAF FC content. A van Krevelen diagram, i.e. a plot of H/C vs O/C ratios, indicated that torrefaction caused a shifting of the thermochemical properties of the *Jatropha curcas* seed cake towards those of coal.

DTG and ¹³C NMR analysis provided insight into the changes occurring in terms of the lignocellulosic make-up as the torrefaction intensity was increased; hemicellulose decomposition occurred first followed by cellulose decomposition, while lignin underwent a slow degradation over a wide range

of temperatures. The results from the two analysis methods corroborated each other and also agreed with existing literature.

(Chapter 5)

4. From the preliminary leaching study, it was determined that leaching temperature and torrefaction state were the most dominant factors. A significant interaction between the temperature and torrefaction state was also suggested, i.e. the effect of the leaching temperature was different between untorrefied and torrefied samples. For the type A biomass, the larger particle size caused a drop in leaching efficacy as expected, although the magnitude of the decrease in overall inorganic content was not substantial.

K and Cl levels were considered crucial since they have been identified in literature as being significant contributors to ash deposition and corrosion issues in biomass combustion. Furthermore, K is the most abundant inorganic element in the unleached *Jatropha curcas* seed cake. Leaching at 20°C was sufficient for the K and Cl content of the untorrefied type B biomass to decrease by 85% and 97%, respectively. For the type B seed cake torrefied at the median torrefaction intensity (hence falling within the recommended torrefaction guidelines), leaching at 50°C was recommended from the point of view of the leaching efficacy; 67% of K was leached out in this case.

The torrefaction intensity had a significant effect on the subsequent leaching process. For the untorrefied type B seed cake and that torrefied at low intensity, leaching at 20°C was adequate. At higher torrefaction intensities, it was evident that higher leaching temperatures were required for effective leaching.

(Chapter 6)

5. The combustion study demonstrated that the different devolatilisation reactivity of untorrefied and torrefied biomass had an effect on the flame properties and on NO_x pollutant formation; the untorrefied biomass underwent early devolatilisation and had a more dispersed flame, and subsequently resulted in higher NO formation. Under co-firing conditions, the higher reactivity of the biomass was also shown to have a positive effect on devolatilisation rate of the coal; this showed the importance of considering the interactions that can occur between coal and biomass during co-firing.

(Chapter 7)

8.2 Future work

This study fulfilled the objectives laid out at the outset and established a useful foundation for the use of *Jatropha curcas* seed cake as a co-firing feedstock. However, there were limitations that were recognised throughout the various phases of the study. Following is a list of recommendations for potential future work that could build on the present study to provide more breadth and depth to the subject:

- The torrefaction guidelines specified here are applicable to the heating rate and torrefaction apparatus used in this study. Future work could include determining the sensitivity of the results to these additional variables and the effects of scaling up the process to a larger scale. In scaling up, the cost implications of the torrefaction procedure have to be investigated. Analysing the cost of N₂ supply and the energy requirements would enable further optimisation of the process parameters and confirm feasibility from an economic standpoint.

- Although higher leaching temperatures were recommended for the torrefied biomass, the cost implications of using these elevated temperatures should be studied in further detail. Alternative heating options such as solar heating can be considered. Furthermore, using leaching temperatures higher than 50°C can potentially have other issues such as evaporation. Further work is required to investigate these practical issues of high-temperature leaching.
- The combustion modelling can be strengthened by gathering further empirical characterisation data for the *Jatropha curcas* seed cake to reduce the uncertainties in the model inputs. These include data such as high-heating rate devolatilisation kinetics, accurate particle size distributions, and nitrogen partitioning between volatiles and char. Furthermore, longer residence times can be modelled and validated using DTF to ensure more complete devolatilisation as well as char oxidation occurring. A stronger, more complete model would enable more meaningful quantitative data to be extracted and provide a more complete understanding of the co-firing process.

References

1. Agar, D., Gil, J., Sanchez, D., Echeverria, I. & Wihersaari, M., 2015. Torrefied versus conventional pellet production – A comparative study on energy and emission balance based on pilot-plant data and EU sustainability criteria. *Appl. Energy*, 138, 621–630.
2. Almeida, G., Brito, J.O. & Perré, P., 2010. Alterations in energy properties of eucalyptus wood and bark subjected to torrefaction: the potential of mass loss as a synthetic indicator. *Bioresour. Technol.*, 101(24), 9778–84.
3. Álvarez, L., Yin, C., Riaza, J., Pevida, C., Pis, J.J. & Rubiera, F., 2014. Biomass co-firing under oxy-fuel conditions: A computational fluid dynamics modelling study and experimental validation. *Fuel Process. Technol.*, 120, 22–33.
4. ANSYS Inc., 2011a. *ANSYS® Fluent 14.0 Theory Guide*,
5. ANSYS Inc., 2011b. *ANSYS® Fluent 14.0 User Guide*,
6. Arias, B., Pevida, C., Feroso, J., Plaza, M.G., Rubiera, F. & Pis, J.J., 2008. Influence of torrefaction on the grindability and reactivity of woody biomass. *Fuel Process. Technol.*, 89(2), 169–175.
7. Backreedy, R.I., Fletcher, L.M., Jones, J.M., Ma, L., Pourkashanian, M. & Williams, a., 2005a. Co-firing pulverised coal and biomass: a modeling approach. *Proc. Combust. Inst.*, 30(2), 2955–2964.
8. Backreedy, R.I., Jones, J.M., Ma, L., Pourkashanian, M., Williams, A., Arenillas, A., Arias, B., Pis, J.J. & Rubiera, F., 2005b. Prediction of unburned carbon and NO_x in a tangentially fired power station using single coals and blends. *Fuel*, 84(17), 2196–2203.
9. Badzioch, S. & Hawksley, P., 1970. Kinetics of thermal decomposition of pulverized coal particles. *Ind. Eng. Chem. Process Des. Dev.*, 9(4), 521–530.
10. Bakis, R., 2007. Alternative Electricity Generation Opportunities. *Energy Sources, Part A Recover. Util. Environ. Eff.*, 30(2), 141–148.
11. Barnes, D.I., 2014. Understanding pulverised coal, biomass and waste combustion - A brief overview. *Appl. Therm. Eng.*, 74, 89–95.
12. Basili, M. & Fontini, F., 2012. Biofuel from *Jatropha curcas*: Environmental sustainability and option value. *Ecol. Econ.*, 78, 1–8.
13. Baxter, L., 2005. Biomass-coal co-combustion: opportunity for affordable renewable energy. *Fuel*, 84(10), 1295–1302.
14. Baxter, L.L., 1993. Ash deposition during biomass and coal combustion: A mechanistic approach. *Biomass and Bioenergy*, 4(2), 85–102.

15. Baxter, L.L., Miles, T.R., Jenkins, B.M., Milne, T., Dayton, D., Bryers, R.W. & Oden, L.L., 1998. The behavior of inorganic material in biomass-fired power boilers: field and laboratory experiences. *Fuel Process. Technol.*, 54(1-3), 47–78.
16. Ben, H., Ragauskas, A. J., 2012. *Green Chem.*, 14, 72–76.
17. Benavente, V. & Fullana, A., 2015. Torrefaction of olive mill waste. *Biomass and Bioenergy*, 73, 186–194.
18. Bergström, D., Israelsson, S., Öhman, M., Dahlqvist, S.-A., Gref, R., Boman, C. & Wästerlund, I., 2008. Effects of raw material particle size distribution on the characteristics of Scots pine sawdust fuel pellets. *Fuel Process. Technol.*, 89(12), 1324–1329.
19. Bernardinelli, O.D., Lima, M.A., Rezende, C.A., Polikarpov, I. & deAzevedo, E.R., 2015. Quantitative ¹³C MultiCP solid-state NMR as a tool for evaluation of cellulose crystallinity index measured directly inside sugarcane biomass. *Biotechnol. Biofuels*, 8(1), 110.
20. Bhuiyan, A. a. & Naser, J., 2015. CFD modelling of co-firing of biomass with coal under oxy-fuel combustion in a large scale power plant. *Fuel*, 159, 150–168.
21. Biagini, E., Lippi, F., Petarca, L. & Tognotti, L., 2002. Devolatilization rate of biomasses and coal-biomass blends : an experimental investigation. , 81, 1041–1050.
22. Black, S., Szuhánszki, J., Pranzitelli, a., Ma, L., Stanger, P.J., Ingham, D.B. & Pourkashanian, M., 2013. Effects of firing coal and biomass under oxy-fuel conditions in a power plant boiler using CFD modelling. *Fuel*, 113(x), 780–786.
23. Boersma, A.R., Prins, M.J., Ptasiński, K.J., Bergman, P. & Kiel, J., 2005. Torrefaction for entrained-flow gasification of biomass.
24. Bonefacic, I., Frankovic, B. & Kazagic, A., 2015. Cylindrical particle modelling in pulverized coal and biomass co-firing process. *Appl. Therm. Eng.*, 78, 74–81.
25. Brewster, B.S., 1996. Model comparisons with drop tube combustion data for various devolatilization submodels. *Fuel Energy Abstr.*, 37(3), 207.
26. Bridgeman, T.G., Jones, J.M., Shield, I. & Williams, P.T., 2008. Torrefaction of reed canary grass, wheat straw and willow to enhance solid fuel qualities and combustion properties. *Fuel*, 87(6), 844–856.
27. Bridgeman, T.G., Jones, J.M., Williams, a. & Waldron, D.J., 2010. An investigation of the grindability of two torrefied energy crops. *Fuel*, 89(12), 3911–3918.
28. Bruker Corporation, 2016. S8 Tiger Overview. Available at: <https://www.bruker.com/products/x-ray-diffraction-and-elemental-analysis/x-ray-fluorescence/s8-tiger/overview.html> [Accessed March 25, 2016].

29. Bryers, R., 1996. Fireside slagging, fouling, and high-temperature corrosion of heat-transfer surface due to impurities in steam-raising fuels. *Prog. Energy Combust. Sci.*, 72.
30. BSI, 2011a. BSI Standards Publication Solid biofuels — Determination of major elements — Al , Ca , Fe , Mg , P , K , Si , Na and Ti, BS EN 15290:2011.
31. BSI, 2011b. BSI Standards Publication Solid biofuels — Determination of total content of carbon , hydrogen and nitrogen — Instrumental methods, BS EN 15104:2011.
32. BSI, 2011c. BSI Standards Publication Solid biofuels — Determination of total content of sulfur and chlorine, BS EN 15289:2011.
33. Carrillo, M. a., Staggenborg, S. a. & Pineda, J. a., 2014. Washing sorghum biomass with water to improve its quality for combustion. *Fuel*, 116, 427–431.
34. Channiwala, S.A. & Parikh, P.P., 2002. A unified correlation for estimating HHV of solid, liquid and gaseous fuels. *Fuel*, 81, 1051–1063.
35. Chen, W., Cheng, W., Lu, K.-M. & Huang, Y.-P., 2011a. An evaluation on improvement of pulverized biomass property for solid fuel through torrefaction. *Appl. Energy*, 88(11), 3636–3644.
36. Chen, W. & Kuo, P.-C., 2010. A study on torrefaction of various biomass materials and its impact on lignocellulosic structure simulated by a thermogravimetry. *Energy*, 35(6), 2580–2586.
37. Chen, W.-H., Du, S.-W., Tsai, C.-H. & Wang, Z.-Y., 2012. Torrefied biomasses in a drop tube furnace to evaluate their utility in blast furnaces. *Bioresour. Technol.*, 111, 433–8.
38. Chen, W.-H., Hsu, H.-C., Lu, K.-M., Lee, W.-J. & Lin, T.-C., 2011b. Thermal pretreatment of wood (Lauan) block by torrefaction and its influence on the properties of the biomass. *Energy*, 36(5), 3012–3021.
39. Chen, Y., Charpenay, S., Jensen, A., Wójtowicz, M.A. & Serio, M.A., 1998. Modeling of biomass pyrolysis kinetics. *Symp. Combust.*, 27(1), 1327–1334.
40. Chin, K.L. et al., 2015. Reducing ash related operation problems of fast growing timber species and oil palm biomass for combustion applications using leaching techniques. *Energy*, 1–9.
41. Christodoulou, C., Grimekis, D., Panopoulos, K.D., Vamvuka, D., Karellas, S. & Kakaras, E., 2014. Circulating fluidized bed gasification tests of seed cakes residues after oil extraction and comparison with wood. *Fuel*, 132, 71–81.
42. Chum, H., Faaij, A., Moreira, J., Junginger, H. & Patel, M., 2011. Bioenergy. *IPCC Spec. Rep. Renew. Energy Sources Clim. Chang. Mitig.*, 1–188.

43. Coats, A.W. & Redfern, J.P., 1964. Kinetic Parameters from Thermogravimetric Data. *Nature*, 201(4914), 68–69.
44. Dai, J., Sokhansanj, S., Grace, J.R., Bi, X., Lim, C.J. & Melin, S., 2008. Overview and some issues related to co-firing biomass and coal. *Can. J. Chem. Eng.*, 86(3), 367–386.
45. Damartzis, T., Vamvuka, D., Sfakiotakis, S. & Zabaniotou, a., 2011. Thermal degradation studies and kinetic modeling of cardoon (*Cynara cardunculus*) pyrolysis using thermogravimetric analysis (TGA). *Bioresour. Technol.*, 102(10), 6230–6238.
46. Davidsson, K., Korsgren, J., Pettersson, J. & Jäglid, U., 2002. The effects of fuel washing techniques on alkali release from biomass. *Fuel*, 81, 137–142.
47. Dayton, D., Jenkins, B. & Turn, S., 1999a. Release of inorganic constituents from leached biomass during thermal conversion. *Energy & Fuels*, 1977(2), 860–870.
48. Dayton, D.C., Belle-Oudry, D. & Nordin, A., 1999b. Effect of Coal Minerals on Chlorine and Alkali Metals Released during Biomass/Coal Cofiring. *Energy & Fuels*, 13(6), 1203–1211.
49. Degereji, M.U., Ingham, D.B., Ma, L., Pourkashanian, M. & Williams, a., 2012. Prediction of ash slagging propensity in a pulverized coal combustion furnace. *Fuel*, 101(January), 171–178.
50. Demirbas, a, 2004. Combustion characteristics of different biomass fuels. *Prog. Energy Combust. Sci.*, 30(2), 219–230.
51. Demirbas, A., 1997. Calculation of higher heating values of biomass fuels. *Fuel*, 76(5), 431–434.
52. Demirbas, A., 2006. Global Renewable Energy Resources. *Energy Sources, Part A Recover. Util. Environ. Eff.*, 28(8), 779–792.
53. Demirbas, A., 2005. Potential applications of renewable energy sources, biomass combustion problems in boiler power systems and combustion related environmental issues. *Prog. Energy Combust. Sci.*, 31(2), 171–192.
54. Demirbas, A., 2003. Sustainable cofiring of biomass with coal. *Energy Convers. Manag.*, 44, 1465–1479.
55. Demirbas, A., Gullu, D., Çağlar, A. & Akdeniz, F., 2007. Estimation of Calorific Values of Fuels from Lignocellulosics Estimation of Calorific Values of Fuels from. , (January 2013), 37–41.
56. Deng, J., Wang, G., Kuang, J., Zhang, Y. & Luo, Y., 2009. Pretreatment of agricultural residues for co-gasification via torrefaction. *J. Anal. Appl. Pyrolysis*, 86(2), 331–337.

57. Deng, L., Zhang, T. & Che, D., 2013. Effect of water washing on fuel properties, pyrolysis and combustion characteristics, and ash fusibility of biomass. *Fuel Process. Technol.*, 106, 712–720.
58. Dionex Corporation, 2005. *ICS-1000 Ion Chromatography System Operator's Manual*, Available at: [http://www.dionex.com/en-us/webdocs/4559-031879_02 ICS-1000 manual.pdf](http://www.dionex.com/en-us/webdocs/4559-031879_02%20ICS-1000%20manual.pdf).
59. Doshi, P., Srivastava, G., Pathak, G. & Dikshit, M., 2014. Physicochemical and thermal characterization of nonedible oilseed residual waste as sustainable solid biofuel. *Waste Manag.*, 34(10), 1836–1846.
60. Douglas Smoot, L., 1984. Modeling of coal-combustion processes. *Prog. Energy Combust. Sci.*, 10(2), 229–267.
61. Dufour, A., Castro-d, M., Marchal, P., Brosse, N., Olcese, R., Bouroukba, M., Snape, C., Cedex, N. & Cedex, N., 2012. In Situ Analysis of Biomass Pyrolysis by High Temperature Rheology in Relations with ¹H NMR.
62. Eastwick, C.N., Pickering, S.J. & Aroussi, a., 1999. Comparisons of two commercial computational fluid dynamics codes in modelling pulverised coal combustion for a 2.5 MW burner. *Appl. Math. Model.*, 23(6), 437–446.
63. Eaton, A.M., Smoot, L.D., Hill, S.C. & Eatough, C.N., 1999. Components, formulations, solutions, evaluation, and application of comprehensive combustion models. *Prog. Energy Combust. Sci.*, 25(4), 387–436.
64. EC, 2000. Addressing the Constraints for Successful Replication of Demonstration Technologies for Co-Combustion of Biomass/Waste. *Bookl. DIS 1743/98-NL*.
65. ECN, 2014. Successful test with innovative renewable energy source at Amer power plant. Available at: <https://www.ecn.nl/news/item/successful-test-with-innovative-renewable-energy-source-at-amer-power-plant/>.
66. EIA, 2013a. International Energy Statistics - Coal Consumption. Available at: <http://www.eia.gov/cfapps/ipdbproject/IEDIndex3.cfm?tid=1&pid=1&aid=2> [Accessed March 15, 2013].
67. EIA, 2013b. International Energy Statistics - Coal Reserves. Available at: <http://www.eia.gov/cfapps/ipdbproject/IEDIndex3.cfm?tid=1&pid=7&aid=6> [Accessed March 15, 2013].
68. EIA, 2013c. International Energy Statistics - Natural Gas Consumption. Available at: <http://www.eia.gov/cfapps/ipdbproject/IEDIndex3.cfm?tid=3&pid=26&aid=2> [Accessed March 15, 2013].
69. EIA, 2013d. International Energy Statistics - Natural Gas Reserves. Available at: <http://www.eia.gov/cfapps/ipdbproject/IEDIndex3.cfm?tid=3&pid=3&aid=6> [Accessed March 15, 2013].

70. EIA, 2013e. International Energy Statistics - Petroleum Consumption. Available at: <http://www.eia.gov/cfapps/ipdbproject/IEDIndex3.cfm?tid=5&pid=5&aid=2> [Accessed March 15, 2013].
71. EIA, 2013f. International Energy Statistics - Petroleum Reserves. Available at: <http://www.eia.gov/cfapps/ipdbproject/IEDIndex3.cfm?tid=5&pid=57&aid=6> [Accessed March 15, 2013].
72. EU, 2009. DIRECTIVE 2009/28/EC OF THE EUROPEAN PARLIAMENT AND OF THE COUNCIL. *Off. J. Eur. Union*, 16–62.
73. EUBIA, 2013. Co-Combustion with Biomass. *Eur. Biomass Ind. Assoc.* Available at: <http://www.eubia.org/index.php/about-biomass/co-combustion-with-biomass> [Accessed March 25, 2013].
74. Felfli, F.F., Luengo, C.A., Suárez, J.A. & Beatón, P.A., 2005. Wood briquette torrefaction. *Energy Sustain. Dev.*, 9(3), 19–22.
75. Fernandes, A.M. a. P. et al., 2015. Chemical Characterization of *Jatropha curcas* L. Seed Oil and Its Biodiesel by Ambient Desorption/Ionization Mass Spectrometry. *Energy & Fuels*, 29(5), 3096–3103.
76. Fernández, C.M., Fiori, L., Ramos, M.J., Pérez, Á. & Rodríguez, J.F., 2015. Supercritical extraction and fractionation of *Jatropha curcas* L. oil for biodiesel production. *J. Supercrit. Fluids*, 97, 100–106.
77. Ferro, D., Vigouroux, V., Grimm, A., Zanzi, R., Mecánica, F. De & Oriente, U. De, 2004. Torrefaction of agricultural and forest residues. *Cubasolar 2004*.
78. Fletcher, T.H., Kerstein, a R., Pugmire, R.J. & Grant, D.M., 1990. Chemical percolation model for devolatilization. 2. Temperature and heating rate effects on product yields. *Energy & Fuels*, 4(1), 54–60.
79. Frey, G.W. & Linke, D.M., 2002. Hydropower as a renewable and sustainable energy resource meeting global energy challenges in a reasonable way. *Energy Policy*, 30(14), 1261–1265.
80. Fründ, R. & Lüdemann, H.-D., 1989. ¹³C-NMR Spectroscopy of Lignins and Lignocellulosic Materials. In *Physico-Chemical Characterisation of Plant Residues for Industrial and Feed Use*. Dordrecht: Springer Netherlands, pp. 110–117.
81. Gani, A., Morishita, K., Nishikawa, K. & Naruse, I., 2005. Characteristics of co-combustion of low-rank coal with biomass. *Energy & fuels*, (11), 1652–1659.
82. Gašparovič, L., Koreňová, Z. & Jelemenský, L., 2010. Kinetic study of wood chips decomposition by TGA. *Chem. Pap.*, 64(2), 45–53.
83. Gera, D., Mathur, M., Freeman, M. & O’Dowd, W., 2001. Moisture and Char Reactivity Modeling in Pulverized Coal Combustors. *Combust. Sci. Technol.*, 172(1), 35–69.

84. Ghenai, C. & Janajreh, I., 2010. CFD analysis of the effects of co-firing biomass with coal. *Energy Convers. Manag.*, 51(8), 1694–1701.
85. Gil, M. V, Casal, D., Pevida, C., Pis, J.J. & Rubiera, F., 2010. Bioresource Technology Thermal behaviour and kinetics of coal / biomass blends during co-combustion. *Bioresour. Technol.*, 101(14), 5601–5608.
86. Gil, M.V., García, R., Pevida, C. & Rubiera, F., 2015. Grindability and combustion behavior of coal and torrefied biomass blends. *Bioresour. Technol.*, 191, 205–212.
87. Gilardi, G., Abis, L. & Cass, a. E.G., 1995. Carbon-13 CP/MAS solid-state NMR and FT-IR spectroscopy of wood cell wall biodegradation. *Enzyme Microb. Technol.*, 17(3), 268–275.
88. Go, A.W., Sutanto, S., Zullaikah, S., Ismadji, S. & Ju, Y.-H., 2016. A new approach in maximizing and direct utilization of whole *Jatropha curcas* L. kernels in biodiesel production – Technological improvement. *Renew. Energy*, 85, 759–765.
89. Gu, M., Wu, C., Zhang, Y. & Chu, H., 2014. Study on combustion characteristics of two sizes pulverized coal in O₂/CO₂ atmosphere. *J. CO₂ Util.*, 7, 6–10.
90. Gubba, S.R., Ingham, D.B., Larsen, K.J., Ma, L., Pourkashanian, M., Tan, H.Z., Williams, a. & Zhou, H., 2012. Numerical modelling of the co-firing of pulverised coal and straw in a 300 MWe tangentially fired boiler. *Fuel Process. Technol.*, 104, 181–188.
91. Gubba, S.R., Ma, L., Pourkashanian, M. & Williams, a., 2011. Influence of particle shape and internal thermal gradients of biomass particles on pulverised coal/biomass co-fired flames. *Fuel Process. Technol.*, 92(11), 2185–2195.
92. Gübitz, G., Mittelbach, M. & Trabi, M., 1999. Exploitation of the tropical oil seed plant *Jatropha curcas* L. *Bioresour. Technol.*, 67, 73–82.
93. Guijun, W. et al., 2011. Pretreatment of biomass by torrefaction. *Chinese Sci. Bull.*, 56(14), 1442–1448.
94. Gupta, M., Yang, J. & Roy, C., 2003. Specific heat and thermal conductivity of softwood bark and softwood char particles. *Fuel*, 82(8), 919–927.
95. Haider, a. & Levenspiel, O., 1989. Drag coefficient and terminal velocity of spherical and nonspherical particles. *Powder Technol.*, 58(1), 63–70.
96. Hansen, L. & Nielsen, H., 2000. Influence of deposit formation on corrosion at a straw-fired boiler. *Fuel Process. Technol.*, 189–209.
97. Hein, K.R.. & Bemtgen, J., 1998. EU clean coal technology—co-combustion of coal and biomass. *Fuel Process. Technol.*, 54(1-3), 159–169.
98. Ho, Y.S., Harouna-Oumarou, H.A., Fauduet, H. & Porte, C., 2005. Kinetics and model building of leaching of water-soluble compounds of *Tilia* sapwood. *Sep. Purif. Technol.*, 45(3), 169–173.

99. Hubbert, M., 1949. Energy from fossil fuels. *Science* (80-), 109, 103–109.
100. Hughes, E. & Tillman, D., 1998. Biomass cofiring: status and prospects 1996. *Fuel Process. Technol.*
101. IEA, 2015. Key World Energy Statistics 2015.
102. IEA, 2007. World Energy Outlook 2007.
103. IEA-ETSAP & IRENA, 2013. Biomass Co- firing: Technology Brief. , (January 2013), 1–28. Available at: www.irena.org.
104. IKA-Werke, *IKA Calorimeter System C5000 - Operating Instructions*, Available at: http://www.ika.com/ika/product_art/manual/ika_c_5000_englisch.pdf.
105. IPCC, 2007. Climate Change 2007 : An Assessment of the Intergovernmental Panel on Climate Change. , (November), 12–17.
106. IPCC, 2014. *Climate Change 2014: Synthesis Report. Contribution of Working Groups I, II and III to the Fifth Assessment Report of the Intergovernmental Panel on Climate Change*,
107. James, D.W., Krishnamoorthy, G., Benson, S.A. & Seames, W.S., 2014. Modeling trace element partitioning during coal combustion. *Fuel Process. Technol.*, 126(3-4), 284–297.
108. Jassim, E.I., 2015. CFD Modeling of Toxic Element Evolved During Coal Combustion. *Arab. J. Sci. Eng.*
109. Jenkins, B., Bakker, R. & Wei, J., 1995. On the properties of washed straw. *Biomass and Bioenergy*, I(4), 177–200.
110. Jenkins, B. & Williams, R., 1999. Combustion of leached rice straw for power generation. *iomass: A growth opportunity in green energy and value-added products. Proceedings of the Fourth Biomass Conference of the Americas*. 1357–1363.
111. Jenkins, B.M., Baxter, L.L., Jr, T.R.M. & Miles, T.R., 1998. Combustion properties of biomass.
112. Jensen, P. a., Sander, B. & Dam-Johansen, K., 2001. Removal of K and Cl by leaching of straw char. *Biomass and Bioenergy*, 20(6), 447–457.
113. Jones, J.M., Patterson, P.M., Pourkashanian, M., Williams, a., Arenillas, a., Rubiera, F. & Pis, J.J., 1999. Modelling NOx formation in coal particle combustion at high temperature: An investigation of the devolatilization kinetic factors. *Fuel*, 78(10), 1171–1179.
114. Kargbo, F.F.R., Xing, J. & Zhang, Y., 2009. Pretreatment for energy use of rice straw: A review. *African J. Agric. Res.*, 4(December), 1560–1565.

115. Kavalek, M., Havrland, B., Ivanova, T., Hutla, P. & Skopec, P., 2013. Utilization of *Jatropha curcas* L. seed cake for production of solid biofuels. *Eng. Rural Dev.*, 536–540.
116. Khodier, A.H.M., Hussain, T., Simms, N.J., Oakey, J.E. & Kilgallon, P.J., 2012. Deposit formation and emissions from co-firing miscanthus with Daw Mill coal : Pilot plant experiments. *Fuel*, 101, 53–61.
117. Kirk, T. & Cullen, D., 1998. Enzymology and molecular genetics of wood degradation by white-rot fungi. *Environmentally Friendly Technologies for the Pulp and Paper Industry*.
118. Kobayashi, H., Howard, J.B. & Sarofim, A.F., 1977. Coal devolatilization at high temperatures. *Symp. Combust.*, 16(1), 411–425.
119. Koppejan, J., Sokhansanj, S., Melin, S. & Madrali, S., 2012. Status overview of torrefaction technologies. , (December), 1–54.
120. KSrividhya, P., Tamizharasan, T., Jayaraj, S. & Muralledharan, C., 2010. Characterization and Gasification using- *Jatropha Curcas* Seed Cake. *J. Biofuels*, 1(1), 30.
121. Lam, P.Y., Lim, C.J., Sokhansanj, S., Lam, P.S., Stephen, J.D., Pribowo, A. & Mabee, W.E., 2014. Leaching Characteristics of Inorganic Constituents from Oil Palm Residues by Water. *Ind. Eng. Chem. Res.*, 53(29), 11822–11827.
122. Lenth, R. V, 1989. Quick and Easy Analysis of Unreplicated Factorials. *Technometrics*, 31(4), 469–473.
123. Li, J., 2014. *Volumetric combustion of torrefied biomass for large percentage biomass co-firing up to 100% fuel switch (Doctoral Thesis)*, KTH-Royal Institute of Technology.
124. Li, M.-F., Li, X., Bian, J., Xu, J.-K., Yang, S. & Sun, R.-C., 2015. Influence of temperature on bamboo torrefaction under carbon dioxide atmosphere. *Ind. Crops Prod.*, 76, 149–157.
125. Li, Z., Jing, J., Ge, Z., Liu, G., Chen, Z. & Ren, F., 2009. Bituminous Coal-Fired Wall Boiler. *Numer. Heat Transf. Part A Appl.*, 55(6), 574–593.
126. Lobell, D.B. & Field, C.B., 2007. Global scale climate–crop yield relationships and the impacts of recent warming. *Environ. Res. Lett.*, 2(1), 014002.
127. Van Loo, S. & Koppejaan, J., 2008. *The Handbook of Biomass Combustion and Co-firing*, Earthscan.
128. Lu, H., Ip, E., Scott, J., Foster, P., Vickers, M. & Baxter, L.L., 2010. Effects of particle shape and size on devolatilization of biomass particle. *Fuel*, 89(5), 1156–1168.

129. Ma, L., Gharebaghi, M., Porter, R., Pourkashanian, M., Jones, J.M. & Williams, a., 2009. Modelling methods for co-fired pulverised fuel furnaces. *Fuel*, 88(12), 2448–2454.
130. Ma, L., Jones, J.M., Pourkashanian, M. & Williams, a., 2007. Modelling the combustion of pulverized biomass in an industrial combustion test furnace. *Fuel*, 86(12-13), 1959–1965.
131. Maciejewska, A., Veringa, H., Sanders, J. & Peteves, S.D., 2006. *Co-firing of Biomass with Coal: Constraints and Role of Biomass Pre-treatment*,
132. Magnussen, B.F. & Hjertager, B.H., 1977. On mathematical modeling of turbulent combustion with special emphasis on soot formation and combustion. *Symp. Combust.*, 16(1), 719–729.
133. Mani, S. & Sokhansanj, S., 2006. Economics of producing fuel pellets from biomass. *Appl. Eng. ...*, 22(3), 421–426.
134. Mann, P., Gahagan, L. & Gordon, M., 2003. *Giant Oil and Gas Fields of the Decade, 1990–1999*, American Association of Petroleum Geologists.
135. Mardon, S.M. & Hower, J.C., 2004. Impact of coal properties on coal combustion by-product quality: Examples from a Kentucky power plant. *Int. J. Coal Geol.*, 59(3-4), 153–169.
136. Mayoral, M., Izquierdo, M., Andres, J. & Rubio, B., 2001. Different approaches to proximate analysis by thermogravimetry analysis. *Thermochim. Acta*, 370, 91–97.
137. McKendry, P., 2002a. Energy production from biomass (Part 1): Overview of biomass. *Bioresour. Technol.*, 83(1), 37–46.
138. McKendry, P., 2002b. Energy production from biomass (Part 2): Conversion technologies. *Bioresour. Technol.*, 83(1), 47–54.
139. Meehl, G. a, Washington, W.M., Collins, W.D., Arblaster, J.M., Hu, A., Buja, L.E., Strand, W.G. & Teng, H., 2005. How much more global warming and sea level rise? *Science*, 307(5716), 1769–72.
140. Melkior, T., Jacob, S., Gerbaud, G., Hediger, S., Le Pape, L., Bonnefois, L. & Bardet, M., 2012. NMR analysis of the transformation of wood constituents by torrefaction. *Fuel*, 92(1), 271–280.
141. Ministry of Economy Trade and Industry of Japan, 2010. Establishment of the Strategic Energy Plan of Japan. Available at: http://www.meti.go.jp/english/press/data/20100618_08.html [Accessed March 20, 2013].
142. Minitab. 2016. *What is a Pareto chart of effects? - Minitab*. [ONLINE] Available at: [253](http://support.minitab.com/en-us/minitab/17/topic-library/modeling-

</div>
<div data-bbox=)

- statistics/doe/factorial-design-plots/what-is-a-pareto-chart-of-effects/. [Accessed 02 September 2016].
143. Molcan, P., Lu, G., Bris, T. Le, Yan, Y., Taupin, B. & Caillat, S., 2009. Characterisation of biomass and coal co-firing on a 3MWth Combustion Test Facility using flame imaging and gas/ash sampling techniques. *Fuel*, 88(12), 2328–2334.
 144. Morsi, S. & Alexander, A., 1972. An investigation of particle trajectories in two-phase flow systems. *J. Fluid Mech*, 55(2), 193–208.
 145. Narvaez, I. & Orío, A., 1996. Biomass gasification with air in an atmospheric bubbling fluidized bed. Effect of six operational variables on the quality of the produced raw gas. *Ind. Eng. Chem. Res.*, 5885(95), 2110–2120.
 146. NASA, 2016. Global Climate Change - Carbon Dioxide. Available at: <http://climate.nasa.gov/vital-signs/carbon-dioxide/> [Accessed March 23, 2016].
 147. National People's Congress, 2005. *The Renewable Energy Law of the People's Republic of China*,
 148. Neupane, S., Adhikari, S., Wang, Z., Ragauskas, a J. & Pu, Y., 2015. Effect of torrefaction on biomass structure and hydrocarbon production from fast pyrolysis. *Green Chem.*, 2406–2417.
 149. Nhuchhen, D.R. & Abdul Salam, P., 2012. Estimation of higher heating value of biomass from proximate analysis: A new approach. *Fuel*, 99, 55–63.
 150. Nielsen, H. & Frandsen, F., 2000. The implications of chlorine-associated corrosion on the operation of biomass-fired boilers. *Prog. Energy Combust. Sci.*, 26, 283–298.
 151. Nikolopoulos, N., Agraniotis, M., Violidakis, I., Karampinis, E., Nikolopoulos, a., Grammelis, P., Papapavlou, C., Tzivenis, S. & Kakaras, E., 2013. Parametric investigation of a renewable alternative for utilities adopting the co-firing lignite/biomass concept. *Fuel*, 113, 873–897.
 152. Niksa, S., 2000. Predicting the rapid devolatilization of diverse forms of biomass with bio-flashchain. *Proc. Combust. Inst.*, 28(2), 2727–2733.
 153. Nimlos, M.M.N., Brooking, E., Looker, M.J., Evans, R. & Robert, J., 2003. Biomass torrefaction studies with a molecular beam mass spectrometer. *Prepr. Pap.-Am. Chem. Soc.*, ..., 48(2), 590–591.
 154. Novaczek, I., 2000. Canada's Fossil Fuel Dependency. *Earth Action PEI*.
 155. Ohm, T.-I., Chae, J.-S., Kim, J.-K. & Oh, S.-C., 2015. Study on the characteristics of biomass for co-combustion in coal power plant. *J. Mater. Cycles Waste Manag.*, 17(2), 249–257.
 156. Öhman, M., Nordin, A. & Skrifvars, B., 2000. Bed agglomeration characteristics during fluidized bed combustion of biomass fuels. *Energy Fuels*, 14(1), 169–178.

157. Oleschko, H., Schimrosczyk, a, Lippert, H. & Muller, M., 2007. Influence of coal composition on the release of Na-, K-, Cl-, and S-species during the combustion of brown coal. *Fuel*, 86(15), 2275–2282.
158. Pandey, V.C., Singh, K., Singh, J.S., Kumar, A., Singh, B. & Singh, R.P., 2012. *Jatropha curcas*: A potential biofuel plant for sustainable environmental development. *Renew. Sustain. Energy Rev.*, 16(5), 2870–2883.
159. Park, J., Meng, J., Lim, K.H., Rojas, O.J., Park, S. & Hun, K., 2013. Transformation of lignocellulosic biomass during torrefaction. *J. Anal. Appl. Pyrolysis*, 100, 199–206.
160. Park, J.-K., Park, S., Kim, M., Ryu, C., Baek, S.H., Kim, Y.J., Kim, H.H. & Park, H.Y., 2015a. CFD analysis of combustion characteristics for fuel switching to bioliquid in oil-fired power plant. *Fuel*, 159, 324–333.
161. Park, S., Jeong, H. & Hwang, J., 2015b. 3-D CFD Modeling for Parametric Study in a 300-MWe One-Stage Oxygen-Blown Entrained-Bed Coal Gasifier. *Energies*, 8(5), 4216–4236.
162. Peng, J.H., Bi, X.T., Sokhansanj, S. & Lim, C.J., 2013. Torrefaction and densification of different species of softwood residues. *Fuel*, 111, 411–421.
163. Peng, P. & Zhou, W., 2014. The Next Generation Feedstock of Biofuel: *Jatropha* or *Chlorella* as Assessed by Their Life-Cycle Inventories. *Agriculture*, 4(3), 217–230.
164. Peng, S., Huang, J., Sheehy, J.E., Laza, R.C., Visperas, R.M., Zhong, X., Centeno, G.S., Khush, G.S. & Cassman, K.G., 2004. Rice yields decline with higher night temperature from global warming. *Proc. Natl. Acad. Sci. U. S. A.*, 101(27), 9971–5.
165. Pérez, J., Muñoz-Dorado, J., de la Rubia, T. & Martínez, J., 2002. Biodegradation and biological treatments of cellulose, hemicellulose and lignin: an overview. *Int. Microbiol.*, 5(2), 53–63.
166. Phanphanich, M. & Mani, S., 2011. Impact of torrefaction on the grindability and fuel characteristics of forest biomass. *Bioresour. Technol.*, 102(2), 1246–53.
167. Pillai, K.K., 1981. Influence of coal type on devolatilization and combustion in fluidized beds. *J. Inst. Energy*, 54, 142–150.
168. Pillai, M., 2014. *CFD Based Coal Combustion and Erosion Modelling for A 660 MWE, Super-Critical Tangentially Fired Pulverized Coal Boiler*. Indian Institute of Technology Gandhinagar.
169. Pimchuai, A., Dutta, A. & Basu, P., 2010. Torrefaction of Agriculture Residue To Enhance Combustible Properties†. *Energy & Fuels*, 24(9), 4638–4645.
170. Pokothoane, P.S., 2010. *Analysis of co-firing biomass with South African coal in pulverised coal boilers*. University of the Witwatersrand.

171. Rapagna, S., Jand, N., Kiennemann, A. & Foscolo, P., 2000. Steam-gasification of biomass in a fluidised-bed of olivine particles. *Biomass and Bioenergy*, 19, 187–197.
172. Ravichandran, P., Gibb, D. & Corscadden, K., 2013. Controlled Batch Leaching Conditions for Optimal Upgrading of Agricultural Biomass. *J. Sustain. Bioenergy Syst.*, 03(03), 186–193.
173. REN21, 2015. *Renewables 2015 Global Status Report*,
174. Retsch Technology, 2016. Camsizer functions and features. Available at: <http://www.retsch-technology.com/en/rt/products/dynamic-image-analysis/camsizer-p4/function-features/>.
175. Rezeau, A., Ramírez, J. a., Díez, L.I. & Royo, J., 2012. Numerical characterization of the aerodynamics in fixed-grate biomass burners. *Comput. Fluids*, 69, 45–53.
176. Rüdiger, H., Kicherer, A. & Greul, U., 1996. Investigations in combined combustion of biomass and coal in power plant technology. *Energy*. 789–796.
177. Sadaka, S. & Negi, S., 2009. Improvements of biomass physical and thermochemical characteristics via torrefaction process. *Environ. Prog. Sustain. ...*, 28(3), 427–434.
178. Said, N., Bishara, T., García-maraver, a. & Zamorano, M., 2013. Effect of water washing on the thermal behavior of rice straw. *Waste Manag.*, 33(11), 2250–2256
179. Sander, B., 1997. Properties of Danish biofuels and the requirements for power production. *Biomass and Bioenergy*, 12(3), 177–183.
180. Sarroza, A., Bennet, T., Eastwick, C., Liu, H. & Duncan, A., 2014. Characterising the effects of moisture on solid fuel combustion using experimental and computational fluid dynamics (CFD) analysis. In *10th European Conference on Coal Research and its Applications*.
181. Savolainen, K., 2003. Co-firing of biomass in coal-fired utility boilers. *Appl. Energy*, 74(3-4), 369–381.
182. Shafiee, S. & Topal, E., 2009. When will fossil fuel reserves be diminished? *Energy Policy*, 37(1), 181–189.
183. Sharma, A., Pareek, V. & Zhang, D., 2015. Biomass pyrolysis—A review of modelling, process parameters and catalytic studies. *Renew. Sustain. Energy Rev.*, 50, 1081–1096.
184. Sharma, R. & Sheth, P.N., 2015. Thermo-Chemical Conversion of Jatropha Deoiled Cake : Pyrolysis vs . Gasification. , 6(5).
185. Sheng, C. & Azevedo, J.L.T., 2005. Estimating the higher heating value of biomass fuels from basic analysis data. *Biomass and Bioenergy*, 28(5), 499–507.
186. Sheng, C. & Azevedo, J.L.T., 2002. Modeling biomass devolatilization using the chemical percolation devolatilization model for the main components. *Proc. Combust. Inst.*, 29(1), 407–414.

187. Sheng, C., Moghtaderi, B., Gupta, R. & Wall, T.F., 2004. A computational fluid dynamics based study of the combustion characteristics of coal blends in pulverised coal-fired furnace. *Fuel*, 83(11-12), 1543–1552. Available at: <http://linkinghub.elsevier.com/retrieve/pii/S001623610400064X> [Accessed September 29, 2014].
188. Shuangning, X., Zhihe, L., Baoming, L., Weiming, Y. & Xueyuan, B., 2006. Devolatilization characteristics of biomass at flash heating rate. , 85, 664–670.
189. Sievers, C., Marzioletti, T., Hoskins, T.J.C., Valenzuela Olarte, M.B., Agrawal, P.K. & Jones, C.W., 2009. Quantitative solid state NMR analysis of residues from acid hydrolysis of loblolly pine wood. *Bioresour. Technol.*, 100(20), 4758–4765.
190. Sindhu, R., Binod, P. & Pandey, A., 2015. Bioresource Technology Biological pretreatment of lignocellulosic biomass – An overview. *Bioresour. Technol.*, 199, 76–82.
191. Singh, R.N., Vyas, D.K., Srivastava, N.S.L. & Narra, M., 2008. SPRERI experience on holistic approach to utilize all parts of *Jatropha curcas* fruit for energy. *Renew. Energy*, 33(8), 1868–1873.
192. Solomon, P.R. & Serio, M. a., 1994. A characterization method and model for predicting coal conversion behaviour. Reply to Herod, A. and Kandiyoti, R. *Fuel* 1993, 72, 469. *Fuel*, 73(8), 1371.
193. Son, J.W. & Sohn, C.H., 2015. Evaluation of burnout performance of biomass wastes in a rocket-engine-based incinerator. *Fuel*, 143, 308–317.
194. Speight, J.G., 2005. *Handbook of Coal Analysis*, John Wiley & Sons.
195. Sricharoenchaikul, V. & Atong, D., 2009. Thermal decomposition study on *Jatropha curcas* L. waste using TGA and fixed bed reactor. *J. Anal. Appl. Pyrolysis*, 85(1-2), 155–162.
196. Stahl, R. & Henrich, E., 2004. Definition of a standard biomass. *RENEW Proj.* , 1–14.
197. Stam, A., Livingston, W., Cremers, M. & Brem, G., 2009. Review of models and tools for slagging and fouling prediction for biomass co-combustion. *ieabcc.nl*, (1), 1–18. Available at: http://www.ieabcc.nl/publications/slagging_fouling_in_cofiring.pdf [Accessed December 26, 2012].
198. Statfold Seed Developments Ltd, 2016. Cold Pressing. Available at: <http://www.statfold-oils.co.uk/natural-oils-and-health-and-beauty-bases/pross-and-service/cold-pressing-70> [Accessed March 22, 2016].

199. Stelte, W., Holm, J.K., Sanadi, A.R., Barsberg, S., Ahrenfeldt, J. & Henriksen, U.B., 2011a. A study of bonding and failure mechanisms in fuel pellets from different biomass resources. *Biomass and Bioenergy*, 35(2), 910–918.
200. Stelte, W., Holm, J.K., Sanadi, A.R., Barsberg, S., Ahrenfeldt, J. & Henriksen, U.B., 2011b. Fuel pellets from biomass: The importance of the pelletizing pressure and its dependency on the processing conditions. *Fuel*, 90(11), 3285–3290.
201. Stroh, A., Alobaid, F., Busch, J.-P., Ströhle, J. & Epple, B., 2015. 3-D numerical simulation for co-firing of torrefied biomass in a pulverized-fired 1 MWth combustion chamber. *Energy*, 85, 105–116.
202. TA Instruments, 2016. Q500 TGA - Specifications. Available at: <http://www.tainstruments.com/q500/> [Accessed March 25, 2016].
203. Tabet, F. & Gökalp, I., 2015. Review on CFD based models for co-firing coal and biomass. *Renew. Sustain. Energy Rev.*, 51, 1101–1114.
204. Tambunan, a. H., Situmorang, J.P., Silip, J.J., Joelianingsih, a. & Araki, T., 2012. Yield and physicochemical properties of mechanically extracted crude *Jatropha curcas* L oil. *Biomass and Bioenergy*, 43, 12–17.
205. Teixeira, P., Lopes, H., Gulyurtlu, I., Lapa, N. & Abelha, P., 2012. Evaluation of slagging and fouling tendency during biomass co-firing with coal in a fluidized bed. *Biomass and Bioenergy*, 39, 192–203.
206. Telmo, C., Lousada, J. & Moreira, N., 2010. Proximate analysis, backwards stepwise regression between gross calorific value, ultimate and chemical analysis of wood. *Bioresour. Technol.*, 101(11), 3808–15.
207. Thermo Electron, 2004. *Flash EA 1112 Elemental Analyzer Operating Manual*,
208. Thermo Fisher Scientific Inc., 2012. *Thermo Scientific iCAP Q ICP-MS Product Specifications*, Available at: <http://www.scispec.co.th/images/products/thermo/iCAPQ/icapq-ps.pdf>.
209. Tillman, D., 2000. Biomass cofiring: the technology, the experience, the combustion consequences. *Biomass and Bioenergy*, 19, 365–384.
210. Tonn, B., Dengler, V., Thumm, U., Piepho, H.-P. & Claupein, W., 2011. Influence of leaching on the chemical composition of grassland biomass for combustion. *Grass Forage Sci.*, 66(4), 464–473.
211. Topell Energy BV, 2015. Topell Torrefaction System. Available at: <http://www.topellenergy.com/technology/the-topell-torrefaction-system/>.
212. Tortosa Masiá, A.A., Buhre, B.J.P., Gupta, R.P. & Wall, T.F., 2007. Characterising ash of biomass and waste. *Fuel Process. Technol.*, 88(11-12), 1071–1081.

213. Trifonova, R., Babini, V., Postma, J., Ketelaars, J.J.M.H. & van Elsas, J.D., 2009. Colonization of torrefied grass fibers by plant-beneficial microorganisms. *Appl. Soil Ecol.*, 41(1), 98–106.
214. Tumuluru, J., Sokhansanj, S. & Wright, C., 2011. A Review on Biomass Torrefaction Process and Product Properties.
215. Turn, S., Kinoshita, C. & Ishimura, D., 1997. Removal of inorganic constituents of biomass feedstocks by mechanical dewatering and leaching. *Biomass and Bioenergy*.
216. Tuurna, S., Cronvall, O., Heikinheimo, L., Hänninen, M. & Tiihonen, H.T.O., 2003. State of the Art Report-Lifetime Analysis of Boiler Tubes. *VTT Ind. Syst. Espoo, Rep. No. TUO74-021828*.
217. Ulloa, C., Borrego, A.G., Helle, S., Gordon, A.L. & García, X., 2005. Char characterization and DTF assays as tools to predict burnout of coal blends in power plants. *Fuel*, 84(2-3), 247–257.
218. UN, 2013. The Secretary-General’s High-Level Group on Sustainable Energy For All. , (September). Available at: <http://www.un.org/wcm/content/site/sustainableenergyforall/home/Initiative> [Accessed March 20, 2013].
219. UN, 2012. The Secretary-General’s High-Level Group on Sustainable Energy For All - Report of the Co-Chairs. , (September). Available at: <http://www.un.org/wcm/content/site/sustainableenergyforall/home/Initiative> [Accessed March 20, 2013].
220. United Nations Foundation, 2013. Sustainable Energy for All. Available at: <http://www.sustainableenergyforall.org/> [Accessed March 20, 2013].
221. US Senate, 2012. *S. 2146 - The Clean Energy Standard Act*,
222. Vamvuka, D., Zografos, D. & Alevizos, G., 2008. Control methods for mitigating biomass ash-related problems in fluidized beds. *Bioresour. Technol.*, 99(9), 3534–44.
223. Vassilev, S. V., Baxter, D., Andersen, L.K. & Vassileva, C.G., 2010. An overview of the chemical composition of biomass. *Fuel*, 89(5), 913–933.
224. Vassilev, S. V., Baxter, D., Andersen, L.K., Vassileva, C.G. & Morgan, T.J., 2012. An overview of the organic and inorganic phase composition of biomass. *Fuel*, 94, 1–33.
225. Veijonen, K., Vainikka, P., Järvinen, T. & Alakangas, E., 2003. Biomass co-firing–an efficient way to reduce greenhouse gas emissions. *VTT Process. March*.
226. Vyas, D.K. & Singh, R.N., 2007. Feasibility study of Jatropha seed husk as an open core gasifier feedstock. *Renew. Energy*, 32(3), 512–517.

227. Wan, K., Wang, Z., He, Y., Xia, J., Zhou, Z., Zhou, J. & Cen, K., 2015. Experimental and modeling study of pyrolysis of coal, biomass and blended coal–biomass particles. *Fuel*, 139, 356–364.
228. Wang, Y. & Yan, L., 2008. CFD studies on biomass thermochemical conversion. *Int. J. Mol. Sci.*, 9(6), 1108–30.
229. Wang, Z., Wan, K., Xia, J., He, Y., Liu, Y. & Liu, J., 2015. Pyrolysis characteristics of coal, biomass and coal-biomass blends under high heating rate conditions: effects of particle diameter, fuel type and mixing condition. *Energy & Fuels*, 150629122348003.
230. Wannapeera, J., Fungtammasan, B. & Worasuwannarak, N., 2011. Effects of temperature and holding time during torrefaction on the pyrolysis behaviors of woody biomass. *J. Anal. Appl. Pyrolysis*, 92(1), 99–105.
231. WEC, 2010. 2010 Survey of Energy Resources.
232. Wen, J.-L., Sun, S.-L., Yuan, T.-Q., Xu, F. & Sun, R.-C., 2014. Understanding the chemical and structural transformations of lignin macromolecule during torrefaction. *Appl. Energy*, 121, 1–9.
233. Werther, J., Saenger, M., Hartge, E.-U., Ogada, T. & Siagi, Z., 2000. Combustion of agricultural residues. *Prog. Energy Combust. Sci.*, 26(1), 1–27.
234. Wever, D.-A.Z., Heeres, H.J. & Broekhuis, A. a., 2012. Characterization of Physic nut (*Jatropha curcas* L.) shells. *Biomass and Bioenergy*, 37, 177–187.
235. Wieck-Hansen, K., Overgaard, P. & Larsen, O., 2000. Cofiring coal and straw in a 150 MW e power boiler experiences. *Biomass and Bioenergy*, 19, 395–409.
236. Williams, a., Pourkashanian, M. & Jones, J.M., 2001. Combustion of pulverised coal and biomass. *Prog. Energy Combust. Sci.*, 27(6), 587–610.
237. Williams, a., Pourkashanian, M. & Jones, J.M., 2000. The combustion of coal and some other solid fuels. *Proc. Combust. Inst.*, 28(2), 2141–2162.
238. Williams, A., Backreedy, R., Habib, R., Jones, J.M. & Pourkashanian, M., 2002. Modelling coal combustion: the current position. *Fuel*, 81(5), 605–618.
239. Wu, C.-T. & Lin, F.-C., 2012. The Properties of Torrefied Biomass from Six Major Bamboos in Taiwan. In *Proceedings of the 55th International Convention of Society of Wood Science and Technology*. pp. 1–8.
240. Yan, W. & Acharjee, T., 2009. Thermal pretreatment of lignocellulosic biomass. ... *Prog. Sustain. ...*, 28(3), 435–440.
241. Yang, H. et al., 2006. In-Depth Investigation of Biomass Pyrolysis Based on Three Major Components : Hemicellulose , Cellulose and Lignin. , (17), 388–393.
242. Yang, Y.B., Sharifi, V.N., Swithenbank, J., Ma, L., I, L., Jones, J.M., Pourkashanian, M., Williams, A. & Darvell, L.I., 2008. Combustion of a Single

- Particle of Biomass Combustion of a Single Particle of Biomass. *Energy*, (8), 306–316.
243. Yin, C., Kaer, S.K., Rosendahl, L. & Hvid, S.L., 2010. Co-firing straw with coal in a swirl-stabilized dual-feed burner: modelling and experimental validation. *Bioresour. Technol.*, 101(11), 4169–78.
 244. Yin, C., Rosendahl, L. a. & Kær, S.K., 2008. Grate-firing of biomass for heat and power production. *Prog. Energy Combust. Sci.*, 34(6), 725–754. Available at: <http://linkinghub.elsevier.com/retrieve/pii/S0360128508000245>
 245. Yin, C., Rosendahl, L., Kær, S.K. & Condra, T.J., 2004. Use of numerical modeling in design for co-firing biomass in wall-fired burners. *Chem. Eng. Sci.*, 59(16), 3281–3292.
 246. Yin, C.-Y., 2011. Prediction of higher heating values of biomass from proximate and ultimate analyses. *Fuel*, 90(3), 1128–1132.
 247. Yu, C., Thy, P., Wang, L., Anderson, S.N.N., VanderGheynst, J.S.S., Upadhyaya, S.K.K. & Jenkins, B.M.M., 2014. Influence of leaching pretreatment on fuel properties of biomass. *Fuel Process. Technol.*, 128, 43–53.
 248. Yuen, R.K.K., Yeoh, G.H., de Vahl Davis, G. & Leonardi, E., 2007. Modelling the pyrolysis of wet wood - I. Three-dimensional formulation and analysis. *Int. J. Heat Mass Transf.*, 50(21-22), 4371–4386.
 249. Zanzi Vigouroux, R., Tito Ferro, D., Torres, A., Beaton Soler, P. & Björnbom, E., 2004. BIOMASS TORREFACTION. *2nd World Conf. Biomass Energy, Ind. Clim. Prot.*, 859–862.
 250. Zawadzki, J., Wisniewski, M., 2002. ¹³C NMR study of cellulose thermal treatment. *J. Anal. Appl. Pyrolysis*, 62, 111–121.
 251. Zevenhoven, M., Yrjas, P., Skrifvars, B.-J. & Hupa, M., 2012. Characterization of Ash-Forming Matter in Various Solid Fuels by Selective Leaching and Its Implications for Fluidized-Bed Combustion. *Energy & Fuels*, 26(10), 6366–6386.
 252. Zhang, J., Prationo, W., Zhang, L. & Zhang, Z., 2013. Computational Fluid Dynamics Modeling on the Air-Firing and Oxy-fuel Combustion of Dried Victorian Brown Coal. *Energy & Fuels*, 27(8), 4258–4269.
 253. Zhang, S., Dong, Q., Zhang, L., Xiong, Y., Liu, X. & Zhu, S., 2015. Effects of water washing and torrefaction pretreatments on rice husk pyrolysis by microwave heating. *Bioresour. Technol.*, 193, 442–448.
 254. Zhou, H., Yang, Y., Liu, H. & Hang, Q., 2014. Numerical simulation of the combustion characteristics of a low NO_x swirl burner: Influence of the primary air pipe. *Fuel*, 130(x), 168–176.

Appendices

Appendix 1 – Matlab script to calculate devolatilisation kinetics

Matlab script to process TGA and apply the Coats-Redfern method to calculate devolatilisation kinetics.

```
clear all
hold on
for k=1:n %Read n number of TGA files in succession, n has to be
set
    %---Read data from TGA file into array-----%
    filename = sprintf('at%d', k);
    fileID = fopen(filename);
    C = textscan(fileID,'%f %f %f %f','headerlines',60);
    fclose(fileID);
    time = [C{1}];
    temp = [C{2}];
    mass = [C{3}];
    dmdt = [C{4}];
    %-----%
    %---Filter devolatilisation segment of data-----%
    indexesInRange = temp>150 & temp<400;
    time = time(indexesInRange);
    temp = temp(indexesInRange);
    mass = mass(indexesInRange);
    dmdt = dmdt(indexesInRange);
    %-----%
    %--Calculation of variables in Coats-Redfern equation-----%
    x = (mass-mass(1))/(mass(end)-mass(1));
    T = temp+273;
    Tsq = power(T,2);
    invT = power(T,-1);
    y = log(-log(1-x)./Tsq);
    invT = invT(2:(length(invT)-1));
    y = y(2:(length(y)-1));
    invT1 = [ones(length(invT),1) invT];
    %-----%
    %---Linear regression and plotting regression line-----%
    rc = invT1\y;
    rx = linspace(invT(1),invT(end));
    ry = rc(1)+(rc(2).*rx);
    plot(invT,y)
    plot(rx,ry)
    %-----%
    %---Calculation of E and A from regression coefficients---%
    E = -8.314*rc(2);
    A = exp(rc(1))*20*E/8.314;
    results(k,1)=E;
```

```

        results(k,2)=A;
        %-----%
end
hold off

```

Appendix 2 – Matlab script for DTG processing

Matlab script to generate DTG plots, pick out the peaks in the DTG plots and store the peak height and temperature at which the peaks occur.

```

clear all
hold on
for k=1:n %Read n number of TGA files in succession, n has to be set
    %---Read data from TGA file into array-----%
    filename = sprintf('%d', k);
    fileID = fopen(filename);
    sample_name = textscan(fileID,'%s %s',1,'headerlines',11);
    sample_name{:}
    C = textscan(fileID,'%f %f %f %f','headerlines',50);
    fclose(fileID);
    time = [C{1}];
    temp = [C{2}];
    mass = [C{3}];
    dmdt = [C{4}];
    %-----%
    %---Filter devolatilisation segment of data-----%
    indexesInRange = dmdt>1 & time<60;
    temp = temp(indexesInRange);
    dmdt = dmdt(indexesInRange);
    %-----%
    %---Find peaks-----%
    [pks,locs] = findpeaks(dmdt,temp,'minpeakprominence',0.1);
    %-----%
    %---Curve plotting-----%
    plot(temp,dmdt,'linewidth',2)
    xlabel = sprintf('Temperature (%C)',
char(176));xlabel(xxlabel,'FontSize',16);
    ylabel('dm/dt (%/min)', 'FontSize',16);
    set(gca, 'FontSize',16)
    %-----%
    %---Storing peak heights and corresponding temperatures---%
    for kk=1:length(pks)
        results(k, (2*kk)-1)=pks(kk);
        results(k, (2*kk))=locs(kk);
    end
end
hold off
legend(sprintf('200%cC',char(176)),sprintf('250%cC',char(176)),sprin
tf('300%cC',char(176)))

```

Appendix 3 – Full data sets: Characterisation

Table A-1: Proximate analysis of untreated *Jatropha curcas* seed cake

	Type A						Type B					
Moisture (% wt)	2.87	3.19	3.50	4.21	4.16	3.80	4.30	4.25	4.36	3.49	3.40	3.70
	3.62 (mean)						3.92					
VM (% wt)	68.97	68.28	69.23	70.17	69.19	69.74	73.56	78.61	74.88	76.11	76.91	74.20
	69.26						75.71					
FC (% wt)	22.13	22.40	22.03	20.05	21.27	20.46	17.82	13.39	16.43	15.93	15.59	17.73
	21.39						16.15					
Ash (% wt)	6.01	6.07	5.23	5.56	5.34	5.98	4.31	3.75	4.31	4.45	4.07	4.36
	5.70						4.21					
Dry ash (% wt)	6.19	6.26	5.42	5.80	5.57	6.22	4.51	3.92	4.51	4.61	4.21	4.52
	5.91						4.38					
Dry VM (% wt)	71.01	70.53	71.74	73.25	72.19	72.49	76.86	82.10	78.30	78.86	79.62	77.05
	71.87						78.80					
Dry FC (% wt)	22.78	23.14	22.83	20.93	22.19	21.27	18.62	13.98	17.18	16.51	16.14	18.41
	22.19						16.81					
DAF VM (% wt)	75.69	75.24	75.85	77.76	76.46	77.30	80.49	85.44	81.99	82.67	83.12	80.70
	76.38						82.40					
DAF FC (% wt)	24.29	24.68	24.14	22.22	23.50	22.68	19.50	14.55	17.99	17.30	16.85	19.28
	23.58						17.58					

Table A-2: Ultimate analysis of untreated *Jatropha curcas* seed cake

	Type A					Type B				
C (% wt)	53.81	54.33	54.20	53.51	54.94	47.65	48.06	47.77	48.75	48.14
	54.16 (mean)					48.08				
Dry C (% wt)	56.00	56.54	56.41	55.69	57.18	49.44	49.86	49.57	50.59	49.95
	56.37					49.88				
DAF C (% wt)	58.57	59.13	59.00	58.25	59.80	52.55	52.99	52.68	53.76	53.09
	58.95					53.02				
H (% wt)	7.49	7.67	8.15	7.27	8.07	6.45	6.21	6.37	6.33	6.32
	7.73					6.33				
Dry H (% wt)	7.80	7.98	8.48	7.57	8.40	6.69	6.44	6.61	6.57	6.55
	8.05					6.57				
DAF H (% wt)	8.16	8.35	8.87	7.91	8.78	7.11	6.85	7.03	6.98	6.97
	8.42					6.99				
N (% wt)	3.74	3.87	5.99	3.41	3.40	5.32	4.57	4.84	3.77	4.77
	4.08					4.65				
Dry N (% wt)	3.89	4.03	6.23	3.55	3.54	5.52	4.74	5.02	3.91	4.95
	4.25					4.83				
DAF N (% wt)	4.07	4.21	6.52	3.71	3.70	5.87	5.03	5.34	4.15	5.26
	4.44					5.13				

Dry O (% wt)	27.93	27.06	24.49	28.81	26.49	32.44	33.05	32.89	33.03	32.64
	26.96					32.81				
DAF O (% wt)	29.21	28.30	25.61	30.13	27.71	34.47	35.12	34.95	35.10	34.69
	28.19					34.87				

Table A-3: HHV of untreated *Jatropha curcas* seed cake

	Type A			Type B		
HHV (MJ/kg)	20.809	20.815	20.668	24.178	24.060	23.926
	20.764 (mean)			24.055		
Dry HHV (MJ/kg)	21.591	21.597	21.444	25.164	25.042	24.902
	21.544			25.036		

Table A-4: Inorganic content of untreated *Jatropha curcas* seed cake, measured by ICP-MS/IC

	Type A					Type B				
K (% wt)	1.95	1.94	1.98	2.11	2.15	1.60	1.65	1.73	2.17	1.58
	2.03 (mean)					1.75				
Mg (% wt)	0.44	0.44	0.45	0.48	0.48	0.36	0.39	0.41	0.49	0.37
	0.46					0.40				
Ca (% wt)	0.22	0.21	0.22	0.24	0.24	0.17	0.18	0.19	0.24	0.17
	0.23					0.19				
S (% wt)	0.26	0.26	0.27	0.30	0.31	0.23	0.25	0.27	0.38	0.24
	0.28					0.27				
P (% wt)	0.76	0.71	0.79	0.78	0.78	0.61	0.66	0.67	0.63	0.65
	0.76					0.64				
Cl (% wt)	-					0.33	0.33	0.34	0.33	0.34
						0.33				

Table A-5: Inorganic content of untreated *Jatropha curcas* seed cake, measured by XRF

	Type A			Type B		
K (% wt)	6.59	6.56	6.77	5.86	5.67	5.93
	6.64 (mean)			5.82		
Mg (% wt)	0.36	0.38	0.43	0.34	0.30	0.27
	0.39			0.30		
Ca (% wt)	0.91	0.91	0.97	0.86	0.86	0.87
	0.93			0.86		
S (% wt)	0.58	0.58	0.55	0.55	0.55	0.48
	0.57			0.53		
P (% wt)	1.38	1.32	1.37	1.38	1.48	1.48
	1.36			1.45		
Cl (% wt)	0.69	0.90	0.74	0.78	0.81	0.75
	0.78			0.78		

Table A-6: Devolatilisation kinetics of untreated *Jatropha curcas* seed cake

	Type A				Type B			
	63168	62879	63314	63037	61435	60214	59830	61258

E (J/mol)	63099 (mean)				60684			
A (s)	1255	1148	1224	1144	634	507	462	624
	1193				557			

Table A-7: Characterisation data of torrefied (250°C/30 min) fine type A used for DTF/CFD

Moisture (% wt)	2.77	3.78	3.01	2.95	2.96	2.92
	3.06 (mean)					
VM (% wt)	58.79	61.94	61.49	61.17	62.30	61.37
	61.18					
FC (% wt)	30.50	26.79	27.93	28.78	27.61	28.86
	28.41					
Ash (% wt)	7.91	7.45	7.55	7.10	7.12	6.85
	7.33					
C (% wt)	56.33		57.23		56.22	
	56.59					
Dry C (% wt)	58.36		59.29		58.24	
	58.63					
DAF C (% wt)	61.49		57.23		56.22	
	58.31					
H (% wt)	5.73		5.79		5.84	
	5.79					
Dry H (% wt)	5.53		5.60		5.65	
	5.59					
DAF H (% wt)	5.52		5.79		5.84	
	5.72					
N (% wt)	4.40		4.20		4.64	
	4.41					
Dry N (% wt)	4.56		4.35		4.81	
	4.57					
DAF N (% wt)	4.80		4.20		4.64	
	4.55					
Dry O (% wt)	25.57		30.76		31.30	
	29.21					
DAF O (% wt)	28.18		32.78		33.30	
	31.42					
E (J/mol)	78195		79841		78646	
	79248					
A (s⁻¹)	11848		14815		12401	
	13805					

Appendix 4 – Full data sets: Torrefaction

Table A-8: Key properties for primary torrefaction study (type B)

Temp (°C)	200														
Time (min)	0			15			30			45			60		
Mass of raw sample (g)	25.11	25.02	25.09	25.28	25.21	25.03	25.26	25.15	25.43	25.1	25.12	25.22	25.08	25.29	25.07
Mass of torrefied sample (g)	24.47	24.35	24.03	23.94	23.89	23.36	23.49	23.35	23.02	22.97	23.26	22.61	22.96	22.95	22.56
Mass yield (%)	97.45	97.32	95.78	94.70	94.76	93.33	92.99	92.84	90.52	91.51	92.60	89.65	91.55	90.75	89.99
	96.85 (mean)			94.26			92.12			91.25			90.76		
Moisture (%)	2.94	4.10	3.56	4.34	4.05	3.17	2.43	2.47	1.28	1.75	2.31	3.21	2.42	2.63	1.93
	3.53			3.85			2.06			2.43			2.33		
VM (%)	74.29	76.83	75.65	75.48	73.82	73.95	72.36	71.29	74.78	61.36	74.04	74.52	74.02	75.18	77.01
	75.59			74.42			72.81			69.97			75.40		
FC (%)	16.89	14.92	14.85	17.02	17.51	16.73	17.36	20.90	18.47	13.09	18.83	17.78	17.11	17.17	16.28
	15.55			17.09			18.91			16.57			16.85		
Ash (%)	5.85	4.21	5.92	3.15	4.62	6.15	7.84	5.34	5.45	23.79	4.80	4.47	6.44	5.00	4.76
	5.33			4.64			6.21			11.02			5.40		
Dry ash (%)	6.03	4.39	6.14	3.29	4.81	6.35	8.03	5.48	5.52	24.21	4.92	4.61	6.60	5.13	4.85
	5.52			4.82			6.34			11.25			5.53		
DAF VM (%)	81.45	83.79	83.57	81.59	80.82	81.55	80.63	77.33	80.17	82.41	79.71	80.71	81.21	81.39	82.53
	82.94			81.32			79.38			80.95			81.71		
DAF FC (%)	18.52	16.27	16.41	18.40	19.17	18.45	19.34	22.67	19.80	17.58	20.27	19.26	18.77	18.59	17.45
	17.07			18.67			20.61			19.04			18.27		
HHV (MJ/kg)	24.468	24.202	24.624	24.514	24.803	26.010	25.149	25.210	25.626	26.382	25.728	25.699	25.571	25.639	25.723
	24.431			25.109			25.328			25.936			25.644		
Energy yield (%)	99.13	97.92	98.04	96.51	97.71	100.91	97.22	97.30	96.44	100.37	99.04	95.78	97.32	96.72	96.23
	98.36			98.38			96.99			98.39			96.76		

Table A-8 (contd.)

Temp (°C)	225														
Time (min)	0			15			30			45			60		
Mass of raw sample (g)	25.06	25.27	25.11	25.02	25.17	25.13	25.13	25.32	25.08	25.12	25.02	25.08	25.04	24.98	25.23
Mass of torrefied sample (g)	24.16	24.38	24.01	23.07	23.04	22.2	21.57	21.84	21.3	21.36	21.28	20.27	21.05	21	20.99
Mass yield (%)	96.41	96.48	95.62	92.21	91.54	88.34	85.83	86.26	84.93	85.03	85.05	80.82	84.07	84.07	83.19
	96.17			90.69			85.67			83.64			83.78		
Moisture (%)	3.97	3.07	3.70	3.05	2.50	3.32	2.64	3.45	3.03	3.28	2.25	2.83	1.91	2.25	2.87
	3.58			2.96			3.04			2.79			2.34		
VM (%)	78.69	74.64	77.23	75.07	75.10	73.14	73.04	71.51	73.06	74.64	72.14	73.06	70.76	73.10	71.85
	76.85			74.44			72.54			73.28			71.90		
FC (%)	14.69	17.28	15.31	17.38	17.17	19.19	19.49	20.34	19.88	16.22	20.35	19.98	21.95	19.17	20.01
	15.76			17.91			19.90			18.85			20.38		
Ash (%)	2.63	5.00	3.74	4.49	5.21	4.33	4.79	4.68	3.47	5.84	5.25	4.08	5.37	5.47	5.26
	3.79			4.68			4.31			5.06			5.37		
Dry ash (%)	2.74	5.15	3.88	4.63	5.35	4.48	4.92	4.84	3.58	6.03	5.37	4.20	5.47	5.60	5.41
	3.93			4.82			4.45			5.20			5.49		
DAF VM (%)	84.25	81.19	83.44	81.19	81.37	79.20	78.90	77.83	78.14	82.12	78.00	78.48	76.31	79.22	78.20
	82.96			80.59			78.29			79.53			77.91		
DAF FC (%)	15.73	18.80	16.54	18.80	18.60	20.78	21.05	22.14	21.26	17.85	22.00	21.46	23.67	20.77	21.78
	17.02			19.39			21.48			20.44			22.08		
HHV (MJ/kg)	25.172	24.959	24.752	26.136	26.248	25.484	26.511	26.263	26.638	27.375	27.069	27.249	27.551	27.725	26.892
	24.961			25.956			26.471			27.231			27.389		
Energy yield (%)	100.89	100.11	98.39	100.18	99.88	93.59	94.60	94.17	94.05	96.77	95.71	91.55	96.28	96.89	93.01
	99.79			97.89			94.27			94.68			95.40		

Table A-8 (contd.)

Temp (°C)	250														
Time (min)	0			15			30			45			60		
Mass of raw sample (g)	25.12	25.2	25.14	25.24	25.14	25.15	24.9	25.03	25.16	25.08	25.13	25.06	24.96	25.1	25.05
Mass of torrefied sample (g)	23.7	23.82	23.53	21.05	20.69	20.42	19.19	19.86	19.31	18.69	18.87	18.37	18.98	18.48	18.86
Mass yield (%)	94.35	94.52	93.60	83.40	82.30	81.19	77.07	79.34	76.75	74.52	75.09	73.30	76.04	73.63	75.29
	94.16			82.30			77.72			74.31			74.99		
Moisture (%)	2.67	3.16	2.28	1.79	2.34	2.97	2.41	3.01	2.43	2.83	2.55	1.02	2.88	2.47	1.58
	2.70			2.36			2.61			2.13			2.31		
VM (%)	74.98	77.12	77.40	72.11	70.80	70.33	65.73	61.49	70.30	66.84	68.13	67.99	67.37	67.12	73.25
	76.50			71.08			65.84			67.65			69.25		
FC (%)	15.55	14.60	15.75	20.51	21.57	19.70	25.54	27.92	21.61	24.63	23.58	24.64	24.40	26.63	20.77
	15.30			20.59			25.02			24.28			23.93		
Ash (%)	6.81	5.10	4.52	5.60	5.27	6.98	6.30	7.56	5.65	5.69	5.73	6.31	5.33	3.78	4.39
	5.48			5.95			6.51			5.91			4.50		
Dry ash (%)	7.00	5.27	4.63	5.70	5.40	7.19	6.46	7.79	5.79	5.85	5.88	6.38	5.49	3.87	4.46
	5.63			6.10			6.68			6.04			4.61		
DAF VM (%)	82.84	84.06	83.05	77.86	76.63	78.09	72.00	68.75	76.48	73.06	74.28	73.37	73.40	71.59	77.90
	83.32			77.53			72.41			73.57			74.30		
DAF FC (%)	17.18	15.91	16.90	22.15	23.35	21.88	27.98	31.22	23.51	26.92	25.71	26.59	26.58	28.40	22.09
	16.66			22.46			27.57			26.41			25.69		
HHV (MJ/kg)	24.847	25.022	25.361	27.701	28.291	27.167	27.533	27.922	28.188	29.384	29.296	28.740	28.210	28.379	28.365
	25.077			27.720			27.881			29.140			28.318		
Energy yield (%)	97.45	98.32	98.68	96.04	96.79	91.70	88.21	92.10	89.94	91.03	91.45	87.58	89.18	86.86	88.78
	98.15			94.84			90.08			90.02			88.27		

Table A-8 (contd.)

Temp (°C)	275														
Time (min)	0			15			30			45			60		
Mass of raw sample (g)	25.12	25.18	25.25	25.03	25.13	25.28	25.24	25.09	25.33	25.21	25.17	25.12	25.23	25.07	25.04
Mass of torrefied sample (g)	23.04	23.08	22.9	17.74	17.34	18.58	17.37	17.35	17.14	16.8	16.94	16.39	16.58	16.25	15.74
Mass yield (%)	91.72	91.66	90.69	70.87	69.00	73.50	68.82	69.15	67.67	66.64	67.30	65.25	65.72	64.82	62.86
	91.36			71.12			68.55			66.40			64.46		
Moisture (%)	2.52	2.73	2.93	2.23	2.71	2.80	2.27	2.66	2.67	2.27	2.58	2.90	2.29	2.83	3.03
	2.72			2.58			2.53			2.58			2.71		
VM (%)	74.47	76.33	75.66	64.71	65.10	69.52	65.31	66.12	68.29	63.23	64.30	65.00	64.18	63.36	64.38
	75.49			66.44			66.57			64.18			63.97		
FC (%)	18.11	15.72	16.54	26.75	26.33	22.44	26.31	25.04	22.77	28.17	26.77	26.26	26.70	26.35	27.16
	16.79			25.17			24.71			27.07			26.74		
Ash (%)	4.89	5.16	4.85	6.31	5.85	5.22	6.07	6.15	6.26	6.30	6.34	5.81	6.91	7.45	5.40
	4.97			5.79			6.16			6.15			6.59		
Dry ash (%)	5.02	5.30	5.00	6.45	6.01	5.37	6.22	6.32	6.43	6.45	6.51	5.98	7.07	7.66	5.57
	5.11			5.94			6.32			6.31			6.77		
DAF VM (%)	80.43	82.86	82.04	70.75	71.20	75.58	71.26	72.51	74.99	69.16	70.60	71.20	70.68	70.61	70.31
	81.78			72.51			72.92			70.32			70.53		
DAF FC (%)	19.56	17.07	17.94	29.24	28.80	24.40	28.71	27.46	25.00	30.81	29.39	28.76	29.40	29.37	29.66
	18.19			27.48			27.06			29.66			29.48		
HHV (MJ/kg)	26.454	26.018	26.213	30.055	29.648	28.624	30.165	29.793	29.723	30.619	30.109	29.811	30.574	30.119	29.951
	26.228			29.442			29.894			30.180			30.215		
Energy yield (%)	100.87	99.14	98.83	88.55	85.05	87.46	86.30	85.65	83.61	84.83	84.24	80.86	83.53	81.16	78.27
	99.61			87.02			85.19			83.31			80.98		

Table A-8 (contd.)

Temp (°C)	300														
Time (min)	0			15			30			45			60		
Mass of raw sample (g)	25.38	25	25.03	25.12	25.12	25.01	25.22	25.16	25.06	25.03	25.08	25.21	24.98	25.2	25.13
Mass of torrefied sample (g)	20.24	18.38	20.91	16.17	15.95	15.75	15.36	15.08	14.88	14.67	14.95	13.83	14.41	14.35	13.76
Mass yield (%)	79.75	73.52	83.54	64.37	63.50	62.97	60.90	59.94	59.38	58.61	59.61	54.86	57.69	56.94	54.76
	78.94			63.61			60.07			57.69			56.46		
Moisture (%)	2.34	2.22	1.65	2.65	2.52	2.84	2.47	2.40	2.63	3.43	2.58	3.05	2.47	2.48	1.85
	2.07			2.67			2.50			3.02			2.27		
VM (%)	70.18	70.79	75.91	63.04	61.61	61.66	60.10	56.87	61.20	56.06	60.83	58.99	57.56	52.79	60.87
	72.29			62.10			59.39			58.63			57.07		
FC (%)	20.38	19.98	18.51	27.63	29.36	28.81	29.93	32.79	29.31	34.04	28.82	30.88	30.83	31.42	30.89
	19.62			28.60			30.68			31.25			31.05		
Ash (%)	7.10	7.00	3.91	6.67	6.48	6.69	7.48	7.93	6.85	6.46	7.75	7.07	9.13	8.83	6.38
	6.01			6.61			7.42			7.09			8.11		
Dry ash (%)	7.27	7.16	3.98	6.85	6.65	6.88	7.67	8.13	7.04	6.69	7.96	7.29	9.36	9.05	6.50
	6.14			6.79			7.61			7.31			8.30		
DAF VM (%)	77.50	77.98	80.38	69.52	67.70	68.15	66.74	63.42	67.61	62.21	67.84	65.63	65.11	59.52	66.33
	78.62			68.46			65.93			65.23			63.65		
DAF FC (%)	22.51	22.01	19.60	30.47	32.26	31.84	33.24	36.57	32.38	37.77	32.14	34.36	34.87	35.43	33.66
	21.37			31.52			34.06			34.76			34.65		
HHV (MJ/kg)	27.615	27.806	27.161	29.688	30.625	30.268	29.990	29.880	30.430	30.710	30.073	30.330	29.765	29.700	30.048
	27.527			30.194			30.100			30.371			29.838		
Energy yield (%)	91.55	84.99	94.33	79.45	80.84	79.24	75.93	74.45	75.11	74.83	74.52	69.17	71.38	70.31	68.40
	90.29			79.84			75.17			72.84			70.03		

Table A-9: Ultimate analysis for primary torrefaction study (type B)

Temp (°C)	200								
Time (min)	0			30			60		
Dry C (%)	54.04	55.23	54.48	57.91	62.72	56.61	58.28	57.67	58.80
	54.59 (mean)			59.08			58.25		
Dry H (%)	7.45	7.15	7.04	8.20	7.30	7.95	7.91	7.50	8.27
	7.21			7.82			7.89		
Dry N (%)	3.40	3.54	3.29	5.12	3.61	4.76	4.77	4.10	5.26
	3.41			4.49			4.71		
Dry O (%)	29.07	29.69	29.05	20.74	20.90	25.16	22.45	25.59	22.82
	29.27			22.27			23.62		
dry H/C	0.14	0.13	0.13	0.14	0.12	0.14	0.14	0.13	0.14
	0.13			0.13			0.14		
dry O/C	0.54	0.54	0.53	0.36	0.33	0.44	0.39	0.44	0.39
	0.54			0.38			0.41		

Temp (°C)	250								
Time (min)	0			30			60		
Dry C (%)	60.17	56.93	56.86	61.80	64.84	62.05	62.69	63.26	62.30
	57.99			62.90			62.75		
Dry H (%)	8.84	7.79	7.98	6.63	8.22	7.49	7.65	7.16	7.75
	8.20			7.45			7.52		
Dry N (%)	5.71	4.55	4.81	3.16	4.57	3.97	4.18	3.33	3.85
	5.02			3.90			3.79		
Dry O (%)	18.28	25.46	25.72	21.94	14.58	20.70	19.99	22.37	21.65
	23.15			19.07			21.34		
dry H/C	0.15	0.14	0.14	0.11	0.13	0.12	0.12	0.11	0.12
	0.14			0.12			0.12		
dry O/C	0.30	0.45	0.45	0.36	0.22	0.33	0.32	0.35	0.35
	0.40			0.30			0.34		

Temp (°C)	300								
Time (min)	0			30			60		
Dry C (%)	62.27	62.22	59.23	66.67	66.68	68.41	67.40	67.91	66.37
	61.24			67.25			67.23		
Dry H (%)	7.97	7.96	7.30	6.73	7.09	7.54	6.51	6.39	6.07
	7.74			7.12			6.32		
Dry N (%)	4.94	4.58	3.52	3.23	3.59	3.16	3.27	3.20	3.23
	4.35			3.33			3.23		
Dry O (%)	17.54	18.08	25.98	15.70	14.52	13.85	13.47	13.45	17.83
	20.54			14.69			14.91		
dry H/C	0.13	0.13	0.12	0.10	0.11	0.11	0.10	0.09	0.09
	0.13			0.11			0.09		
dry O/C	0.28	0.29	0.44	0.24	0.22	0.20	0.20	0.20	0.27
	0.34			0.22			0.22		

Table A- 10: Key properties for secondary torrefaction study (type A)

Temp (°C)	200						250						300					
Time (min)	0		30		60		0		30		60		0		30		60	
Mass of raw sample (g)	25.06	25.01	25.46	25.39	24.99	25.41	25.18	24.9	25.64	25.41	25.42	25.39	25.08	24.99	25.08	25.24	25.15	25.45
Mass of torrefied sample (g)	24.5	24.6	23.63	23.76	22.59	23.23	24.08	23.69	18.86	19.67	17.72	18.25	20.37	19.95	13.77	13.52	13.08	14.06
Mass yield (%)	97.77	98.36	92.81	93.58	90.40	91.42	95.63	95.14	73.56	77.41	69.71	71.88	81.22	79.83	54.90	53.57	52.01	55.25
	98.06 (mean)		93.20		90.91		95.39		75.48		70.79		80.53		54.24		53.63	
Moisture (%)	4.40	3.78	3.44	3.12	3.14	4.12	3.67	2.93	2.77	3.78	3.55	2.91	3.61	2.93	3.28	2.74	3.99	3.89
	4.09		3.28		3.63		3.30		3.27		3.23		3.27		3.01		3.94	
VM (%)	69.02	69.55	68.35	68.29	67.16	66.57	69.13	68.93	58.79	61.94	56.17	58.71	63.89	64.65	45.73	44.59	42.18	43.89
	69.29		68.32		66.87		69.03		60.37		57.44		64.27		45.16		43.04	
FC (%)	20.88	21.06	22.21	22.93	23.76	23.07	21.66	22.62	30.50	26.79	30.76	30.44	25.65	25.41	41.01	41.56	41.49	42.28
	20.97		22.57		23.42		22.14		28.65		30.60		25.53		41.29		41.89	
Ash (%)	5.66	5.60	5.99	5.63	5.93	6.21	5.52	5.50	7.91	7.45	9.47	7.86	6.84	7.01	9.99	11.12	12.32	9.92
	5.63		5.81		6.07		5.51		7.68		8.66		6.92		10.55		11.12	
Dry ash (%)	5.92	5.81	6.20	5.81	6.12	6.48	5.73	5.66	8.14	7.74	9.82	8.09	7.10	7.22	10.32	11.43	12.83	10.32
	5.87		6.01		6.30		5.70		7.94		8.96		7.16		10.88		11.58	
DAF VM (%)	23.22	23.24	24.52	25.13	26.13	25.73	23.85	24.70	34.15	30.18	35.37	34.11	28.64	28.21	47.28	48.24	49.57	49.05
	23.23		24.83		25.93		24.28		32.16		34.74		28.43		47.76		49.31	
DAF FC (%)	76.74	76.75	75.47	74.84	73.85	74.24	76.13	75.28	65.82	69.77	64.58	65.79	71.34	71.78	52.72	51.76	50.40	50.92
	76.74		75.15		74.05		75.70		67.80		65.19		71.56		52.24		50.66	
HHV (MJ/kg)	20.666	20.742	21.597	21.550	22.078	21.899	21.185	21.119	24.456	23.974	24.990	24.958	23.453	23.762	26.291	26.353	25.930	25.983
	20.704		21.574		21.989		21.152		24.215		24.974		23.608		26.322		25.957	
Energy yield (%)	97.30	98.26	96.54	97.12	96.12	96.42	97.57	96.77	86.64	89.38	83.90	86.40	91.74	91.36	69.52	67.98	64.95	69.13
	97.78		96.83		96.27		97.17		88.01		85.15		91.55		68.75		67.04	

Appendix 5 – Full data sets: Leaching

Table A-11: Inorganic content (XRF) from primary leaching study (type B)

Leaching temp (°C)	20											
Torr. state	UT			LT			MT			HT		
K (%)	0.94	0.88	0.88	1.32	1.54	1.38	4.75	5.39	5.03	8.09	7.78	8.46
	0.90 (mean)			1.41			5.06			8.11		
Ca (%)	1.27	1.15	1.2	1.2	1.37	1.26	1.39	1.25	1.39	1.35	1.29	1.41
	1.21			1.28			1.34			1.35		
Mg (%)	0.16	0.15	0.16	0.24	0.25	0.24	0.47	0.48	0.47	0.51	0.49	0.56
	0.16			0.24			0.47			0.52		
P (%)	0.21	0.19	0.17	0.83	0.99	0.92	1.8	1.94	1.88	1.89	1.88	2.03
	0.19			0.91			1.87			1.93		
Cl (%)	0.04	0.03	0	0	0.05	0.04	0.35	0.45	0.36	0.76	0.85	0.78
	0.02			0.03			0.39			0.80		
S (%)	0.63	0.56	0.61	0.51	0.51	0.57	0.29	0.25	0.27	0.14	0.13	0.14
	0.60			0.53			0.27			0.14		

Leaching temp (°C)	35											
Torr. state	UT			LT			MT			HT		
K (%)	0.68	0.64	0.75	0.9	0.99	0.79	3.48	3.98	3.57	7.49	8.59	7.97
	0.69			0.89			3.68			8.02		
Ca (%)	1.23	1.15	1.32	1.21	1.35	1.39	1.55	1.37	1.4	1.32	1.46	1.46
	1.23			1.32			1.44			1.41		
Mg (%)	0.13	0.12	0.16	0.18	0.21	0.2	0.49	0.48	0.47	0.52	0.64	0.62
	0.14			0.20			0.48			0.59		
P (%)	0.17	0.17	0.16	0.71	0.88	0.79	1.92	1.77	1.76	1.9	2.26	2.22
	0.17			0.79			1.82			2.13		
Cl (%)	0	0	0.07	0	0.05	0.05	0.21	0.27	0.21	0.77	0.83	0.83
	0.02			0.03			0.23			0.81		
S (%)	0.57	0.59	0.63	0.49	0.49	0.43	0.29	0.23	0.25	0.14	0.17	0.14
	0.60			0.47			0.26			0.15		

Leaching temp (°C)	50											
Torr. state	UT			LT			MT			HT		
K (%)	0.37	0.43	0.51	0.46	0.47	0.5	2.1	3.09	2.13	7.22	7.69	6.84
	0.44			0.48			2.44			7.25		
Ca (%)	1.22	1.2	1.29	1.29	1.45	1.43	1.48	1.63	1.57	1.51	1.69	1.53
	1.24			1.39			1.56			1.58		
Mg (%)	0.14	0.15	0.15	0.2	0.22	0.21	0.44	0.47	0.48	0.62	0.64	0.56
	0.15			0.21			0.46			0.61		
P (%)	0.14	0.17	0.2	0.63	0.76	0.71	1.66	1.7	1.65	2.21	2.3	2.1
	0.17			0.70			1.67			2.20		
Cl (%)	0	0	0.03	0	0.04	0.04	0.12	0.2	0.09	0.8	0.78	0.68
	0.01			0.03			0.14			0.75		
S (%)	0.58	0.6	0.64	0.5	0.47	0.55	0.28	0.23	0.24	0.17	0.18	0.15
	0.61			0.51			0.25			0.17		

Table A-12: Leachate properties (net, after 24 h) from primary torrefaction study

Leaching temp (°C)	20											
Torr. state	UT			LT			MT			HT		
K (mg/L)	222.4	222.1	223.4	225.1	216.5	220.4	153.0	130.8	214.8	41.1	40.8	48.1
	222.6 (mean)			220.7			166.2			43.3		
Mg (mg/L)	23.3	22.8	24.0	16.9	15.8	16.9	2.7	1.9	16.5	0.5	0.5	0.6
	23.4			16.6			7.0			0.5		
P (mg/L)	71.1	67.5	68.9	44.3	40.1	45.3	11.1	8.5	43.6	1.4	1.3	2.1
	69.2			43.2			21.1			1.6		
Cl (mg/L)	13.1	12.7	13.4	14.0	14.0	14.1	10.8	9.2	14.1	4.0	4.4	5.3
	13.0			14.0			11.4			4.6		
PO4 (mg/L)	15.7	16.4	17.8	9.8	8.8	10.3	2.1	1.6	10.0	0.0	0.0	0.0
	16.6			9.6			4.5			0.0		
EC (µS/cm)	444	436	467	454	440	458	309	248	288	92	91	107
	449			451			282			97		

Leaching temp (°C)	35											
Torr. state	UT			LT			MT			HT		
K (mg/L)	229.6	229.5	226.9	235.3	230.7	220.6	179.1	163.6	175.9	75.0	69.3	67.6
	228.7			228.9			172.9			70.6		
Mg (mg/L)	25.6	25.1	26.0	20.5	17.1	17.7	3.1	2.4	2.7	1.0	0.9	0.9
	25.6			18.4			2.7			1.0		
P (mg/L)	70.5	73.2	72.7	52.6	42.9	46.0	15.8	12.6	14.1	3.6	3.1	2.9
	72.2			47.2			14.2			3.2		
Cl (mg/L)	12.7	12.7	12.5	13.8	13.8	13.5	13.6	12.0	12.8	6.1	6.1	6.3
	12.6			13.7			12.8			6.2		
PO4 (mg/L)	4.2	4.1	4.6	4.9	4.4	4.5	2.2	1.8	2.1	0.7	0.0	0.0
	4.3			4.6			2.0			0.2		
EC (µS/cm)	530	515	517	481	458	449	368	334	359	153	143	142
	521			463			354			146		

Leaching temp (°C)	50											
Torr. state	UT			LT			MT			HT		
K (mg/L)	254.2	242.8	238.9	248.1	252.2	261.4	230.2	202.1	233.8	112.5	119.0	112.0
	245.3			253.9			222.0			114.5		
Mg (mg/L)	27.0	27.1	25.6	21.6	21.2	23.0	4.6	2.9	4.2	1.2	1.5	1.3
	26.6			21.9			3.9			1.3		
P (mg/L)	73.1	76.3	72.2	56.5	56.4	58.9	25.8	17.4	24.6	6.0	6.6	5.6
	73.8			57.3			22.6			6.1		
Cl (mg/L)	13.1	13.2	13.1	14.2	14.3	14.2	17.5	14.8	18.0	8.6	9.5	8.4
	13.1			14.3			16.8			8.8		
PO4 (mg/L)	14.2	15.4	5.1	5.1	5.2	7.9	3.3	2.0	3.1	0.7	0.9	0.7
	11.6			6.1			2.8			0.8		
EC (µS/cm)	532	514	496	481	493	492	445	388	441	221	239	225
	514			489			425			228		

Table A-13: Inorganic content (XRF) from secondary leaching study (type A)

Torr. state	UT											
Particle size	<1 mm (fine)						1–2.36 mm (medium)					
Leaching temp (°C)	Unleached			35			Unleached			35		
K (%)	6.59	6.56	6.77	0.54	0.42	0.49	5.66	5.36	5.67	0.48	0.53	0.51
	6.64 (mean)			0.48			5.56			0.51		
Ca (%)	0.91	0.91	0.97	1	0.85	0.96	0.83	0.78	0.93	0.85	0.8	1.07
	0.93			0.94			0.85			0.91		
Mg (%)	0.36	0.38	0.43	0.13	0.12	0.13	0.32	0.33	0.33	0.16	0.15	0.16
	0.39			0.13			0.33			0.16		
P (%)	1.38	1.32	1.37	0.18	0.15	0.14	1.2	1.14	1.21	0.24	0.15	0.19
	1.36			0.16			1.18			0.19		
Cl (%)	0.69	0.9	0.74	0	0	0	0.81	0.82	0.73	0	0.02	0
	0.78			0.00			0.79			0.01		
S (%)	0.58	0.58	0.55	0.44	0.36	0.4	0.56	0.51	0.55	0.41	0.36	0.38
	0.57			0.40			0.54			0.38		

Appendix 6 – Regression plots for HHV vs DAF FC content

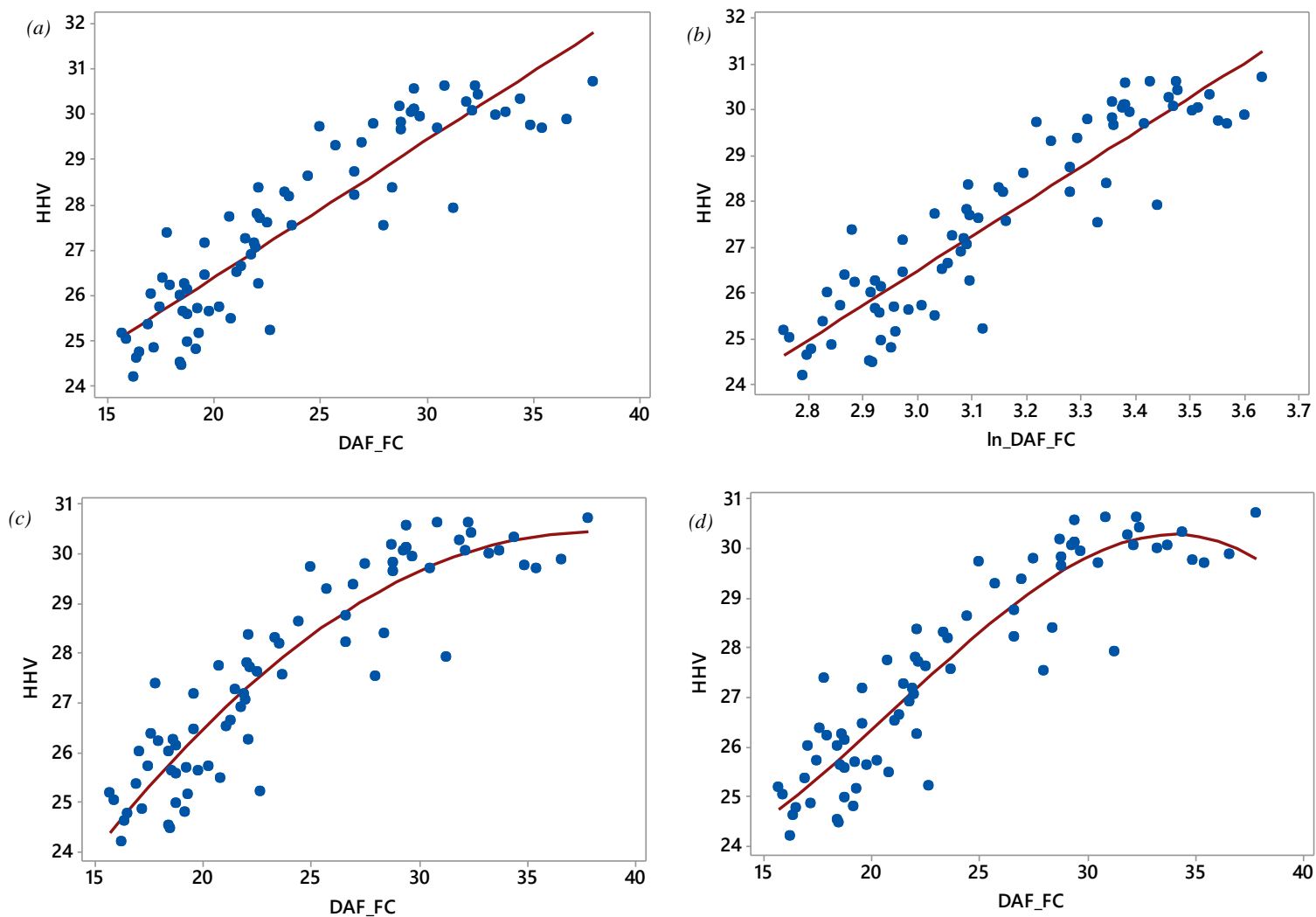


Figure A6-1: Regression plots for torrefied type B seed cake: (a) linear, (b) linear logarithmic, (c) quadratic, (d) cubic models.

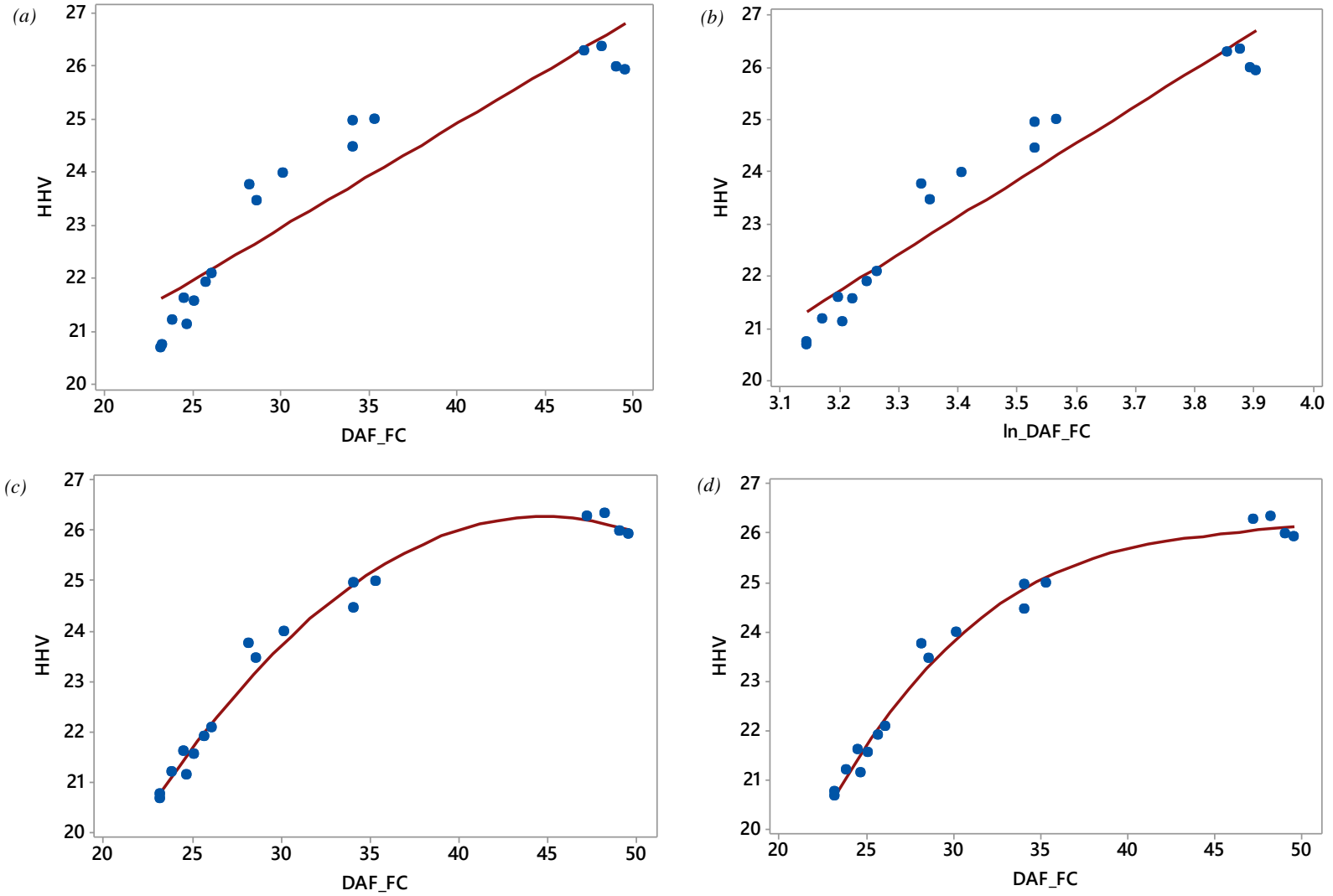


Figure A6-2: Regression plots for torrefied type A seed cake: (a) linear, (b) linear logarithmic, (c) quadratic, (d) cubic models.

Appendix 7 – Lenth’s pseudo-standard-error

Lenth’s pseudo-standard error (PSE) is based on the assumption that the variation in the smallest effects is caused by random error, i.e. the concept of “sparse effects”.

The standard deviation, S , of a sample with a normal distribution can be calculated by:

$$S = 1.5 \times M_1 \quad \text{Eqn A7-1}$$

where M_1 is the median of the effects.

The PSE is taken to be:

$$PSE = 1.5 \times M_2$$

$$PSE = 1.5 \times M_2 \quad \text{Eqn A7-2}$$

where M_2 is the median of the effects, but those effects higher than $2.5 \times S$ are excluded.

The margin of error (ME) with 95% confidence is calculated by:

$$ME = PSE \times t \quad \text{Eqn A7-3}$$

where t is the 0.975th quartile of the t -distribution.

The margin of error is illustrated as the “reference line” in the Pareto charts of effects (see Figure 6-7), with effects higher than this reference line deemed to be significant.

(Lenth, 1989; Minitab, 2016)